UNIVERSITÀ
DEGLI STUDI
FIRENZE

PhD in
Industrial Engineering

CYCLE XXXV

COORDINATOR Prof. Giovanni Ferrara

Multi-Fidelity Simulation of Floating Offshore Wind Turbines: a Critical Comparison

Simulazioni Multi-fidelity di Turbine Eoliche Galleggiati: un Confronto Critico

Academic Discipline (SSD) ING-IND/09

Doctoral Candidate
Dr. Papi Francesco

Supervisor
Prof. Ferrara Giovanni

Coordinator
Prof. Ferrara Giovanni

Years 2019/2023

Università degli Studi di Firenze, Dipartimento di Ingegneria Industriale (DIEF).

Acknowledgments

Un ringraziamento sincero ad Alessandro Bianchini e Giovanni Ferrara, che hanno creduto in me fin dal primo giorno e mi hanno incoraggiato lungo tutto il tragitto senza mai dubitare. Grazie a Francesco Balduzzi, che mi ha guidato e consigliato, soprattutto nei primi difficili mesi. Grazie a Carla e alla mia famiglia che mi hanno supportato nei momenti più duri. Grazie ai ragazzi del gruppo REASE, miei compagni di viaggio, che hanno reso il tragitto più leggero. Il dottorato che ho intrapreso è stata, di gran lunga, la mia esperienza più difficile. Guardando indietro, la rifarei cento volte ancora.

Abstract

Floating Offshore Wind Turbines are one of the most promising technologies to increase energy harvested from the wind worldwide. These machines are designed to harvest the abundant wind resource available in deep waters where installation of fixed-bottom offshore turbines would be too expensive. Floating wind turbines are challenging to design and operate as their dynamic behavior depends on the influence of many coupled physics. In fact, in addition to the wind-induced aerodynamic actions, wave-induced hydrodynamic forces and control also influence the response of the system. Moreover, modern multi-MW rotors feature large flexible blades and therefore loading also depends on the elasto-dynamic characteristics of the elements. In comparison to onshore wind turbines, floating offshore turbines introduce additional challenges, since the turbine is now allowed to move as it is supported by a floating foundation. Reliable numerical models are crucial, as these machines have to operate for extended periods of time with minimal maintenance and low costs. Therefore, accurate prediction of extreme and fatigue design loads is pivotal to optimize these machines and lower levelized cost of energy. In this thesis, multi-fidelity numerical models for the simulation of wind turbines are critically compared. Most of the focus is put on aerodynamics. In fact, many state-of-the-art medium fidelity codes, that are widely adopted during the design and certification phases of wind turbines, rely on Blade element Momentum theory. These models need several empirical corrections to reproduce the unsteady behavior of a floating rotor, which is introduced by the additional degrees of freedom afforded by floating installation. In the first phase of this work, multi-fidelity aerodynamic models, ranging from momentum theory to computational fluid dynamics are compared to experiments on a rotor undergoing unsteady pitch and surge motion. All the compared theories behaved well, but differences emerged if rotor speed and blade pitch oscillations were introduced and during operation in low wind speeds. In particular, the dynamic wake engineering correction for blade element momentum theory that was tested performed well, and was able to improve the agreement to higher fidelity models of rotor force predictions. In the second phase, complexity is increased and comparisons on a wave-basin experimental test case are performed. During this phase all of the tested models were able to reproduce the dynamic behavior of the system comparatively well. In the final phase, code-to-code comparisons in realistic inflow conditions are discussed. In these tests, the influence of the multi-fidelity aerodynamic modeling is apparent in fatigue loads, with blade element momentum theory based models consistently predicting higher fatigue loading. The influence of the structural modeling on the other hand is apparent in both fatigue and extreme loads. As discussed in detail within this work, OpenFAST, that features a modal-based structural model, shows large undamped response in absence of aerodynamic damping, impacting both extreme and fatigue loads.

Abstract

Le turbine eoliche galleggianti rappresentano una delle più promettenti tecnologie volte all'incremento della produzione mondiale di energia eolica, in quanto tali macchine sono progettate per sfruttare i forti venti presenti offshore. In particolare, questa tecnologia permette di sfruttare per la produzione di energia eolica zone di mare profonde, troppo costose per le tradizionali turbine offshore bottom-fixed. Tuttavia, le turbine eoliche galleggianti sono particolarmente complesse da progettare e gestire in quanto il loro comportamento dinamico dipende dalla simultanea e reciproca influenza di vari fattori. Tra questi, in aggiunta all'azione aerodinamica del vento, deve esser considerata anche l'azione idrodinamica dal mare e l'influenza del sistema di controllo. Inoltre, a causa della loro dimensione, le pale delle moderne turbine eoliche sono molto flessibili, e conseguentemente, le loro caratteristiche elastiche influenzano la dinamica del sistema. In confronto a turbine eoliche onshore, le turbine eoliche galleggianti comportano delle complicazioni aggiuntive, in quanto l'installazione su piattaforme di tipo galleggiante introduce delle significative non-stazionarietà, causate dagli ulteriori gradi di libertà che questo tipo di installazione comporta. In questo contesto, disporre di modelli numerici affidabili è fondamentale, in quanto queste macchine sono progettate per avere una lunga vita utile, con bassi costi di realizzazione e manutenzione. Per soddisfare queste esigenze e ridurre il costo dell'energia prodotta, si rende indispensabile una accurata previsione dei carichi di punta e affaticanti dei vari componenti della macchina. In questa tesi sono confrontati modelli numerici multi-fidelity per la simulazione di turbine eoliche galleggianti. Al centro del confronto sono i modelli aerodinamici. Infatti, in molti moderni codici numerici, la modellazione dell'aerodinamica è basta sulla teoria Blade Element Momentum, che necessita di esser corretta ed estesa tramite sottomodelli empirici in modo da poter modellare le condizioni non-stazionarie tipiche delle turbine eoliche galleggianti. Durante la prima fase di questo lavoro, vari modelli aerodinamici sono confrontati rispetto a misure sperimentali di un rotore sottoposto ad oscillazioni armoniche, da semplici modelli Blade Element Momentum a modelli basati su fluidodinamica computazionale. Tutte le teorie confrontate hanno mostrato buoni risultati, ma alcune differenze sono emerse in presenza di contemporanee oscillazioni armoniche di velocità di rotazione o calettamento delle pale oppure in test con basse velocità del vento. In particolare, la correzione per adattare la teoria blade element momentum a condizioni di flusso non stazionarie ha prodotto buoni risultati, migliorando l'accordo di tale teoria con modelli più accurati. Successivamente, sono stati effettuati confronti su un modello in scala galleggiante, per il quale sono disponibili risultati sperimentali ricavati in una vasca di prova. Durante questa fase tutti i modelli numerici hanno prodotto risultati simili, con un grado di accordo rispetto agli esperimenti confrontabile. Nella fase finale del lavoro i codici numerici sono stati confrontati in condizioni di vento e di mare realistiche. I risultati hanno evidenziato delle differenze tra le teorie aerodinamiche nella predizione dei carichi affaticanti, con modelli basati sulla teoria blade element momentum che hanno predetto carichi più elevati. L'influenza del modello strutturale è stata notata sia nei carichi affaticanti che nei carichi massimi. Infatti, in quei casi in cui non è presente smorzamento aerodinamico, il modello strutturale di tipo modale in OpenFAST ha mostrato grandi oscillazioni alle frequenze di risonanza dei vari componenti strutturali della macchina.

Contents

List of Figures

List of Tables

Glossary

C_P Power Coefficient. 20, 62

C_T Thrust Coefficient. 20, 55, 62

C_d Drag Coefficient. 11

C_l Lift Coefficient. 11

C_n Normal Force Coefficient. 24

a Axial Induction Factor. 5

ALM Actuator Line Model. 11, 24, 26, 36, 52, 55, 129, 130

AMR Active Mesh Refinement. 27

BEM Blade Element Momentum. 5, 7, 9, 17, 24, 36, 48, 51, 55, 56, 57, 60, 116, 129

CFD Computational Fluid Dynamics. 12

DBEM Dynamic Blade Element Momentum. 14, 24, 36, 55, 60, 95, 116, 129

DEL Damage Equivalent Load. 116, 120, 127

DLC Design Load Case. 89

DOF Degree Of Freedom. 19, 20

DTU Danish Technical University. 1, 19

ECN École Centrale Nantes. 93, 95

ESS Extreme Sea State. vii, 88, 90

FOWT Floating Offshore Wind Turbine. 5, 7, 14, 15, 19, 63, 64, 116

HAWT Horizontal Axis Wind Turbine. 15

HPC High Performance Computing. 30

HWA Hot Wire Anemometry. ix, 21, 22

IEA International Energy Agency. 19

IFORM Inverse First Order Reliability Method. xii, 88, 89

LLFVW Lifting Line Free Vortex Wake. 9, 15, 24, 25, 36, 52, 55, 60, 95, 116, 129, 130

LPMD Linear Potential Morrison Drag. 64, 95

MARIN MAritime Research Institute Netherlands. 61

MSL Mean Sea Level. 65

NREL National Renewable Energy Laboratory. 14, 63

NSS Normal Sea State. vii, 86, 87, 90

OLAF cOnvection LAgrangian Filaments. 9, 15, 25

PDF Probability Density Function. 84

PIV Particle Image Velocimetry. ix, 21, 22

PoliMi Politecnico di Milano. ix, 19, 20, 22, 23, 31, 35

QTF Quadratic Transfer Function. 63, 64, 95

REASE Reciprocating Engines and Advanced Systems for Energy (REASE). 12

SiL Software in the Loop. 93

SSS Severe Sea State. vii, 87, 88, 90

TNO The Netherlands Organisation for Applied Research. 19

TSR Tip Speed Ratio. 34, 48, 130

TUB Technical University Berlin. 15, 63

UDF User Defined Function. 26

UNAFLOW UNsteady Aerodynamics for FLOating Wind. 19

UNIFI University of Florence. 12

Synopsis

Backgroud

Many governments and institutions around the world have pledged to drastically reduce green house gas emissions in the coming decades. Decarbonization of the energy sector is key to reaching the 2050 net-zero emission goals that many countries have set upon themselves. Reaching such goals will require wind energy to grow from the approximately 5% of global electricity share it holds now up to 35%-50% by 2050 [1] [2]. In addition to being a clean energy source, wind energy can be domestically produced in many parts of the world, ensuring energy stability and independence. Moreover, it also complements solar power in terms of seasonal and diurnal production.

Turning wind energy from the cost-competitive intermittent energy source it is today, into a stable, low cost abundant energy source it is envisioned to be in the future requires bridging several technological and socio-economic gaps. From a R&D perspective, a panel of experts has recently identified three main topics, summarized by Veers et al. (2019): *"(i) improved understanding of the physics of atmospheric flow in the critical zone of wind power plant operation, (ii) materials and system dynamics of individual wind turbines, and (iii) optimization and control of fleets of wind plants comprising hundreds of individual generators working synergistically within the larger electric grid system."* [3]. This work was recently expanded into a series publications, focusing on the technical aspects involved in addressing these Grand Challenges [1]. Within this work, Floating Offshore Wind (FOW) is seen as one of the most promising technologies to harvest wind energy offshore [4], in water depths greater than 60 m [3]. In fact, wind resource is abundant offshore: as shown in the International Energy Report redacted by DTU [2], offshore wind turbines have, on average, a higher capacity factor than onshore turbines.

FOW is currently a novel technology. The first wind farms have only recently been deployed and they are currently small scale, mostly demonstrative projects, featuring a small number of turbines. This is the case, for instance, of Hywind Scotland [5], Hywind Tampen and WindFLoat Atlantic [6] projects. The green state of the technology is also demonstrated by the fact that more than seventy floater concepts have been proposed or are currently being developed and tested, indicating that the industry has still to converge on the most cost-effective and well proven concepts. From a technical perspective, the dynamics of Floating Offshore Wind Turbines (FOWTs) are complex as these structures are placed in an offshore environment and are thus subject to the combined actions of

wind and waves. As noted in [3], while the technical challenge of designing and operating large offshore structures is not new, in particular the energy industry has been building and operating offshore oil and natural gas rigs for decades, the problem of floating wind poses new challenges as these systems experience large motions and coupled dynamics at a scale that was not assessed previously. In fact, aerodynamic forces induce floater motions and vice-versa the hydrodynamic-induced platform motions cause the apparent inflow on the rotor to change, influencing aerodynamic forcing: the problem is fully coupled. These aspects are compounded by the size of these machines. Industrial prototypes are quickly reaching and surpassing 15MW in size, with rotor diameters up to 240 m.

The need for multi-fidelity modelling

In this context, understanding the limitations and applicability of the simulation and design tools that are used to develop and optimize these offshore structures is crucial. In fact, any innovation and technical solution is arguably only as good as the tools that were used to envision it are. This is particularly true in the case of wind turbines, that can be unfeasible to study experimentally. In fact, the correct simultaneous scaling of the structural and aerodynamic characteristics is very difficult. Moreover, these machines are subject to stochastic environmental conditions, which can also complicate experimental studies. Multi-fidelity tools are used in the wind turbine industry in order to address the various needs of wind turbine and wind farm designers. One of the biggest challenges in this field is the staggering amount of physical scales that are involved. In fact, from an aerodynamic perspective alone, scales range from the boundary layer height on the blade, that is millimeters tall, up to entire wind farms that are up to kilometers in size. At even larger scales, as wind energy penetration increases, and larger and larger wind farms are developed, their interaction at a mesoscale level becomes a topic of interest [1].

To address the multiple scales of the problem, multi-fidelity models are needed. The limits of current models do not allow for computationally efficient omni-comprehensive models, and the various strengths and weaknesses of the theories need to be played into depending on the specific needs and interests.

High fidelity models are used to better understand underlying physics and for wind turbine wakes and wind farm interactions, but require High Performance Computing (HPC) resources. This level of computational power is still rare at industrial level, and would anyhow be able to handle only a number of simulations much lower than that needed in certification process of extended energy assessments. Mid-fidelity models require significantly less computational resources, and can be typically run real-time on a desktop workstation. They are used to evaluate the response of these systems to specific combinations of environmental inputs. These models are used during the turbine certification process, through which the reliability of floating designs is assessed by a certification body, and where tens of thousands of simulations are routinely performed. Finally low-fidelity models, which use frequency-based approaches or engineering surrogate models, are used for design exploration. Each model tier is tuned and validated against the respective higher fidelity tier [4].

Aerodynamics of FOWTs

Within the research community, many are questioning the validity and applicability of the aerodynamic theories used in medium-fidelity engineering tools. Aerodynamic models based on Blade Element Momentum Theory (BEMT) are still at the core of many design codes. With certain assumptions, BEMT allows for the effects of the wind turbine's wake on the inflow local to the rotor blades to be estimated. Thereafter, aerodynamic loads can be determined using blade element theory: assuming that each blade section behaves as a 2-D airfoil. The added value of BEMT is that it allows a fundamental understanding of the effects of varying geometrical and aerodynamic parameters on a wind turbine [7]. It also works very well in practice, which is undoubtedly important in engineering. The limitations of this aerodynamic theory are however apparent. As explained in detail in the following, various engineering models have been developed and implemented into BEM-based aerodynamic models to extend their range of validity. For instance, empirical corrections have allowed to extend these models to compute aerodynamic loads in the vortex ring state (VRS) or turbulent wake state (TWS), as defined in section 1.5.1. Empirical corrections to model tip and root losses, non-uniform inflow and unsteady inflow and skewed flow are also introduced into most design-level BEM-based codes. Critical comparisons of medium-fidelity aerodynamic theories on onshore rotors have been performed in the past, examples of which are the studies by Perez-Becker et al. [8] and Boorsma et al. [9]. While BEM-based models have been found to perform adequately, some deficiencies in the prediction of cyclic loads are highlighted.

Floating wind turbines introduce additional challenges from an aerodynamic standpoint as the rotor is subject to unsteady motion. Some authors have highlighted how rotor-wake interaction is possible in a FOWT due to the rotor rocking in and out of its own wake [1]. This phenomenon was observed in numerical simulations by [10] and [11], when simulating high frequency and high amplitude platform oscillations in the wind heading direction - i.e. surge or pitch oscillations. This is seen as a source of concern as if rotor-wake interaction occurs, the streamtubes upon which the momentum balance is applied are effectively chocked and momentum theory is invalid. Moreover, some have come to the conclusion that in the case of severe oscillations, the rotor may enter wake states where momentum theory is invalid, such as the TWS or VRS. The underlying assumption when applying momentum theory to a rotor is that it is in an inertial reference frame. Momentum balance is applied in the rotor reference frame, and because the rotor is static or moving with constant speed (this could be the case for a helicopter rotor), rotor movement is treated the same way as wind speed is, as its only effect is to introduce an apparent wind speed on the rotor itself. When the rotor motion becomes unsteady, the reference frame is not inertial and a momentum balance cannot be performed in such a reference frame. Based on this consideration, Ferreira et al. [12] proposed to apply the momentum balance for a FOWT in the static reference frame and developed a correction to account for the dynamic inflow.

It must be noted that applying the momentum balance in the rotor, non-inertial frame, is effectively no different from considering unsteady inflow on the rotor. This condition is routinely treated in BEM models, and engineering corrections for dynamic inflow exist to

extend the validity of BEM to these conditions. Moreover, although momentum theory is invalid when the rotor enters TWS of VRS, empiric corrections such as Glauert's correction for TWS [13] are implemented into engineering codes. Therefore, if the rotor enters such states as a consequence of unsteady motion and the way the momentum balance is applied, it is the validity of these engineering corrections that should be challenged, rather than momentum theory itself.

Outline

This work aims at better understanding the validity and applicability of various medium-fidelity wind turbine simulation codes to FOWTs. A comparative, multi-fidelity study is performed on three levels. At each level complexity and the amount of physics involved increase. In Chapter 1, the numerical wind turbine simulation models that are used in this study are introduced. In Chapter 2, aerodynamic loads on an oscillating rotor tested in the wind tunnel are compared. Simplified harmonic oscillations in pitch and surge are considered, in order to isolate unsteady aerodynamic effects from the rest of the coupled physics involved. Blade Element Momentum Theory based models are compared to results from a Lifting-Line Free Vortex Wake (LLFVW) model, an Actuator Line Model (ALM) and experiments. In Chapter 3, BEM-based and LLFVW codes are compared to experimental results of wave-tank model tests performed during the OC5 Phase II campaign. The ability of the numerical models to capture the coupled influence of aerodynamic and hydrodynamic loads is evaluated herein. The results are also explained and the dynamic response of the system is described in detail. Finally in Chapter 4, code-to-code comparisons in realistic environmental conditions are performed. In this section a LLFVW model is compared to a BEM model in several hundreds of combinations of sea and wind conditions. Performance metrics as well as design and fatigue loads on key components of the structure are comparatively analyzed. In this section the impact of different fidelity structural models is also evaluated, as the LLFVW code uses a multi-body FEA model, while the BEM code features a more basic modal-based model. The analysis performed in this thesis find that DBEM models perform well if compared to higher fidelity theories. However, some deficiencies, such as general over-estimation of cyclic loads, remain, and the use of higher fidelity vortex-based models (for example LLFVW) is suggested when possible.

Chapter 1

Introduction to Numerical Methods for Wind Turbine Simulation

Over the years, many numerical methods for the simulation of wind turbines have been developed. Reproducing the behavior of a FOWT, involves solving many coupled phisics, such as aerodynamics, structural dynamics, hydrodynamics, moorings and control. Arguably, at the core of every wind turbine are the aerodynamics, as these machines are specifically built to extract energy from the wind through aerodynamically shaped rotor blades. In this context, this work is focused on comparing multi-fidelity aerodynamic models. Different structural models are also compared, but the core-focus remains on aerodynamics. This Chapter provides an introduction to numerical models for the simulation of wind turbines. The introduction is limited to the methods that are relevant to the results and discussion contained in the following Chapters. The basics of the aerodynamic wake models that are used are introduced first. Some theoretical aspects relevant to the interpretation of the results of this work are then presented: the concept of wake state and the wake memory effect. Finally, the main features of the aero-hydro-servo-elastic wind turbine simulation codes that are compared in this manuscript will be discussed.

1.1 Blade Element Momentum Theory

Blade Element Momentum combines momentum theory with blade element theory to model the effects of a turbine or propeller's wake on the rotor itself. According to blade element theory, the wind turbine blade is broken up into a series of elements that can be modeled two dimensionally. Each blade elements acts upon an annulus of the rotor. The blade elements apply a force to the fluid in each annulus, therefore slowing the fluid down. To model this effect, the induction factor a is introduced. For each annulus, this parameter relates the velocity on the rotor plane W is related to the undisturbed velocity U:

$$W = (1 - a)U \tag{1.1}$$

On each annulus, often referred to as streamtube, a momentum balance is applied according to momentum theory. An important implication is that the annuli are thus

considered independent from one-another and no radial flow interaction is considered. By equating the force balance on each annulus obtained through momentum theory and that obtained through blade element theory, we obtain the blade element momentum theory solution equation:

$$2a(1-a)\rho U^2(2\pi r dr) = \frac{1}{2}N_b\rho W^2 C_n \tag{1.2}$$

where r is the local blade element radius, U is the undisturbed wind inflow velocity, N_b is the number of blades of the rotor, W is the local inflow velocity and C_n and C_t are defined as the normal and tangential force coefficients:

$$C_n = C_l cos\phi + C_d sin\phi \tag{1.3}$$
$$C_t = C_l sin\phi - C_d cos\phi \tag{1.4}$$

Lift and Drag coefficients are are often lookup tables from precomputed airfoil data and depend on the angle of attack, that can be defined based on the local inflow angle ϕ, the blade twist angle θ and pitch angle θ_P:

$$C_l = f_L(\alpha, Re) \tag{1.5}$$
$$C_d = f_D(\alpha, Re) \tag{1.6}$$
$$\alpha = \phi - (\theta + \theta_P) \tag{1.7}$$

A graphical representation of a blade element, with flow angles and inflow velocities is shown in Fig. 1.1. The rotor also imparts a tangential swirl to the fluid, which can be accounted for through the tangential induction factor a', which can be defined based on the tangential velocity in the wake V_θ as [14]:

$$a' = V_\theta / 2\Omega r \tag{1.8}$$

The blade-element torque predicted by momentum theory and blade element theory can be written as:

$$4\pi r dr \Omega r U(1-a)a'r = \frac{1}{2}N_b\rho W^2 C_t r \tag{1.9}$$

Equations 1.2 and 1.9 can be solved for the induction factors a and a' for all the rotor annuli. The local velocity can be computed:

$$W^2 = (U_x(1-a))^2 + (U_y(1+a'))^2 \tag{1.10}$$

The problem is thus completely solved and the blade element forces can be obtained for each annulus and integrated along the blades to obtain the rotor's performance characteristics as:

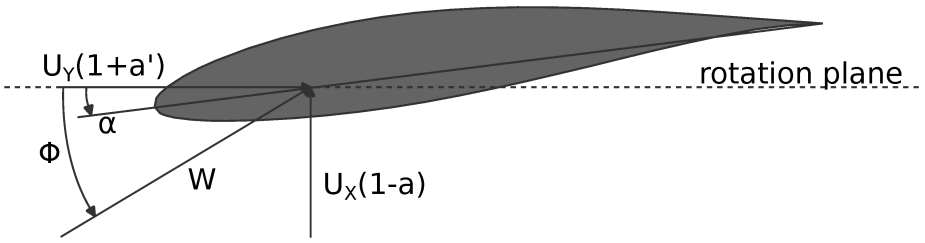

Figure 1.1: graphical representation of the inflow angles and velocities on a blade section

$$F_t = \frac{1}{2} c \rho W^2 C_t(\alpha, Re) \tag{1.11}$$

$$F_n = \frac{1}{2} c \rho W^2 C_n(\alpha, Re) \tag{1.12}$$

This conceptually simple aerodynamic theory neglects several effects that wind turbines are subject to. First and foremost, the theory is valid only for lightly loaded rotors, and is completely non-predictive for axial induction factors greater than 0.4 - 0.5. In this region, axial induction is not derived from equations 1.2 and 1.9 but rather it is modeled empirically through one of the adaptations of Glauert's correction [13]. Wind turbine rotors can, at times, operate in these region, typically when wind speed is low and tip speed ratio is high. Secondly, 3-D effects such as root and tip losses are not accounted for as the stream tubes are radially independent. Moreover, the inflow must be uniform within each stream tube, and thus must be perpendicular to the rotor plane and homogeneous.

1.1.1 BEMT Implementation in AeroDyn

Most of these hypothesis are relaxed in most BEM implementations. The BEM implementation of AeroDyn v15, the aerodynamic module that is part of OpenFAST and used in this dissertation, will be discussed in the following, and is explained in great detail in [15], [16].

Equations 1.5, 1.6 and 1.7 remain valid. Equation 1.10 also remains valid. However, U_x and U_y include the structural velocities due to deformations in aeroelatic calculations, or in the case of a FOWT, rigid displacement velocities due to platform motion. As for inflow velocities, the velocity local to each blade section is used, allowing for non-homogenous inflow. Finally, one last important consideration is that the equations discussed in the following are applied separately for each blade, effectively allowing for different induction factors for each blade.

AeroDyn uses Prandt's hub and tip loss model defined first as:

$$F_{tip} = \frac{2}{\pi} arccos\left(exp\left(-\frac{B}{2}\left(\frac{R-r}{r|sin\phi|}\right)\right)\right) \tag{1.13}$$

$$F_{hub} = \frac{2}{\pi} arccos\left(exp\left(-\frac{B}{2}\left(\frac{r-R_{hub}}{r|sin\phi|}\right)\right)\right) \tag{1.14}$$

$$F = F_{tip}F_{hub} \tag{1.15}$$

Two non-dimensional parameters can be defined as:

$$k = \frac{\sigma' C_n}{4Fsin^2\phi} \tag{1.16}$$

$$k' = \frac{\sigma' C_t}{4Fsin\phi cos\phi} \tag{1.17}$$

If $\phi > 0$ and $k <= 2/3$ the solution lies in the momentum region, and axial induction can be computed as:

$$a = \frac{k}{1+k} \tag{1.18}$$

If $\phi > 0$ and $k > 2/3$ BEM equations are not valid as radial independence of the stream-tubes cannot be assumed. The solution is therefore computed with Buhl's modification of Glauert's correction [13]:

$$a = \frac{\gamma_1 - \sqrt{\gamma_2}}{\gamma_3} \tag{1.19}$$

where γ_1, γ_2 and γ_3 are a function of k and F as shown in [16]. Finally if $\phi < 0$ and $k > 1$, the solution lies in the propeller brake region or vortex ring state and axial induction is computed as:

$$a = \frac{k}{k-1} \tag{1.20}$$

The tangential induction factor is computed, independently of the wake state, as:

$$a = \frac{k'}{1-k'} \tag{1.21}$$

1.1.2 Skewed wake correction

When wind turbine blades are not perpendicular to the wind inflow, skewed inflow effects must be accounted for. From a blade-element perspective, the V_x and V_y components must be corrected to effectively become the velocity normal and tangential to blade element, as shown in [16]. From the momentum perspective, induction needs to be corrected to account for disuniformities across the rotor disk. In AeroDyn this correction is applied using the

Pitt-Peters skewed wake correction model [17], [18]. The correction in based on Glauert's proposal of a non-uniform induction model to better match experimental data [16]:

$$a_{yaw} = \left(1 + K(\chi)\frac{r}{R} sin\psi\right) \tag{1.22}$$

$$K(\chi) = \frac{15\pi}{64} tan\frac{\chi}{2} \tag{1.23}$$

1.1.3 Dynamic wake (DBEMT)

Dynamic inflow effects, as discussed by [19], cannot be modeled by blade element momentum theory and must be included through an empirical correction. A theoretical introduction to the dynamic wake effect can be found in section 1.5.2, while in this paragraph the dynamic wake correction model used in AeroDyn is introduced. In AeroDyn, the correction developed by Øye is used [20]. The induced velocity computed as $V_x = aU$, $V_y = a'U$ with the algorithm discussed in section 1.1.1 and corrected for skewed wake effects as shown in section 1.1.2, are corrected for dynamic inflow effects using two first-order differential equations:

$$V_{int} + \tau_1 \dot{V}_{int} = V_{qs} + k\tau_1 \dot{V}_{qs} \tag{1.24}$$

$$V + \tau_2 \dot{W} = W_{int} \tag{1.25}$$

The time constants τ_1 and τ_2 were calibrated using a vortex model and are needed to model the time-lag on induction caused by the presence of the far wake and near wakes respectively [19]:

$$\tau_1 = \frac{1.1}{1 - 1.3min(\bar{a}, 0.5)} \frac{R}{\bar{U}} \tag{1.26}$$

$$\tau_2 = \tau_1 \left[0.39 - 0.26 \left(\frac{r}{R}^2\right)\right] \tag{1.27}$$

1.2 Lifting Line Free Vortex Wake

In the current work the Lifting Line Free Vortex Wake codes cOnvection LAgrangian Filaments(OLAF) [21] and QBlade [22] are used. Both tools are theoretically based on the work of Van Garrel [23]. Like BEM, LLFVW models the blades through tabulated 2-D airfoil coefficients. Unlike BEM, however, the wake is modeled through vortex elements. As shown in Fig. 1.2, each blade element is modeled through a vortex ring of strength Γ. According to Kutta-Joukouski's theorem for the lift of infinite wings in a potential flow field, the lift per unit span of the blade elements can be written as the vectorial product of the local inflow velocity and the blade element orientation:

$$d\vec{L} = \rho\Gamma(\vec{W}d\vec{l}) \tag{1.28}$$

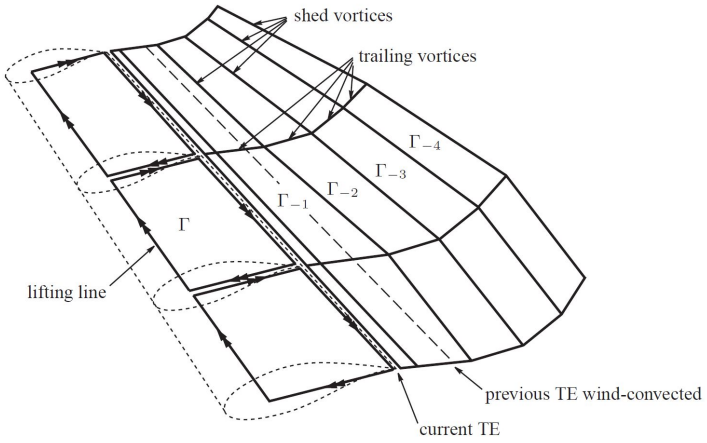

Figure 1.2: wvae and lifling line vorticity discretized into vortex rings. Image from [23].

This can be equated to the lift computed through the blade element's airfoil coefficients:

$$d\vec{L} = \frac{1}{2} c C_l \rho \vec{W}^2 dl \tag{1.29}$$

Equations 1.28 and 1.29 can be equated and solved for the only unknown Γ for each blade element. The local inflow velocity $\vec{W}$ is computed as:

$$\vec{W} = \vec{U} + \vec{U}_{struct} + \vec{U}_{\Gamma} \tag{1.30}$$

At each time step the vortex rings are shed into the wake and form a vortex lattice. The induced velocity $\vec{U}_{\Gamma}$ represents the effect on the rotor of the vortex elements that are shed in the wake and is computed using Biot-Savart law, as shown in [23].

A de-singularization function is needed to avoid the singularity in the induced velocity in correspondence of each vortex filament that would be caused from the direct application of Biot-Savart rule. In Fig. 1.3 the use of a linear regularization function is shown, as used in QBlade. In OLAF, various regularization functions can be used. In this dissertation, the Vatistas method is used [21]. The regularization radius r in Fig. 1.3 is imposed as 5% of the local chord based on experience.

The position of the vortex elements that are shed in the wake depends on the incoming wind speed and the mutual induction of the surrounding wake elements. In other terms, the wake is free to convect downstream, hence the "free vortex wake" denomination of the method.

The strength of the vortex elements Γ remains constant once the vortices have been shed. The viscous dissipation of the vortices is modeled empirically through vortex spreading functions. In practice, this means that the regularization radius r in Fig. 1.3 expands as a function of vortex age, effectively decreasing the strength of the filament itself. In both OLAF [21] and QBlade [22] the viscous core radius is modeled as:

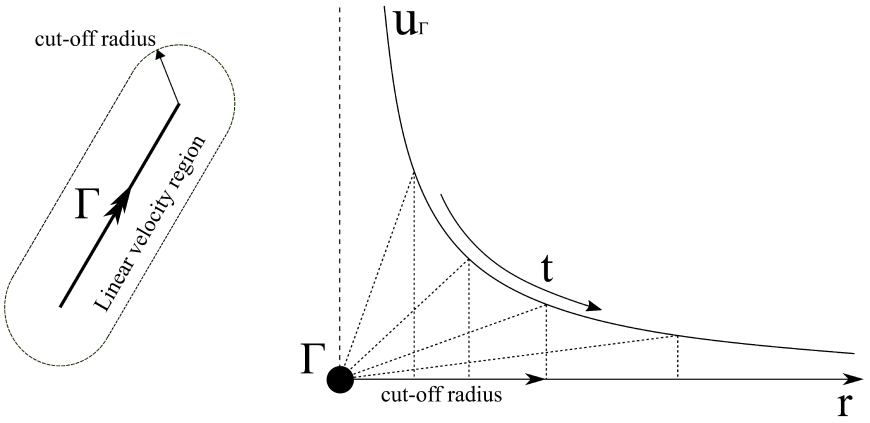

Figure 1.3: Vortex core radius evolution. (left) schematic representation. (right) induced velocity as a function of distance from vortex filament and evolution of linear regularization function as vortex age (t) increases.

$$r_c(\zeta) = \sqrt{r_{c0}^2 + 4\alpha\delta v\zeta} \tag{1.31}$$

Where $\alpha = 1.2564$, v is the kinematic viscosity, and δ is a viscous diffusion parameter, between 1 and 1000.

Although an empirical model is introduced to model the effect of viscous dissipation, the lack of this effect is the main limit of LLFVW methods that are unable to realistically model the far wake.

1.3 Actuator Line Model

The concept of an Actuator Line Model was first proposed by Sorensen and Shen [24], and allows the wind turbine wake to be resolved using Navier-Stokes equations (i.e. Computation Fluid Dynamics), with limited computational cost respect to a full CFD solution. In place of solving the flow around the actual blade geometry, body forces are inserted along each of the rotor blades into the CFD domain. On the other hand, wake kinematics are determined using full 3D Navier-Stokes simulations.

The basics of an ALM model can be described as follows. The wind turbine blades are divided into a series of blade sections, for which 2D characteristics (C_l, C_d) are determined, as is the case for other *"lifting-line"* based approaches such as those described in sections 1.1 and 1.2. For each blade section, the relative velocity W is determined by combining the velocity that is sampled from the CFD domain and the structural velocity as $\vec{W} = \vec{U}_{CFD} + \vec{U}_{st}$. Once the relative velocity is obtained, blade forces are calculated along th blade span using eqs. 1.11, 1.12. Various methods of inserting the body forces into the CFD domain have been proposed. In the current work body forces are distributed onto a spherical volume (often referred to as "kernel") using a piecewise function [25]. The process through which velocities are obtained from the CFD domain is called *velocity sampling* while the

force-insertion process is called *force-projection*. In this work, an ALM model implemented in the commercial CFD software CONVERGE is used. Consequently, the main features of this specific ALM implementation will be discussed in more detail.

1.3.1 Velocity sampling

Correctly sampling the velocity computed in the Computational Fluid Dynamics (CFD) domain is a non-trivial task. In fact to maintain consistency with the tabulated lift and drag coefficients that are used to compute the blade forces, the local flow disturbance introduced by the presence of the wind turbine blade (in the ALM model introduced as body-forces) must no be accounted for. At the same time, the effects of the wake on the local inflow must be included. Various strategies have been proposed by various authors, with various degrees of complexity, as discussed in [26]. The ALM model in use in the current study has been successfully validated in [27] using Lagrangian-Average velocity sampling, as proposed in [25]. As explained in detail in [25], the sampled velocity is obtained for each blade section as the average average velocity along the flow streamlines or Lagrangian average. Because of the averaging process, this method intrinsically adds a time delay to the sampling process. Conceptually speaking this is similar to the phenomenon observed when filtering a signal using a moving-average approach. To overcome this issue, the REASE research group of the University of Florence recently extended the ALM with the line-average velocity sampling method, which is the method used in the current study. This method was proposed by Jost [26] and consists of sampling the velocity on a number of points uniformly distributed on a circle that is centered on the section's aerodynamic center and one chord in radius. The idea is that the induced velocities sampled at two opposite points in the circle due to the presence of the body forces cancel each-other out. This approach was successfully tested on vertical-axis wind turbines by the research group [28]. One notable difference from the method present in [26] is that in the method used in this dissertation the sampling is performed on a circle normal to the local blade axis, as show in Fig. 1.4, rather then on a circle projected on a cylinder with the radius of the projected blade section.

More specifics regarding the details of the line average sampling approach as employed in this dissertation are reported in section 2.2.4. It is important to note that while no specific tuning and calibration of the velocity sampling approach was performed in this study, some general tests and verifications were performed within the REASE research group, the results of which can be generally summarized as: *i)* as long as six or more circumferential points are used, the sampled velocity is found to be interdependent of the number of circumferential sampling points, *ii)* the line average approach has shown to be stable if compared to alternative sampling methods such as the ones discussed in [25], *iii)* the angle of attack predicted with the line average approach is in line with predictions of lower fidelity methods, within the limitations of such a comparison to a lower fidelity model.

1.3.2 Force projection

To effectively insert the body forces calculated through eqs. 1.11, 1.12 and the velocity-sampling procedure into the CFD domain a smearing function is needed. In fact, through

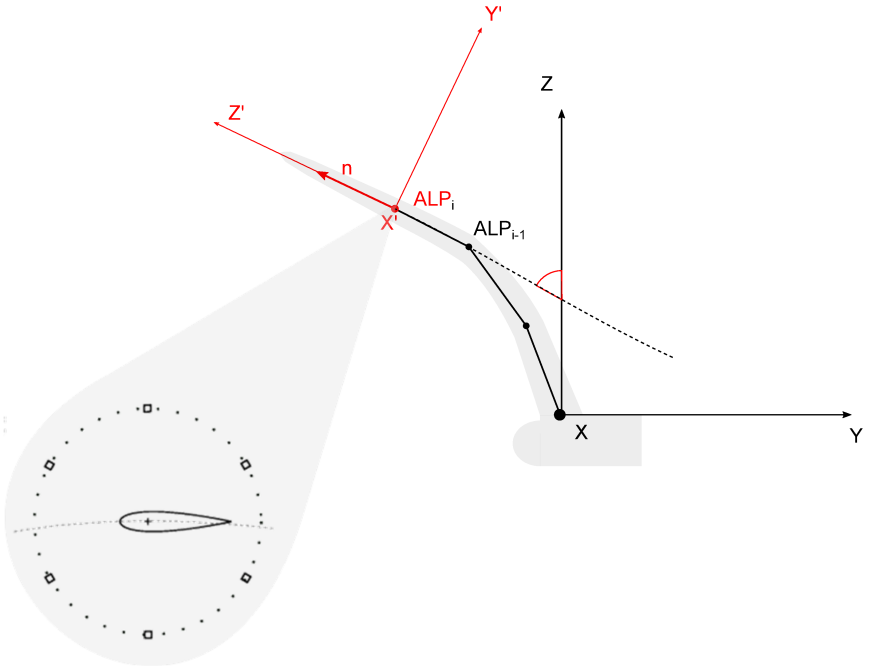

Figure 1.4: Line Average velocity sampling as implemented in CONVERGE

eqs. 1.11, 1.12, point loads are computed. These loads need to be distributed across a number of cells in the CFD model for them to become volume forces. In the ALM method used in this work, forces are projected into the CFD domain using a piecewise function δ, defined as:

$$\delta(d) = \frac{1}{\beta^3}\phi\left(\frac{d_1}{\beta}\right)\phi\left(\frac{d_2}{\beta}\right)\phi\left(\frac{d_3}{\beta}\right) \tag{1.32}$$

As shown in [25], this function is very similar to a Gaussian kernel, which is a popular choice among ALM modelers, but is defined on a limited support and does not need to be truncated. The radius of the projection function β is chosen as a compromise between numerical stability and accuracy. In practice, when the grid size allows it, forces are distributed on a sphere with the same radius of the blade chord. If cell size is too large, kernel size is limited by cell dimension, as shown in eq. 1.33.

$$\beta = max\left(\frac{c}{4}, \xi V^{\frac{1}{3}}\right) \tag{1.33}$$

ξ is a tuning parameter and V is the cell volume. A schematic representation of the force-projection in CONVERGE is shown in Fig. 1.5.

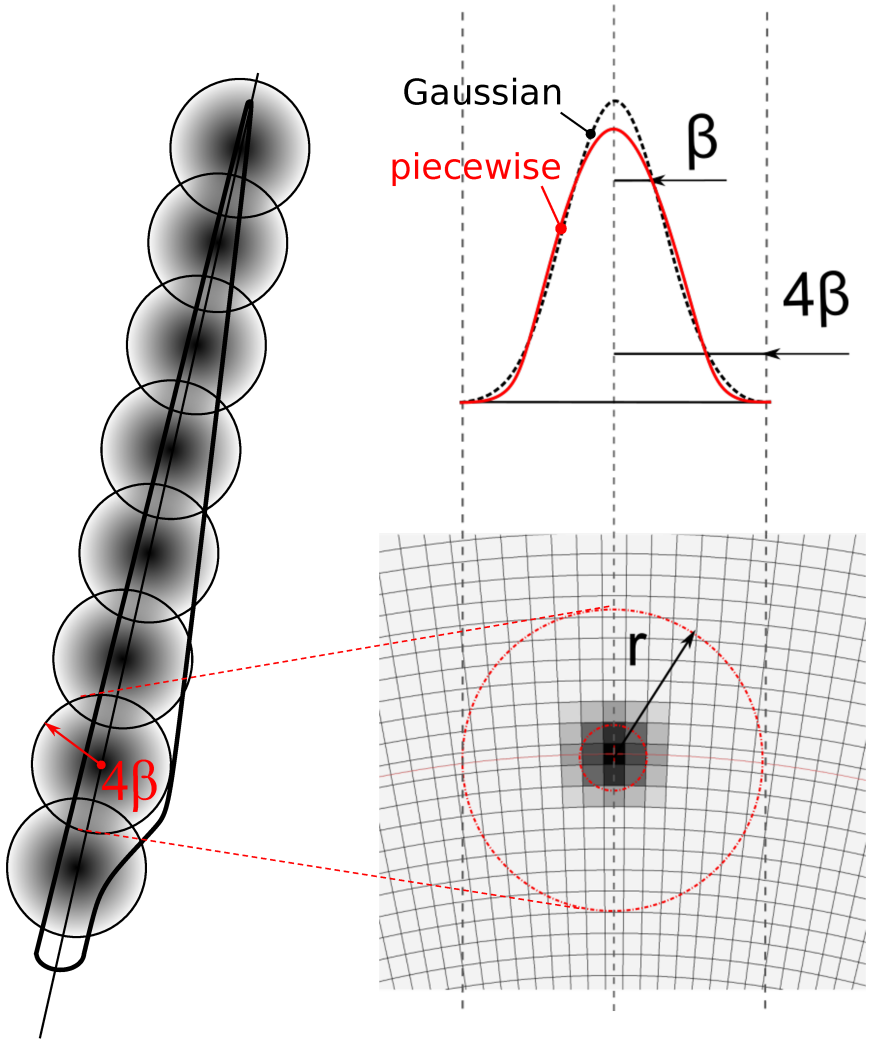

Figure 1.5: Force projection in CONVERGE. Piecewise fuction used for force projection (in red) compared to more common Gaussian kernel

1.4 Wind Turbine Simulation Codes

1.4.1 OpenFAST

OpenFAST (hereafter OF), is a state-of-the-art multi-physics wind turbine simulation code developed by the National Renewable Energy Laboratory. It is available open source and is able to model FOWTs. All the calculations shown in this work are performed with OpenFAST v3.0.0.

The code features a modular structure, and the user can decide what features to use. Aerodynamics are modelled using AeroDyn v15 [18], the same code that was used in section 2. Two wake models are compared in this section, the DBEM, for which a theeoretical

overview is provided ins ections 1.1.1 and 1.1.3, and the LLFVW model, that is explained in section 1.2.

The floating support substructures are modeled as 6-DOF rigid bodies. Their interaction with the sea is computed using HydroDyn [29], OF's hydrodynamics module. Hydrodynamics can be modeled using potential flow theory, a Morison equation approach or a mix of the two. For test cases presented in this work, potential flow theory is used, with the addition of the Morison equation to model quadratic drag. Regarding the potential flow solution, added mass, linear damping and wave-response coefficients are pre-computed in the frequency domain using an external potential flow solver, such as WAMIT [30]. Second order difference frequency forces can also be accounted for in OF. The structural dynamics are solved using a modal-based structural module, ElastoDyn [31]. The structural deformations are calculated as linear superposition of the pre-determined mode shapes, allowing for a very fast solution with limited degrees of freedom to solve for [10]. Moorings are modeled using MoorDyn [32], a dynamic lumped-mass mooring line model. The model accounts for internal axial stiffness and damping forces, weight and buoyancy forces, hydrodynamic forces from Morison's equation, and vertical spring-damper forces from contact with the seabed.

1.4.2 QBlade-Ocean

Qblade-Ocean (hereafter QB) is a state-of-the-art multi-physics wind turbine simulation code developed by Technical University Berlin. Like OF, it is available open source and is able to model FOWTs. A user and theory guide of the software package is available online.

A LLFVW model is used for aerodynamic calculations. The theoretical foundation of the model is the same as the more recent OLAF model implemented in AeroDyn v15 [21], and is briefly explained in section 1.2. As an alternative with lower computational requirements, aerodynamics of HAWTs can also be modeled using an unsteady polar-BEM implementation. This model is not used in this work.

Structural dynamics are modeled using a 1D multi-body formulation. The components of the model can be either point masses or rigid/flexible Euler-Bernoulli beam elements in a co-rotation formulation. The multi-physics solver Project CHRONO [33] is used to solve the structural dynamics and allows for treatment of highly nonlinear deflections of beam elements. Mooring lines are integrated through the absolute nodal coordinate formulation (ANCF) [34].

Like OF, QB can model hydrodynamic loads on the floating substructure via potential flow theory, Morrison's equation or a combination of the two approaches. For the test cases tested herein Linear Potential flow theory is combined with quadratic drag modelled with Morrison's equation. Linear potential flow coefficients are pre-computed in the frequency domain using an external potential flow solver, such as WAMIT [30].

1.4.3 DeepLines-Wind

DeepLines^{TM} is a commercial integrated software solution to perform in-place and installation analyses of various offshore structures, based on the finite element method.

DeepLines^{TM} is part of the marine software solutions suite developed by Principia and IFP Energies Nouvelles. This numerical tool is based on the program Flexan, initially developed for flexible risers and used from 1980.

DeepLines^{TM} is also closely coupled with Diodore^{TM}, a diffraction/radiation solution. This allows calculation of the interactions between any floating unit and its mooring lines or risers. The mooring elements are treated as cable elements with purely axial stiffness without compression. External links with other diffraction/radiation software tools were also made possible. The buoyancy forces are explicitly calculated with a discrete approach. DeepLines^{TM} can also handle vortex induced vibrations analysis, structural fatigue damage analysis, as well as line contact and soil interaction modeling. To address the needs for an overall design tool raised by the development of offshore wind turbines platforms, a new module DeepLines WIND (hereafter DL) was created in 2011. DL is designed to perform fully-coupled dynamic finite element analysis. It accounts for combined effects of aerodynamic loads on the blades, active pitch control, hydrodynamic loads on the floating platform and dynamic moorings loads. Several BEM models are implemented in an external .dll library to calculate the aerodynamic loads. DL is able to simulate both horizontal and vertical axis wind turbines. The aerodynamic model in DL uses a BEM approach coupled with a dynamic inflow model. In this case no unsteady blade aerodynamics model has been applied.

1.5 Theoretical Background

In this section theoretical concepts on the topic of wind turbine wakes that are functional to the findings in this manuscript are presented. Attention is focused mainly on two concepts that were previously mentioned but not looked into in detail: the wake state of a rotor and the dynamic wake effect.

1.5.1 Wake states

The general state a wind turbine rotor operates in can be described through a wake state. Thrust coefficient as a function of axial induction of the rotor as predicted by BEM theory and measured in experiments, and the corresponding wake states are shown in Fig. 1.6. As introduced in section 1.1, momentum theory is, strictly speaking, valid for axial induction factors lower than 0.4. Above this value the rotor enters the so-called *turbulent wake state*. In this operating condition, the drop in pressure across the rotor disk is high, leading to flow mixing in the wake and the breakdown of the hypothesis of non-interacting stream tubes, which is at the foundation of momentum theory. In particular, it is interesting to note that according to momentum theory (section 1.1) if axial induction exceeds 0.5 the velocity in the far wake becomes negative an the streamtubes are effectively choked [35], violating the hypothesis at the basis of the theory itself. When axial induction exceeds unity, flow reversal occurs on parts of the rotor, starting at the tip region. This operating state is the *vortex ring state*, where momentum theory is, again, unpredictive. At even higher values of axial induction the rotor enters the propeller brake state. Both these rotor states may also be encountered by a helicopter during rapid descent. A more exhaustive discussion on

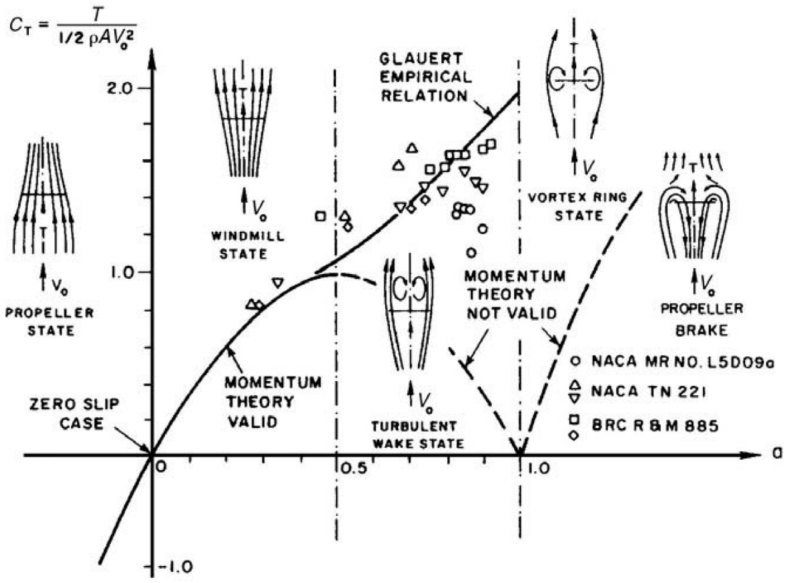

Source: Eggleston and Stoddard (1987), reproduced with permission.

Figure 1.6: Rotor thrust coefficient as a function of axial induction coefficient and corresponding wake states. Image from [14]

turbulent wake state, vortex ring state and propeller brake state can be found in the work of Sørensen et al. [35]

1.5.2 Dynamic wake effect

The dynamic wake effect was observed during experiments and high-fidelity numerical simulations during step-changes in rotor speed and blade pitch [36] [37]. Due to this effect, after such a step-change, there is a time delay before the rotor reaches it's new equilibrium operating conditions. In particular, after step-changes in blade pitch and over or undershoot of rotor torque and blade bending moments is noted in experiments. This is shown in Fig. 1.7, where the time series of rotor torque during two step-changes in blade pitch measured on the Tjaereborg wind turbine is shown. This delay effect is liked to the fact that the wake needs time to adjust to the new operating condition as the vorticity shed and trailed by the blades are convected downstream. BEM theory is a quasi-steady aerodynamic theory and therefore it cannot capture this dynamic effect. During the years, several engineering models to account for this effect in BEM models have been developed, such as the one developed by Øye that is described in section 1.1.3. A more complete discussion on dynamic induction models can be found in [19]

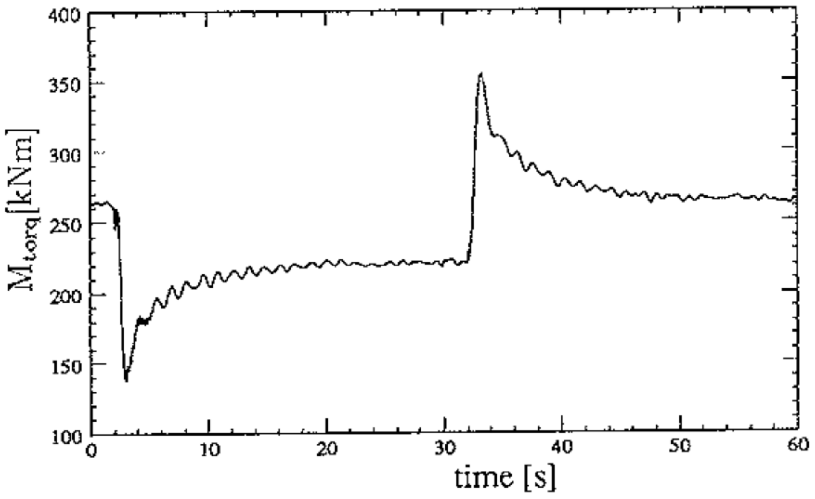

Figure 1.7: Experimentally measured rotor torque as a function of time during a step change in blade pitch form 0.1° to 3.7° on the Tjaereborg turbine. Image from [19]

Chapter 2

Unsteady Aerodynamic Loads: the OC6 Experiment

Floating Offshore Wind Turbine rotors can experience large motions under the combined influence of waves and wind. The influence of rotor motion on unsteady aerodynamic loads and the ability of current standard aerodynamic theories to predict the unsteady loads is studied in this chapter. To remove the influence of other aspects as much as possible, with the aim of evaluating the performance of aerodynamic theories in presence of large rotor displacements, simulations are performed on an wind tunnel test rotor. In addition to removing the influence of control, elasticity and inflow conditions, this also allows for comparison to experimental data.

The data comes from the OC6 Phase III collaborative project, promoted by the International Energy Agency (IEA). Some of the results presented in this chapter are part of this collaborative task and have been discussed in the recent publication [38]. In this collaborative effort, data from two experimental campaigns is used. The first campaign was conducted in the wind tunnel of Politecnico di Milano during the UNsteady Aerodynamics for FLOating Wind (UNAFLOW) project [39], including PoliMi, The Netherlands Organisation for Applied Research, University of Stuttgart and Danish Technical University. The second campaign was conducted in October 2021 and included a different actuator system that allowed for forced motion in all 6 platform Degree Of Freedom. During this campaign, in addition to tests with forced surge oscillations, tests with forced pitch oscillations were performed.

This section is organized as follows: first some details regarding the experimental facility and test model will be provided. The numerical models that are compared in this chapter are introduced next, focusing on the set-up rather than on theory. Finally results are presented, followed by a discussion and conclusions.

2.1 Scaled Model Description

The test-case is a 1:75 scale version of the DTU 10MW RWT [40] that was tested in the PoliMi wind tunnel. Rotor diameter is geometrically scaled, while wind speed is one third of

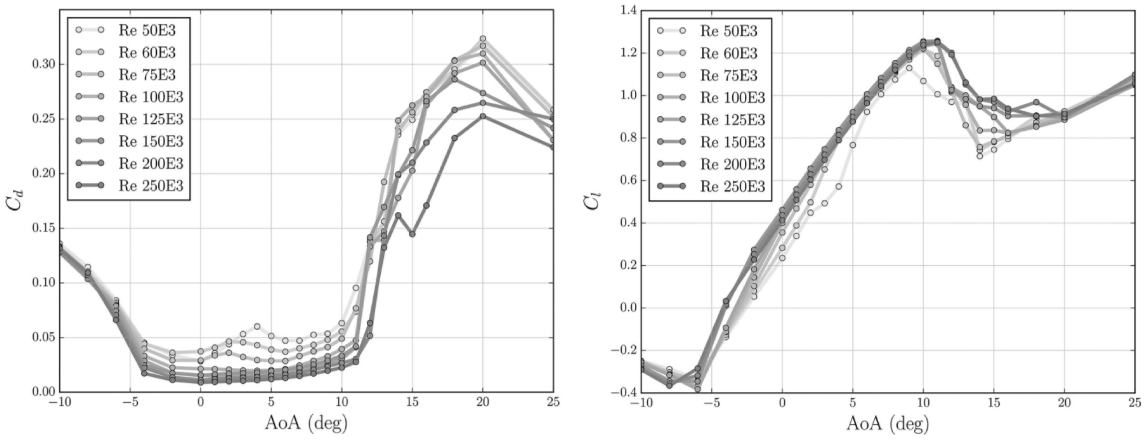

Figure 2.1: Lift and drag coefficients at various Reynolds numbers for the SD0732 airfoil as measured in the DTU Red wind tunnel. Image from [43].

the full scale wind speed. Consequently, the Reynolds number is reduced by approximately 225 times in the experimental model [41]. To counter this, the blades are not geometrically scaled but rather they are designed so that the full-scale Thrust Coefficient and Power Coefficient are matched as much as possible at model scale. The full details regarding the scaling procedure and the rotor design approach can be found in [42] and [43]. For the sake of completeness however, the information that was provided to the OC6 Phase III participants, necessary for the set-up of the numerical models, is presented.

For the aerodynamic design, the Selig-Database (SD) SD0732 airfoil was chosen. This 10% thick airfoil is optimized for low Reynolds numbers and was found to be fitting for the current analysis. Sectional lift and drag coefficients were measured experimentally for angles of attack between -10 and 25 in the DTU Red tunnel [39]. Measurements were conducted for Reynolds numbers between $50 * 10^3$ and $200 * 10^3$. The resulting sectional aerodynamic properties are shown in Fig. 2.1. The measured data was extrapolated to the full -180 to $+180$ range with Viterna's post-stall extrapolation method [44]. In OC6 Phase III the blade is discretized in 20 radial sections, as shown in table 2.1. On a section-by-section basis, the aerodynamic coefficients are corrected for stall-delay effects with the Du-Selig model; the magnitude of the correction depends on the span-wise location of each section. To avoid un-physically high values of lift for the inboard sections of the blade, for blade station with $r/R < 0.35$ the 3D corrections are the same as for those at $r/R = 0.35$.

From a structural stand point, the blades are Carbon Fiber and [43], and are considered rigid in the numerical models. The tower was not considered in the numerical models, neither from an aerodynamic nor from a structural point of view. The experimental set-ups in the PoliMi wind tunnel during the two experimental campaigns are shown in Fig. 2.2. In the first campaign the rotor is mounted on a sled that allows for surge and pitch motion, while during the second campaign the rotor is mounted on a hexapod that allows for full 6-Degree Of Freedom (DOF) motion.

Table 2.1: Chord and Twist distribution of DTU 10MW scaled rotor

Span [m]	Twist [°]	Chord [m]
0.00000	17.076	0.05585
0.05817	17.041	0.05678
0.13641	15.775	0.07573
0.21766	12.305	0.10620
0.30059	9.982	0.11490
0.38379	8.651	0.11044
0.46581	7.565	0.10236
0.54530	6.381	0.09272
0.62105	5.080	0.08288
0.69211	3.790	0.07356
0.75778	2.616	0.06516
0.81765	1.590	0.05778
0.87153	0.717	0.05141
0.91947	0.037	0.04604
0.96171	-0.535	0.04163
0.99860	-1.033	0.03796
1.03056	-1.462	0.03440
1.05807	-1.611	0.03054
1.08162	-1.607	0.02541
1.10166	-1.722	0.00998

Available Measurements

During the experimental campaign, information on rotor forces and wake characteristics were collected. Regarding the former, the 6 force resultants at the hub are collected, and processed to remove the contributions of non-aerodynamic loads such as inertial loading (see [41] for further details). Regarding wake information, Particle Image Velocimetry measurements are available in the near wake, while Hot Wire Anemometry (HWA) data is collected in the mid to far wake. HWA data is collected on two traverses, the first aligned with the inflow direction, called the along-wind HWA line, the second perpendicular to the incoming inflow; the cross-wind HWA line. Both the along-wind and cross-wind measurements are collected at turbine hub-height. Preliminary results of this data collection efforts are discussed in [46]. The locations of the PIV plane and HWA collection points is shown in Fig. 2.3. During OC6 Phase III, vorious numerical models were compared with respect to the experimental PIV and HWA data, as discussed in [47]. For further information regarding wake data collection and in-depth insight into the wake characteristics of this testcase see [47].

(a) (b)

Figure 2.2: (a) experimental set-up of the DTU 10 MW scaled rotor in the PoliMi wind tunnel during the UNAFLOW project. (b) experimental set-up of the DTU 10 MW scaled rotor in the PoliMi wind tunnel during the tests conducted in fall 2021. Images from [44] and [45]

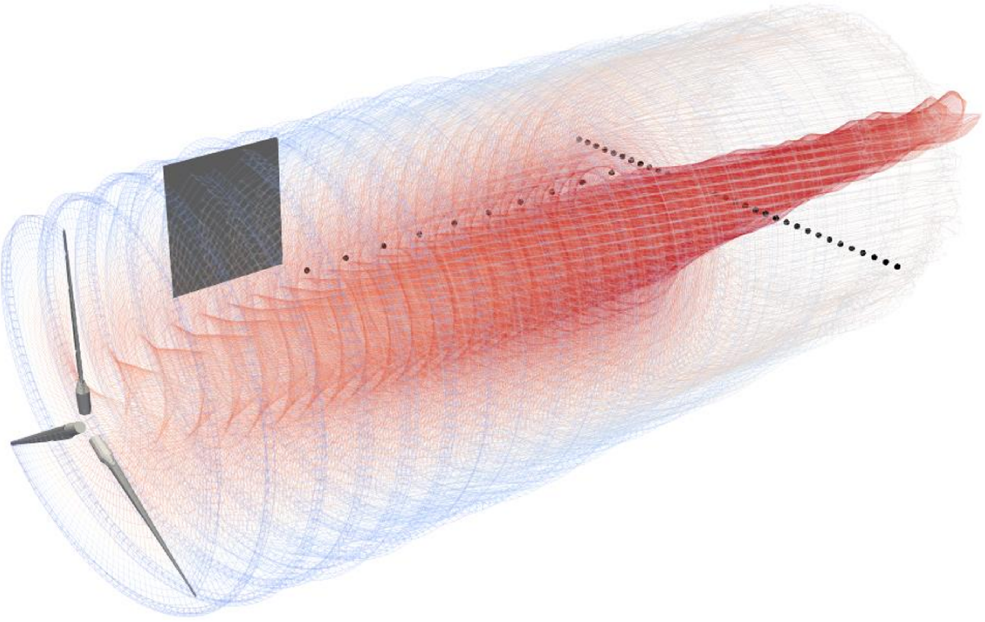

Figure 2.3: Lifting-Line Free Vortex Wake simulation of the UNAFLOW rotor. Particle Image Velocimetry measuring plane (gray box), along-wind and cross-wind Hot Wire Anemometry measuring points (black dots). Image from [38]

2.1.1 Experimental Facility

The scaled rotor is tested in the low-speed boundary layer test section of the PoliMi wind tunnel. The test section is 13.84 m wide and 3.84 m tall and is specifically designed for wind engineering tests on structures subject to atmospheric flow conditions. A vertical distribution of velocity was measured without the wind turbine in place to determine the inflow conditions for numerical models to use. As discussed in [44], the flow was found to be fairly uniform across the entire test section. The boundary layer height was estimated to be of approximately 10 cm [44] in height in correspondence of the test article.

2.1.2 Correcting for wind-tunnel blockage

The reduction in cross sectional area caused by the presence of the test article in the wind tunnel causes flow to speed-up at the test section, an effect that is commonly known as blockage. In the case of a wind turbine, two main effects contribute to blockage:

- solid blockage: the presence of the wind turbine itself reduces the passage area and causes flow speed-up
- wake blockage: in the wind turbine's wake flow velocity is reduced. Therefore, in order to maintain the same volumetric flow-rate, the flow must speed-up around the test article

In the current set-up, the blockage ratio, as defined below, is estimated to be 8%:

$$\epsilon = \frac{A_d}{c} = \frac{\pi R^2}{L * H} = 0.084 \tag{2.1}$$

Where $L = 13.84m$ and $H = 3.84m$ are the wind tunnel section width and height. According to Glauert [48], for moderate blockage ratios, the disturbed velocity at the rotor disk (U'_∞) can be calculated based on the imposed undisturbed velocity (U_∞) as:

$$U'_\infty = U_\infty * (1 + \epsilon \frac{C_T}{4 * \sqrt{1 - C_T}})^{-1} \tag{2.2}$$

The trust coefficient C_T can be calculated as:

$$C_T = \frac{T}{1/2 \rho A_d U_\infty^2} \tag{2.3}$$

For the present test-case, operating with air density of 1.177 kg/m^3, wind speed of 4 m/s and C_T of approximately 0.88, $U'_\infty / U_\infty = 1.0475$. Therefore, a corrected velocity value of 4.19 m/s is calculated.

2.2 Numerical Model Set-up

Four different aerodynamic theories are compared in this section: BEM, DBEM which introduces an empirical dynamic wake correction to BEM, LLFVW and ALM. The four models differ on how the wake is modeled, as the blades are modeled using tabulated lift and drag coefficicients in all four theories. An overview of the principles of the four aerodynamic theories as well as some theoretical aspects are provided in section 1.

2.2.1 Lifting-line approach

All the numerical models that are compared in this dissertation model the blades with a *lifting-line* approach. Following this approach, the blade is divided into sections, for which aerodynamic coefficients are considered to be constant. These aerodynamic coefficients are used to compute lift and drag forces per unit lenght along the blades. Some of the tested models use a Beddoes-Leishman type [49] unsteady aerodynamic formulation that allows for the modeling of unsteady aerodynamic effects such as dynamic stall and, more importantly for the current analysis, unsteady airfoil behavior in attached-flow regime. More specifically, Gonzalez's variant of the Beddoes-Leishman dynamic stall model is used [49]. Like most Beddoes-Leishman type models the aerodynamic coefficients in the attached-flow region are replaced by a linear approximation of the Normal Force Coefficient, defined with the 0-lift angle of attack and the slope of the normal force coefficient. Due to the shape of the lift and drag coefficients of the SD0732 airfoil at the Reynolds numbers of this study, some calibration was required. In fact, as shown in Fig. 2.1, the lift curve is not linear, but instead shows a distinct "bump", especially for lower Reynolds numbers that cannot be fully reproduced by replacing the aforementioned curve with a linear trend-line. Therefore, the slope of the normal force coefficient was calibrated so that simulations performed in the nominal, steady, operating conditions tested in the experiments produced the same results both using unsteady polars and static tablulated coefficients.

2.2.2 Blade-Element Momentum Theory

Blade Element Momentum and Dynamic Blade Element Momentum simulations are performed using the standalone version of the aerodynamic solver built into OpenFAST, AeroDyn v15 [18].

Axial and tangential induction are considered. Hub and tip losses are included using Pradtl's tip and root loss model, as discussed in section 1.1. Skewed wake is accounted for with the Pitt-Peters correction for axial induction. When Dynamic wake is considered (DBEM), the default settings for the time constants τ_1 and τ_2 shown in section 1.1.3 are used, as determined by equations 1.26 and 1.27. A more complete discussion of the theoretical aspects and limitations of the BEM model included in this study can be found in section 1.1.

2.2.3 Lifting-Line Free Vortex Wake

The Lifting Line Free Vortex Wake module cOnvection LAgrangian Filaments [21] built into AeroDyn v15 [50] is used. The code is based on a free-vortex wake implementation whose main theoretical aspects are brushed upon in section 1.2, and explained in detail in [21] and [50]. The same blade representation as used with BEM is used 2.2.2: the blade is divided in the same 20 radial sections and the same lift and drag coefficients are used.

In terms of numerical settings, induced velocities are determined using Biot-Savart's law, vortex core radius is defined as 5% of the blade chord and vortex core spreading as a function of vortex age is used (eq. 1.31). The wake length and core-spreading eddy viscosity (δ in eq. 1.31) are chosen based on a preliminary sensitivity study, where various combinations of these parameters were tested.

Calibration of the LLFVW Model

In OLAF, the near wake is modeled using a vortex lattice approach, while in the far wake only the tip and root vortices are maintained [21]. The influence of wake length in terms of rotor thrust and torque is shown in figure 2.4, where results with varying wake lengths are shown. Experimental results, BEM and ALM results, as well as LLFVW results using the combination of wake length and core eddy viscosity that were ultimately chosen are also shown as reference. As shown in 2.4, wake length does not significantly influence thrust and torque. In fact, no clear trend has emerged from the various combinations of near and far wake lengths that were tested. Therefore, the shortest wake length that was tested (two revolutions for near wake and twelve revolutions for total wake length) was used. It must be noted that his wake length remains consistent with wake-length recommendations from [21]. In contrast to wake length, a clear trend is noted in mean rotor thrust and torque when the core eddy viscosity is varied. In fact, as shown in Fig. 2.5, increasing core eddy viscosity increases rotor thrust and torque.

Mean flow velocity in the wind direction is also used as a benchmark to evaluate the tuning parameters. In figure 2.6, the velocity measured on the cross-wind HWA line (section 2.1), located approximately 2.5 rotor diameters downstream of the turbine at hub height is shown. Experimental, ALM and LLFVW results using the combination of wake length and core eddy viscosity that were ultimately chosen are shown for comparison.

Increasing wake length, both for the near and far wake, tends to decrease velocity in the rotor area. However, as was shown with rotor forces, increasing wake length does not yield a significant benefit in terms of wake deficit for the current test case (Fig. 2.6 (a)). In fact, increasing this parameter brings the LLFVW simulations more in line with experiments at the center of the wake, but less so in the rest of the wake region. On the other hand, increasing core eddy viscosity improves agreement in the mid and outer portions of the wake. Indeed, with respect to experimental data, the ALM and LLFVW models with default values of core eddy viscosity predict more confined shear layers both in the tip and root regions. By increasing this parameter, as shown in Fig. 2.6 (b), tip and root vortex dissipation is increased and thus the wake shear layer is widened. Finally, at the rotor center, both ALM and LLFVW overestimate velocity. This is in part due to the

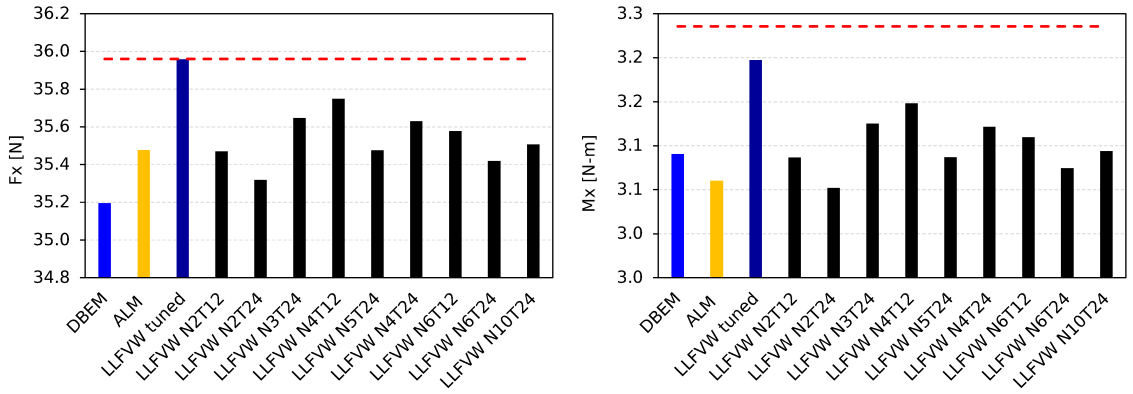

(a) **(b)**

Figure 2.4: Rotor thrust (a) and torque (b) as a function of LLFVW length compared to experiments and other numerical models in rated wind speed conditions ($U_{wind} = 4.19$ m/s, $\Omega = 240$ rpm). "N" stands for *"near wake"* and "T" stands for *"total wake"*. Wake length expressed in terms of rotor revolutions.

fact that no nacelle and nose-cone are present in the LLFVW simulations. The influence of the nacelle and nose cone on wake velocity on the cross-wind measuring plane is evaluated using the ALM model and discussed in more detail in section 2.2.4, where the nacelle is found to influence the center portion of the wake only, with very little effect on the mid and outer portions of the wake itself. Therefore, LLFVW and experiments can be reasonably compared in the mid and outer portions of the wake, where increasing the default value of core eddy viscosity is found to greatly improve agreement.

Based on these findings, a near wake length of 2 rotor revolutions, a total wake length of 12 revolutions and a core eddy viscosity δ of 500 are selected as final "tuned" parameters and are used in the rest of this study. For simulations at cut-in wind speed (LCs 2.26, 2.27, 3.26 and 3.27), a near wake length a 3 revolutions and a total wake length of 15 revolutions is used to compensate for the higher tip-speed ratio of these simulations.

2.2.4 Actuator Line Model

For the Actuator Line Model simulations, the commercial software COVERGE, is used. The Actuator Lines themselves are introduced into the CFD domain using a custom User Defined Function developed by Convergent Science Inc. in collaboration with the University of Florence [25] [27].

The flow around the actuator lines is modeled with an U-RANS approach. The $k - \epsilon$ turbulence closure model is used and is preferred over $k - \omega$ closure because it allows for better representation of the effects of turbulence in the free-stream.

As noted in [38], and discussed in section 2.1.2, although the wind tunnel test section is particularly large, the presence of the wind tunnel walls cause a certain degree of flow

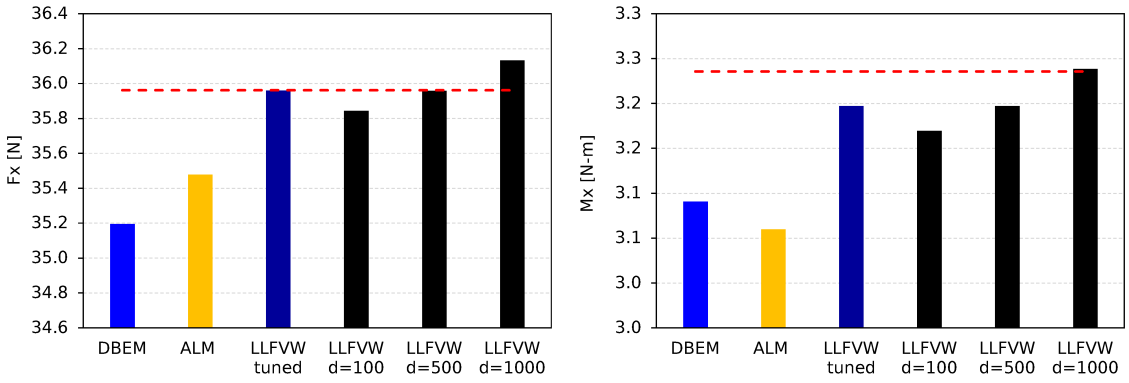

(a) **(b)**

Figure 2.5: Rotor thrust (a) and torque (b) as a function of core eddy viscosity δ in LLFVW simulations compared to experiments and other numerical models in rated wind speed conditions (U_{wind} = 4.19 m/s, Ω = 240 rpm). δ influences the vortex core radius as a function of time, with higher values leading to larger vortex cores over age (section 1.2). Wake length expressed in terms of rotor revolutions.

blockage to occur. To include this effect in the ALM simulations, the wind tunnel domain is modeled as closely as possible. To limit the computational cost, the boundary layer on the wind tunnel walls is not included but rather the walls are shifted inwards accounting for the boundary layer displacement thickness δ^* on the floor and ceiling. The integration of the wind profile measured 5 m upstream of the rotor during the UNAFLOW campaign [44], results in the boundary layer thickeness on the floor of the wind tunnel $\delta^*_{bottom} = 12.5cm$ and on the ceiling $\delta^*_{top} = 9.5cm$ [44]. The resulting simulation domain is a box that is 3.6 m high ($3.82 - \delta^*_{top} - \delta^*_{bottom}$), 13.44 m wide and 19.04 m long. The rotor center is placed 8.33 m from the inlet (approximately 4D) and 1.961 m from the wind tunnel floor. Dimensions of the domain are shared amongst all the OC6 phase III participants that use CFD and were chosen to be the same as those used during the UNAFLOW project by the University of Stuttgart, that performed blade-resolved simulation [44]. The simulation domain is shown in Fig. 2.7.

The nose-cone and nacelle geometry are included as a wall-boundary in the ALM simulations, but the tower and bottom shroud (visible in Fig. 2.2) are not included for consistency with the LLFVW and BEM results, as chosen by the OC6 Phase III participants.

The base mesh consists of a Cartesian grid with cubic elements of 0.25 m in size. In the rotor region a mesh size of $0.25 * 2^{-4} = 0.0156$ m is used. In the near wake, up to 0.85 diameters downstream of the rotor, cell size is $0.25 * 2^{-3} = 0.031$ m, ensuring that the PIV measuring plane (shown in Fig. 2.3) is enclosed in the refined region. The far wake is modeled with a cell size of 0.0625 m. The use of such a small near wake region and relatively coarse grid in the mid to far wake regions is allowed by the use of Active Mesh Refinement, which is used to locally refine the mesh based on the local velocity gradient

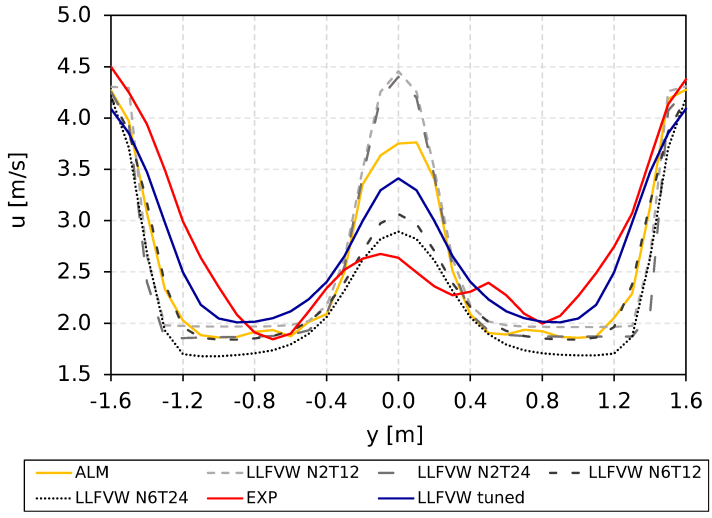

(a)

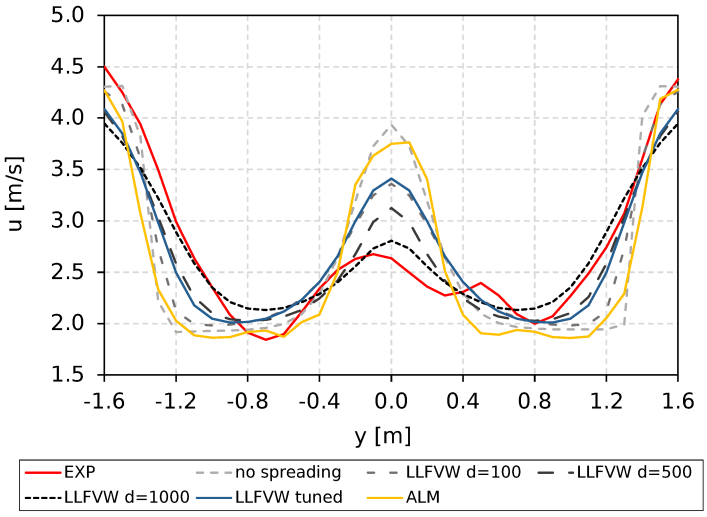

(b)

Figure 2.6: along-wind velocity V_x measured on the cross-wind HWA line (section 2.1) as a function of wake length (a) and core eddy viscosity (b) in rated wind speed conditions ($U_{wind} = 4.19$ m/s, $\Omega = 240$ rpm). Other numerical models and experiments inserted for reference. Rotor is approximately 1.2 m in radius.

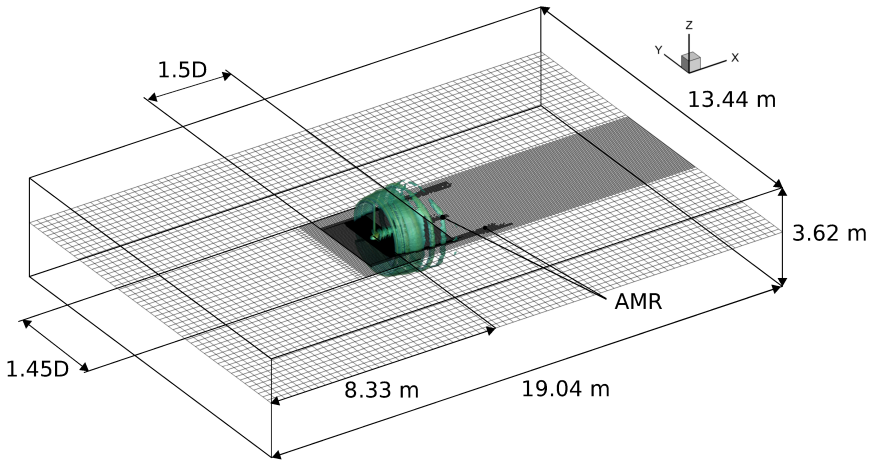

Figure 2.7: Wind tunnel CFD domain used in ALM simulations. Local refinements in rotor and wake region are visible on the mesh cut-plane

[51] in the entire wake region, up to a minimum mesh size of $0.25 * 2^{-4} = 0.0156$ m. This ensured a good reproduction of the tip-vortices in the near wake region, as demonstrated by the results presented in [47].

Velocity sampling is performed using the line-average algorithm (section 1.3). Each blade is divided in 55 sections and forces are inserted using a Delta-shaped spherical kernel (see section 1.3). Kernel size is defined through eq. 1.33 and is equal to one quarter of the chord with a minimum limit on size imposed for numerical stability reasons. ξ in eq. 1.33 is equal to 1.6.

Nacelle Influence on Wake

The ALM model allows for the unique opportunity of evaluating the influence of the nacelle on the wake of the turbine. As discussed previously, many of the lower order models such as BEM and LLFVW do not include this effect, and thus an over prediction of the velocity in the wake in this region is expected. On the other hand, in the ALM model, the nacelle and nose cone are included as an immersed boundary. By removing them, the effect of this component on the flow in the wake can be evaluated. As shown in Fig 2.8, when the nacelle is removed a higher axial velocity is observed in the center of the wake, roughly matching the free stream velocity measured at the edges of the wake. Both these velocities are higher than the 4 m/s wind speed that is imposed at the wind tunnel inlet, indicating that indeed the effects of blockage are significant. When the nacelle is introduced, the mean velocity deficit in the three most central points of the wake is approximately 0.65 m/s. Moreover, as is apparent in Fig. 2.8, the presence of the nacelle only influences the central portion of the wake, and not the mid and outer portions. It is important to remark that while this comparative analysis may give some quantitative indication of the influence removing the nacelle may have on the wake, it's effect may be different in other aerodynamic models based on the characteristics of the models themselves.

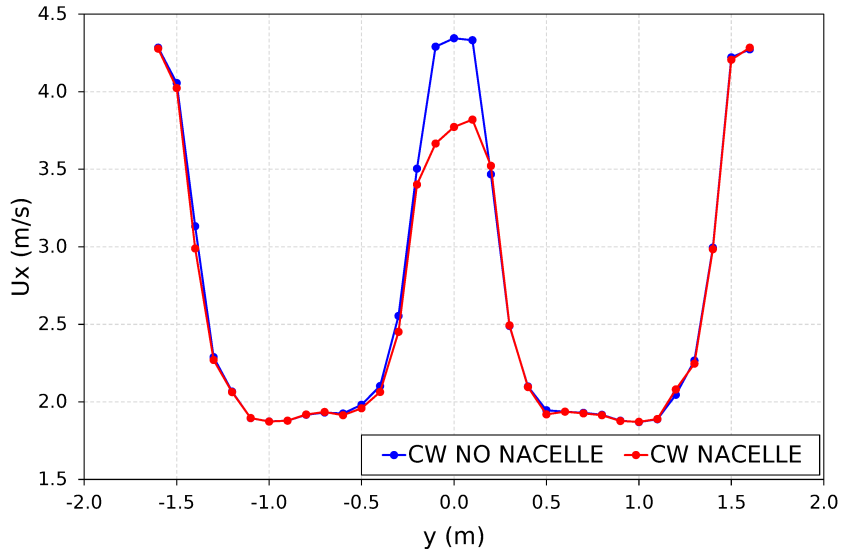

Figure 2.8: Influence of nacelle on mean x-velocity on cross-wind HWA measurement line evaluated with ALM. Load Case 1.1 [38], steady state rated wind operation.

2.2.5 Computational Time

The computational time it took to run each model cannot be quantitatively compared, as each model was run on different hardware depending on how demanding it is. Moreover, computational time is highly dependent on the specific load case (shown in section 2.3) that is being run. It must also be noted, that the time that was simulated in each model is different. In fact, the time it took to reach a steady-state behavior and remove initial transients is different in each theory, and depends on initial conditions and numerical settings. Nonetheless, quantitative indications on the time required to run each model are given in this paragraph. BEM and DBEM models ran in minutes on a single CPU core. These models were ran for fifty surge or pith cycles. The LLFVW model took hours to run on a 24-core dual-socket Intel Xeon Gold 5118 CPU (2.30 GHz) HPC node. The least demanding cases ran in approximately 4 hrs, while the most demanding took up to 36 hrs approximately. Between five and thirty surge or pitch cycles depending on the specific load case. The ALM is by far the most demanding of the tested aerodynamic theories. This model was run on a 52-core dual-socket Intel Xeon Gold 5320 CPU (2.20 GHz). It took days to run, more specifically between 30 and 120 hours depending on the specific load case and simulation length required to reach a steady-state behavior.

It is important to note that the LLFVW simulations performed in this section do not feature GPU acceleration, as the ones that are performed in sections 3 and 4 with QBlade-Ocean do. GPU acceleration can reduce the computational time of LLFVW models to a fraction of what they would be without it [22]. The increase in computational cost with respect to BEM models still remains significant.

Table 2.2: Surge tests. Load Cases (LCs) 2.1, 2.5 and 2.7 also tested experimentally

LC	2.1	2.5	2.7	2.20	2.21
f [Hz]	0.125	1	2	3	4
A [m]	0.125	0.035	0.008	0.008	0.008
U [m/s]	4.19	4.19	4.19	4.19	4.19
Ω [rpm]	240	240	240	240	240
f_r [-]	0.07104	0.5683	1.1367	1.705	2.2733
f_{fs} [Hz]	0.005	0.04	0.08	0.12	0.16
$A_{fs}[m]$	9.375	2.625	0.6	0.6	0.6

Table 2.3: Pitch tests. Load Cases (LCs) 3.1, 3.5 and 3.7 also tested experimentally

LC	3.1	3.5	3.7	3.20	3.21
f [Hz]	0.125	1	2	3	4
A [°]	3.0	1.4	0.3	0.3	0.3
U [m/s]	4.19	4.19	4.19	4.19	4.19
Ω [rpm]	240	240	240	240	240
f_r [-]	0.07104	0.5683	1.1367	1.705	2.2733
f_{fs} [Hz]	0.005	0.04	0.08	0.12	0.16
A_{fs}^{hub} [m]	6.3	2.625	0.6	0.6	0.6

2.3 Testcases

In order to attempt to understand the implications of pitch and surge motion on aerodynamic loads of a FOWT, simplified tests are performed. Rather than being subject to complex motion as a result of the combined effect of aerodynamic loads, hydrodynamic loads and control actions, tests are conducted with the UNAFLOW rotor oscillating under imposed sinusoidal pitch and surge motion. Various combinations of amplitude and frequency of the surge and pitch oscillations are tested. The surge tests are shown in Table 2.2. Load cases (LC)s 2.1, 2.5 and 2.7 are also tested experimentally in the PoliMi wind tunnel and are used for validation of the aerodynamic models.

The characteristics of the pitch tests are shown in Table 2.3. Experimental measurements are available for LCs 3.1, 3.5 and 3.7 that are used for validation of the aerodynamic models. Pitch tests are performed during the second measurement campaign that was conducted in the fall of 2021 in the PoliMi wind tunnel, as mentioned previously.

Additional surge tests with cyclic variations of rotor speed and blade pitch are performed. These tests were performed within the framework of the OC6 Phase III project [38], and are inspired by the work of Ramos et al. [11]. The characteristics of these additional tests are shown in table 2.4. These tests, while still simplified, attempt to mimic a more

Table 2.4: Additional surge tests with cyclic variations in rotor speed and blade pitch

LC	2.16	2.17
f [Hz]	2	2
A [m]	0.008	0.008
U [m/s]	4.19	4.19
Ω [rpm]	$240 + / - 34$	240
θ_{blade} [°]	0	$1.5 + / - 1.5$
f_r [-]	1.1367	1.1367

Table 2.5: Additional surge and pitch tests at low wind speed

LC	2.26	2.27	3.26	3.27
f [Hz]	2.5	2.5	2.5	2.5
A	0.08 m	0.008 m	2°	1°
U [m/s]	1.6667	1.6667	1.6667	1.6667
Ω [rpm]	150	150	150	150
θ_{blade} [°]	0	0	0	0
f_r [-]	1.2566	0.1256	1.4523	0.7261

realistic operating scenario. Below rated wind speed, as relative wind speed fluctuates due to the turbine surge motion, aerodynamic torque fluctuations induce a cyclic fluctuation in rotor speed. This condition is reproduced in LC 2.26. In this study any inertial effects are neglected and rotor speed is assumed to vary in phase with the relative velocity. Above rated wind speed on the other hand, the blade pitch controller is active, thus blade pitch will fluctuate to maintain constant rotor speed. This condition is reproduced in LC 2.27.

Tests with a lower wind speed, approximately corresponding to the cut-in wind speed, are also performed.

2.4 Results

In this section, results of the unsteady aerodynamic tests are discussed. The amplitude and phase-shift with respect to excitation of aerodynamic thrust and torque are analyzed. Test with force harmonic rotor oscillation in pitch and surge at rated wind speed and rated rotor speed are discussed first. This is the operating condition where aerodynamic forces are highest for a pitch-regulated rotor and is thus investigated first. As discussed in the following, all the tested aerodynamic theories performed well in these conditions. Differences start to emerge in surge tests with sinusoidal variation in rotor speed and blade pitch at rated wind speed, that are discussed next. Finally, test in below-rated operating conditions, near cut-in wind speed are discussed. In these conditions the rotor is operating

at high TSR and is highly loaded. Results show how in these conditions the dynamic wake effect is relevant.

2.4.1 Unsteady surge tests at rated wind speed

The aerodynamic load fluctuation in presence of a sinusoidal surge oscillation of the wind turbine rotor is shown in Fig. 2.9. The position and velocity of the rotor subject to imposed motion surge in LC 2.5, with a frequency of 1 Hz and an amplitude of 0.035 m is shown in Fig. 2.9 (a). The respective values of thrust force are shown in Fig. 2.9 (b). The oscillation frequency corresponds to an oscillation with a 25 second period at full scale, which is representative of the pitch natural frequency of many floaters.

Rotor thrust is sinusoidal in shape and roughly in-phase with the surge velocity, and thus lags behind the surge oscillation approximately 90°. The apparent change in wind speed caused by the rotor motion is the main factor that causes the oscillations in aerodynamic forces. Aerodynamic rotor thrust appears to respond linearly to a rotor surge excitation: given a periodic oscillation in surge at a certain frequency, the model response in terms of aerodynamic thrust is also a periodic with the same frequency of the excitation.

A difference in mean thrust of approximately 5% between the two experimental campaigns can be noted that appear to be fairly similar in terms of amplitude of the thrust oscillation. This value can be used as an estimate of the experimental uncertainty, given that no such metrics were provided. All the numerical models tested appear to be able to reproduce the experimental behavior well (Fig. 2.9). For this test case, all the model-predicted responses fall between the values of the two experimental campaigns. The models based on Blade-Element-Momentum theory (BEM_{st}, BEM, DBEM), predict lower mean thrust than the actuator line and lifting line based models, that can be fine-tuned by acting on model-specific numerical parameters. For instance, in ALM models altering the kernel size often has significant influence on results. Similarly, in a LLFVW model, total wake length plays an important role on mean aerodynamic forces. Focusing again on he BEM-based models, overall there are very little differences between them, although the use of dynamic polars and dynamic induction seems to amplify the amplitude of the thrust oscillation slightly.

Given the linear response highlighted in Fig. 2.9, numerical models can be compared in terms of the amplitude and phase-shift of the aerodynamic loads respect to the excitation. The mean value of the response will be neglected for the moment since it reflects the steady-state behavior of the different models. In fact, Corniglion et al. [52] found that when subject to a periodic surge oscillation, the mean aerodynamic thrust of the NREL 5MW rotor decreases and the mean rotor torque increases as the frequency of the oscillation increases. The authors have linked this behavior to the shape of the power and thrust curves of the machine, calculated with constant rotational speed. The power curve is convex, leading to increases in mean aerodynamic torque as oscillation frequency increases, while the thrust curve is concave, leading to the opposite.

Concentrating on the amplitude of the aerodynamic force oscillations, it is possible to show, through simple analytical steps, that if rotor thrust is linearly proportional to surge velocity, then the thrust amplitude normalized by the amplitude of the surge motion is

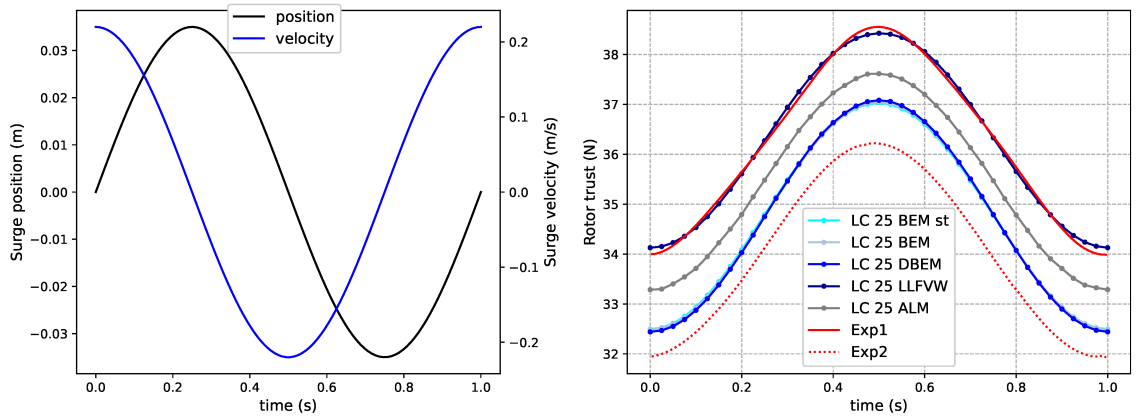

(a) **(b)**

Figure 2.9: Rotor surge position and velocity (a), Resulting rotor thrust computed with various numerical models in comparison with experiments

linearly proportional to the oscillation frequency. For a sinusoidal surge oscillation, the position and velocity of the rotor for a given amplitude A and frequency f can be written as:

$$x = A * sin(2\pi ft) \tag{2.4}$$

$$\dot{x} = 2\pi Af * cos(2\pi ft) \tag{2.5}$$

Assuming that the thrust response is linearly dependent from the apparent velocity (i.e. $\frac{dT}{dt} = k\frac{d\dot{x}}{dt}$, where $k = const.$), and only considering the total amplitude:

$$\Delta T = \Delta x = k * 2\pi Af \tag{2.6}$$

Which leaves us with the thrust amplitude being proportional to the surge motion amplitude and frequency. By normalizing by the amplitude however:

$$\frac{\Delta T}{A} = \Delta x = k * 2\pi f \tag{2.7}$$

Leading to the desired conclusion: assuming the thrust force to be linearly dependent on the relative velocity, the normalized thrust $\frac{\Delta T}{A}$ is linearly dependent on the surge frequency f. In practice, the actual response may differ from this linear assumption due to several factors:

- **steady response**. The steady response of the turbine depends on the operating point (TSR). If the rotor speed is held constant, such as in this case, surging motion causes the TSR to change, and consequently the turbine to operate at different TSRs during a surge cycle. Aerodynamic forces are a function of TSR. Moreover, the relationship between TSR and aerodynamic forces is highly non-linear, and can generally only be

approximated as linear in the vicinity of the considered operating point. Therefore, depending on the operating condition, a large enough variation in relative velocity will cause aerodynamic forces to not be linearly proportional to relative inflow speed.

- **unsteady aerodynamic effects**. Rapid variations in relative velocity cause the operating conditions of the wind turbine blades to vary dynamically. On a wind turbine rotor this has an effect on the strenght and position of the vorticity that is shed and trailed from the blades trailing edge. This evolutionary process depends on the prior time-history of the rotor loads and appears as a time-lag in the development of steady inflow at the rotor disk [7]. The effect is referred to as *dynamic induction* of *dynamic inflow* and results in an over or undershoot of aerodynamic rotor forces respect to their steady state (or quasi-steady) values. This effect is observed experimentally in the case of step changes in blade pitch [36] or rotor speed [37]. High frequency oscillations in inflow on the blades may also cause the pressure distribution on the blades to deviate from the one that is observed on an airfoil operating in steady-state conditions. As a consequence, the tabulated aerodynamic coefficients as a function of the angle of attack may not be valid in dynamic inflow conditions. This topic is extensively treated in [7] and will be expanded in the following of this study.

- **flow misalignment**. In case of pitching motion, flow incidence on the rotor plane changes. This adds to the unsteadiness of the problem, as rotor-flow misalignment introduces a synchronous oscillation in angle of attack on the blades, but also may have an effect on wake shape.

In Fig. 2.10 results of the forced surge oscillation tests are shown. The characteristics of the various tests are shown in table 2.2. The operating conditions in terms of wind speed and rotor speed roughly correspond to the operating conditions of the full-scale DTU 10MW rotor in rated conditions. These conditions are relevant as for a pitch controlled wind turbine, as they correspond to the conditions for which aerodynamic forces are highest. Fig. 2.10 (a) shows the thrust amplitude normalized by the surge amplitude, while in Fig. 2.10 (b) the phase shift of the aerodynamic thrust respect to the rotor surge motion is shown. Both amplitude and frequency are shown as a function of surge frequency.

Experimental data is present up to 2 Hz, as the wind tunnel model was only tested up to this frequency. A linear amplitude-frequency relationship is noted in the experimental data up to 2Hz, where especially results of the second campaign start to deviate from the linear trend. A peculiar trend can also be seen in the phase shift of the experimental data. At 1Hz, phase shift is smaller than at 0.125 Hz and 2 Hz in both experimental campaigns but in campaign 2 especially. According to researchers from PoliMi, who performed the experiments, this could be due to two reasons: i) velocity is not exactly constant in the test section. For the 1 Hz tests, velocity fluctuations due to turbulence are approximately 10% of the velocity fluctuation due to the surge motion. This introduces a disturbance across all frequencies that cannot be completely filtered out during post-processing. ii) rotor speed is not exactly constant during tests. In particular, due to limitations of the experimental system in the second campaign, rotor speed regulation is poorer in campaign 2: during the first test rotor speed variation of $+/-1rpm$ was observed,but this value increased

to $+/-4-5rpm$ in in the second tests. At 1 Hz the most fluctuations in rotor speed are observed, possibly explaining part of the observed behavior. Unfortunately, a proper quantification of the experimental uncertainty is, to our knowledge, not available. However, speaking to the researchers that performed some of the tests, the confidence interval of the phase-shift measurements can be assumed to be $+/-5$

The behavior of the numerical models in terms of thrust amplitude appears to be linear up to the frequency of 4 Hz. These results are consistent with those presented by Mancini et al. [41], who tested various numerical models up to the frequency of 2 Hz, Ribero et al. [53], who performed simulations using a panel code up to 8 Hz, finding linear behavior up to 4 Hz. The highlighted linear frequency - surge amplitude relationship is also consistent with results of OC6 Phase III [38], of which the DBEM results presented in this dissertation are part of. In comparison to experiments, very good matching is noted for all the numerical models at 0.125 Hz and 1 Hz, while at 2 Hz an underestimation of the surge amplitude can be seen, especially if compared to results from the second experimental campaign. The DBEM model consistently predicts slightly higher amplitudes than the BEM and BEM_{st} counterparts. Looking at phase-shift, in general a phase-lag greater than 90° is predicted. This phase-shift tends to increase as the frequency increases. The DBEM model shows the greatest phase-shift of all. It must be noted that this is the only model that was tested to include both unsteady blade and unsteady wake effects. BEM predictions are in line with ALM and LLFVW, although the latter two models do not include unsteady blade aerodynamics. Finally the BEM_{st} model, which uses static polars and includes no dynamic induction corrections shows a phase shift of almost exactly 90°. At 4 Hz even this latter model predicts a small phase-shift, which could be due to the variation in operating conditions that the rotor experiences.

Amplitude and phase-shift of rotor torque is shown in Fig. 2.11. The same trends that were discussed for rotor thrust (Fig. 2.10) can be noted.

For the combinations of surge amplitude and frequency that were tested in this study, aerodynamic forces appear to be linearly dependent of relative velocity and no significant deviations from this linear trend are noted. The dynamic inflow effect, that was observed experimentally for step changes in pitch angle and rotor speed, as discussed at the beginning of this section, was not observed, as no significant increases in the amplitude of the rotor thrust and torque are noted in the experiments and in the numerical models that are able to resolve the wake dynamics such as LLFVW and ALM. In terms of amplitude of the aerodynamic forces, quasi-steady methods, that do not account in any way for the time-history of the flow, such ase BEM, appear to perform similarly to higher-order models.

Some degree of non-linearities are noted in the phase-shift of the aerodynamic forces, which slightly lag the quasi-steady value of 90° as the oscillation frequency increases. This phenomenon is mainly caused by the effects of unsteady flow on the rotor blades. Unsteadyness in the wake's induction also contributes to this phenomenon but will be discussed in detail later on.

As the turbine surges, the angle of attack on the blades varies. This causes small hysteresis in the aerodynamic coefficients on the blades if this effect is included with an unsteady aerodynamic model. An example of this is shown in Fig. 2.12, where results

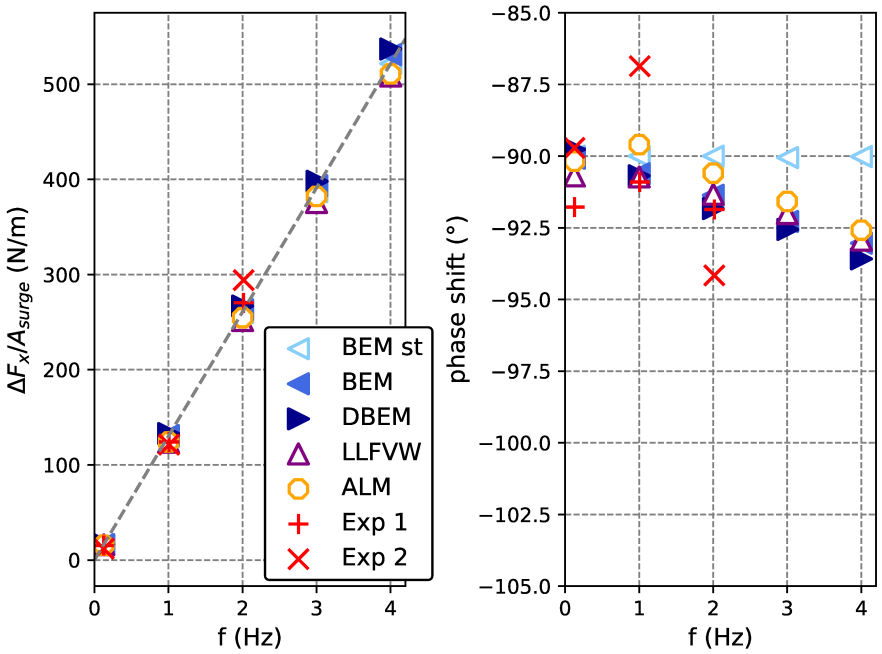

Figure 2.10: (a) amplitude and (b) phase shift of rotor thrust per unit surge with respect to sinusoidal surge excitation. Experimental data from the UNAFLOW test campaign [39] and OC6 phase III code-to-code comparison [38]

computed using BEM are shown. The hysteresis cycle is clearly visible and is introduced in the BEM model thanks to the use of a Beddoes-Leishman type dynamic stall model [49]. As surge frequency increases, so does the magnitude of the hysteresis loop. Hysteresis due to rapid changes in angle of attack can be observed in attached flow conditions, such as in Fig. 2.12, or in proximity or past the stall point of the airfoil, at which point the phenomenon is referred to as dynamic stall. In the flow conditions that are being examined here, attached-flow unsteady aerodynamics are the most relevant. As shown in Fig. 2.13 (a), angle of attack is fairly low for most of the blade span, especially for the parts of the blade where tangential and axial forces (Fig. 2.13 (b, c)) are highest, and thus parts of the blade that are most relevant for global rotor aerodynamic forces.

To explain the observed trend in Figs. 2.10 and 2.11, where phase-shift increases as oscillation frequency increases, a reduced frequency analysis, as proposed by Lackner [54] can be performed. Reduced frequency is a metric used to characterize the degree of unsteadiness in the aerodynamics of a system:

$$k = \frac{\omega c}{2V} \tag{2.8}$$

As k increases, the flow is more and more likely to be unsteady. Based on the scientific literature on the topic, for an airfoil in a plunge or pitch oscillation, a common threshold above which unsteady effects may be observed is defined to be $k = 0.05$ [7]. Neglecting

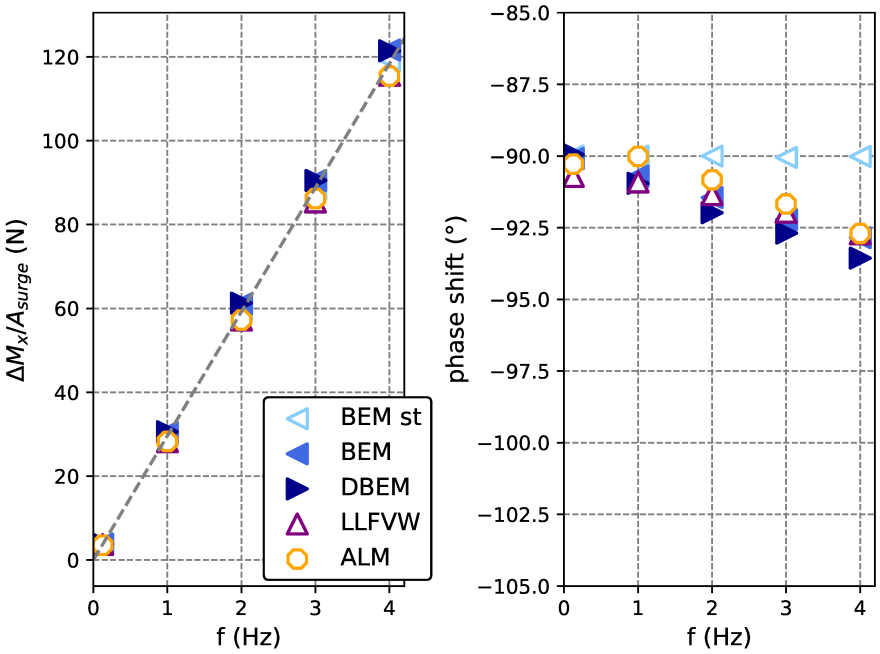

Figure 2.11: (a) amplitude and (b) phase shift of rotor torque per unit surge with respect to sinusoidal surge excitation.

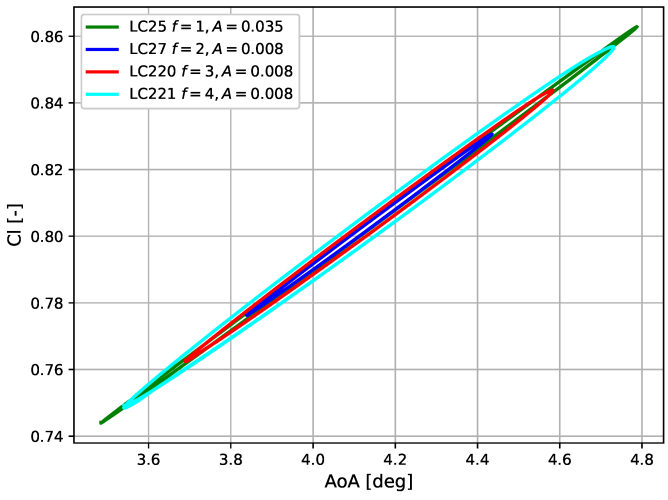

Figure 2.12: Lift coefficient as a function fo angle of attach at 53% rotor span in BEM simulations

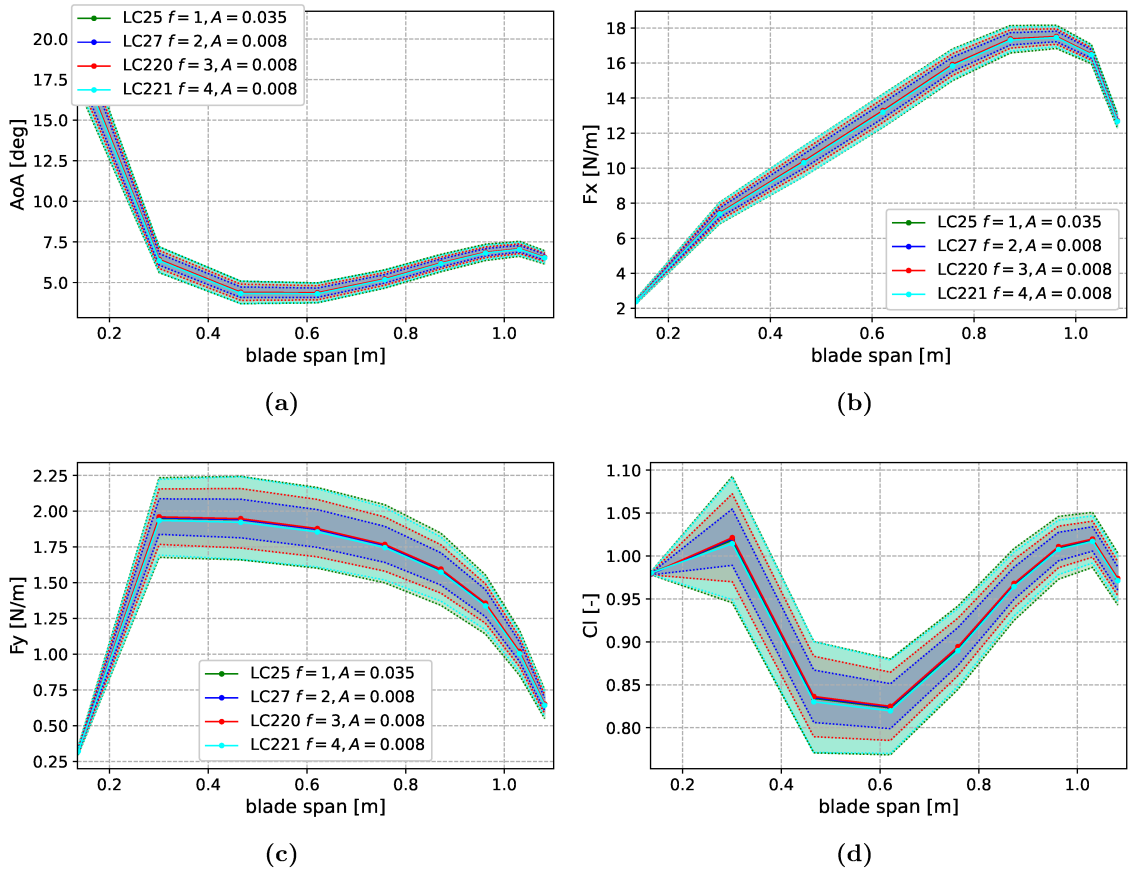

Figure 2.13: Aerodynamic parameters as a fucntion of blade span for lifting-line free vortex wake simulations with imposed surge motion. Mean values (lines) and min-max range (shaded area). (a) Angle of attack, (b) thrust force per unit length, (c) tangential force per unit lengh, (d) lift coefficient.

induction as a first rough approximation, the incoming velocity to each local blade point can be written as:

$$V = \sqrt{U_{\text{inf}}^2 + (r\omega)^2} \tag{2.9}$$

By substituting eq. 2.9 into 2.8, imposing $k = 0.05$ and solving for ω [54]:

$$f_d = \frac{0.05\sqrt{U_{\text{inf}}^2 + (r\omega)^2}}{\pi c} \tag{2.10}$$

f_d is a demarcation frequency and is defined as a function of the local blade radius. It indicates the oscillation frequency above which unsteady blade effects may occur. For the current test case, f_d is shown as a function of the surge frequency in figure 2.15. The

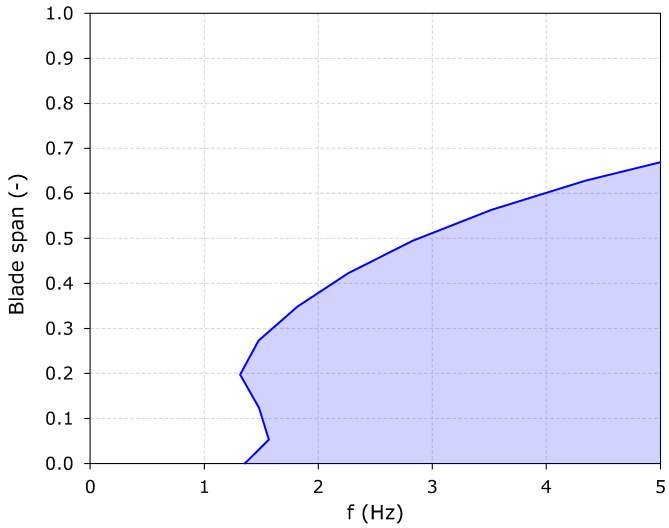

Figure 2.14: area of the blade were unsteady blade aerodynamics may occur as a function of oscillation frequency

shaded area to the right of f_d represents the blade regions where unsteady blade effects may occur. It is interesting to note how the blade span interested by unsteady effects increases as frequency increases. As more of the blade is interested by unsteady effects, the hysteresis of the aerodynamic coefficients also increases, as shown in Fig. 2.12. These two factors combined explain the increase of phase shift that is observed as surge frequency increases.

As for unsteady wake effects, as the surge frequency increases so does the reduced frequency f_r, introduced first by Bayati et al. [55] and explained in detail by Mancini et al. [41]. As noted by [41] [39], the higher the reduced frequency, the more likely unsteady effects are.

The phase shift with respect to surge motion of the relative velocity in the axial direction (V_x) is shown in Fig. 2.15. A phase shift smaller than -90° indicated that the wake introduces a lag in the relative velocity while the opposite is true for a greater than -90° angle.

Despite the use of a dynamic blade model, the relative velocity in the BEM model lags surge motion by -90°, indicating a quasi-steady behavior. This is because in AeroDyn the dynamic stall model is applied after the BEM iterations are solved and only influences the loads, not the wake behavior. In fact, the momentum balance is solved using the steady tabulated airfoil coefficients. Once the induction, and consequently inflow velocities and angle of attack are found, the forces are corrected to account for unsteady effects. While the theoretical validity of this approach is debated [56], in this case it allows for the separation of attached-flow dynamic behavior at a blade level from dynamic inflow at a rotor level. In fact, the phase-shift that is shown in the DBEM model is entirely attributable to the Øye dynamic inflow model, discussed in section 1.1.3. According to this model's predictions, phase shift is not uniform across the blade; a cross-over point between the relative velocity being ahead of the surge velocity and lagging behind it can be identified around 60% of the blade span. A similar behavior is also shown for the LLFVW and ALM models, although

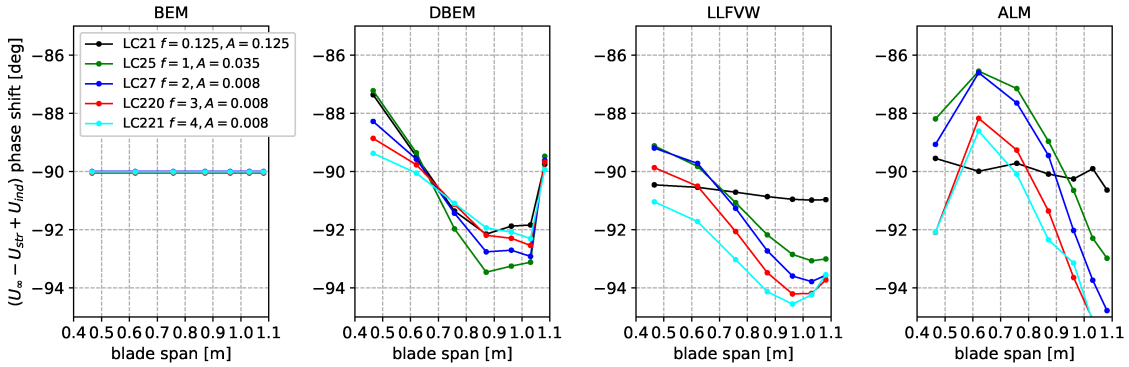

Figure 2.15: Phase shift in local relative windward velocity in (V_x) as a function of blade span for the various tested aerodynamic theorie. BEM and DBEM models include unsteady blade aerodynamic models, while LLFVW and ALM do not.

some differences can be noted. First both LLFVW and ALM predict very small phase shifts for LC 2.1, while DBEM doesn't. Secondly, in both the ALM and LLFVW models, phase lag tends to increase as frequency increases, more or less uniformly on the entire blade, while for DBEM this is true up to 2 Hz, after which phase-shift tends to decrease.

It must be noted that although unsteady attached flow effects are not explicitly included in the blade definitions used in the LLFVW and ALM models, which use static aerodynamic coefficients instead, the effect of shed vorticity on unsteady airfoil behavior is in part captured in these models. In fact, as blade loads change, the shed vorticity from the blades changes in the ALM and LLFVW models alike, in turn influencing the angle of attack on the blade. This effect is similar to that included in the circulatory part of Theodorsen's model, explained in detail in [7]. Therefore, the observed phase-shift in aerodynamic loads, which increases as oscillation frequency increases, can likely be attributed to the described unsteady circulatory effects.

In an attempt to increase non-linearities and possibly observe some sort of dynamic inflow effect, an additional load case was simulated: LC 2.12. This load case has the same characteristics as LC 2.7 (table 2.2) with the exception of surge amplitude, which is increased tenfold to the value of 0.08 m. The normalized thrust amplitude and phase shift of the thrust force is shown in Fig. 2.16. Even increasing surge amplitude tenfold there are very little differences in normalized thrust. Therefore, the linear relationship between normalized amplitude and frequency that was highlighted in Fig. 2.10 is maintained.

Axial induction, as measured in the LLFVW code, as a function of blade span is shown in Fig. 2.17. As shown in Fig. 2.17 (a), in LCs 2.5 to 2.21 axial induction does not vary significantly during the surge cycle, a consideration that is especially valid for the lower frequency load cases that were tested experimentally. On the other hand, in LC 2.12, variations in axial induction are significant. Despite this, no dynamic inflow effects are noted in Fig. 2.16, where the BEM models continue to be in line with the higher order models. This aspect will be discussed in further detail in the following.

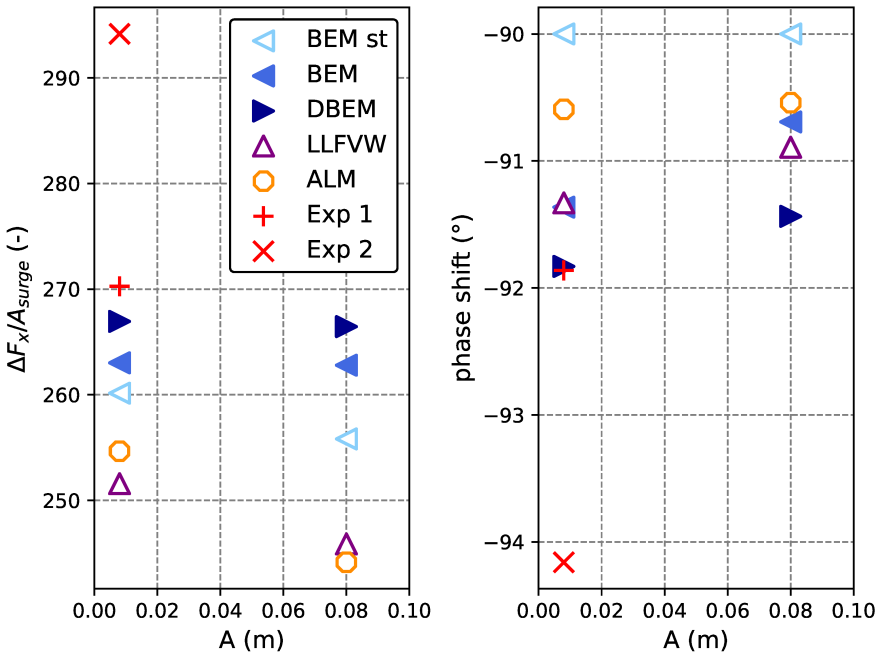

Figure 2.16: (a) amplitude and (b) phase shift of rotor thrust per unit surge with respect to 2 Hz sinusoidal surge excitation as a function of oscillation amplitude. Experimental data from the UNAFLOW test campaign [39] and OC6 phase III code-to-code comparison [38].

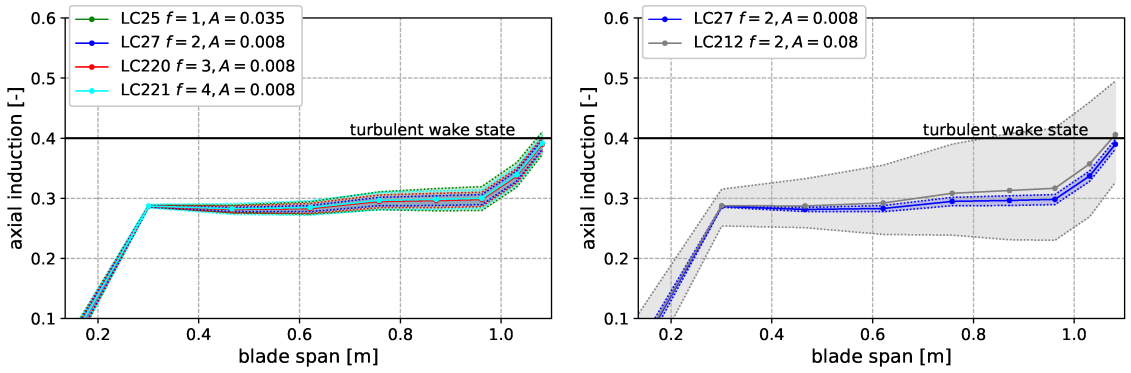

(a) (b)

Figure 2.17: Axial induction during a pitch cycle as a function of rotor span for LLFVW simulations. Mean values (solid line) and maximum/minimum ranges (shaded area). (a) Load Cases 2.5, 2.7, 2.20 and 2.21. (b) Load Cases 2.7 and 2.12.

2.4.2 Unsteady pitch tests at rated wind speed

When a forced pitch oscillation is imposed, the rotor moves in the fore-aft direction with a non-uniform speed during one oscillation cycle and a misalignment between the rotor and the flow is introduced. Characteristics of the tests conducted in pitch are show in table 2.3. The amplitude of the pitch cases is chosen so that the hub-height fore-aft oscillation is the same of the surge cases, with the exception of LC 3.1 that is limited to 3° of pitch oscillation by the test apparatus.

Aggregated results in terms of amplitude and phase shift for the pitch tests are shown in Fig. 2.18: in terms of normalized amplitude, the numerical models are close to the linear trend-line. Overall trends are similar to those observed in the case of surge oscillations. Two factors can be identified as a cause of this: i) the amplitudes are selected so that hub-height surge oscillation amplitude is the same as the surge cases and ii) pitch oscillations are small leading to small flow-misalignment angles. In contrast to numerical predictions, the experimental measurements tend to deviate from the linear trend especially at higher frequencies (1 Hz and 2 Hz). At the current stage it is unclear whether the numerical models are unable to reproduce the effects that are leading to the observed experimental trend or if the experimental value is affected by uncertainty. To this end, it would be useful to have an estimate of the experimental uncertainty that was not provided to the OC6 Phase III participants.

The BEM model's predictions are in line with the surge cases (Fig. 2.10): $DBEM$ shows a greater oscillation amplitude than BEM and BEM_{st}. All the tested numerical models appears to behave linearly with respect to frequency, albeit with a different slope coefficient. This effect was also present in the surge tests but appear to be more accentuated for the pitch load cases.

In terms of phase-shift, the numerical models show again a trend that is similar to the surge cases. However, all the numerical models fail to predict the experimental trends. Focusing on the latter, large differences of phase-shift are shown if we compare the 0.125 Hz and 2 Hz cases to the 1 Hz one. This trend was also noted when discussing the surge cases but appears to be more accentuated (Fig. 2.10). The observed trend could again be due to the oscillations in rotor speed during the tests caused by limitations in the experimental apparatus.

The causes that lead to the observed phase shift are the same as in the imposed surge tests (section 2.4.1): hysteresis in the lift coefficient due to unsteady attached flow aerodynamics and a time-lag in induced velocity on the blade.

Amplitude and phase-shift of rotor torque is shown in Fig. 2.19 for the pitch cases. As for the surge cases, the same trends that were discussed for rotor thrust (Fig. 2.18) can be noted.

2.4.3 Unsteady surge tests at rated wind speed with blade pitch and rotor speed variation

The load cases that were discussed up to this point feature a constant rotor speed and blade pitch. During actual operation however both rotor speed and blade pitch are adjusted based

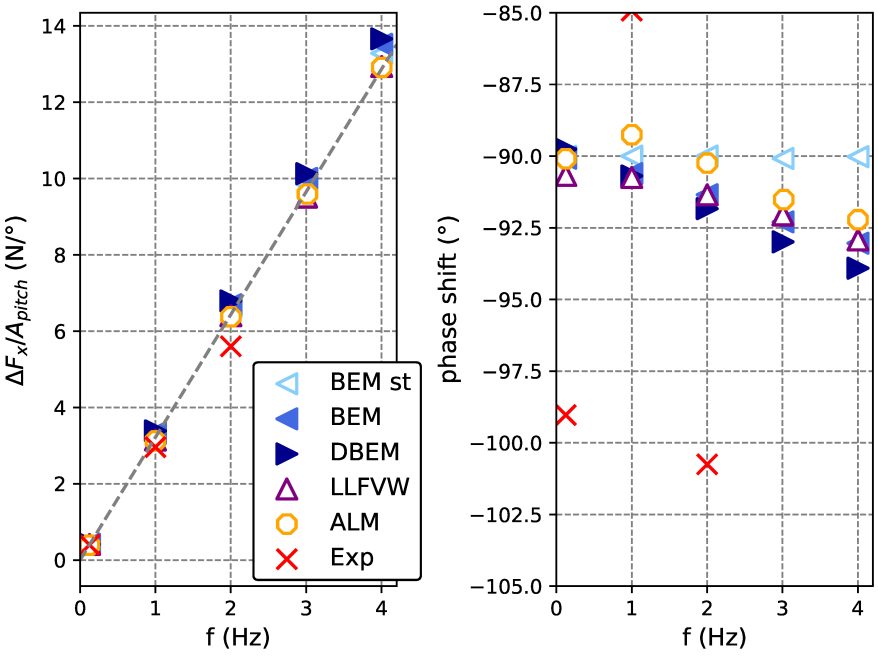

Figure 2.18: (a) amplitude and (b) phase shift of rotor thrust per unit pitch with respect to sinusoidal pitch excitation. Experimental data from the UNAFLOW test campaign [39] and OC6 phase III code-to-code comparison [38]

on the inflow conditions to keep loads in check and maximize power output. An insight on the behavior of the numerical models in such conditions is provided in LCs 2.16 and 2.17. LC 2.16 mimics below rated operation, where variations in torque caused by the surge motion cause variations in rotor speed. It is assumed that rotor speed variations follow the variations in relative velocity, neglecting the effects of inertia. In LC 2.17 above-rated operation is mimicked. Above rated, the controller holds rotor speed constant by adjusting blade pitch. Once again it is assumed that blade pitch variation follows the apparent velocity, neglecting inertia and controller-lag effects. The rotor speed and blade pitch variations respect to the surge motion are shown in Fig. 2.20.

The amplitude and phase shift of rotor thrust force recorded in LCs 2.16 and 2.17 are shown in Fig. 2.21, while the same metrics are shown for rotor torque in 2.23. Unfortunately, no results are present for the ALM model, as imposed rotor speed and blade pitch variations cannot yet be simulated in this model.

Significant differences between the modeling approaches now start to emerge in both LCs. Quantitative differences are shown in Tab. 2.6. Differences in predicted amplitude appear to be larger for both thrust and torque in LC 2.17. For thrust, this is partly due to the fact that variations are smaller in case of blade pitch variation (LC 2.17). Comparing the BEM and BEM_{st} models allows us to gage the influence that including unsteady aerodynamics in the test case makes. In terms of amplitude there seems to be very little difference

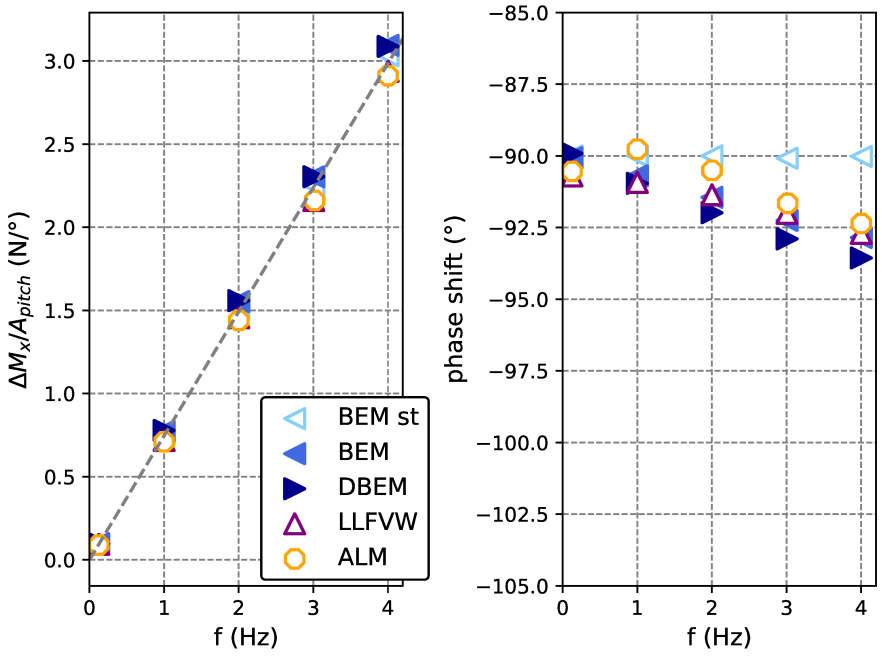

Figure 2.19: (a) amplitude and (b) phase shift of rotor torque per unit surge with respect to sinusoidal surge excitation.

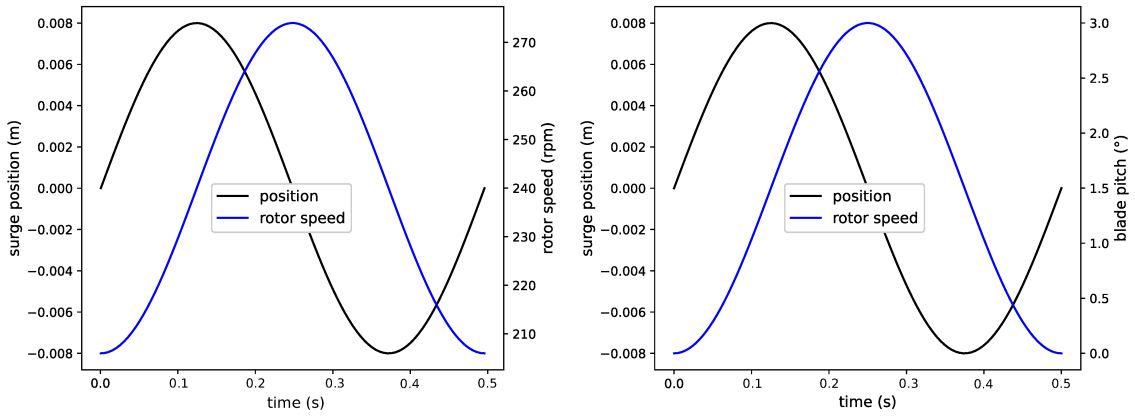

(a) **(b)**

Figure 2.20: (a) Rotor surge position and rotor speed in LC 2.16, (b) Rotor surge position and blade pitch in LC 2.17

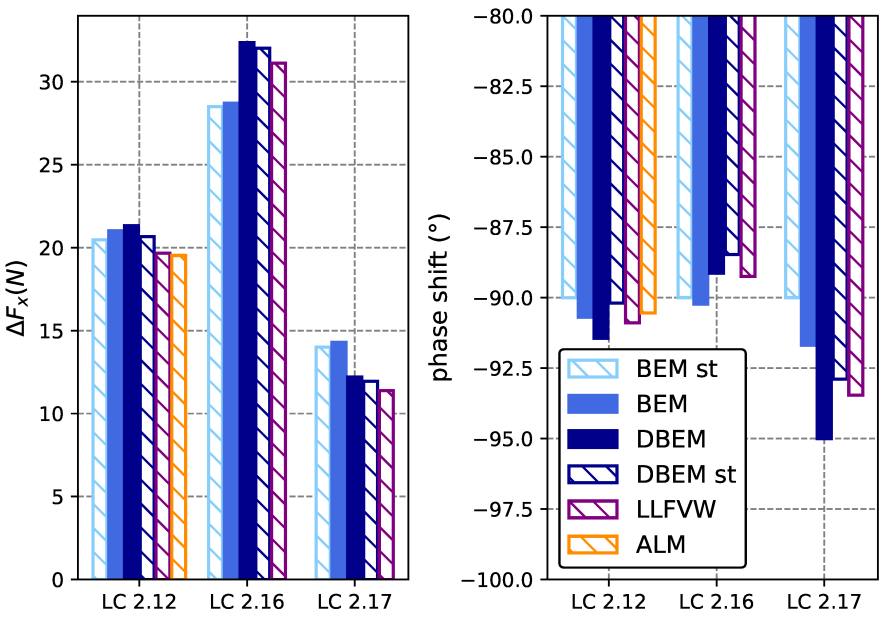

Figure 2.21: (a) amplitude and (b) phase shift of rotor thrust with respect to sinusoidal surge excitation at 2 Hz. $+/-1.5$ of blade pitch oscillation (LC2.17) and $+/-34rpm$ of rotor speed (LC 2.16)

between these models for both thrust and torque. Some differences can be noted regarding phase-shift, especially in LC 2.17, where modeling unsteady aerodynamics introduces an additional lag of approximately 1°. More quantitatively, in case of rotor speed variations (LC 2.16), thrust variations of up to 8% respect to the LLFVW results are noted. The latter is assumed as reference as it is the only examined model that is able to resolve wake unsteadiness. On the other hand in case of blade pitch variations (LC 2.17) differences in thrust are larger and can reach up to 25%. Respect to LLFVW, BEM models underestimate the thrust amplitude in the case of rotor speed variation (LC 2.16) and overestimate it in the case of blade pitch variation (LC 2.17). In all cases the use of a dynamic induction model ($DBEM$) reduces the difference between the former and the LLFVW reference.

In more realistic conditions, where simultaneous variations in rotor speed, blade pitch, wind speed and direction are common, based on the results shown in Figs. 2.21 and 2.23, including a dynamic inflow model into BEM-based simulations appears to be important.

2.4.4 Unsteady tests at cut-in windspeed

Up to this point tests with imposed pitch and surge motion were conducted at a wind speed and a tip speed ratio corresponding to approximately rated conditions at full scale. As mentioned previously, this condition is important because aerodynamic loads are highest in rated conditions for a pitch regulated wind turbine, therefore any difference between

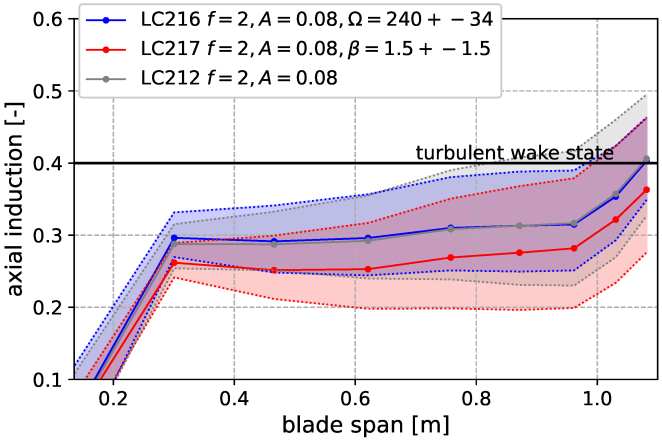

Figure 2.22: Axial induction during a surge cycle as a function of rotor span for LLFVW simulations. Mean values (solid line) and maximum/minimum ranges (shaded area). Load Cases 2.12, 2.16 and 2.17

Table 2.6: Predicted amplitude variations in thrust and torque by the various fidelity aerodynamic models for LC 2.16 and 2.17. Relative variations with respect to the amplitude predicted by the LLFVW model are also shown.

LC	model	ΔF_x	$\Delta F_x(\%)$	ΔM_x	$\Delta M_x(\%)$
2.16	BEM st	2.850e+1	-8.42%	3.888e+0	-11.91%
2.16	BEM	2.870e+1	-7.79%	3.907e+0	-11.47%
2.16	DBEM	3.235e+1	3.94%	4.688e+0	6.22%
2.16	DBEM st	3.203e+1	2.89%	4.640e+0	5.14%
2.16	LLFVW	3.113e+1	-	4.414e+0	-
2.17	BEM st	1.400e+1	23.04%	4.238e+0	15.86%
2.17	BEM	1.429e+1	25.56%	4.377e+0	19.67%
2.17	DBEM	1.221e+1	7.24%	3.875e+0	5.95%
2.17	DBEM st	1.195e+1	5.00%	3.745e+0	2.39%
2.17	LLFVW	1.138e+1	-	3.658e+0	-
2.12	BEM st	2.047e+1	4.04%	4.562e+0	4.43%
2.12	BEM	2.102e+1	6.88%	4.734e+0	8.37%
2.12	DBEM	2.132e+1	8.37%	4.700e+0	7.60%
2.12	DBEM st	2.066e+1	5.03%	4.525e+0	3.58%
2.12	LLFVW	1.967e+1	-	4.368e+0	-
2.12	ALM	1.953e+1	-0.70%	4.355e+0	-0.30%

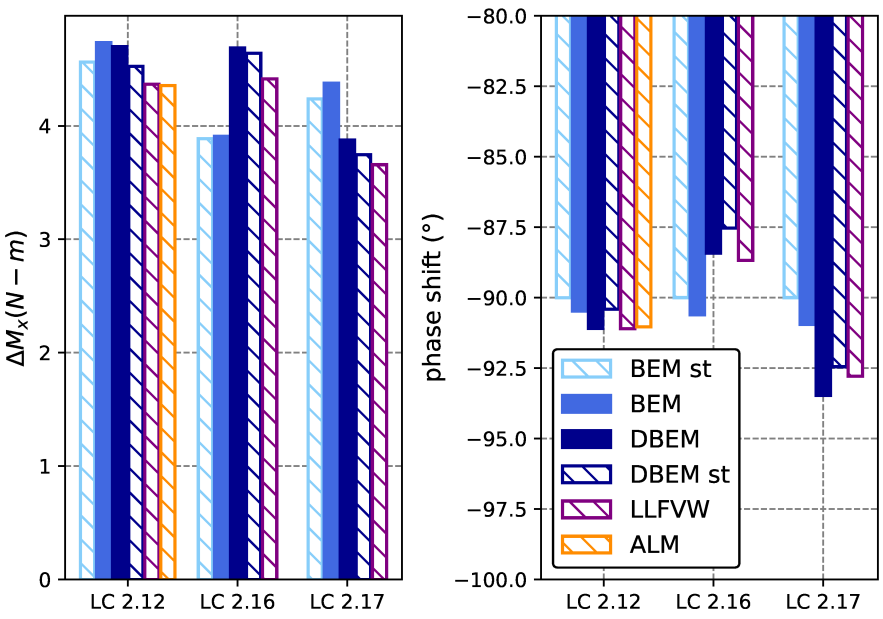

Figure 2.23: (a) amplitude and (b) phase shift of rotor torque with respect to sinusoidal surge excitation at 2 Hz. $+/-1.5$ of blade pitch oscillation (LC2.17) and $+/-15rpm$ of rotor speed (LC 2.16)

aerodynamic theories in this condition is particularly relevant.

In this section, aerodynamic loads in a condition that is close to cut-in wind speed at full scale is simulated. At low wind speeds, many wind turbines are not able to reduce rotor speed enough to maintain nominal TSR, and therefore operate at a higher TSR. This is the case, for instance, for many research wind turbines, such as the NREL 5MW [57], the DTU 10MW [40], of which the UNAFLOW rotor is the scaled-down version, and the IEA 15 MW [58].

At higher TSR, axial induction increases, effectively lowering the axial flow velocity in the wake. In these conditions the rotor is more likely to enter turbulent wake state, if axial induction exceeds the value of 0.4 [13], or if axial induction increases even further, some authors have observed the inception of vortex ring state [7]. In both conditions, Blade Element Momentum Theory is theoretically invalid, and aerodynamic forces in AeroDyn are computed using empirical functions, as discussed in section 1.1.1.

In addition, because the rotor is operating near cut-in wind speed, pitch and surge oscillations of the rotor are more likely to lead to rotor-wake interaction. In other terms, it is more plausible in these conditions that the rotor moves in and out of its own wake due to surge or pitch motion.

The characteristics of the pitch and surge tests are shown in Tab. 2.5. The oscillation frequency of 2.5 Hz corresponds to a period of 10 s at full scale, close to the peak spectral

period of many sea states, and therefore representative of a wave-induced oscillation of the turbine. The rotational frequency in the tests is 150 rpm, or 2.5 Hz. As in previous tests, revolution frequency is a multiple of the oscillation frequency, thus the tests are periodic.

Discussion is focused on tests with imposed pitch motion as pitch oscillations of 1° in normal seas and of 2° in severe seas appear to be more reasonable then surge oscillations of 6 m (LC 2.26) at cut-in wind speed. The time series of rotor thrust and torque predicted by the various numerical models in LCs 3.26 and 3.27 are shown in Fig. 2.24. Although mean aerodynamic torque is positive, in both load cases rotor torque is negative during some parts of the pitch cycle. Therefore, in a more realistic scenario, constant rotor speed would not be possible, and some fluctuations in rotor speed would be present instead.

For a more quantitative analysis of the results presented in Fig. 2.24, amplitudes and phase shifts of rotor thrust and torque are shown in Fig. 2.25 and 2.26. A significant difference (around 10%) in rotor thrust is observed when using dynamic polars in the BEM model. Therefore, results with static polars using the DBEM model are also included, as the higher-order wake models do not include dynamic polars. It must be noted that, as discussed previously, dynamic circulatory effects due to shed vorticity (theorized by Theodorsen [7]) are partly included in the LLFVW and ALM models. This is however a feature of the higher order models, and the comparison remains valid since the same exact aerodynamic tables were used. The difference between including dynamic polars or not may be down to model tuning. In AeroDyn, when B-L dynamic stall model is used, the tabulated aerodynamic coefficients are replaced by the normal force coefficient intercept and slope. This implicitly assumes that the aerodynamic coefficients are linear in the attached flow region. In the current test case, with low Reynolds numbers, this is not the case (Fig. 2.1). In these cases, the slope and intercept of the normal coefficient are tipically tuned so that they are a good approximation of the steady coefficients in proximity of the operation point. In the current study this operation was performed at rated conditions (LCs 2.1 - 2.20) and was not repeated herein, possibly leading to a poor fit. This is shown in Fig. 2.29, where lift coefficient as a function of angle of attack is compared for various blade sections.

If we compare results obtained with static polars in Fig. 2.25, BEM underestimates thrust amplitude, while DBEM is in much better agreement with the higher order models. This is also true for rotor torque in Fig. 2.26.

For these near cut-in conditions, with high TSR and low wind speed, axial induction is expected to increase with respect to rated conditions. AeroDyn calculates induction for each of the three wind turbine blades separately. Axial induction is shown as a function of time in LC 3.26 in Fig. 2.27. The use of Oye's dynamic wake correction mostly improves agreement with LLFVW, especially in the inboard sections of the blade, as shown in Fig. 2.27 (b), where improvements are most notable.

Axial induction along blade #1 mean and min-max range for LC 3.26 and 3.27 is shown in Fig. 2.28. In LC 3.27 axial induction is above 0.4 for approximately the outer 35% of the blade approximately. As discussed in section 1.1.1, momentum theory is invalid in these conditions, and is replaced by an empirical equation within AeroDyn. If we consider LC 3.27, the induction reaches even higher values, and is at times above unity. According to classical momentum theory this would mean that parts of the rotor are in the so-called

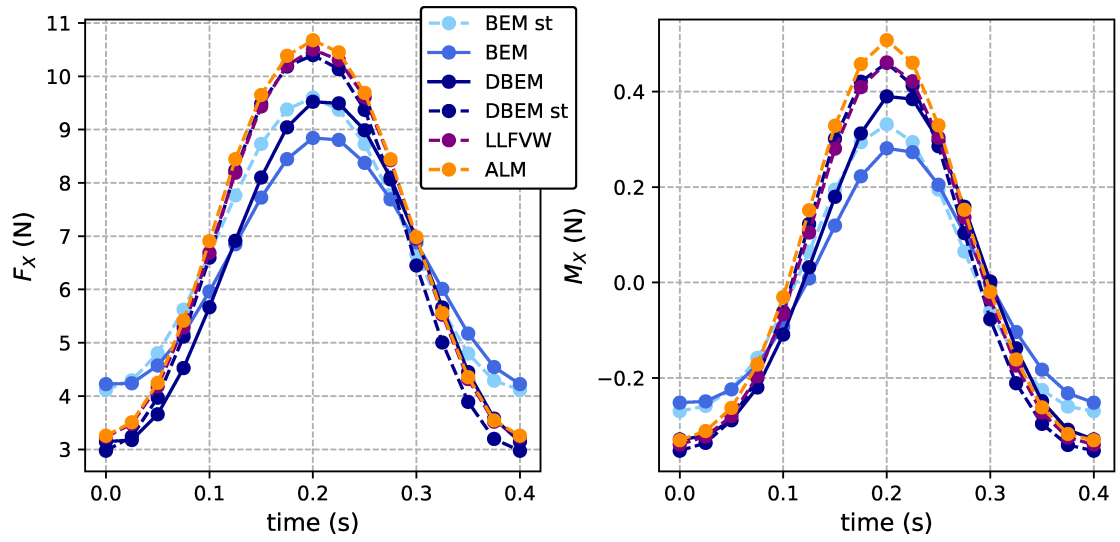

(a)

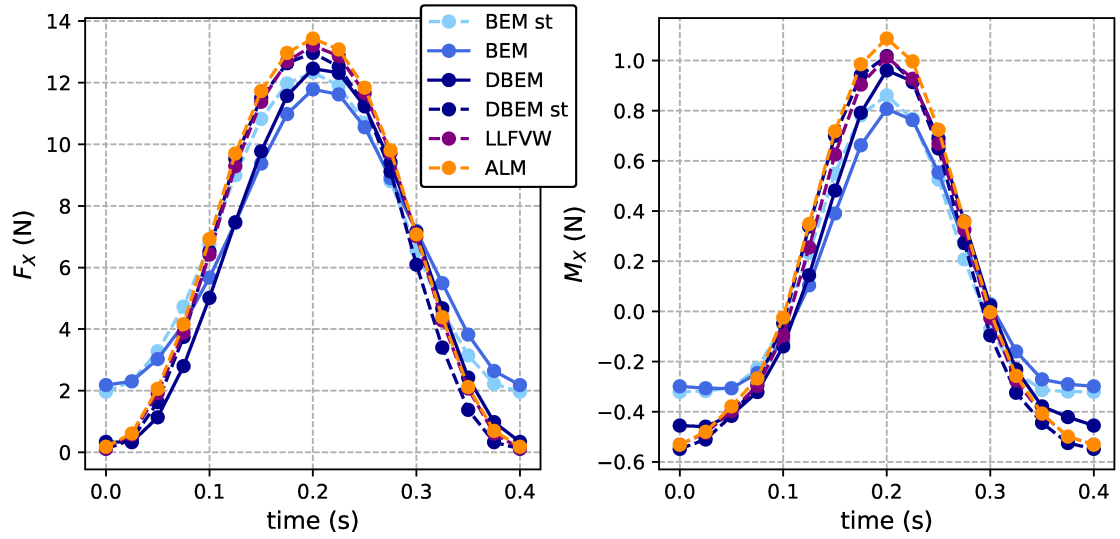

(b)

Figure 2.24: Rotor thrust and torque as a function of time during a rotor pitch oscillation at near cut-in wind speed (5 m/s at full scale). (a) $f = 2.5Hz$, $A = 1$ (LC 3.27) (b) $f = 2.5Hz$, $A = 2$ (LC 3.26)

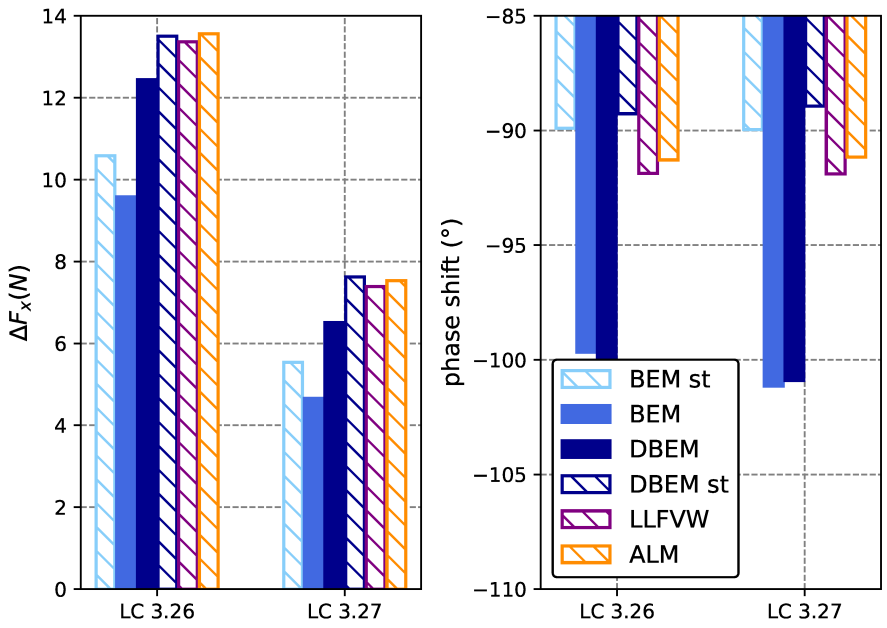

Figure 2.25: (a) amplitude and (b) phase shift of rotor thrust with respect to sinusoidal pitch excitation at 2.5 Hz. 1 of platform pitch oscillation (LC3.27) and 2 of platform pitch oscillation (LC 2.16)

vortex ring state or *propeller brake state*.

The high variations in axial induction that are observed are a consequence of the fact that in AeroDyn, the momentum balance is computed in the reference system that is relative to the blade-elements, and thus moves with them. In other words, the following balance equation is valid for the axial velocity:

$$U_x^{BE} = (U_x^{wind} + U_x^{struct}) * (1 - a) \tag{2.11}$$

where the apex ^{BE} indicates the velocity local to each blade-element. In LC 3.27 and 3.26 especially, the pitching velocity of the rotor is comparable to the inflow velocity for the upper parts of the rotor, thus leading to large fluctuations in axial induction. This aspect has been recently challenged by some authors within the wind energy community and will be discussed in detail later on.

2.5 Discussion

2.5.1 Is BEM able to model non-stationary rotors?

In this section, various-fidelity wake models, ranging from simple Blade Element Momentum to 3D RANS CFD, are compared in terms of the predicted rotor aerodynamic forces on

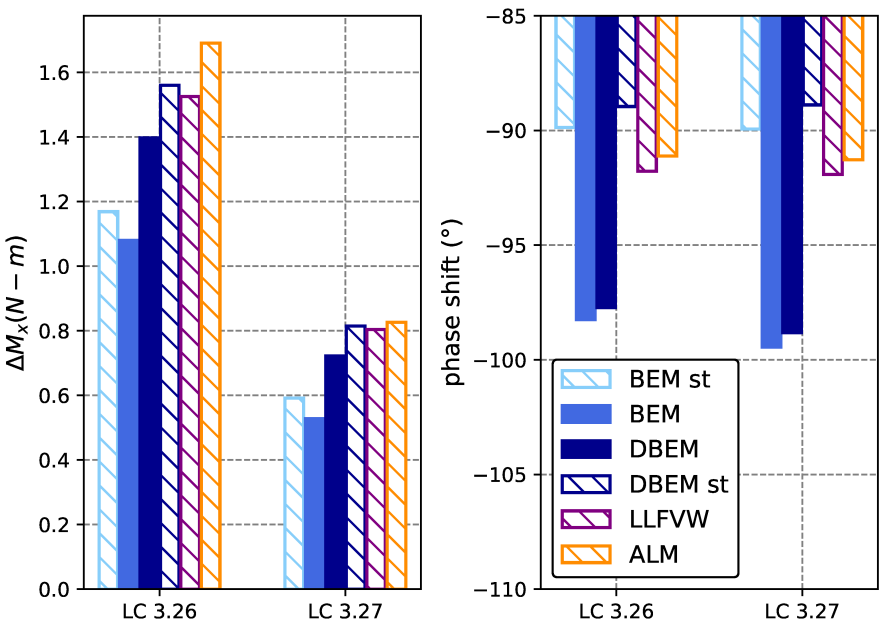

Figure 2.26: (a) amplitude and (b) phase shift of rotor torque with respect to sinusoidal pitch excitation at 2.5 Hz. 1 of platform pitch oscillation (LC3.27) and 2 of platform pitch oscillation (LC 2.16)

the UNAFLOW model turbine during surge and pitch oscillations. At rated wind speed and rpm, all the aerodynamic theories are able to predict the variations in aerodynamic forces induced by the forced rotor motion well. When the rotor is subject to a sinusoidal pitch or surge motion, aerodynamic thrust and torque are also sinusoidal and lag behind rotor motion approximately 90°. Combining the results of tests with various oscillation frequencies, a linear trend relating aerodynamic thrust and torque to oscillation frequency is found, indicating that for this testcase, near rated operating conditions, aerodynamic forces are proportional to the surge velocity. This linear trend is noted both in the case of surge and pitch tests.

With regards to amplitude of the predicted thrust and torque, little to no effect of dynamic inflow is noted, as even BEM, that does not model dynamic inflow in any way, produces results similar to ALM near rated conditions. With respect to phase-shift, a small phase lag of the aerodynamic forces can be seen. The phase lag increases as oscillation increases and is mostly caused by hysteresis in the lift coefficient due to dynamic attached flow effects on the blades. More specifically, this phase lag is noted in the BEM and DBEM model, which include an attached flow unsteady aerodynamic blade formulation, but also in the LLFVW and ALM models, which do not include a dynamic stall model in the blade lifting-line formulation. This indicates that the phase lag is caused by unsteady shed vorticity; the circulatory part of Theodorsen's model, as explained in [7]. The absence

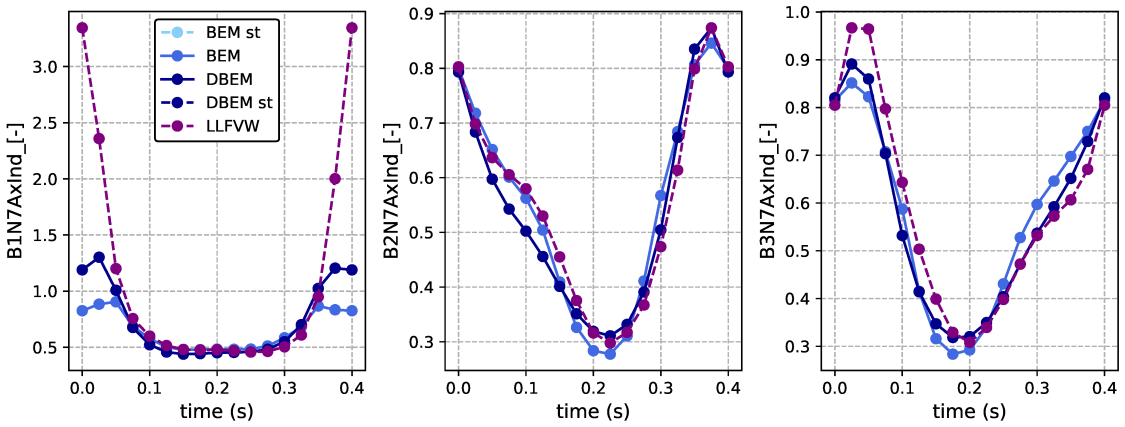

(a)

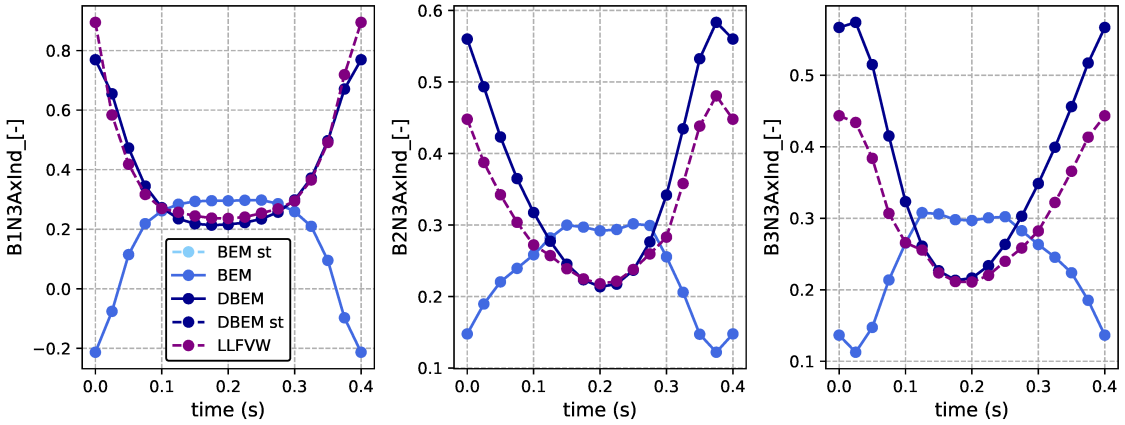

(b)

Figure 2.27: axial induction at (a) 88.2% blade span and (b) 46.6% blade span exported from AeroDyn for the three blades. Sinusoidal pitch excitation at 2.5 Hz. 2 of platform pitch oscillation (LC3.27)

of dynamic wake effects was noted also il LC 2.12, where surge oscillation amplitude was purposely increased tenfold with respect to wind tunnel experiments to increase variations in relative velocity on the rotor, despite significant variations in axial induction along the blades. These results are in line with those of other authors that have performed tests on the UNFLOW rotor have found little to no dynamic effects [41] [53].

Corniglion et al. [59] performed rotor speed, blade pitch and platform surge step tests. They found very little dynamic wake effects in the case of a surge step. The authors focused their efforts in analyzing the tip-vortices, as they are the main feature of the near wake of the turbine, especilly in design conditions, where circulation is fairly constant along the span of a well designed blade. In the case of a rotor speed step or a surge step, the axial spacing

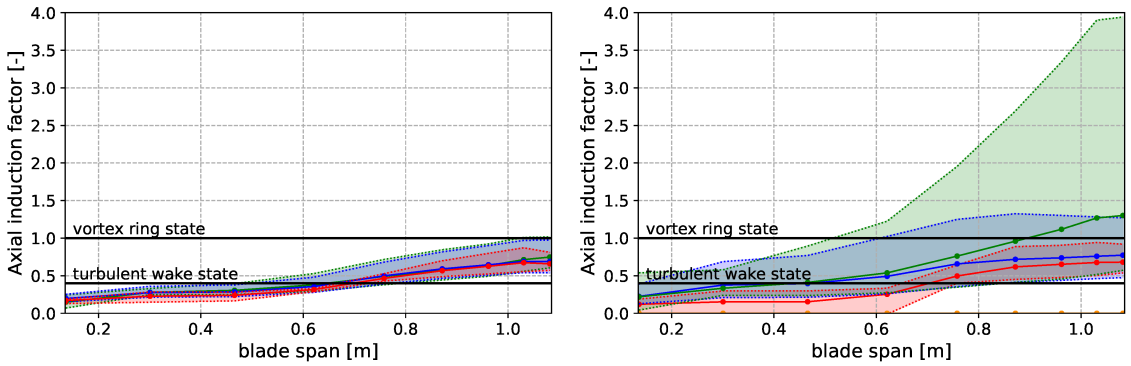

Figure 2.28: Axial induction during a pitch cycle as a function of rotor span. Mean values (solid line) and maximum/minimum ranges (shaded area). (a) $f = 2.5Hz$, $A = 1$ (LC 3.27) (b) $f = 2.5Hz$, $A = 2$ (LC 3.26)

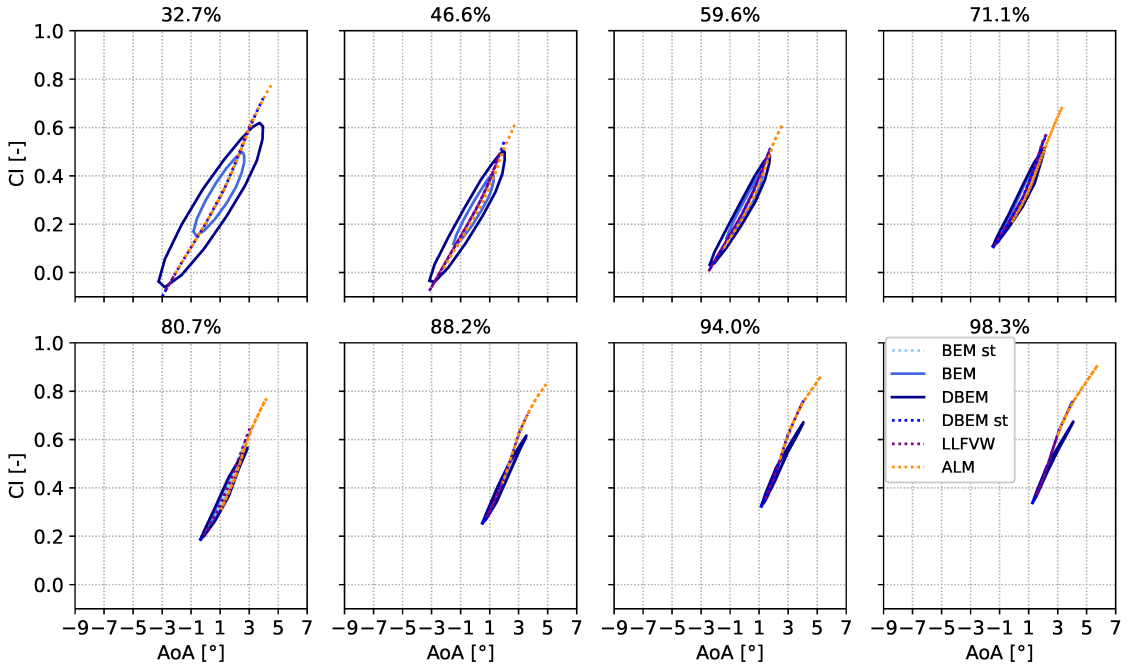

Figure 2.29: C_l as a fuction of AoA at varios blade spans for the various tested aerodynamic theories in LC 3.27 with static (dashed lines) and dynamic (solid lines) polars

of the tip vortices (and of all the rest of the trailing and shed vorticity) change: if the TSR increases, tip vortices are closer together and the opposite is true if TSR decreases. In the case of a surge step, the change in the shape of the tip vortex helix partially compensates the change in circulation of the tip vortices. In fact, according to [59], in the case of a surge step, induced velocity is related to $TSR * a$, and therefore a change in axial induction is not sufficient to cause induced velocity to change. As a consequence, variations in induced velocity are found to be small in the case of a surge step if compared to those induced by a rotor speed change or a blade pitch change. More importantly however, they are small respect to the surge velocity. Relative velocity due to surge motion has no time-lag with, as the wake-memory effect is generated by the lag in induced velocity. Therefore, if variations in induced velocity are small, due to the fact that the different shape of the tip-vortex helix compensates for the variation in tip vortex circulation, dynamic wake effects are also small.

In the current tests, variations in induced velocity appear to be small if compared to the surge and pitch velocity, possibly explaining the apparent little influence of wake dynamics on rotor thrust and torque.

When in addition to sinusoidal rotor surge motion a sinusoidal blade pitch or rotor speed variation is introduced in LCs 2.16 and 2.17, differences emerge between the models, despite variations in axial induction being faily similar to those observed in LC 2.12. In particular, BEM, that does not model wake dynamics, falls short of the predictions of LLFVW, which intriscially accounts for them. According to Corniglion et al.[59], in presence of a rotor speed step the change in spacing of the tip vortices cannot compensate for the circulation change of the vortex itself, and in presence of a blade pitch change, no change in the tip-vortex spacing occurs. While the combination of a step-change in surge with one of rotor speed or blade pitch have not yet been, to my knowledge, studied, the dynamic inflow effect was noticed in the case of step changes in blade pitch [36], and rotor speed [37], as discussed in section 1.5.2. Results from LC 2.16 and 2.17 suggest that wake dynamics are indeed relevant in this case of combined rotor surge motion and blade pitch and rotor speed variation.

The importance of wake dynamics in the load prediction of unsteady aerodynamic loads caused by platform pitch and surge motion is apparent in the additional tests in pitch and surge that were performed with low inflow velocity (LCs 2.26, 2.27, 3.26, 3.27). In these conditions the amplitude of the aerodynamic thrust and torque predicted by BEM is again different than that predicted by LLFVW and ALM. These results also seem to be in line with [59]. In fact, in these tests the turbine is operating at a TSR on approximately 11.5, with a C_T of approximately 1. For the UNAFLOW turbine, $TSR*a$ is not constant around this operating point (Corniglion et al. [59], Fig. 11), indicating that wake dynamics may indeed influence aerodynamic loads, as observed herein.

2.5.2 Wake states

DBEM predictions of rotor thrust and torque near cut-in wind speed are in sound agreement with higher order wake theories such as ALM and LLFVW. This is notable because axial induction is high in this case. As discussed in section 1.1.1 and 2.4.4, in AeroDyn, the momentum balance is applied in the referece system relative to each blade element. From a practical standpoint, rotor motion is treated in the momentum balance the same way a

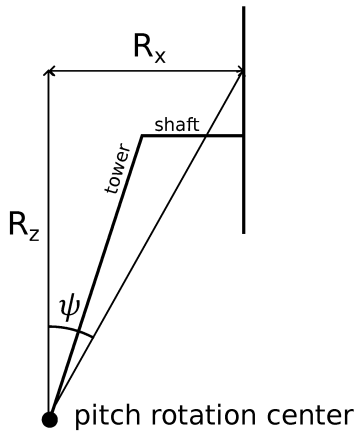

Figure 2.30: Schematic representation of the 1:75 scale rotor tested in the PoliMi wind tunnel

variation in inflow is. This is the same approach used in some commercial codes. such as AeroDeep [60] [61]. Moreover, Boorsma and Carboni [9] have found improved agreement with experimentally measured rotor thrust on the UNAFLOW rotor when the momentum balance is performed in the rotor reference frame.

In the low wind speed cases that are tested herein the windward velocity due caused by the pitching motion of the rotor is, at times, comparable to the inflow velocity, leading to very high induction factors. In the case of LC 3.26, axial induction computed by inverting equation 2.11, reaches values in excess of unity, where BEM theory is unpredictive. As a matter of fact, when axial induction instantanously exceeds the value of 0.4, AeroDyn applies empirical corrections, that were derived based on mean thrust and axial induction measurements on an entire rotor, to obtain induction coefficients at each blade section.

Ferreira et al. [12] have recently challenged this approach. According to the authors, for a rotor oscillating in surge, the momentum balance should be applied in the static inertial reference frame. Moreover, vortex ring state or turbulent wake state, which the turbine enters when axial induction exceeds 0.4, should be considered a status of the stream tube and not of the rotor. Authors argue that flow reversal may occur on the rotor blades themselves due to the motion of the rotor, but as long as no flow reversal occurs in the stram tube in the static reference frame, the rotor is still operating in windmill state, where BEM thoery is applicable. The fact that very high induction factors are observed, leading to the belief that the rotor is operating in vortex ring state, are a consequence of the incorrect application of the momentum balance to a non-inertial reference frame.

Based on these considerations, an analysis of the flow field in the near wake of the UNFALOW rotor during a pitch oscillation in LC 3.27 and 3.26 is shown in Figs. 2.31 and 2.32. The flow fields are extracted from LLFVW simulations, which do not rely on a momentum balance to solve the wake induction and are thus not affected by any inconsistencies on mis-applications of momentum theory.

Figs. 2.31 and 2.32, contours windward (directed along the X-axis) velocity are shown in the absolute and relative to the rotor reference frames. The velocity in the absolute reference

frame is exctracted directly from the LLFVW simulations. For the relative reference frame on the other hand, the structural velocity in the X direction of the rotor plane is subtracted using eq. 2.12. A graphical representation of the quantities in eqs. 2.12-2.15 are shown in Fig. 2.30.

$$V_{rel} = V - V_{stx} * R \tag{2.12}$$
$$V_{stx} = V_{st} * cos(\theta + \psi) \tag{2.13}$$
$$\psi = tan^{-1}(R_x/R_z) \tag{2.14}$$
$$R = \sqrt{R_x^2 + R_z^2} \tag{2.15}$$

In both LC 3.27 and 3.26 where pitch oscillations of 1° and 2° are imposed, flow reversal is observed in the refrence system relative to the rotor, but not in the static one. This explains the high induction factors, since this parameter is computed in the relative reference frame in AeroDyn. It also confirms the arguments of Ferreira et al. [12]: despite instantaneous flow reversal on the rotor, a stream tube in the static, inertial reference frame remains in windmill state.

Applying a momentum balance in the reference frame relative to the rotor is theoretically correct as long as the rotor is in an inertial reference frame and is thus either stationary, or moving with a constant velocity (for example in the case of a helicopter rotor at constant speed). Appling a momentum balance in a non-inerital reference frame is theoretically incorrect. The argument can be made that this is just one of many hypothesis that are violated by BEM-based wind turbine design codes. In fact, the hypothesis of steady, uniform inflow on the annular stream tubes is ignored in case of turbulent inflow that features spatial variations in wind speed. Other hypothesis, such as steady inflow, are also relaxed, and dynamic induction correction models are introduced [19].

How momentum theory can be extended and adapted to these unique conditions is an aera of active research. In fact, Ferreira et al. [12] have proposed a dynamic inflow model that can be applied in the inertial reference frame. At the moment the model was validated only in the case of surge oscillations, with no flow misalignment. Mancini et al. discussed this topic extensively in a recent publication [62]. The authors argue that, as was noted by a previous endeavour by some of the same authors [9], better agreement is observed with respect to higher-order wake theories when the platform velocity is treated as an apparent windspeed, including it in the momentum part of the balance equations. Although authors argue differently, this appears to be the same approach used in AeroDyn: including the platform velocity as apparent wind in the momentum part of the equations is in practical terms the same as performing the momentum balance in the rotor reference frame. An indication that the two approaches are indeed consistent with each other is apparent in the fact that both in this work and in [62] and [9], good agreement is seen between experiments and BEM.

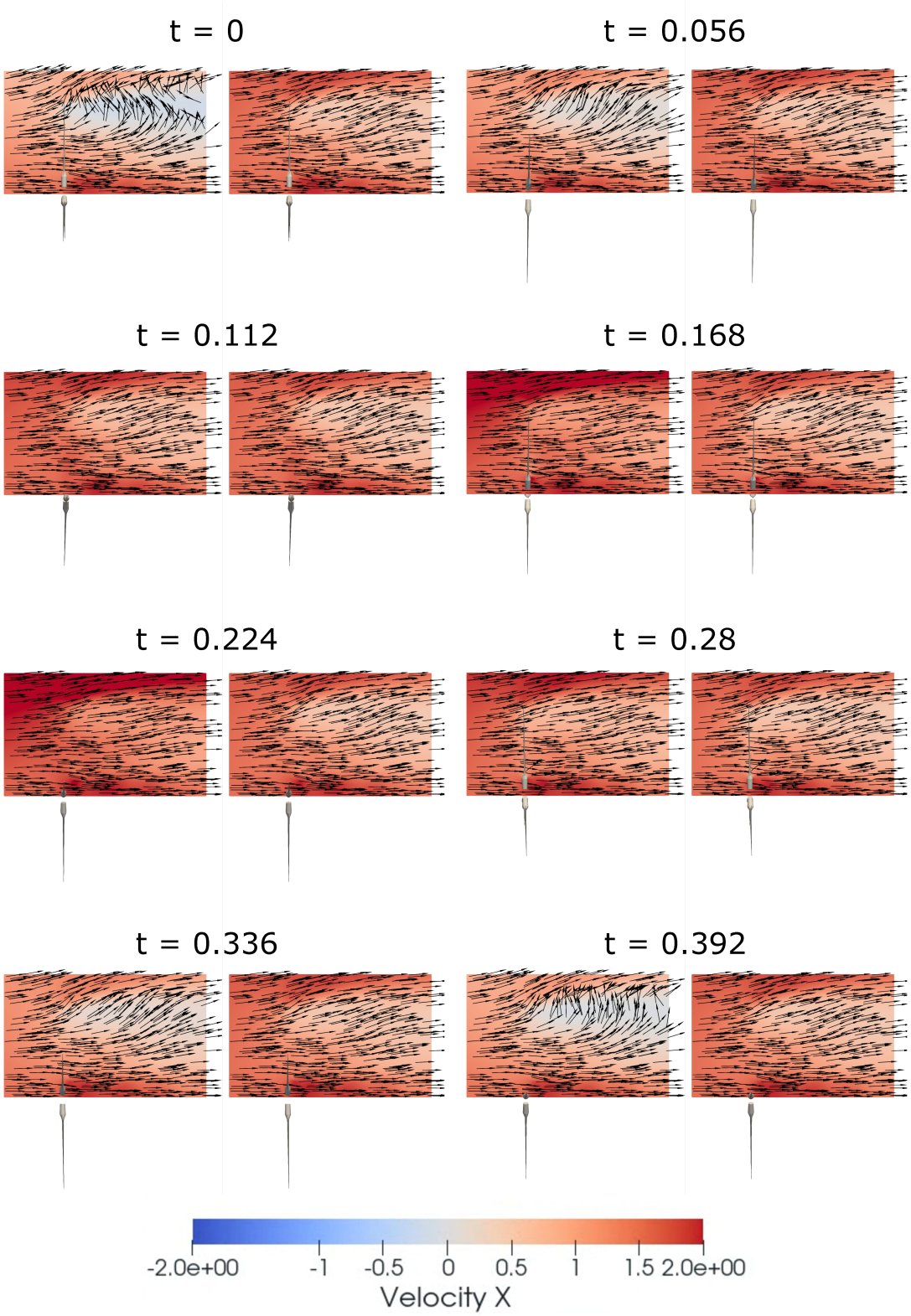

Figure 2.31: Snapshots of X-velocity for one pitch cycle with $f = 2.5$ Hz and $A = 1$ (LC 3.27). Foer each frame, on the left X-velocity in rotor reference system (V_{rel}), computed with eq. 2.12. On the right X-velocity in absolute reference system V.

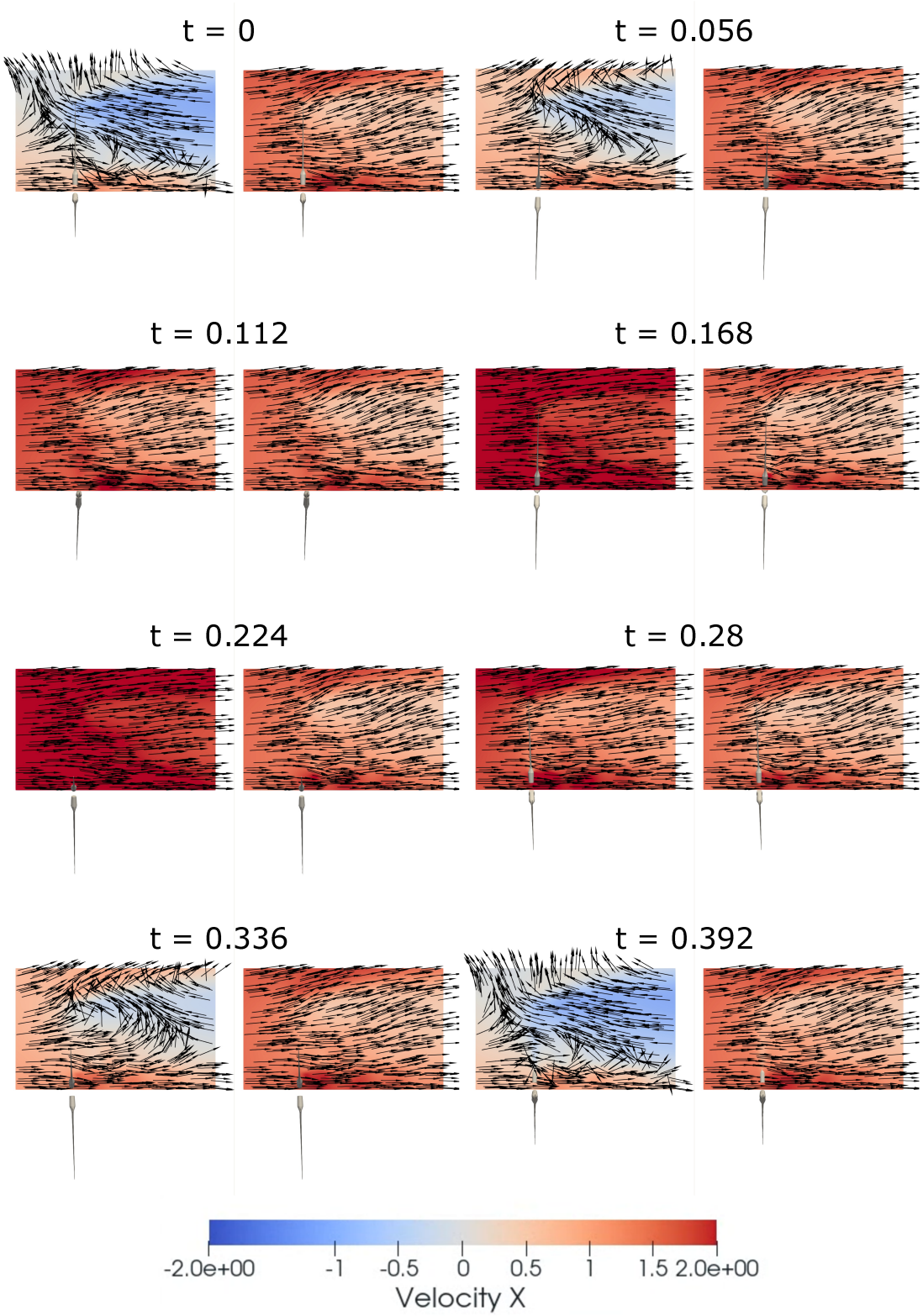

Figure 2.32: Snapshots of X-velocity for one pitch cycle with $f = 2.5$ Hz and $A = 2$ (LC 3.26). For each frame. on the left X-velocity in rotor reference system (V_{rel}), computed with eq. 2.12. On the right X-velocity in absolute reference system V.

2.5.3 Conclusions and outlook

In conclusion, the BEM model tested herein is in good agreement with higher order wake theories and experimental measurements when predicting unsteady aerodynamic forces resulting from pitch and surge oscillations. When the UNAFLOW rotor is oscillating in rated operating conditions with fixed rotor speed little to no dynamic inflow effects are noted, and the aerodynamic forces are mostly well reproduced by a quasi-steady model such as BEM. In more complex tests, such as when rotor speed or blade pitch variations are introduced in addition to the surge motion, or when the rotor is operating in low wind speeds and high TSRs, the use of a dynamic wake correction model, such as the one tested herein in the DBEM model, improved agreement with the higher order wake theories. Although using a more physically complete models such as LLFVW removes the question of if and when the aerodynamic model is applicable, in the conditions tested herein DBEM performed well, and was able to model the complex interactions between rotor motions and aerodynamic forces. This result is true despite the apparent inconsistencies in the DBEM model, such as the fact that momentum balance is applied despite the rotor being in a non-inertial reference frame. Small differences in aerodynamic forces may still however cause different controller reactions, or influence platform motions differently. Therefore, the aerodynamic theories will be compared in more complex conditions in the following chapters.

Chapter 3

Dynamic FOWT response: OC5 Phase II

After analyzing rotor aerodynamic loads predicted during simplified tests in chapter 2, the coupled response of a floating wind turbine system is studied in this Chapter.

The objective of this section is to evaluate if and to what extent modeling differences, in particular the use of higher-fidelity aerodynamic models, can influence the response of a floating wind turbine system, possibly leading to large discrepancies in the predicted loads and performance.

The work presented in this chapter has been performed within the framework of the H2020 project FLOATECH (https://www.floatech-project.com/). Within the FLOATECH project, the aim of this work phase is twofold: to understand the differences that improved numerical modeling may have with respect to an experimental reference and to validate the coupled FOWT simulation capabilities of QBlade-Ocean, a wind turbine simulation tool developed within the project.

In this chapter comparisons on the semi-submersible experimental model developed during the OC5 test campaign [63] are performed. This model was tested by the DeepCWind consortium in two different campaigns at MAritime Research Institute Netherlands. Experimental data of the downscaled 1/50 model is publicly available together with a large database of other established aero-hydro-servo-elastic codes. It is therefore a case that allows a good categorization of differences one might obtain between experimental results from the wave test facility and the ones from the numerical simulation. In addition, comparing numerical models of different fidelity to experiments, allows to quantify the differences that the improved accuracy of some of the tested models may have, bearing the experimental tests as reference.

Some simplifications with respect to a real operating environment are still present in this section; namely only aligned wind and waves are tested during the experiments, the rotor blades are rigid and the rotor speed is constant, without any rotor speed or blade pitch control is considered.

The chapter is structured as follows; the OC5 semi-submersible test case is presented first. Then the set-up of the numerical tools used in the comparison is presented. In the

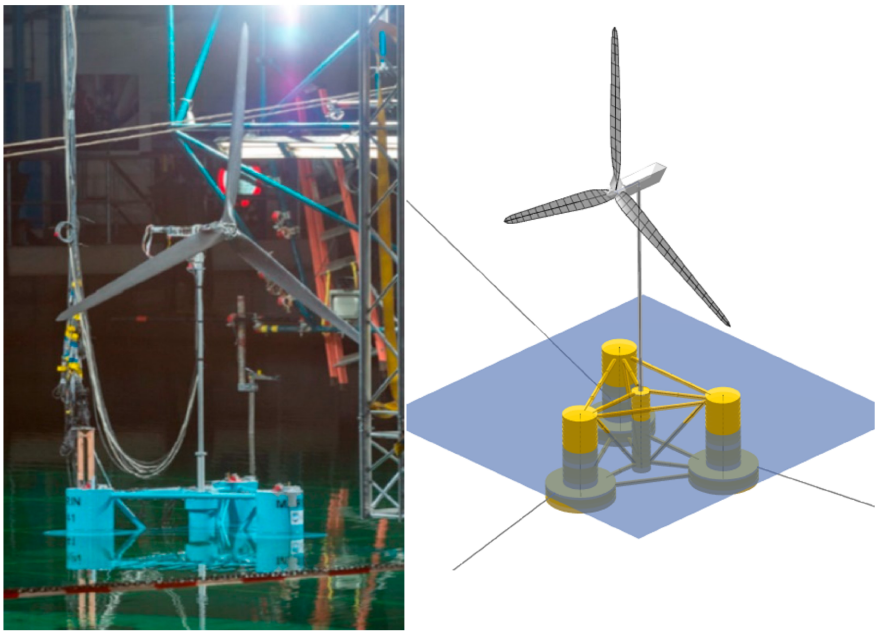

(a) (b)

Figure 3.1: (a) Experimental and (b) QBlade models of the NREL 5MW OC5 semi-submersible wind turbine

results section, the calibration procedure, featuring tests such as static offset tests, free-decay tests and regular wave tests will be presented first, followed by results of irregular wind and waves tests.

3.1 Description of the NREL 5MW OC5 turbine

A definition summary of the OC5 test case, made available for the OC5 code-to-code comparison, is provided in [63]. The results analyzed herein are relative to the second set of tests that were performed using this test case in 2013 [64]. The OpenFAST and QBlade models of this turbine, which are used in this comparison, comply as closely as possible to this definition. The experimental model and the numerical model in QB are shown in Fig. 3.1.

The turbine rotor used in the wave tank experiments is a performance-scaled version of the NREL 5MW RWT. Much like the UNAFLOW rotor that was described in the previous chapter, rather than geometrically scaling the rotor, the blades were scaled to maintain Thrust Coefficient and Power Coefficient as similar as possible to the full-scale turbine. Further details regarding the performance-scaling procedure of the rotors are provided in [65].

The rotor blades are built from carbon fiber and are very stiff. Thus, they are considered rigid in the numerical models. The tower is made from two hollow aluminum tubes and

it was designed to match the first fore-aft and side-side natural frequency of the full scale model. In the set-up of the numerical models used herein, an overestimation of the first fore-aft and side-side tower natural frequency was noted. To better match the experimental results, tower stiffness was uniformly reduced along the tower. While this is not ideal, it must be stated that the material properties of the as-built tower material is not provided in the test case definition document [63]. The presumable cause for the need to reduce the stiffnesses by 25% may lie within the fact that the experimental tower consists of two aluminum rods that overlap at their connection point. Although the cause of the overestimation is not fully understood, the model definition, overestimation of natural frequencies and consequent stiffness tuning are all consistent among the codes that are compared herein, making the comparison fair. The tower natural frequencies (shown in table 3.1) of the experimental model of the 5 MW OC5 model are matched closely with differences below 5%.

Table 3.1: First tower natural frequencies of the 5MW OC5 FOWT model

mode name	Value QB	Value OF	Value Exp.
1^{st} tower side-side	0.316 Hz	0.330 Hz	0.325 Hz
1^{st} tower fore-aft	0.331 Hz	0.327 Hz	0.315 Hz

Potential-flow hydrodynamic coefficients are pre-computed in WAMIT and were provided to the OC5 participants. The same coefficients are used in this work in both models. Quadratic Transfer Functions are also provided to the participants and are used as-are. As-built floater weight and inertial properties as well as mooring line properties are defined in [63] and are used with no changes in the codes compared herein.

No blade-pitch or generator torque control was used in the experimental tests, that feature constant rotor speed.

The QBlade-Ocean model of the turbine is available publicly on Zenodo (doi.org/10.5281/zenodo.6397352).

3.2 Numerical tool set-up

In this chapter two wind turbine simulation codes that include varying fidelity approaches for aerodynamics and structural dynamics are compared: OpenFAST (OF), and QBlade-Ocean (QB).

OpenFAST, is a state-of-the-art multi-physics wind turbine simulation code developed by the National Renewable Energy Laboratory. A description of the code is provided in section 1.4.1. All the calculations shown in this chapter are performed with OpenFAST v3.0.0. Qblade-Ocean is a state-of-the-art multi-physics wind turbine simulation code developed by Technical University Berlin. Like OF, it is available open source and is able to model FOWTs. A description of the code is provided in section 1.4.2.

While the modeling choices in QB and OF are largely consistent, both codes were set up independently and particular care was given to use each tool to its fullest ability to

represent the actual physical phenomena. In the following the main modeling choices and the differences between QB and OF will be explained in detail.

3.2.1 Aerodynamics

Aerodynamics are modeled using LLFVW theory in QB. In OF, two different aerodynamic models are compared: LLFVW and DBEM.

3.2.2 Structural Dynamics

Structural dynamics are modeled with very different approaches in the compared codes. QB employs a multibody finite-element model based on Euler-Bernoulli beams, while OF uses a much simpler modal approach. As shown in [66], QB is able to account for complex phenomena such as large deformations and asymmetric full system modes, while OF is not. Within the context of the 5 MW OC5 model, this does not influence the structural dynamics of the rotor as the blades are modeled as stiff structures [63]. Therefore, despite the multibody model included in QB being significantly more advanced that the one included in OF, this aspect is not expected to impact greatly on the OC5 test case.

3.2.3 Hydrodynamics

Hydrodynamics actions of the semi-submersible are modeled with a Linear Potential Morrison Drag (LPDM) approach, whereby excitation, added mass and radiation damping effects are computed through a potential-flow solution and quadratic drag is included through the use of Morrison's equation. Several additions to this LPMD core model have been included, as Robertson et al. have found that they improve aggrement with experiments [67]. In fact, second-order wave excitation has been included through the use of difference-frequency and sum-frenquency QTFs in both QB and OF. To improve agreement with respect to experiments during Free-Decay tests, the transversal and axial drag coefficients on the semi-submersible columns and heave plates respectively have been tuned. In OF a value of 1.35 for the transversal C_d and a double-sided axial C_d of 4 are used. As noted in [68], these values are significantly higher than those expected for similarly sized floating substructures. A constant force was added in the surge direction in both the QB and OF model, to improve agreement regarding the undisplaced position of the FOWT, as the experimental model features a significant cable bundle, that is found to offset the undisplaced position of the model [68]. Additional stiffness in surge and sway is also introduced to account for the effect of the cable bundle on the sway and surge natural periods. In OF, additional linear damping is included to improve agreement in this aspect during free-decay tests.

Despite the overall approach to modeling hydrodynamics being very similar amongst the two codes, some differences remain:

- In OF buoyancy is modeled as the sum of a constant buoyancy force, which depends on the volume of the submerged substructure, and a deviatory buoyancy force, which is calculated using a hydrodynamic stiffness matrix that models restoring forces that

arise when the body is displaced. In QB, the hydrostatic buoyancy force is discretely calculated based on the displaced volume by the floating structure with respect to the Mean Sea Level. Thereby, the volume of the partially submerged elements at the sea surface is calculated upon the intersection of the MSL and the centerline of the cylindrical element. This approach introduces an error since the assumption of a constant sea level along the horizontal extension of one of the large cylindrical elements of the OC5 platform is flawed. Therefore, the partially submerged cylindrical elements are discretized into 100 prismatic elements. The intersection of the MSL with the centerline position of each of these elements is now considered and the error thus minimized. This approach should yield improved results compared to the approach of OF as nonlinearities (e.g. for large pitch angles) are captured.

- The Wheeler kinematic stretching method is applied in QB to approximate the water kinematics above MSL. This method stretches the scaling term E(z)[1] during a crest and contracts it in a through. Without the application of kinematic stretching, this scaling term is always referring to the MSL, neglecting the unsteady nature of the water kinematics caused by gravity waves. OF currently does not account for kinematic stretching. Including wave stretching was found to improve agreement with experiments in [67].

3.2.4 Numerical tool calibration

3.2.5 Static offset tests

Static displacement tests aim to validate the definition of the mooring system. The floating structure is displaced from its neutral stand-still position (NP) and the loads that act at each of the three fairlead connectors in x-direction (surge) and y-direction (sway) are summed up respectively to give the cumulative mooring loads. The results of the static test are displayed in Fig. 3.2. Good agreement is observable between the experimental and both numerical models of the 5 MW OC5 FOWT. Even for large surge-displacements (more than 15 m), where the line connection points of each of the three mooring lines are displaced considerably, very close alignment with the experimental results is present.

3.2.6 Free-decay tests

The aim of the decay test load cases was the validation of the calibration of the model. Thereby, the six rigid-body natural frequencies and damping coefficients as well as the resonance-critical first tower bending frequencies in fore-aft and side-side directions are extracted. The latter are presented in Table 3.1. The natural frequencies of the six DoFs from both numerical codes and the experiment are displayed in the bar chart in Fig. 3.3. It can be seen that very good agreement was reached. To validate the quadratic and linear damping terms, it was decided to not follow the route of the OC5 experiments, in which linear and quadratic damping coefficients were compared. This decision is based on the fact that, due to the regression analysis, both coefficients, and in particular the linear damping

[1] E(z) defines the particle velocity distribution between the sea bed and the sea surface

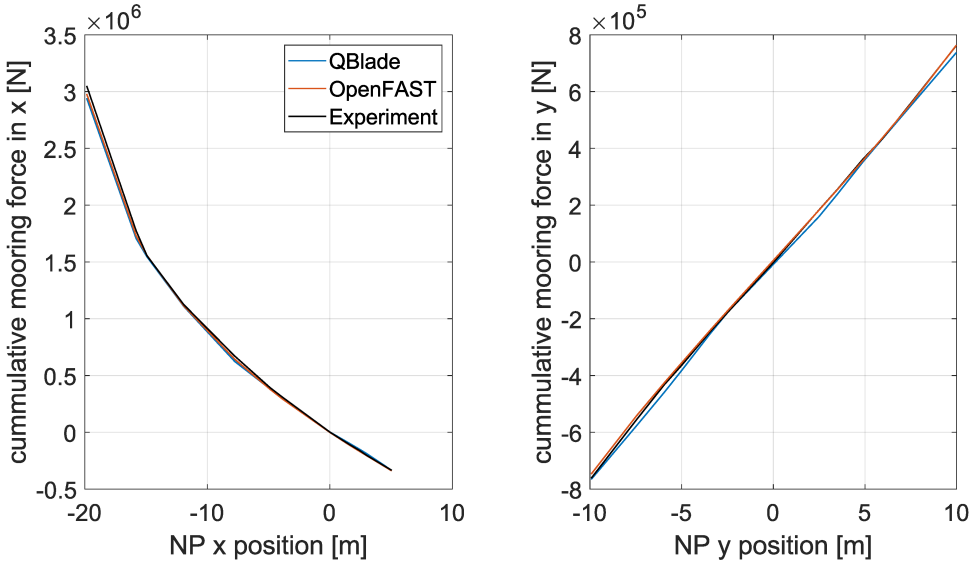

Figure 3.2: Global mooring line restoring force for static offset tests in surge and sway direction

coefficient, are very sensitive to sampling rate and the peak identifying algorithms. Since a visual comparison of the time series offer insight into the quadratic damping (first peaks) and the linear damping (peaks at the end of the time series), it was decided to follow this approach. Experimental data of the decays was not publicly available but thanks to NREL, this information was shared upon request. Fig. 3.4 displays the time series of the decay in the surge and pitch DoFs . Generally, good agreement of the time series may be obtained. The visual comparison of the damping yields that QB is overestimating the quadratic damping in surge and underestimating it in pitch direction. The linear damping aligns very well in both DoFs.

3.2.7 Regular waves tests

Regular wave tests are analyzed with the objective of demonstrating that hydrodynamic excitation in the wave frequency range is properly captured by the numerical models and to evaluate system response to waves in a simplified scenario. In LC3.1 a regular wave with an amplitude of 7.37 m and period of 12.07 s is imposed. As opposed to a perfectly sinusoidal wave excitation, the external wave height time series that was measured in the wave basin during the experimental tests was used. As the waves in the experiment are not perfectly sinusoidal, higher-order harmonics of the dominant frequency are also excited. Using the basin-measured waves allows the introduction of this excitation in the numerical models as well. Initial tests with a perfectly regular wave did not capture this effect. In Fig. 3.5 the recorded time series of selected load sensors as measured in LC3.1 are shown: platform surge, pitch and heave to evaluate platform motion, fairlead tensions of the three mooring lines, and tower base fore-aft shear force (TB Fx) and fore-aft bending moment (TB My). As

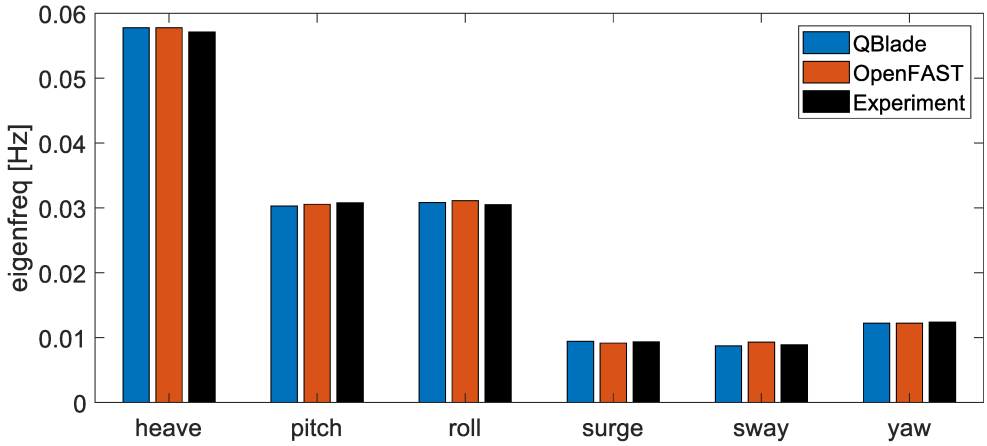

Figure 3.3: Eigenfrequencies from free-decay tests in the six flatform DOFs

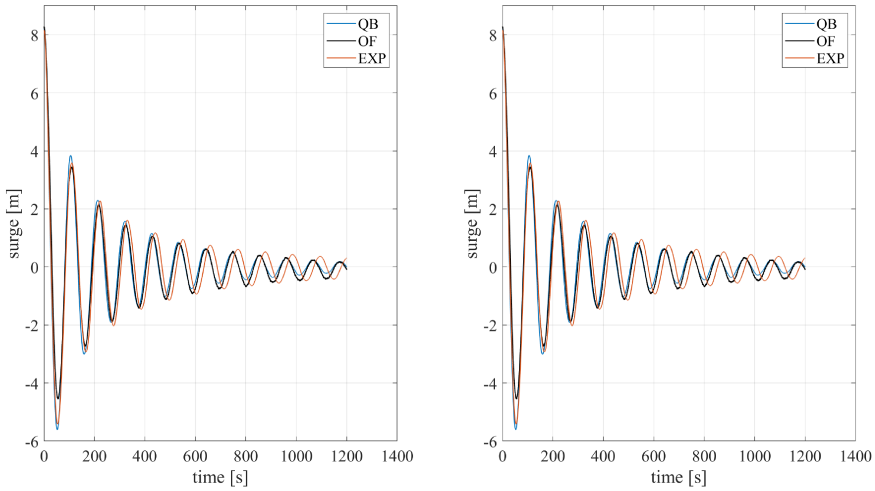

Figure 3.4: Time series comparison of surge and pitch free decay tests

shown in Fig. 3.5, when excited by a regular wave, the floating system responds linearly in terms of motions and fairlead tensions. In other terms, when excited by a harmonic wave, the system responds harmonically at the same frequency of the exciting wave. Overall, system response in terms of amplitude and phase shift with respect to the incoming waves is very good for both OF and QB, especially for motions and fairlead tensions. The mean values also appear to be in good agreement with the experiments. Tower base fore-aft shear force (TwrBsFxt) and fore-aft bending moment (TwrBsMyt) show strong excitation at the tower resonance frequency. The tower resonance frequency of approximately 0.32 Hz

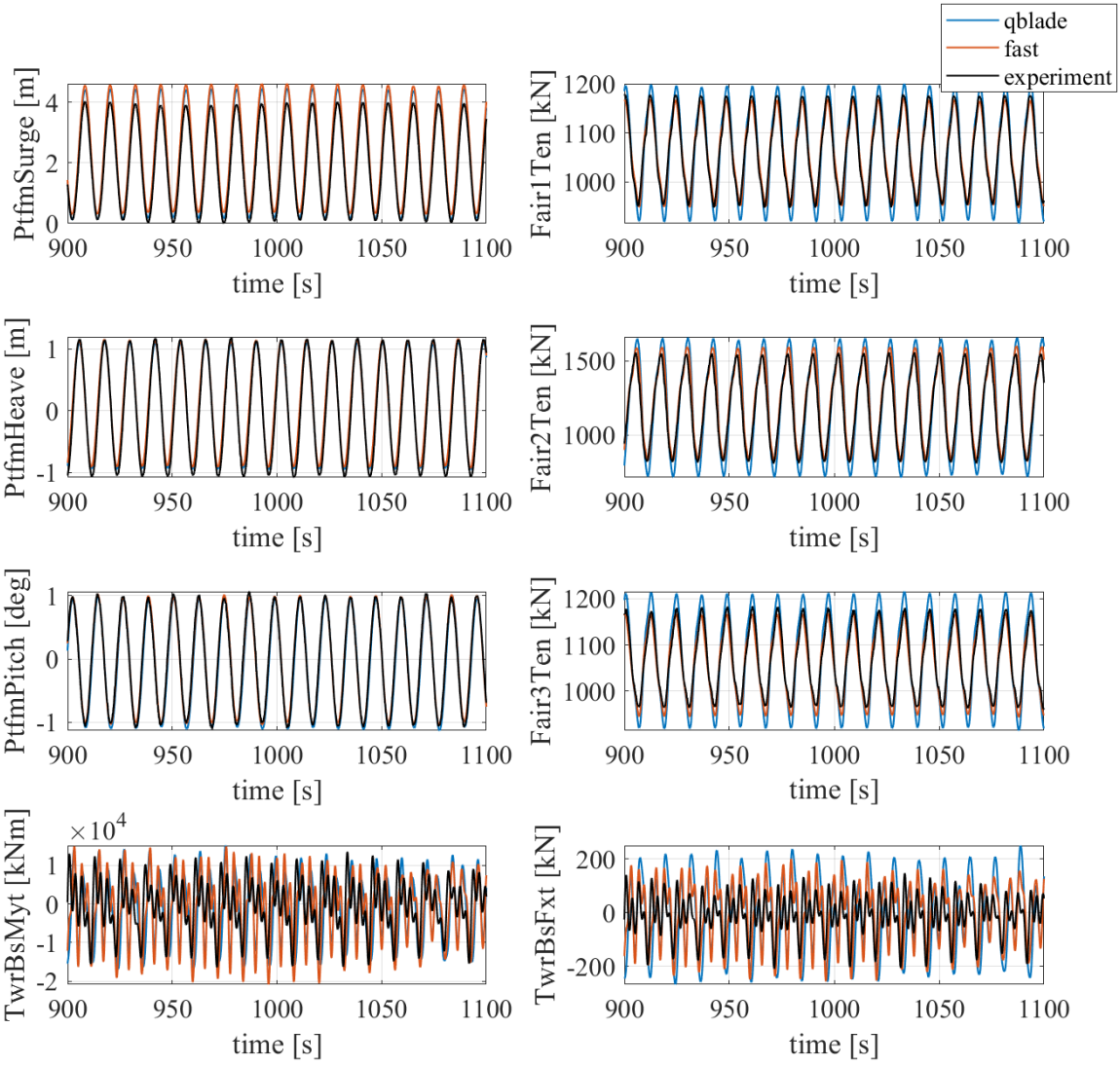

Figure 3.5: Comparison of system response and motion in regular waves (LC3.1). Wave height of 7.37 m and wave period of 12.07 s (full scale)

happens to be very close to the third harmonic of the wave frequency. Because the waves generated in the basin are not perfectly harmonic, excitation close to the first tower fore-aft mode is present, thus explaining the behavior observed in Fig. 3.5. Both OF and QB are able to capture this effect but both codes overestimate the response at the tower natural frequency.

In LC3.2 a regular wave with an amplitude of 10.5 m and period of 14.3 s is imposed. Results are shown in Fig. 3.6. Similarly to LC3.1, platform motions and fairlead tensions are well captured by both codes. In LC3.2 wave-frequency excitation seems to be dominant even for tower base loads. The harmonics of the wave excitation in LC3.2 are further from

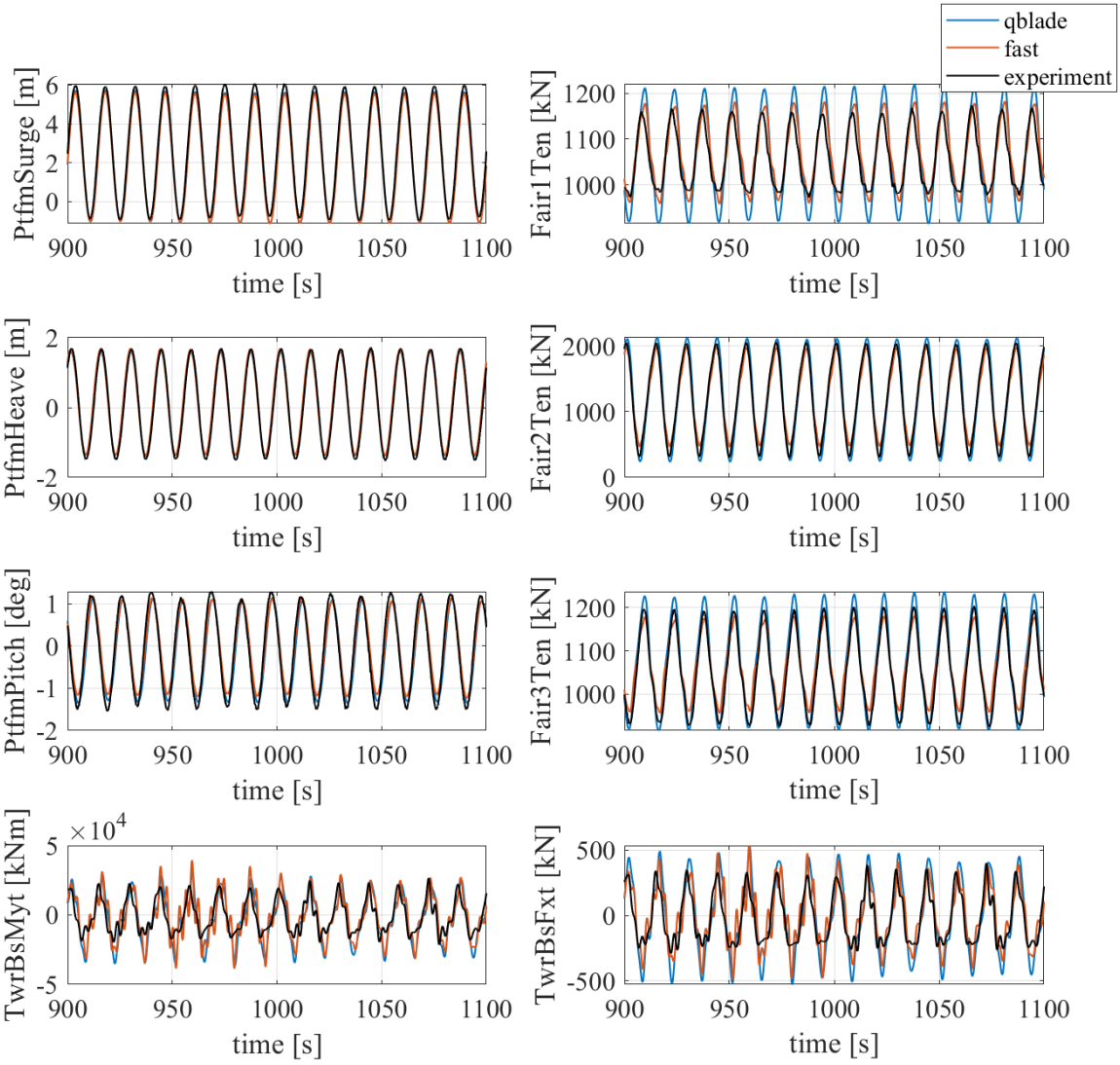

Figure 3.6: Comparison of system response and motion in regular waves (LC3.2). Wave height of 10.5 m and wave period of 14.3 s (full scale)

the tower natural frequency and thus the excitation effect that can be seen in Fig. 3.5 is less marked.

3.2.8 Steady aerodynamic tests

Aerodynamic forces play a key role in the response of a FOWT. The goal of the aerodynamic tests presented in Fig. 3.7 is to validate the aerodynamic predictions of the OF and QB models. The tests are performed by cantilevering the tower, removing any influence that platform motion may have. In LC 2.1 rated conditions are modeled, and a wind field with approximately 5% turbulence intensity and 12.91 m/s mean is imposed, while in LC 2.2

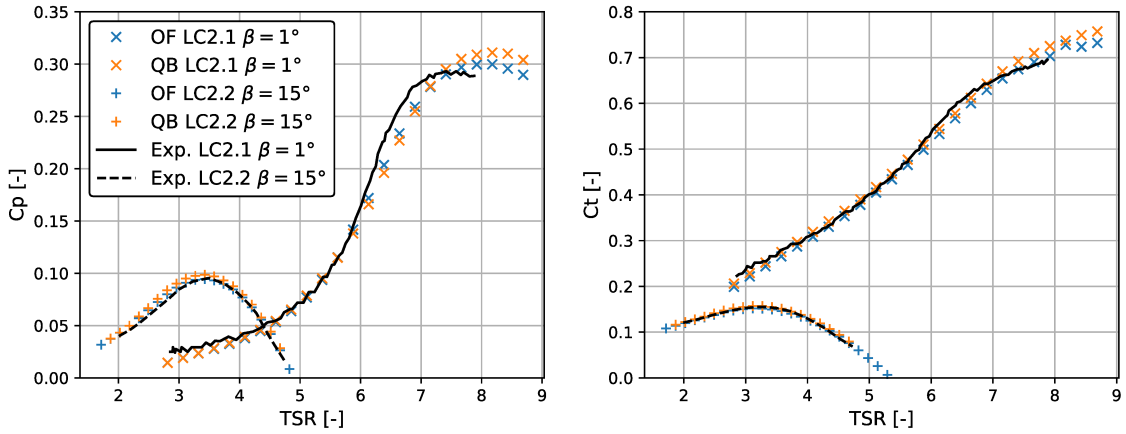

Figure 3.7: Thrust and power coefficient in steady wind conditions compared to experimental data from [69]

above-rated wind conditions are reproduced, and a wind field of 21.19 m/s mean and 5% turbulence intensity is used. Blade pitch is 1° and 15° respectively in the two tests. For each point shown in Fig. 3.7, a 20-minute long simulation is performed in QB and OF, respectively. Cp and Ct are computed and averaged to obtain the data points in Fig. 3.7. The tip-speed ratio (TSR) is varied by increasing the rotor speed from 6 to 17 rpm. The numerical models are compared to experimental data from [69] as no results for these test cases are available in the OC5 repository. Very good agreement is shown for rotor thrust for both load cases. Similarly, power coefficient is also in very good agreement in LC 2.2. For LC 2.1 both OF and QB underestimate Cp between TSR 6 and TSR 7 and overestimate Cp above TSR 7. Overall however, the discrepancies are small. Moreover, the turbine operating point in the experimental tests is slightly below TSR 6, where very good agreement between numerical and experimental models is shown. Although a similar level of agreement between numerical and experimental tests can be noted in [69], details regarding the experimental test procedure are absent. The fact that the lower fidelity BEM model of OF shows similar accuracy as the higher fidelity LLFVW model QB uses may be explained by the geometric properties of the 5MW MSWT rotor. The stiff blades and almost no out-of-plane pre-bend of the rotor make it align very well with the planar actuator disk assumption on which the BEM approach is based.

3.3 Results

During the OC5 campaign various irregular wind and wave test runs were performed. Focus will be placed on LC4.1, 4.2 and 4.3. In LC4.1, the rotor is operating at its nominal design point in terms of blade pitch, mean TSR and wind speed. In the following, these conditions will be referenced as *"steady rated wind"* conditions. For a pitch-regulated wind turbine this corresponds to the operating point where mean aerodynamic thrust is at its peak, causing

mean platform displacements to also be at their respective peaks. In LC4.2 on the other hand the turbine was tested in high winds with pitch-to-feather blades. Analyzing this LC allows us to validate the numerical models in a low TSR condition. In the following these conditions will be referenced as *"steady above-rated wind"*. Finally, in LC4.3 the system response to a dynamic turbulent wind field close to rated wind speed is analyzed. In this LC, the blades are pitched to their operating pitch angle of 1° and the rotor is held at nominal mean TSR. In the following these conditions will be referenced as *"unsteady rated wind"*. For all aforementioned LCs, irregular waves with a peak spectral period of 12.1 s and a significant wave height of 7.1 m are imposed.

In addition to results in irregular wind and waves, test results in irregular waves only, without the influnce of wind excitation are also shown, as they are functional to explaining the trends observed in the irregular wind and waves tests.

Statistics of the time series are compared. In particular mean values and the 99% quantile are compared. The latter is assumed as an estimate of the extreme value for the sensor that is analyzed, eliminating any outliers in the experimental or numerical data.

3.3.1 Irregular Waves and no Wind

The hydrodynamic and mooring line models used in QB and OF are built largely on the same theoretical basis. Therefore, the two codes are expected to produce similar results in an irregular waves with no wind test. While not strictly related to the multi-fidelity comparison of wind turbine design codes, which is the topic of this study, results of irregular tests without wind are shown herein as some important considerations can be drawn.

Comparing statistics in Fig. 3.8, general good agreement can be seen. In terms of platform motion, mean values of surge are higher for OF than for QB, with the latter code being closer to experimental values. The other examined sensors agree well. However, focusing on 99% quantiles, underestimation of TB Fx of approximately 20.8% and 16.7% for QB and OF can be noted, while TB My is underestimated 21.8% by QB and 6% for OF. Similar underestimations in tower base loads are noted in the results of the OC5 code-to-code comparison campaign for LPMD models, and both QB and OF are within the range of the participants' predictions [67]. The reason for such underestimation can be better explained by analysing frequency-domain results as shown in Fig. 3.9.

The PSDs of the examined load-sensors for LC3.3 are shown in Fig. 3.9. Three distinct regions can be discerned: low-frequencies below 0.05 Hz where the floating system natural frequencies are located, the wave excitation range between 0.05 and 0.15 Hz and the tower natural frequencies located approximately at 0.032 Hz. It is crucial to observe the amplitude of the peaks in these three regions relative to each-other; while for some load sensors such as the fairlead tensions the peaks in the low and wave frequency ranges are comparable, for platform pitch, surge and tower base sensors the low frequency peak greatly exceeds the wave-frequency excitation. In terms of frequency, peak response of platform motion in the wave frequency range roughly corresponds to the peak in the wave spectra (Fig. 3.9), while tower base fore-aft bending moment and force show two distinct peaks of response around 0.07 and 0.14 Hz. These results are in line with results from the OC5 Phase II campaign, as noted in [67]. In summary, if compared to experiments, response at wave frequency appears

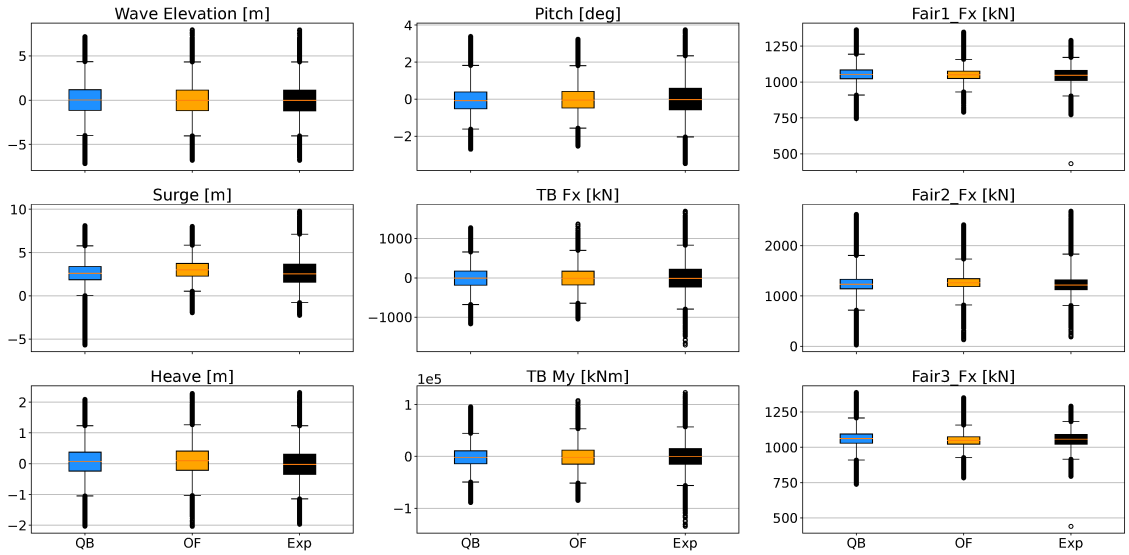

Figure 3.8: Comparison of statistical values for irregular waves with no wind case. Median, First (Q1) and third quantiles (Q3) (box edges), inter quantile range (IQR) (boh height), upper and lower wiskers ($Q1 - 1.5 * IQR$, $Q3 + 1.5 * IQR$) and flier values above and below the wiskers.

to be well captured by both codes. On the other hand, response at the FOWTs natural frequency is not captured properly by OF or QB.

To investigate this phenomenon further, in Fig. 3.10 PSDs in low frequency ranges are shown. Only a subset of the most relevant load sensors are shown for brevity. As noted in [67], outside of the wave frequency range, platform motion must be excited by non-linear forces, which could be a result of second-order potential flow excitation, higher-order wave hydrodynamics or wave stretching. As noted in Section 3.2, both models include second-order potential flow excitation through QTFs. Moreover, although QB includes some additional non-linear loading sources such as Wheeler wave stretching and discrete buoyancy computation, no significant improvement in natural-frequency response prediction is noted for the present test case.

3.3.2 Steady Rated Wind

In LC4.1 the wind profile has a mean of 12.91 m/s and 5% turbulence intensity. To model the drop-off in rotor speed near the bottom of the rotor, due to limitations of the experimental apparatus, wind shear is imposed in the numerical simulations using a power-law with exponent, as suggested in [70].

Statistics for LC4.1 are compared in Fig. 3.11. Both QB and OF fail to predict the mean surge position of the platform, QB underpredicting it by 7.5% and OF by 2.5%. Mean platform pitch is well predicted, with the numerical models being within 0.3° from the experiment. A tendency to underestimate tower base extreme loads can be noted in

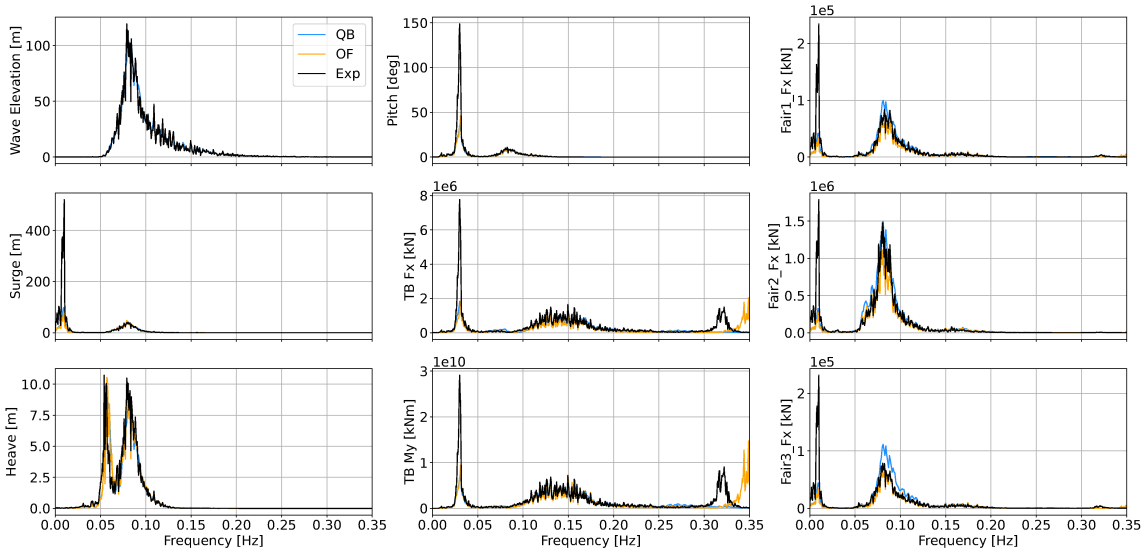

Figure 3.9: Power Spectral Density (PSD) of no-wind, irregular waves case

both codes. This tendency was also noted in the OC5 campaign [67] and in also present in tests with irregular waves only (section 3.3.1). In LC 4.1, when subject to irregular waves and steady wind, QB underpredicts the 99% quantile of TB Fx by 12% and of TB My by 9%, while OF also underpredicts the 99% quantile of TB Fx by 18% and of TB My by 6%. The statistics of aerodynamic thrust are also shown in Figure 16. Only the numerical codes are compared as aerodynamic thrust was not measured in the experiment (thrust coefficient was measured, but upon examination of the data, this measurement appears to include inertial and gravitational loads, that are hard to remove completely). The two codes are close in the median thrust (OF approximately 2% below QB), but OF is showing larger variations in rotor thrust, visible in the IQR and 1-99% quantiles.

Analyzing the signals in the frequency domain can give more insight on where the differences are located. The PSDs of a selection of relevant load sensors in LC4.1 are shown in Fig. 3.13. Qualitatively speaking, the results appear similar to irregular wave test with no wind (LC3.3): two distinct peaks in the wave excitation range and in the low frequency range can be noted for most load sensors in Fig. 3.13. Focusing on tower base loads however, it can be noted that the peak in the low-frequency range is now much lower for both experiments and numerical models, and comparable to the peaks in the wave frequency range. As noted in [67], aerodynamic loading has a damping effect on platform oscillations at the system's natural frequency, reducing the discrepancies in the low-frequency range between numerical models and experiments. Moreover, as shown in the wind spectrum in Fig. 3.13, higher-order hydrodynamic effects are not the only phenomena that may be driving low-frequency excitation, as wind excitation is present in the low-frequency range (0-0.05 Hz). These two factors explain the better agreement that is noted for the numerical models regarding extreme tower base loads. Overall, this result is again in line with what was noted in the

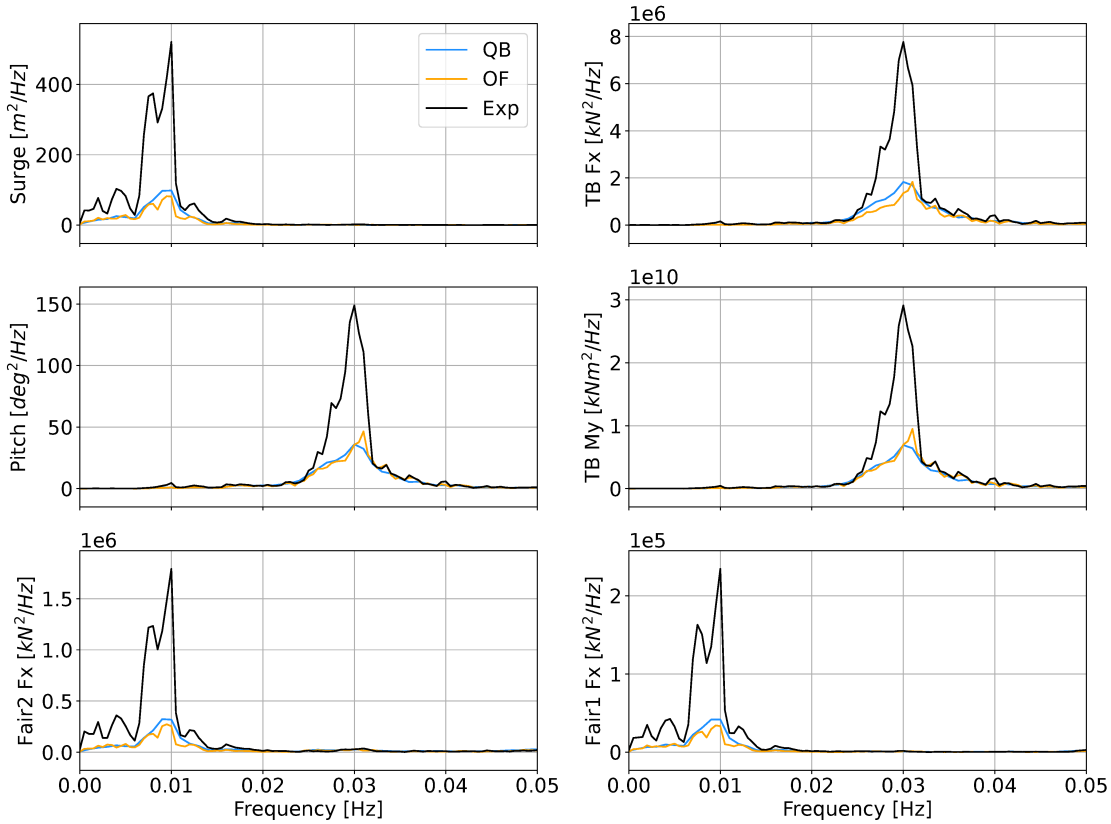

Figure 3.10: Power Spectral Density (PSD) of turbulent rated wind, irregular waves case. Focus on low frequency spectrum

OC5 code-to-code comparison study [67]. As for aerodynamic thrust, both codes capture several excitation peaks: at very low frequencies where wind excitation is dominant, at low frequencies where platform natural frequencies are excited and at wave frequency, where two distinct peaks arise around 0.07 Hz and 0.12 Hz. The greater variability in this metric shown by OF is noticeable as the SD signal of OF tends to be above that of QB across the entire frequency range. It must be noted that a high peak in excitation in correspondence of the 3P frequency (approximately 0.6 Hz, not shown in Fig. 3.13) is present for both codes. The same peak is noted in the TT Fx and TB Fx sensors for the experimental data (Wendt et al. [70]) but appears to not be adequately captured by the numerical codes. As discussed in [70], this 3P excitation may be caused by i) non-uniformities in incoming wind – especially wind shear and ii) a slight pitch angle imbalance between the three blades. Since this work is focused on code-to-code comparison, only the former effect was introduced into QB and OF, and even this effect may be underestimated, due to uncertainties in the actual experimental wind field [70].

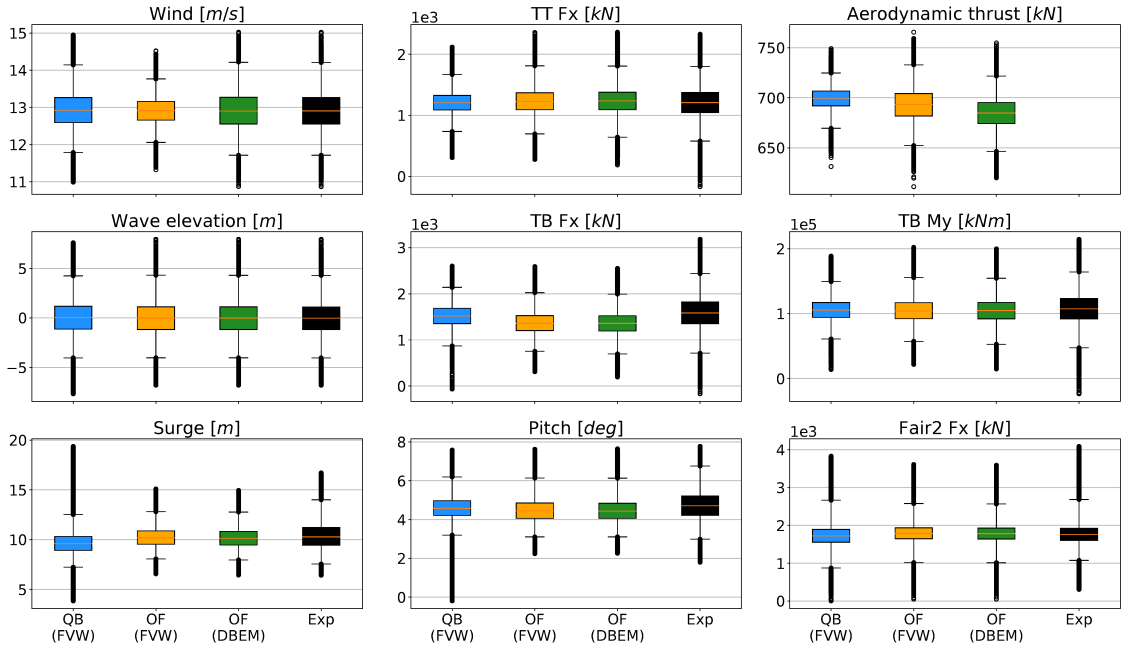

Figure 3.11: Comparison of statistical values for steady rated wind, irregular waves case. Median, First (Q1) and third quantiles (Q3) (box edges), inter quantile range (IQR) (boh height), upper and lower wiskers ($Q1 - 1.5 * IQR$, $Q3 + 1.5 * IQR$) and flier values above and below the wiskers.

3.3.3 Unsteady Rated Wind

In LC4.3 the same wave field is used as in LC4.1, but a dynamic wind field with a mean of 13.05 m/s and a turbulence intensity of 7.5% is imposed. The term dynamic in this case refers to a varying mean velocity of the turbulent flow over the duration of the simulation [63]. Globally the models behave very similarly to LC4.1 relative to each-other and to the experiments. Therefore, focus will be put on the differences relative to LC4.1. Statistically QB and OF appear to be reproducing well the overall behaviour of the FOWT model (Fig. 3.17). With respect to OF, QB still slightly underestimates rotor thrust, however 99% quantiles are now very similar. The only somewhat significant difference is in the 1% quantiles that are lower for OF. In terms of frequency response (Fig. 3.19), results look again very similar to LC4.1. Because the wind field is now dynamic, wind excitation is greatly increased with respect to LC4.1, especially at very low frequencies. The trace of such very-low frequency excitation is also visible in the tower-top and tower-base load sensors, as well as in the surge signal.

3.3.4 Steady Above-Rated Wind

In LC4.2 the turbine was tested with an equivalent full-scale wind speed of 21.09 m/s and a turbulence intensity of approximately 5%. As for LC4.1 and 4.3 in the numerical simula-

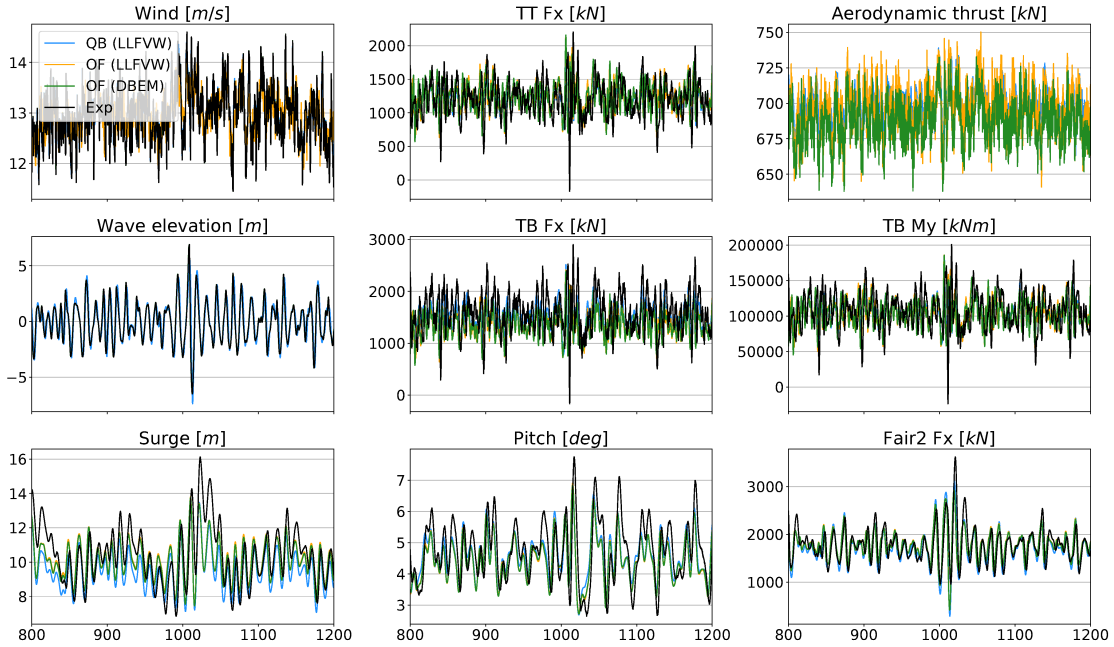

Figure 3.12: Timeseries of steady rated wind, irregular waves case.

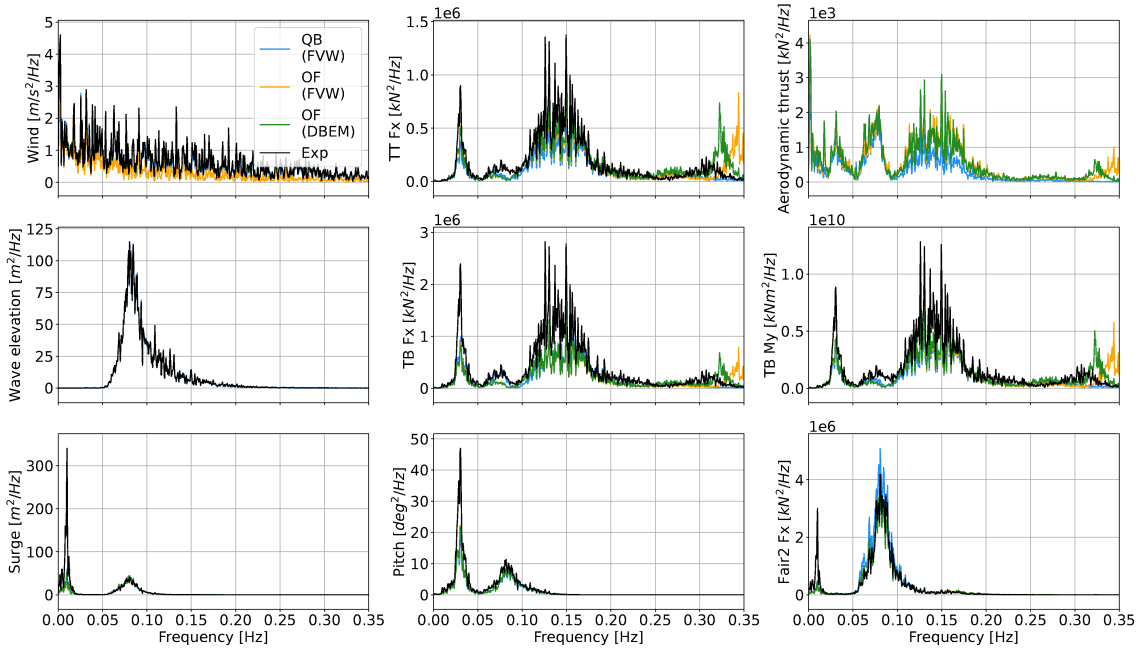

Figure 3.13: Power Spectral Density (PSD) of steady rated wind, irregular waves case

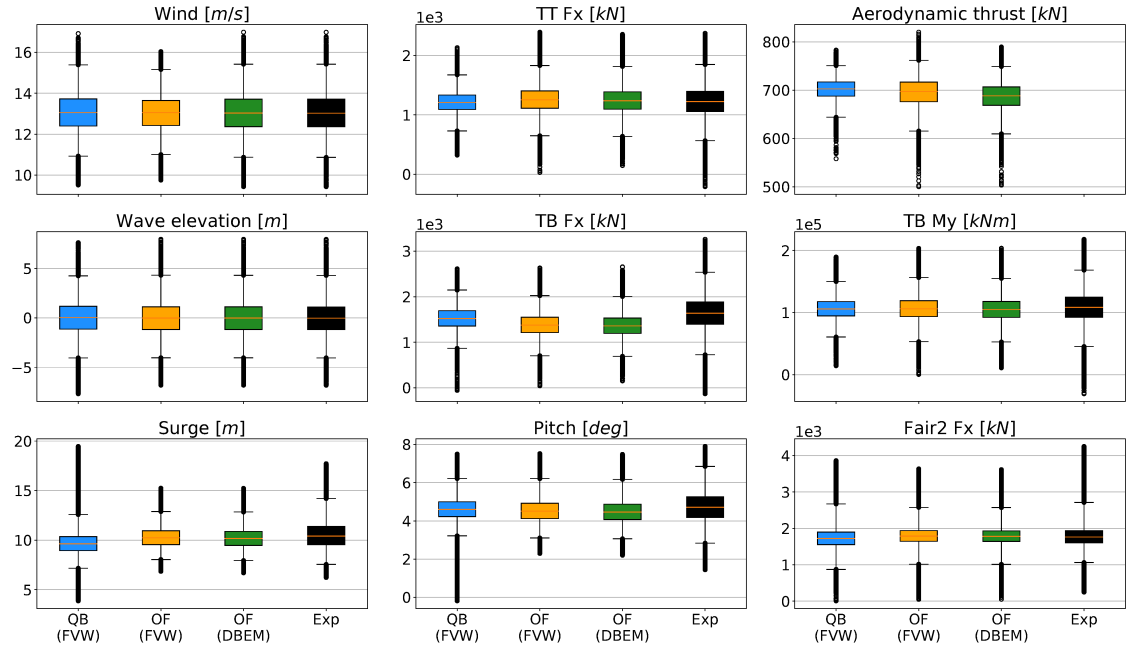

Figure 3.14: Comparison of statistical values for turbulent rated wind, irregular waves case. Median, First (Q1) and third quantiles (Q3) (box edges), inter quantile range (IQR) (boh height), upper and lower wiskers ($Q1 - 1.5 * IQR$, $Q3 + 1.5 * IQR$) and flier values above and below the wiskers.

tions, the vertical wind profile follows a power law with shear exponent of 0.2. Analyzing statistics in LC4.2, the same overall trends as discussed for LC4.1 can be seen. The numerical codes generally underestimate the surge motion, underestimation is similar to LC4.1 being of 7% for QB and 2% for OF. Median fairlead tension values follow from the differences observed in surge: the tension in the upwind mooring line (line 2) is underpredicted and the tension in the downwind mooring lines is overpredicted. Focusing on tower base extreme loads, the 99% quantiles are in even better agreement with the experiments in this operating condition, although some underprediction remains. TB My is underpredicted by 4% and 1% by QB and OF respectively and TB Fx is underpredicted by 14% and 10%, respectively. Once again, the causes for the observed differences can be seen in Fig. 3.19, where PSDs are shown. In this above-rated operating condition, the peak in correspondence of the system pitch natural frequency in the tower base loads is now smaller than the peaks in the wave-excitation region. The numerical models continue to fail to properly predict excitation in this region, but since this loading source is less significant in these conditions, and both QB and OF are much closer to the experiments, 99% quantiles are in better agreement. Physically speaking, this is again due to the combined action of wind excitation and aerodynamic damping. Respect to LC4.1, wind excitation seems to be more relevant, but not as much as in LC4.3. Very low frequency (f<0.05 Hz) excitation appears in the PSDs of TB Fx and TT Fx for QB and OF (Fig. 3.19), but not for the experiments, which is

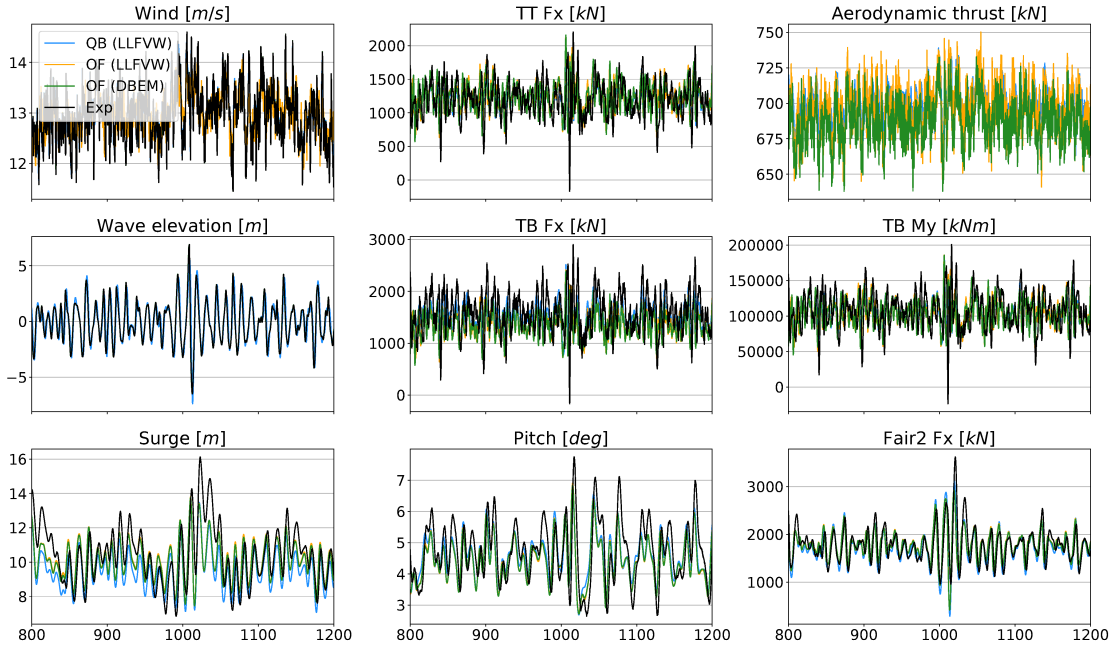

Figure 3.15: Timeseries of turbulent rated wind, irregular waves case.

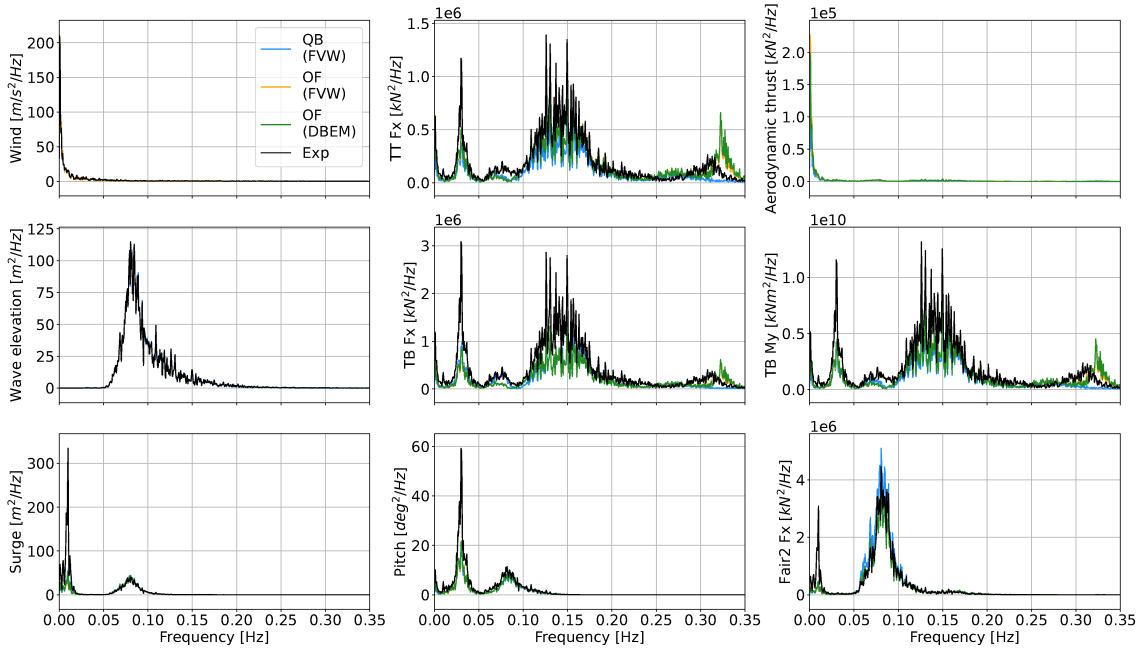

Figure 3.16: Power Spectral Density (PSD) of turbulent rated wind, irregular waves case

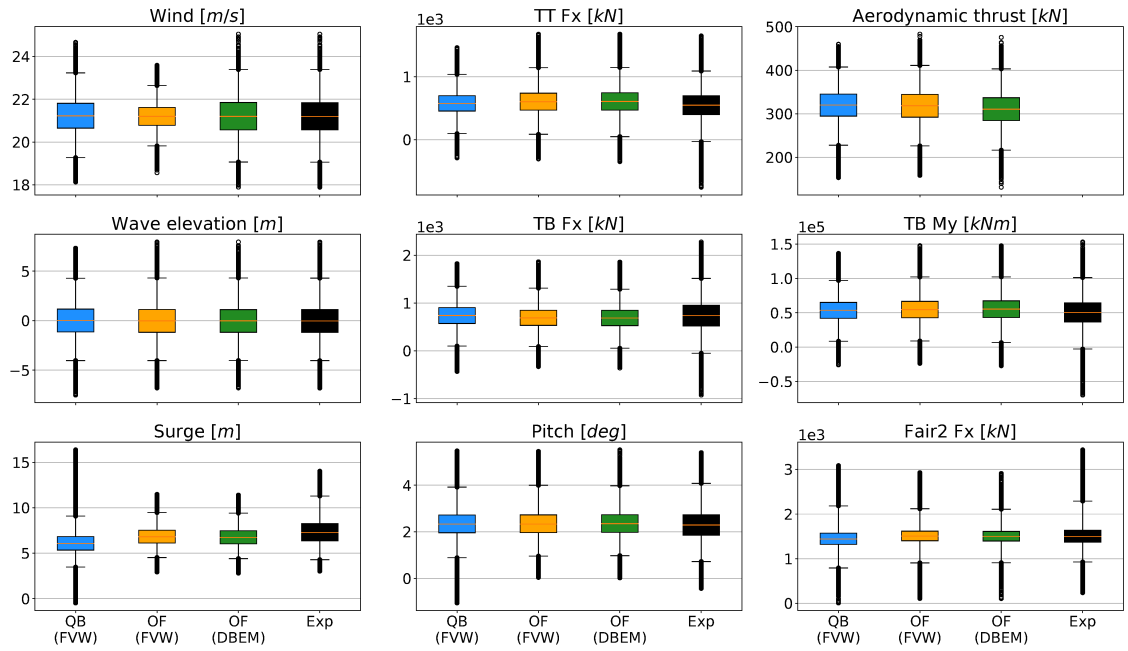

Figure 3.17: Comparison of statistical values for steady above-rated wind, irregular waves case. Median, First (Q1) and third quantiles (Q3) (box edges), inter quantile range (IQR) (boh height), upper and lower wiskers ($Q1 - 1.5 * IQR$, $Q3 + 1.5 * IQR$) and flier values above and below the wiskers.

unexpected. Overall, system dynamics are very well captured in above-rated conditions.

3.4 Conclusions and outlook

The 5MW OC5 FOWT model, a 1:50 scale model wind turbine mounted on a semi-submersible type platform, was investigated. A range of test cases from the experimental campaign were chosen for comparisons. Both first- and second-order hydrodynamic loads have been accounted for in the models. Decay tests were first simulated to demonstrate that natural frequencies and damping behaviour was correctly captured by the models. Very good agreement was noted between the numerical models and experiments in these tests. Following this, tests in regular wave fields were carried out. Overall, system response in amplitude as in phase shift with respect to the incoming waves was very good for both OF and QB in terms of motions and fairlead tensions. The mean values also appear to be captured very well by both numerical codes. In these tests, better agreement with experiments was noted when wave time series from the basin tests are used as input to the numerical models. A spectral analysis of the signal revealed the presence of higher-order harmonics, exciting system frequencies other than the wave frequency. A number of irregular wave tests were then carried out in order to inspect frequency content of the turbine response. From a visual

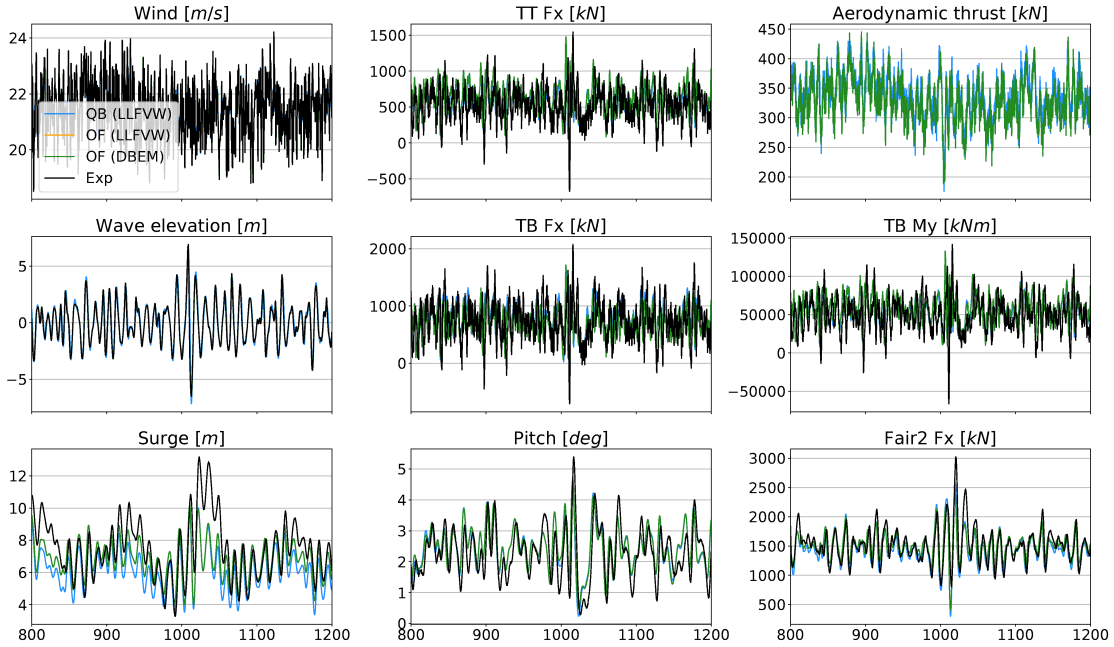

Figure 3.18: Timeseries of steady above-rated wind, irregular waves case.

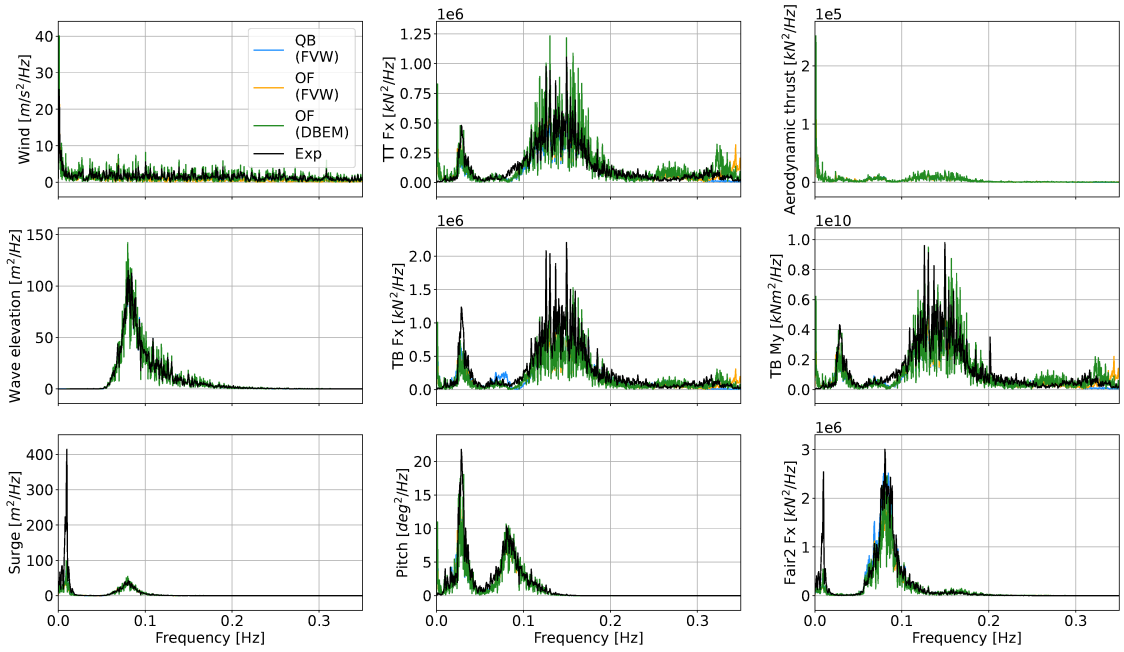

Figure 3.19: Power Spectral Density (PSD) of steady above-rated wind, irregular waves case.

comparison, the response of the various load sensors are well in-phase even several minutes into the test-runs. A statistical analysis revealed an underprediction of low-frequency platform response caused by the excitement of the system's natural frequencies. This also led to underestimations in the 99% quantiles of tower base fore-aft shear force and bending moments of about 25-20%. As noted in [67] this is due to higher-order wave hydrodynamic effects, for which including second-order excitation is not sufficient. The response of the numerical set-ups compared herein is aligned with the performance of the other codes used for comparison in the OC5 campaign. Finally, a range of fully coupled tests were carried out where aerodynamic loads were acting on the rotor. In these cases, both the BEM-based and LLFVW-based codes were able to capture excitation due to the turbulent wind field at rated and above rated wind conditions very well. Tower base loads are found to be underpredicted. This is concluded to be caused again by higher-order hydrodynamic effects. The deviation from experimental results is however shown to be relatively small, between 4% and 15% depending on the specific error metric and wind/wave condition. From the visual comparison of time series, good agreement between QB and OF can be noted even several minutes into a turbulent wind and irregular wind simulation, and the outputs of the two models remain well in-phase. Overall the two state-of-the-art codes performed similarly in these simulations. The use of a higher-order LLFVW model with respect to a DBEM model did not influence the system dynamics significantly. The underprediction of low-frequency platform excitation in the LLFVW code remains, and both codes underestimate extreme loads with respect to experiments. If this result is compared to the outcomes of the simplified aerodynamic tests on the UNAFLOW rotor shown in Chapter 2, it is not completely unexpected. In fact, in the OC5 experiments the influence of the controller, which could introduce differences between the aerodynamic models, is neglected and the wind turbine is tested at wind speeds that are at or above rated wind speed, where very little differences between aerodynamic models are noted in the UNAFLOW results in Chapter 2. Moreover, analysis is focused only on global parameters that were measured during the experiments, neglecting values such as blade root bending moments. These outputs, and the influence of control and of diverse environmental conditions will be studied in the following section.

The results shown herein highlighted the fact that hydrodynamic models can still be improved, ultimately leading to better estimations of loading of FOWTs. This topic has been recently investigated by Robertson et al. [71]. Moreover, some preliminary actions to improve the low-order hydrodynamic models used in the wind turbine simulation tools presented herein has been performed. An example of such undertaking is the work by Wang et al. [72]. This topic remains an area of active research and an area where the two codes tested herein can be improved.

Chapter 4

Code-to-code Comparisons in Realistic Met-ocean Conditions

In this chapter, multi-fidelity aerodynamic wind turbine wake models are compared on two floating wind turbine test cases. Unlike previous chapters, the influence of complex environmental conditions and diverse operating conditions and the complex interactions between aerodynamics, structural dynamics, hydrodynamics and control are studied. Differently from previous chapter, the full structure including the blades and tower are considered flexible and a torque and blade pitch controller is used. This work was performed within the H2020 Projet FLOATECH, and is one of the first endeavors of this kind. As detailed in the following, many of the datasets and assets that were generated during this project have been made publicly available, and represent a resource that could be expanded upon in the future and serve for future code or technology verification studies.

Within the context of this dissertation, it represents another notable step in complexity with respect to Chapters 2 and 3, where simplified aerodynamic tests of an oscillating rotor and the response of a simplified wave basin test case were studied. In this chapter an extensive code-to-code comparison in realistic inflow conditions is performed. European environmental conditions are obtained and processed through the procedure described in section 4.1, and include wind speed, significant wave height, peak spectral period and wind-wave misalignment. Two test cases are simulated for a variety of Design Load Cases (DLCs), a spar-buoy and a semi-submersible design. They are described in section 4.3. As described in section 4.5, the test cases are simulated using three offshore codes, OpenFAST, DeepLines Wind and QBlade, which was recently extended (QBlade-Ocean) to include offshore conditions within the H2020 project FLOATECH. The latter code includes stand-out features such as LLFVW wake modeling, and explicit buoyancy calculation. The predicted dynamics are compared in terms of extreme loads and statistics. Time series are also compared in detail to give an insight into the differences in dynamics. The observed differences and possible implications are discussed and compared to other peer reviewed studies.

4.1 Met-ocean Conditions for Offshore Wind Turbine Simulation

Offshore wind turbines are subject to varying inflow and sea conditions. The former are typically referred to as meteorological conditions, while the latter as ocean conditions. The combination of the two will be referred to as met-ocean conditions throughout this work. For sake of completeness, meteorological conditions for the purpose of wind turbine design are summarized. They are defined based on wind speed and direction, with the latter parameter being previously neglected under the assumption that the wind turbine is able to yaw. Ocean waves on the other hand are modeled by superimposing individual regular waves with a certain amplitude (H), period (T) and direction. The combination of these wave trains defines a sea state. Design standards assume that an individual sea state can be modeled with three aleatoric variables: the mean amplitude of the highest third of the waves (significant wave height H_S), the peak spectral period of the waves (T_P) and the mean wave direction. If we combine wind and wave direction by defining wind-wave misalignment (M_{WW}), a generic offshore site can be characterized with four aleatoric variables U, H_S, T_P, M_{WW}.

Any combination of the four environmental variables is theoretically possible. What differences one installation site from another is the probability with which combination of these four parameters, which define a certain *"event"*, occur. Events with low probability of occurrence that lead to high combinations of, for instance H_S and U, are *extreme events* and are considered as they may be the cause of peak loads on the structure. On the other hand, events with high probability of occurrence are important to evaluate performance and fatigue loads. Therefore, to determine appropriate met-ocean conditions for a certain installation site, a statistical model of the for variables needs to be built.

In order to build a statistical model an installation site must be chosen. In this work a site west of the island of Barra (Scotland 56.886$^{\text{o}}$N, 7.948$^{\text{o}}$W) is chosen. Water depths are in excess of 120 m, thus representative of the range of depths that are currently being proposed for FOWT installation. The site was used in two H2020 projects, [73] and Corewind [74]. This site is also used in WP3 of the H2020 FLOATECH project, of which this work is a part of. Moreover the site is located in Europe and met-ocean conditions are particularly severe. In this work this is seen as a bonus as it is hoped that the extreme environmental conditions will magnify the non-linearities and differences between the simulation codes.

A procedure to obtain a statistical representation of the West of Barra site was developed. Consequently the fatigue-driving and extreme-driving events have been defined. Rather than using the post-processed conditions found in [73], the development of this procedure allowed for the inclusion of wind-wave misalignment into the analysis, a parameter that is relevant for loading on FOWTs according to the work of Stewart [75]. The contents of this section have been published in IOP Journal of Phisics [76]. The dataset and tools that were developed are publicly available on Zenodo (doi.org/10.5281/zenodo.6972014).

4.1.1 Hierarchical probabilistic model

The four environmental variables are not statistically independent. For instance, waves are generated by the interaction between the wind and the ocean surface. At the same time, higher waves tend to have longer return periods in the open ocean. Therefore, a probabilistic model that accounts for the interdependency of the aleatoric variables needs to be built. This interdependency of the variables is accounted for through the use of conditional probability distributions. A conditional probability distribution expresses the probability of a random variable given information on other, conditioning, random variables. Because at least one random variable must be considered statistically independent from the others, these models are often referred to as hierarchical models. The probability of a generic event (joint probability density function) is defined as:

$$f_{U,H_S,T_P,M_{ww}}(U, H_s, T_p, M_{ww}) = f_U(U) f_{H_s}(H_s|U) f_{T_P}(T_p|H_s) f_{M_{ww}}(M_{ww}|U) \tag{4.1}$$

The wind speed is modeled as an independent random variable, H_S is conditioned on U, T_P is conditioned on H_S and M_{WW} is conditioned on U. As mentioned previously, these PDFs are referred to as conditional because their parameters are dependent or conditioned on the conditioning parameter. In more detail, if μ_i and σ_i are the parameters of a conditional distribution (the mean and variance of a normal distribution for instance), then these parameters will be modeled with dependence functions:

$$\mu_i = f(x_{(i-1)}, c_1, \ldots, c_n) \tag{4.2}$$
$$\sigma_i = f(x_{(i-1)}, c_1, \ldots, c_n) \tag{4.3}$$

where x_{i-1} is the conditioning parameter (for instance U in the case of H_S) and c_n are fit coefficients. To fit the analytical model, data is binned in the dimension of the conditioning variable. For each bin a pdf is fitted, and the best fit pdf parameters are found. The set of values $\mu_i(x_{(i-1)})$ and $\sigma_i(x_{(i-1)})$ are then used to find the coefficients c_n of the dependence functions, obtaining a continuous joint probability model. The procedure is illustrated schematically in figure 4.1 but is general and can be extended to an n-dimensional probability space.

The hierarchical model structure shown in equation 4.1, as well as the marginal PDFs to use, are entirely the modeller's choiche, and are problem-dependent. In the current study, the approach proposed by Haselsteiner et al. [77] is followed. According to this approach, the marginal PDFs and the dependence functions are chosen based on phisical observations, and are thus tailored for this specific application. The procedure that is presented herein leverages on the open-source Python package Virocon [78]. Wind speed is considered an independent variable and is modeled with a three-parameter Weibull distribution:

$$f(U) = \left(1 - e^{\left(\frac{U}{\alpha}\right)^{\beta}}\right)^{\delta} \tag{4.4}$$

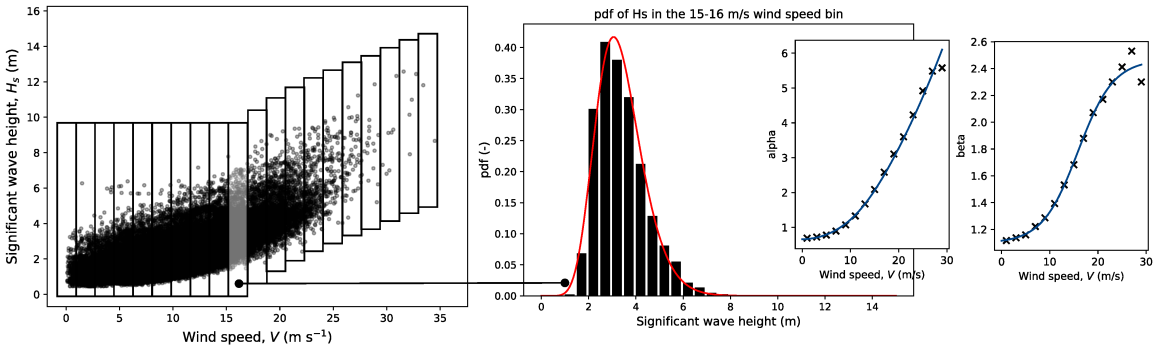

Figure 4.1: Schematic illustration of the procedure to derive a join probability model. i) data is binned based on values of the independent parameter (U), ii) for each bin a best-fit distribution of the conditioned parameter (H_S) is found iii) best-fit parameters of H_S are fit with a dependence function

Significant wave height is conditioned on wind speed and is also modeled with a three parameter Weibull distribution:

$$\left(1 - e^{\left[-\left(\frac{H_s}{\alpha_{H_s}}\right)^{\beta_{H_s}}\right]}\right)^5 \tag{4.5}$$

Peak spectral period is conditioned on significant wave height and is modeled with a log-normal distribution:

$$\frac{1}{2}\left(1 + erf\left(\frac{lnT_p - \mu_{T_P}}{\sqrt{2}\sigma^2}\right)\right) \tag{4.6}$$

Wind-wave misalignment is modeled using a Von Mises distribution, following the approach proposed by Stewart et al. [79]. This distribution is also known as circular norm distribution and is periodic on the support $[-\pi, \pi]$:

$$\frac{e^{kcos(M_{ww} - \mu_w)}}{2\pi I_0\,(k)} \tag{4.7}$$

where I_0 is the modified Bessel function of order zero. This distribution was not present in Virocon, and therefore it was implemented on this occasion. Full details on the dependence functions that were used can be found in the full accompanying publication [76].

Once the model structure is defined it can be fed with observations of the four environmental variables that define the site's environmental state and the best-fit coefficients of the marginal PDFs can be found using a Maximum Likelihood Estimation algorithm [78].

4.1.2 Hindcast data

For the creation of the long-term probabilistic model of the West of Barra site following the procedure presented in the previous sections, hindcast data from the open-source Copernicus

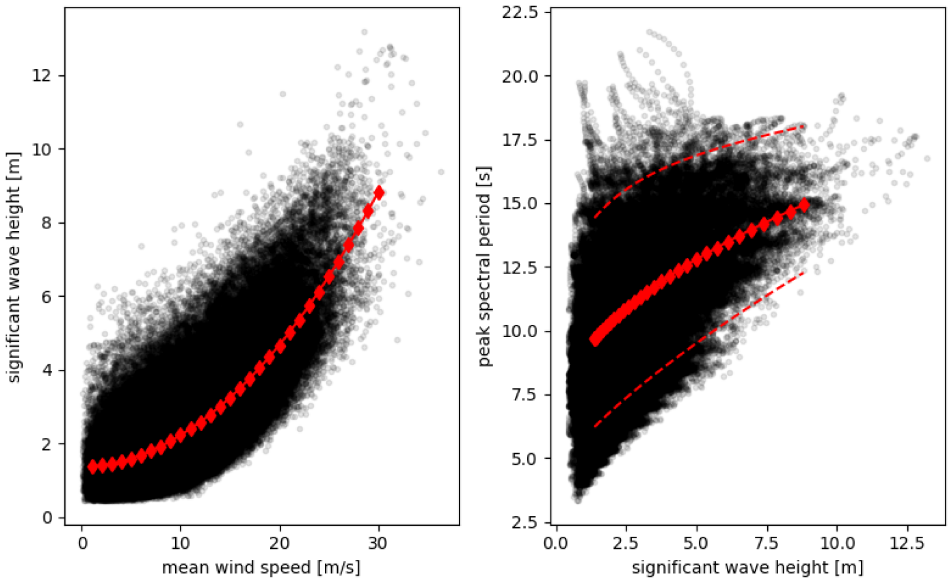

Figure 4.2: Expected values of H_S and T_P for west of Barra site corresponding to NSS conditions for extreme load calculation (in red), $\pm 2\sigma_{T_p}(H_s)$ range (red dashed lines) and scatter data from ERA5 database [80]

re-analysis database ERA5 [80] is used. Re-analysis combines forecasts with observations to obtain a more realistic representation of the past states of the environment [81]. This database is used as it contains reanalysis data of both atmospheric and oceanographic parameters, spans a total of more than 40 years, and has been thoroughly validated with observations. Moreover, data can be obtained worldwide on a 31km grid, a reasonably fine spacing for offshore applications, and most importantly, is available open source.

4.1.3 Normal Sea State

Normal Sea State for extreme load calculations

For extreme load calculations, according to international standards (IEC 61400-3 [82]), co-directional wind and waves can be assumed as worst-case scenario (eliminating the need to define M_{ww}), and for each wind speed, the expected peak spectral period and significant wave height are assumed:

$$E\left(Hs|U\right) = E\left(f_{H_s}\left(H_s|U\right)\right) \tag{4.8}$$

$$E\left(T_p|H_s\right) = E\left(f_{T_P}\left(T_p|H_s\right)\right) \pm 2\sigma_{T_p}(H_s) \tag{4.9}$$

The result for the West of Barra site is shown in Fig. 4.2 in red.

Normal Sea State for fatigue load calculations

For fatigue load calculations, multiple NSSs must be considered, each being defined by a unique combination of the four environmental variables (U, H_s, T_p, M_{ww}). As explained in detail in [82] and [75], the procedure is as follows:

- The ranges of each of the four random variables are found
- The ranges are divided into intervals (bins) of a certain width. The process is repeated for all the aleatoric variables so that the design space is divided into a series of n-dimensional bins
- The probability of each bin is estimated either using the stochastic model illustrated in section 4.1.1 or by counting the number of events in each bin. The latter is much more straightforward if enough raw data is available and was used in the current study
- The numerical wind turbine model is evaluated at least once for each bin. Lifetime fatigue loads can be evaluated by weighing the computed loads by the probability of each bin

IEC 61400-1 [82], suggests bin ranges for the examined variables. However, as noted by Stewart [75], using these ranges will often lead to an unrealistic number of bins, many of which will have no or extremely little probability of occurrence. According to the same research the number of bins can be drastically reduced without significantly impacting the accuracy of the fatigue-load estimate by coarsening the bin ranges and by eliminating bins with low probability of occurrence. Both these strategies were applied and yielded a reasonable amount of bins to compute, as summarized in table 4.1. It must be noted that the aim of the current study is to perform a code-to-code comparison, therefore the sensitivity of the examined test cases to the number of bins was not tested. The final design space is a 4-dimensional box. The edges of the box are the rages of the environmental variables in table 4.1.

The number of bins shown in table 4.1 is still considered excessive. The 4158 bins ins table 4.1 can be further reduced if we consider that not all the combinations of the four environmental variables have any likelihood of being recorded. In fact, many of the wind speed bins in 4.1 have no or very little probability of occurrence. Therefore, as shown in [75], these bins can be reasonably excluded without appreciable loss in accuracy in the estimation of fatigue loads. In this work it was chosen to exclude the least likely bins, until the total cumulative probability of the remaining bins is 90% of the cumulative probability of the entire design space, that is equal to one by definition. Using this method the number of bins is reduced to 252.

4.1.4 Severe Sea State

Severe Sea State conditions are defined as the combination of operating wind speed and sea conditions with a combined probability of occurrence of 50 years. As IEC 61400-3 (Annex F) suggests, SSS met-ocean conditions may be found using an environmental

Table 4.1: number of bins as a function of bin ranges and width

Parameter	Range	bin width IEC	bin width
$U(m/s)$	4-26	2	2
$H_S(m)$	0-14	0.5	2
$T_P(s)$	3-21	0.5	2
$M_{WW}()$	-180 - 180	15	60
total bins	-	252747	4158

contour method. In more detail, the Inverse First Order Reliability Method is suggested to obtain a 2-D contour of wind speed and significant wave height. The IFORM method exploits the Rosemblatt transformation [83]. The process can be described as follows; given a vector of dependent random variables (such as the environmental variables in the current study) $X = \{X_1, X_2, ..., X_n\}$, this vector may be transformed into a vector of independent random variables through the Rosemblatt transformation:

$$R = TX = \{F_1(X_1), F_2(X_2|X_1), ..., F_n(X_n|X_1, ..., X_n)\} \tag{4.10}$$

When F_n are the marginal cumulative distributions of the random variables. The probability of exceeding a certain threshold can be computed as:

$$\beta = 1 - n_{events}/t_{events} \tag{4.11}$$

In the current case, where we are looking for the probability of excedance of a one hour sea state over a duration of fifty years $n_{events} = 1hr$, and $t_{events} = 365.25 * 24 * 50$. In the marginal cumulative distribution space (equation 4.10), the points with probability of excedance β lie on a hypersphere of radius β. Once the points have been found, the inverse Rosemblatt transform can be computed to obtain the environmental contour in the environmental variable's space. An example for a 2-D space is shown in Fig. 4.3. The IFORM method physically assumes that the conditions with recurrence probability greater than the threshold to be located beyond any possible line tangent to the contour [84].

For the computation of SSS, co-directional wind and waves may be assumed. While multiple peak spectral periods should be evaluated, in this work it was chosen to use the most likely peak spectral period for the given $U - H_s$ combination to limit the number of total simulations required. The environmental contour that defines SSS conditions is shown in Fig. 4.4. The severity of the west of Barra site is apparent, with significant wave heights between four and ten meters during normal operation.

4.1.5 Extreme Sea State

The Extreme Sea State is defined in a similar manner to the Severe Sea State. It is defined as the combination of environmental conditions with an overall return period of one year or of fifty years. For an onshore turbine, the only variable to consider is wind speed. Therefore,

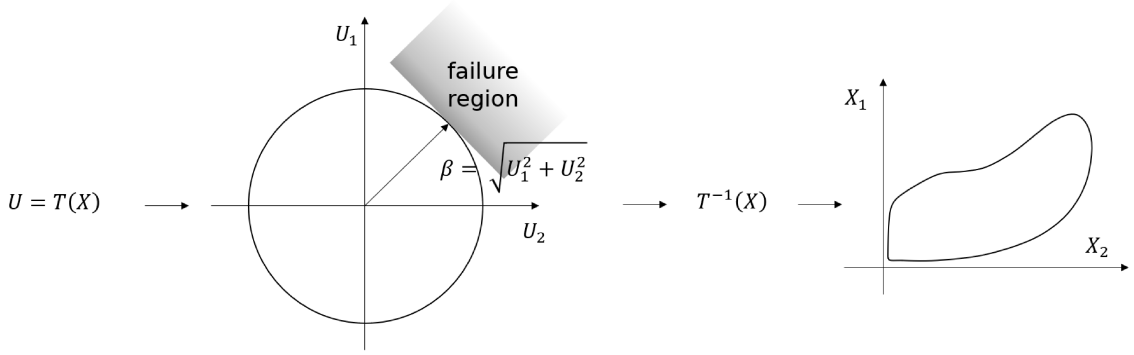

Figure 4.3: graphical representation of the Inverse First Order Reliability Method method applied to a bi-dimensional space

this condition will typically result in a very high wind speed, where the turbine is parked to protect itself. In offshore conditions, where multiple environmental variables need to be considered, this condition can be found, similarly to SSS, on an environmental contour. As for SSS conditions, variations in peak spectral period are neglected, and the most likely T_P for each $U - H_s$ combination is chosen. Wave misalignment of $+/-30$ is accounted for as an empirical measure, but this parameter is not taken into account in the estimation of the ESS $U - H_s$ combination.

As discussed in [85], various methods can be used to estimate ESS conditions. In this study, the simplest method will be used, which also arguably leads to the most severe, and thus conservative, ESS conditions. Based on the environmental contour in Fig. 4.4 the 1-D excedance of U and H_s (vertical and horizontal dashed lines) are combined, and determine the ESS conditions, represented in Fig. 4.4 by the blue and red dots for the 1-year and 50-year conditions, respectively.

4.2 Design Load Cases

As mentioned previously, in order to evaluate the performance of wind turbine simulation codes in realistic inflow conditions, the long-term definition of an installation site is needed, defined in section 4.1, and a set of design conditions relevant for performance evaluation and ultimate and fatigue component loading is needed, and defined in this section. To define a set of design situations relevant for FOWT loading, international design standards, such as IEC 61400-3 (2019) part 2 can be used [82], which complements the more general standard on offshore wind turbines [86]. These standards specify essential design requirements to ensure the engineering integrity of FOWTs, including their five main subsystems such as the RNA, tower, floating substrucutre, station-keeping system and on-booard machinery. In such standards, in analogy to onshore wind turbines, Design Load Cases (DLCs) are defined. A DLC, is the combination of a certain operating condition (power production,

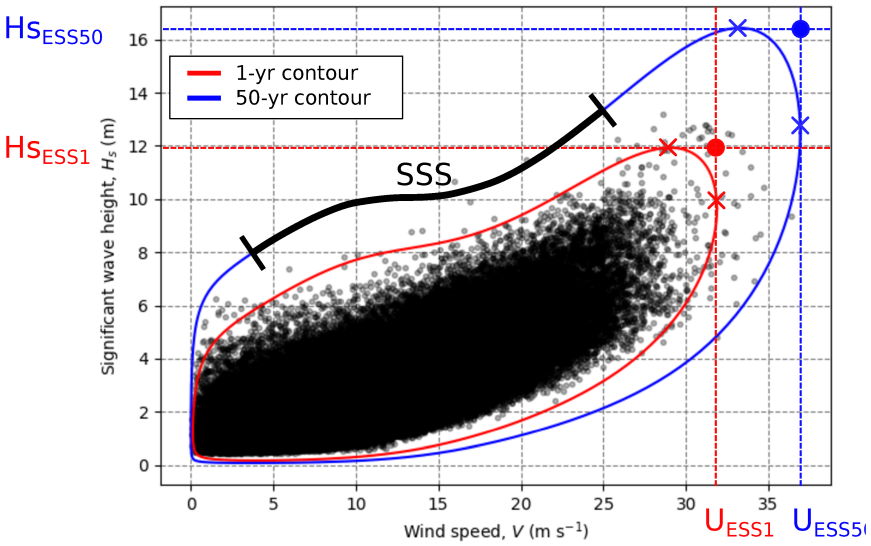

Figure 4.4: Wind speed – significant wave height environmental contours compute with IFORM method in Virocon for the West of Barra site. 1-D excedance values of wind speed and significant wave height in dashed lines, corresponding to ESS conditions.

parked, fault, etc...) with a certain environmental condition, like the Normal Sea State (NSS), Severe Sea State (SSS) or Extreme Sea State (ESS). DLCs are intended for wind turbine load calculation and certification: the process through a third party certifies that the machine is built according to the standard. In particular, the technical specification IEC 61400-3-2 adds a table of DLCs specific for FOWTs (namely DLCs 2.6, 4.3, 9.1-9.3, and 10.1-10.3) that aim at evaluating the performance both in normal operation and parked conditions, with a special focus on those less-frequent, but high-demanding, conditions.

In this case, the standard, and DLCs, are used as a guideline, in order to include relevant engineering simulations into this study. Therefore, the DLCs that are selected need to provide a good estimation of fatigue and extreme loads for the comparison to be effective. In fact, even in a comparative study, the validity of the outcomes may be undermined if the estimates of fatigue and extreme loads are far from those obtained during a certification process. On the other hand, when not focusing strictly on turbine certification, it is not necessary to consider the full design spectrum and the analysis can be limited to a subset of relevant DLCs: a balance between the number of computations to run and the coverage of the wind turbine design space needs to be struck. To simplify the analysis, no DLCs with faults (DLC 2.X) were simulated. Also, maintenance and installation were not considered. Only power-production and parked conditions are considered herein.

A subset of DLCs is typically defined based on experience in similar load calculations, with similar turbine and floater concepts and in similar met-ocean conditions. In the present study, DLCs are defined on the basis of a literature review. In fact, in recent years, some authors have attempted load calculations on FOWTs. One of the first examples is the work

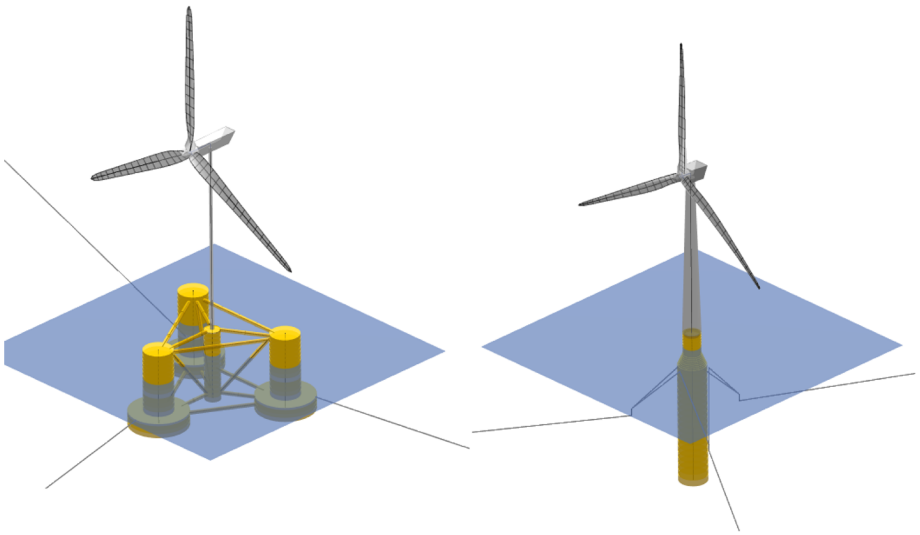

Figure 4.5: QBlade-Ocean models of the NREL 5MW OC4 and DTU 10MW SOFTWIND test cases. Image from [34].

by Jonkman an Buhl [87]. Here, a subset of power production, power production with occurrence of fault and parked DLCs is considered. Namely DLCs 1.1, 1.3, 1.4, 1.5, 1.6, 2.1, 2.3, 6.1 and 6.2 are considered. On the test case that was considered (NREL 5MW mounted on the ITI Energy Barge concept), most extreme loads were found in DLC 1.1, 1.3 and 1.4. Ramachadaran [88] presents the DLCs that were used in the H2020 Project LifeS50+ for the evaluation of four floater concepts, two semi-submersibles, one spar-buoy and one tension-leg platform. The list includes the DLCs simulated by Jonkman and Buhl with the omission of DLCs 1.5 and 2.1. Finally in the load evaluation of the IEA 15MW RWT in a floating configuration, Allen et. al. [89] use a subset of IEC61400-3 DLCs defined based on experience. The subset includes the DLCs of the previous studies but further reduces the subset, also not including DLC 2.3.

Upon synthesis of the aforementioned studies, a list of DLCs is proposed. It comprises of DLCs 1.2, 1.3, 1.4, 1.6, 6.1, 6.3 and 6.3. Similar to Ramachadaran, DLCs 1.5 and 2.1 are not considered. In addition, no fault cases are considered, as was done by Allen et al. DLC 1.1 was also not considered as it was considered superfluous with respect to DLCs 1.3 and 1.6, which have more severe turbulence and wave conditions, respectively. DLC 1.2 was added to the list for an estimation of fatigue loads, while DLC 6.2 was also included in order to evaluate the effect of inflow from multiple directions on a FOWT. The DLCs that are used in the current study are summarized in table 4.2.

Table 4.2: List of considered DLCs

DLC	wind		waves				dur.	seeds/ws	yaw	n ws	sims	type
	model	speed	model	height	period	direction						
1.2	NTM	Vin-Vout	NSS	$1 < H_S < 7$	$8 < T_P < 14$	MUL	1800	1	0,10°	11	504	F
1.3	ETM	Vin-Vout	NSS	E[Hs|Vhub]	E[Tp|Hs]	COD	1800	9	0,+-10	11	99	U
1.4	ECD	Vr +- 2 m/s	NSS	E[Hs|Vhub]	E[Tp|Hs]	COD	600	-	0	6	12	U
1.6	NTM	Vin-Vout	SSS	Hs,SSS	E[Tp|Hs]	COD	3600	9	0,+-10	11	99	U
6.1	EWM50	V50	ESS	Hs50	E[Tp|Hs]	0°,+-30°	3600	2	0,+-10	1	12	U
6.2	EWM50	V50	ESS	Hs50	E[Tp|Hs]	0°,+-30°	3600	2	0,45,90 135,180	6	12	U
6.3	EWM1	V1	ESS	Hs1	E[Tp|Hs]	0°,+30°	3600	2	0, +-20	1	12	U

4.3 Test Cases

4.3.1 NREL 5MW OC4 semi-submersible

The NREL 5MW OC4 semi-submersible FOWT (hereafter OC4) is an open-source test case defined in [90]. It makes use of the NREL 5MW RWT rotor [57], representative of a utility-scale multi-MW rotor. This turbine has been used during all phases of the OC3 [91], OC4 [90] and OC5 [67] code-to-code comparison projects. The rotor is mounted on the DeepCwind semisubmersible floating platform. DeepCwind is a project aimed at generating test data for use in the validation of FOWT modeling tools.

The same tower design that was developed for use on the OC3-Hywind spar platform [91] is used. The semi-submersible floater consists of a main central column connected to the tower and three side columns spaced 120° apart. The offset columns feature heave plates at their base to control the vertical motion of the FOWT and are connected together through a series of braces.

A catenary mooring system is used. Three 120° lines are used to anchor the turbine to the seabed with one mooring line pointing directly upwind and the other two downwind.

4.3.2 SOFTWIND spar

The DTU 10 MW SOFTWIND spar FOWT (hereafter SW) is a floating platform designed by École Centrale Nantes to simulate the behavior of the DTU 10MW RWT [40] at 1:40 scale. The test case was designed to demonstrate and validate a Software in the Loop approach where instead of modeling the rotor blades geometry, an actuator is used to emulate the thrust force acting on the FOWT. The test case and the experiments are described in [92].

Respect to the experimental model tested in ECN's wave basin, some modifications ha been made. Firstly, the tower designed by Olav-Olsen for the DTU10MW on the OO-Star platform [1] is used. This tower is stiffer and heavier than the full scale counterpart of the tower used in the SOFTWIND experiments, avoiding natural frequency excitation issues in the 3P range. Second, the mass and inertial properties of the floater were changed to improve the stability of the design in severe seas and to partially offset the effect of the heavier tower. Therefore, mass was lowered approximately 1%, while the center of gravity was also lowered. This measure may not have been necessary but was considered prudent. A MagnaDense concrete ballast is used, similarly to the approach followed by Leimeister et al. in [93]. In line with the work of these authors, a uniform wall thickness of 100 mm is used. Steel density of 8000 kg/m^3 is considered in order to include additional weight due to welded or bolted connections and paint that were not considered herein. A more exhaustive description of the changes to the models can be found in [94].

The external floater geometry as well as the mooring line design is the same as tested in the work by Arnal [92]. A three line catenary mooring system is used. Before connecting

[1] The OO-Star Wind Floater has been developed dy Dr. Techn. Olav Olsen (OO) since 2010 and is the property of Floating Wind Solutions AS. OO has approved that the public model from LifeS50+ can be used for the research activities within FLOATECH. The model shall not be used for other purposes unless it is explicitly approved by OO.

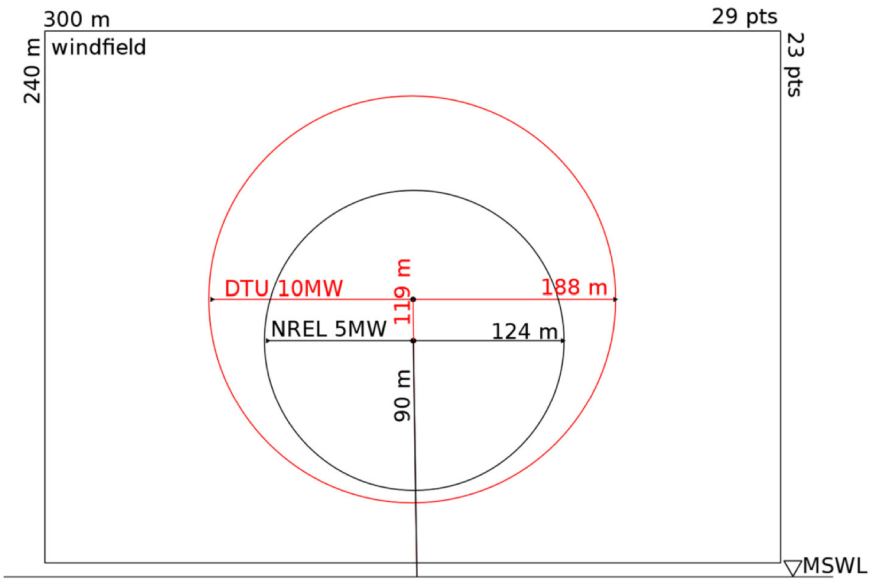

Figure 4.6: Schematic view of the turbulent wind box used in the simulations, DTU 10MW RWT wind turbine and NREL 5MW RWT turbine sizes.

to the floaters, the lines are split into two with a delta-connection in order to provide yaw stability to the system.

4.4 Simulation Set-up

Despite the fact that multiple wind and wave realizations are used, the same external inputs are used in all three codes. Using the same inputs in the three codes allows for punctual comparisons between them in addition to comparisons in the frequency domain. Time histories of irregular waves are generated in DeepLines Wind and imported in QBlade-Ocean and OpenFAST. Turbulent wind fields are generated using TurbSim v2.0.0 [95], with IEC-Kaimal spetral model and spectral coherence model. The same wind fields are shared in both test cases, despite them using different turbine rotors. Mean wind speed is imposed at 100 m above mean sea water level (MSWL), in consistency with the ERA5 hindcast database that was used to derive the environmental conditions of the examined installation site. Because of wind shear, wind speed is slightly lower for the OC4 test case than it is for the SOFTWIND test case, as would happen if these machines were installed in the same site. Despite the differences in hub height, all the simulations are in the same wind speed bin, regardless of the test case.

4.5 Numerical Models

Three distinct numerical tools are used in this section. The 5MW OC4 semi-submersible and the 10MW SOFTWIND models are simulated in both OpenFAST (OF) and QBlade-Ocean (QB). The latter is also simulated using DeepLines Wind (DL). The main features and characteristics are discussed in section 1.4.

From a modeling standpoint, the biggest differences between the codes lie in the approaches that are used for aerodynamics and for structural dynamics. In fact, as detailed in the following, the same controller is used in all the models. Moreover, while the three codes differ on the use of different sub-models, all three share the same approach with regards to hydrodynamics and mooring line dynamics. Particular care was put into keeping the models as consistent as possible, so that and differences between them can be ultimately imputed to the different-fidelity modeling.

Aerodynamics

A DBEM wake model is used in OF and DL, while a higher-order LLFVW model is used in QB. The same aerodynamic lift and drag tables are used in all three codes for both models. Gonzalez's variant of the Beddoes-Leishman dynamic stall model [49] is used in OF. In QB dynamic stall is modeled with Øye's model [22], while in DL no unsteady airfoil aerodynamics are accounted for.

Structural Dynamics

Structural dynamics are modeled with a modal-based linear superposition approach in OF, through the submodule ElastoDyn. In QB and DL on the other hand, a higher fidelity approach is used, whereby the structural dynamics are included thanks to the use of a multi-body Finite-Element model.

Hydrodynamics

A LPMD approach is used in all three codes, whereby hydrodynamics are modeled by combining a potential flow solution with quadratic drag computed with Morrison's equation. Full difference-frequency QTFs are used in both QB and OF in the OC4 test case. They were computed and provided for this geometry by ECN using NEMOH, a potential flow hydrodynamic solver developed by ECN themselves. On the SOFTWIND test case, quadratic hydrodynamic excitation forces are included in OF and DL with Neumann's approximation [96], but are not accounted for in QB. The same hydrodynamic coefficients are used for both test cases in all three models. Buoyancy is modeled differently in the three codes: QB and DL model this force explicitly. The spar structure is divided into a series of cylindrical sections and buoyancy forces are discretely applied, very similarly to the OC5 test case discussed in chapter 3. OF on the other hand models buoyancy force as constant term and a linear stiffness matrix to include the contributions of buoyancy to the restoring forces on the platform.

Table 4.3: Natural frequency and damping ratio of the ROSCO pitch controller

Model	Nat. f (ω)	Damping ratio (β)
NREL 5MW OC4	0.2 [rad/s]	1 [-]
DTU 10MW SOFTWIND	0.14 [rad/s]	1 [-]

Control

For both the NREL 5MW OC4 and the DTU 10MW SOFTWIND models the ROSCO open-source controller [97] is used. More specifically, ROSCO v2.4.1 is used. This controller has been selected as it is open-source and it includes an automatic tuning toolbox [98] that can be used to determine the proportional and integral gains of the blade pitch controller in a simple manner [99]. A traditional $K - \omega^2$ law is used for the torque controller below rated wind speed. Above rated wind speed constant-torque control strategy is used. The pitch controller gains are tuned using ROSCO controller's automatic pitch-tuning routine [99][97], based on the OpenFAST models of the two rotors. The controller includes a nacelle-velocity feedback loop developed especially for FOWTs, with the objective of avoiding negative blade-pitch controller damping that can occur in the case of FOWTs. However, this feature is not used in this work package but rather, the more traditional strategy of de-tuning the pitch controller is used. The natural frequencies and damping ratios of the pitch controller used for the three models are shown in table 4.3. For both models the natural frequency of the blade pitch controller is set below the platform pitch natural frequency, mitigating possible controller-driven system instabilities.

In the OC4 test case, a peak-shaving minimum pitch saturation schedule is considered. Peak shaving is used to reduce loads near rated wind speed by imposing a minimum pitch angle as a function of the 1-second low pass filtered wind speed at hub height, as explained in [97]. In this test case the same settings as in the public example that can be found in the ROSCO repository are used.

4.5.1 Mooring lines

Dynamic mooring line models are used in all three codes. Hydrodynamic actions on the cables are introduced through MOrrison's equation. The same added mass and drag coefficients are used in all three codes.

4.5.2 Tuning of the DeepLinesWind Model

For the DL model of the SOFTWIND spar floater, large discrepancies in the response of the structure from a dynamic standpoint were noted, with large differences in free-decay tests being noticed. To better align the DL model to OF and QB, the following was done:

- A transverse drag coefficient (Ca) of 0.5 is applied to the spar structure through strip theory. As described previously, a hybrid potential flow – strip theory approach was used in all three codes. In particular, Morrison's equation is used to account

for quadratic drag in the models, while radiation damping, added mass and linear excitation force are included through an externally computed potential flow solution. In the DL model however, to align the surge and sway free-decay natural frequencies, an added mass coefficient of 0.5 was added in the strip-theory solution, effectively counting added mass twice respect to OF and QB;

- Roll and Pitch floater inertias are decreased approximately 40% to align the natural frequencies in roll and pitch;
- Mooring line lengths were tuned in each numerical models as a compromise between natural frequency in surge and mean mooring line tension. It is worth pointing out here that the compromise found for DL led to slightly longer lines and thus lower tensions than the tunings that were done for OF and QB

Moreover, for compatibility reasons, the ROSCO controller needed to be re-compiled to be coupled to DeepLines Wind. This operation was performed by an external contractor within the H2020 project FLOATECH. Analyzing results, it is apparent that minimum rotor speed is not enforced in the SOFTWIND DL simulations at cut-in wind speed.

Finally, not all the outputs that are available in the OF and QB results were made available in the DL results computed within WP2 of the FLOATECH project.

For all of these reason combined, the DL results shown herein are used in a more broad sense, to compare general trends and dynamics predicted by this wind turbine simulation code. More rigorous and quantitative comparisons are possible between OF and QB, since the set-ups of these two codes are consistent.

4.5.3 Computational Time

Some qualitative information regarding computational requirements of each of the compared software tools will be given herein. It must be noted that this information is valid strictly for the test cases and set-ups that they are relative to and is not referred to te specific softwares that could run much faster or slower depending on the hardware configurations and set-up choiches. For a DLC 1.2 simulation of the SOFTWIND testcase, that is simulated with all three codes (4000 s of simulated time):

- Qblade-Ocean is run on a desktop workstation equipped with a 12th Gen Intel Core^{TM} i7-12700KF processor and an NVIDIA GeForce RTX 3070 Ti graphics card. 20 simulations are run in parallel and average wall clock time per simulation is approximately 10400 s.
- OpenFAST is run on a desktop workstation equipped with a 10th Gen Intel Core^{TM} i9-10900K processor. 12 simulations are run in parallel and average wall clock time per simulation is approximately 1140 s.
- DeepLines Wind^{TM} is run on a cloud computing service with Intel Xeon Processors (Skylake), (2.4 GHz). 34 simulations are run on a 36-core server, or 16 simulations are run on a 14-core server. Average wall clock time is 24900 s per simulation. Standard

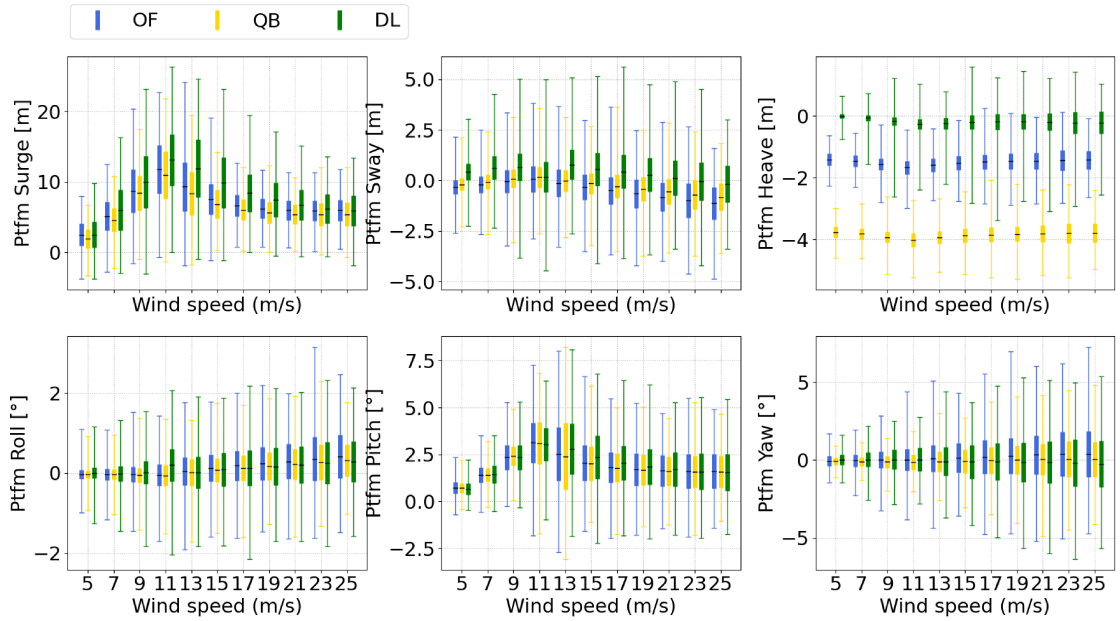

Figure 4.7: Platfrom motion statistics for the SOFTWIND test case grouped by wind speed. Means (horizontal line), standard deviations (boxes), and min/max ranges (whiskers).

hard-drives are used for storage. This is relevant as I/O time is often significant, and calculations will run faster if SSDs are used.

The wake is solved with a medium-fidelity LLFVW model in QB featuring GPU acceleration. The use of Quadratic Transfer Functions (QTFs) can add significant computational time to QB simulations. In comparison to the other codes, OF required much less computational time to run in this study. It must be noted however that this code was run with lower fidelity modal based structural dynamics and lower fidelity dynamic-BEM aerodynamics.

4.6 Results

4.6.1 Statistics

Platform motion statistics for the SOFTWIND test case are shown in Fig. 4.7. Better agreement is seen between OF and QB in Surge, Sway and Pitch. Predictions form DL tend to differ from the other two codes especially past rated wind speed in mean standard deviation and also extreme values. Significant differences between the codes are also noted in the heave DOF. These are attributed to the different buoyancy models and to the fact that they are fine-tuned differently in each of the three codes [34]. If compared to the nominal platform draft of 90 m, these differences are rather small, and are not concerning.

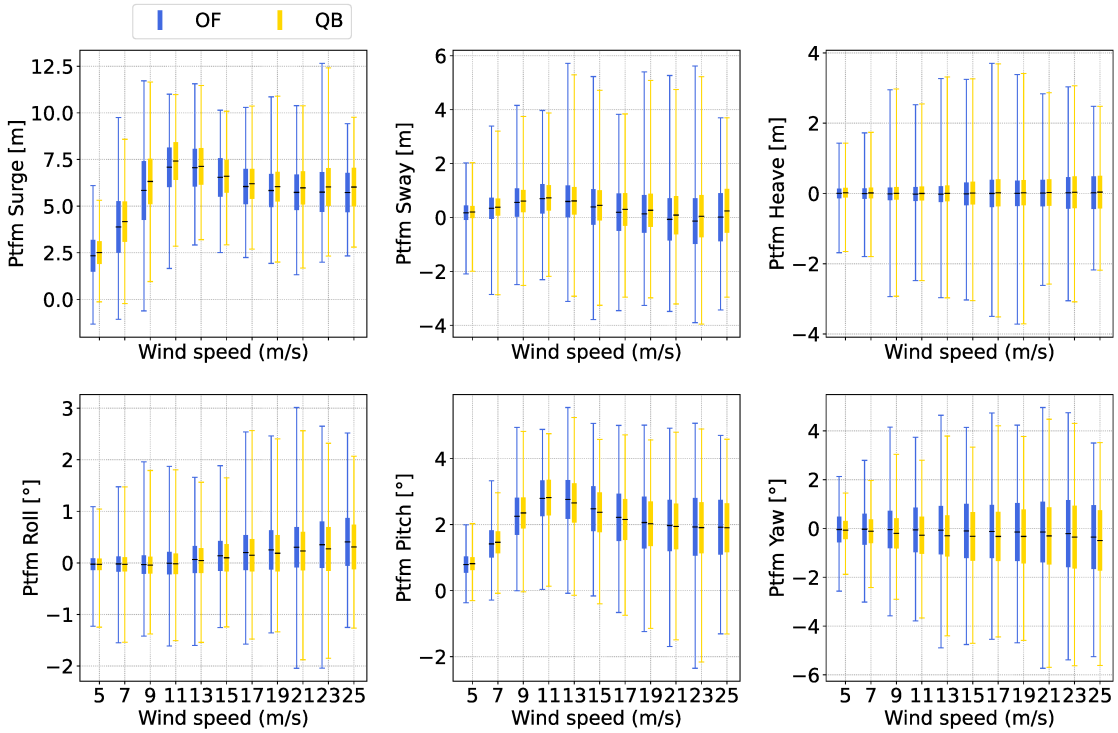

Figure 4.8: Platfrom motion statistics for the OC4 test case grouped by wind speed. Means (horizontal line), standard deviations (boxes), and min/max ranges (whiskers).

For the OC4 test case, platform motion statistics in DLC 1.2 are shown in Fig. 4.8. Better agreement between OF and QB is noted than what was achieved for the SOFTWIND test case (Fig. 4.7). Slightly larger standard deviations and peak loads can be noted for OF.

Statistics of control sensors such as generator power and torque, rotor speed and blade pitch are shown in Fig. 4.9. Below rated wind speed rotational speed and generator torque are higher for QB. These two quantities are related by the so-called $k - \omega^2$ law [97] below rated wind speed, therefore increases in rotor speed cause increases in generated torque. The ultimate cause of he higher speed and torque is slightly higher aerodynamic power produced by QB below rated. As wind speed increases, mean blade pitch increases to regulate power. For most wind speeds, mean blade pitch for QB is between OF, that is higher, and DL. In these off-design conditions, it is OF that produces the most power, not QB. Generator torque is constant past rated wind speed due to the constant-torque regulation strategy that was employed. The three codes agree well in terms of rotational speed although larger standard deviations and min/max values can be seen for DL and OF. Moreover the minimum rotor speed is not enforced correctly at 5 m/s average wind speed in DL, a result of an implementation issue of this control routine in DL.

The same control statistics that are shown for the SOFTWIND test case are shown for

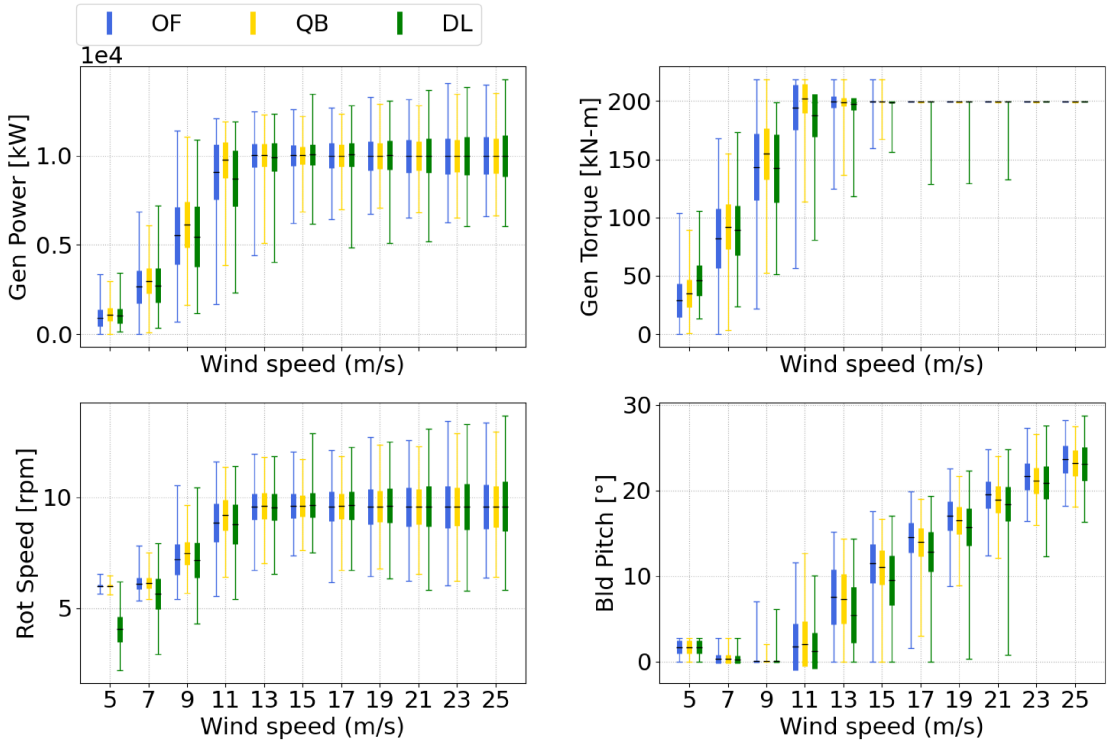

Figure 4.9: Control and Operation statistics for the SOFTWIND test case grouped by wind speed. Means (horizontal line), standard deviations (boxes), and min/max ranges (whiskers).

the OC4 semi-submersible test case in Fig. 4.10. OF and QB behave very similarly relative to each-other. Mean generator power, torque and rotor speed are higher for QB below rated, while mean blade pitch is higher for OF above rated, as a result in small differences in the aerodynamic model tuning. Rotor speed standard deviations and min/max ranges are greater for OF. Differently form the SOFTWIND test case, variations in generator torque can be seen past rated wind speed, and torque is fairly constant only at 25 m/s mean wind speed. This is due to the fact that the hub height of the NREL 5MW OC4 test case is lower (90 m as opposed to 119 m for the SOFTWIND test case), and thus wind speed on the rotor is lower. Secondly, a peak-shaving minimum pitch saturation routine is used in this test-case, as describe in section 4.5.

The presence of the peak-shaving algorithm leads to significant differences in mix/max rages for the side-side yaw bearing bending moment, shown in Fig. 4.11. The reason this load is higher in OF is specific to this controller tuning and test case. On a real wind turbine such behavior may be considered unacceptable regardless of the simulation code used and eliminated by re-tuning the controller. Nonetheless it is interesting to analyze in the context of this study as it highlights a case where the complex interactions between control, aerodynamics and structural model lead to different extreme loads.

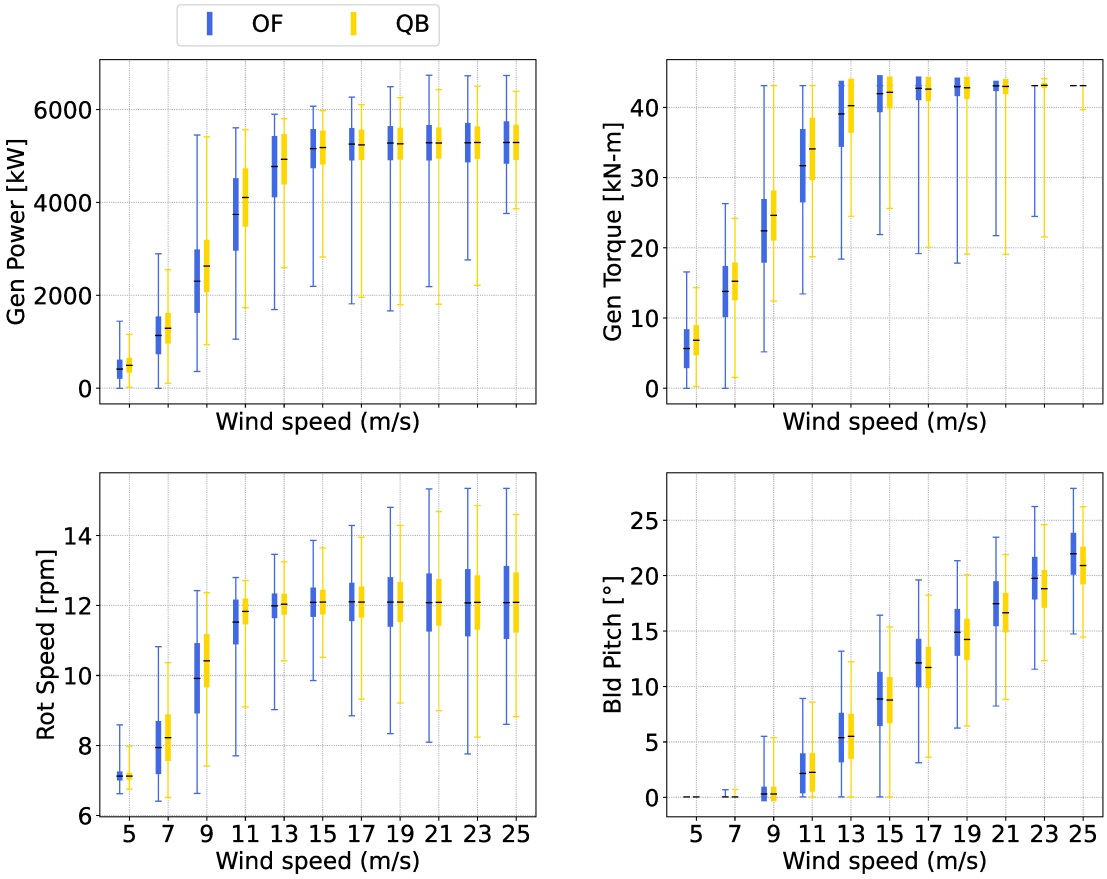

Figure 4.10: Control and operation statistics for the OC4 test case grouped by wind speed. Means (horizontal line), standard deviations (boxes), and min/max ranges (whiskers).

The time series of TT Mx and some contemporaneous load sensors relevant to the understating of why these peak loads are recorded are shown in Fig. 4.12. When both the minimum and maximum values in the time series for OF are recorded, an abrupt change in generator torque can be seen. In fact, as rotor speed decreases, the generator abruptly transitions from above-rated to below-rated torque. Once the minimum pitch angle as a function of the 1-second low-pass filtered velocity is reached, the generator transitions to below-rated operation to maintain rotor speed at its rated value. The cause of rotor speed decrease can be traced back to decreasing aerodynamic torque, as wind speed decreases because of turbulence and platform pitch increases due to the instantaneous wave field, lowering relative velocity on the rotor even further. Because of the difference in blade pitch between QB and OF (as shown in Fig. 4.10), pitch saturation is reached earlier by QB, that transitions to below-rated torque earlier than OF. Moreover, once the transition occurs for OF, a relatively large oscillation at the first side-side tower natural frequency can be noted. On the other hand, the step change in generator torque does not initiate such an oscillation

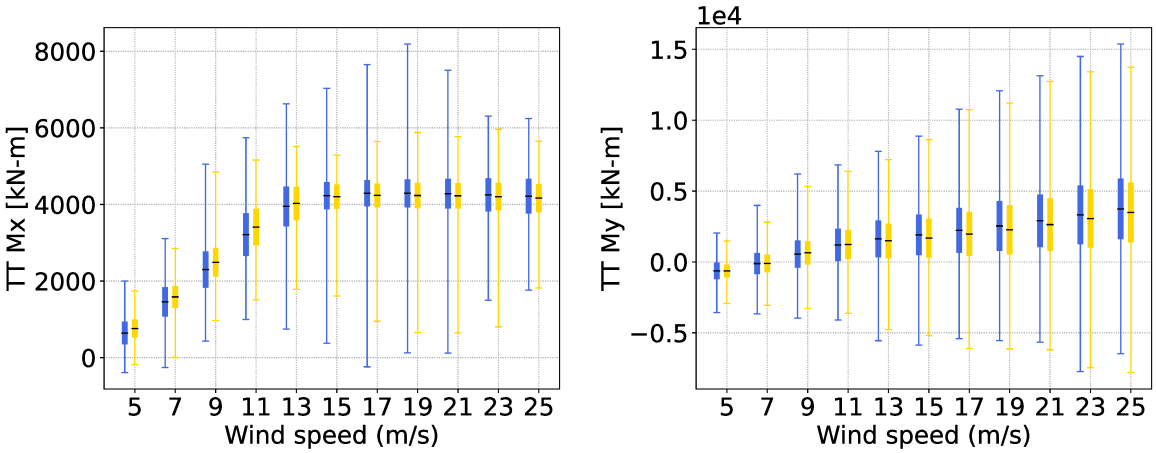

Figure 4.11: Yaw bearing fore aft (My) and side-side (Mx) bending moment statistics for the OC4 test case grouped by wind speed. Means (horizontal line), standard deviations (boxes), and min/max ranges (whiskers).

in QB, which in turn predicts lower peak TT Mx. Although damping ratios were not compared when the numerical models were set-up, 1% of critical damping ratio is specified in OF, while a Rayleigh damping coefficient of 0.00127 is specified in QB, leading to similar damping ratios at the tower natural frequency. As discussed in the following sections, the modal structural model in OF has shown the tendency to predict large un-dampened load oscillations at the system natural frequencies, that are not observed in the other tow codes.

4.6.2 Extreme loads

As structurally stressed components, wind turbine parts must be able to resist extreme design loads. In this section the highest loads at the blade root and tower base predicted by the three codes are compared. These loads will be hereafter referred to as *ultimate* or *extreme* loads.

The ultimate loads are computed with the extreme load averaging technique described in the MExtremes theory guide [100], which is in line with the recommendations of IEC 61400-1 (2019) [86]. If multiple turbulent realizations (seeds) are present for a given wind speed, simulations are grouped (binned) based on mean wind speed on a DLC-per-DLC basis. The average of the maximum recorded for all the simulations within one wind speed bin is recorded (mean of max). The closest event that is larger than the mean of max value is taken as extreme event. This ensures that contemporaneous loads can be recorded: the selected ultimate load comes from the time history of the data, and thus the values of other load sensors at the time the peak load occurs can be recorded.

For completeness, the absolute extreme loads without any averaging are also recorded. These values can serve as indicators of instabilities, both numerical or phisical, in the analyzed systems.

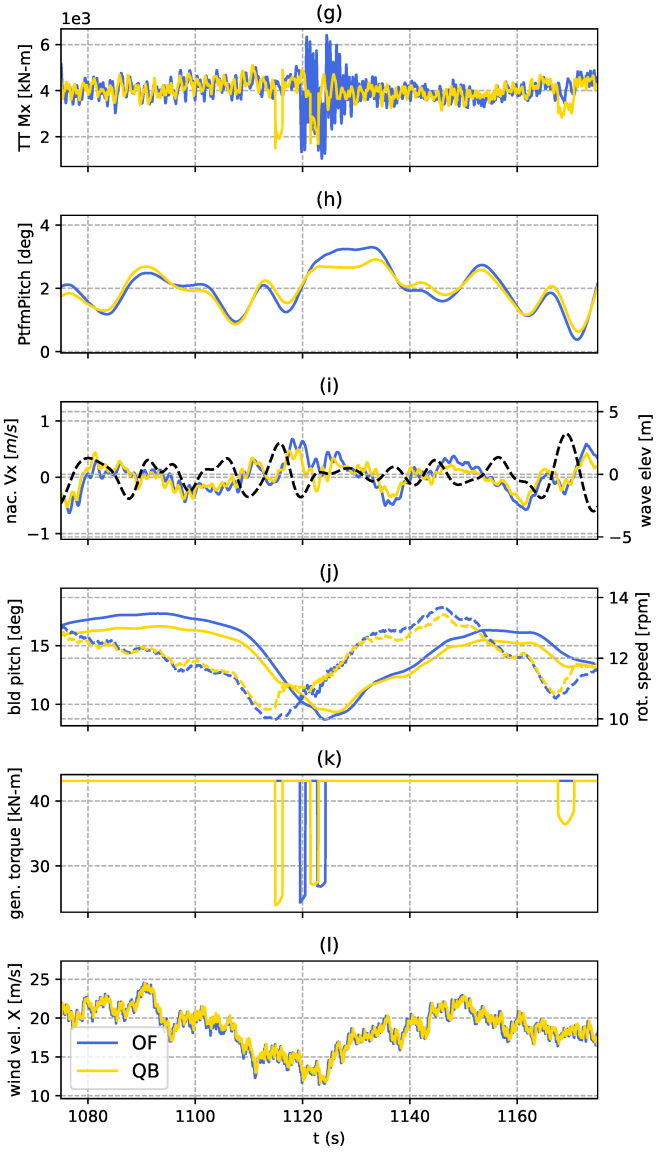

Figure 4.12: Time series near maximum TT Mx (DLC 1.2 seed 223, mean wind speed 19 m/s) during normal operation (DLC 1.2). (top to bottom) platform pitch, nacelle fore-aft velocity, blade pitch, generator torque, wind X velocity

SOFTWIND 10MW

Flapwise (Myb) and edgewise (Mxb) blade root bending moment aggregated maximum values for the three blades are shown in table 4.4. Flapwise maximum root bending moment is located in DLC 1.6 for all three codes. This metric is slightly higher for OF than it is for QB, while DL is approximately 10% lower than QB. For flapwise and out of plane loads (My) especially, maximum values are similar for all three blades, suggesting that good statistical convergence of the maximum loads was reached. As for edgewise root bending moment (BR Mxb), QB predicts the maximum to be located in a mix of DLC 1.4 and 1.6, indicating that both DLCs are similar for this load sensor. On the other hand, maximum edgewise root bending moment is in DLC 6.3 for all three blades for OF. As shown in the following, this is caused by a resonance in DLC 6.3 that is not removed by the mean of max method.

Time-series in correspondence of peak blade root flapwise loads are shown for OF and QB in Fig. 4.13. In (a-f) the recorded maximum QB load is shown, in (g-l) maximum OF load is recorded. The ultimate loads are in different time instants and different simulations. For both time instants, in addition to the Time series of BR Myb, Time series of other sensors are shown; platform pitch to give an indication of gravitational loading on the structure, RNA fore-aft acceleration for an indication of inertial loads on the structure, blade pitch and rotor speed to gage the operating conditions of the machine, aerodynamic thrust for an indication of aerodynamic loading on the rotor. Finally, wave height and wind speed at hub height are also reported. For this test case, the peaks are located in DLC 1.6 for all three codes. In both the time-instants analyzed in Fig. 4.13, peak loading occurs in correspondence of a severe wave-train (Fig. 4.13 (c, i)).

DL values are shown for completeness but they are affected by the fact that BR Myb is not in the pitching reference system but in the coned one, that does not pitch with the blades, and by the presence of a time-shift in the wind field. By comparing Fig. 4.13 (a-g) and (e-k), good correlation between rotor thrust and flapwise bending moment can be noted. This is not surprising as flapwise loads are typically driven by aerodynamic loading. No clear correlation btween platform pitch, nacelle fore-aft acceleration and blade flapwise bending moment can be seen. Modern multi-MW wind turbine blades are relatively lightweight with respect to the other structural components such as the nacelle and tower. Therefore, although the gravitational and inertial loads driven by structural motion play a role, they are not as significant as those acting on the tower. Nonetheless, the platform motion contributes to the unsteady loading on the rotor, as fore-aft platform motion introduces variations in the apparent wind speed. As shown in Fig. 4.13 (b) and (d) rotor speed correlates well with the pitch motion, which in turn drives blade pitch variations. Comparing QB and OF in Fig. 4.13 (d), both rotor speed and blade pitch are very similar. Rotor thrust and torque in Fig. 4.13 (d) show how, once again, QB and OF are very similar. In both seeds shown in Fig. 4.13, rotor thrust goes from a positive peak to a negative one between 3000 and 3100 s, as a consequence of platform motion and blade pitch that rapidly rises from feather to more than 20°. Even in such dynamic inflow conditions, the DBEM wake model in OF is very close to the LLFVW model in QB in the prediction of global rotor aerodynamic loads (thrust and torque) as well as blade root bending moments. As for DL, platform dynamics (platform pitch and nacelle fore-aft acceleration) appear to be well predicted around the

Table 4.4: Maximum component loads for the SOFTWIND test case predicted with QB, OF and DL

Sensor	Units	DLC QB	DLC OF	DLC DL	QB value	OF value	DL value	OF-QB diff. (%)	DL-QB diff. (%)
B1R Mxb	kNm	1.6	6.3	-	1.82e+4	3.191e+4	-	75.29%	-
B2R Mxb	kNm	1.4	6.3	-	2.46e+4	3.025e+4	-	23.04%	-
B3R Mxb	kNm	1.4	6.3	-	2.40e+4	2.879e+4	-	19.77%	-
B1R Myb	kNm	1.6	1.6	-	5.14e+4	5.394e+4	-	4.96%	-
B2R Myb	kNm	1.6	1.6	-	5.21e+4	5.331e+4	-	2.32%	-
B3R Myb	kNm	1.6	1.6	-	5.05e+4	5.546e+4	-	9.76%	-
BR Mxb	kNm	1.4	6.3	-	2.46e+4	3.19e+4	-	29.79%	-
BR Myb	kNm	1.6	1.6	-	5.21e+4	5.55e+4	-	6.46%	-
B1R Mxc	kNm	1.3	1.3	1.3	2.20e+4	2.500e+4	2.270e+4	13.84%	3.35%
B2R Mxc	kNm	6.1	1.3	1.3	2.16e+4	2.424e+4	2.199e+4	12.31%	1.88%
B3R Mxc	kNm	6.1	1.3	1.4	2.33e+4	2.507e+4	2.947e+4	7.79%	26.70%
B1R Myc	kNm	1.6	1.6	1.6	5.14e+4	5.294e+4	4.682e+4	3.08%	-8.84%
B2R Myc	kNm	1.6	1.6	1.6	5.20e+4	5.328e+4	4.508e+4	2.44%	-13.33%
B3R Myc	kNm	1.6	1.6	1.6	5.07e+4	5.416e+4	4.617e+4	6.88%	-8.89%
BR Mxc	kNm	6.1	1.3	1.4	2.33e+4	2.51e+4	2.95e+4	7.79%	26.70%
BR Myc	kNm	1.6	1.6	1.6	5.20e+4	5.42e+4	4.68e+4	4.13%	-9.97%
RotThrust	kN	1.6	1.6	1.6	3.26e+3	3.373e+3	2.921e+3	3.59%	-10.29%
B1 Tip DX	m	1.6	1.6	-	1.41e+1	1.478e+1	-	4.79%	-
B1 Tip DY	m	1.4	1.4	-	4.65e+0	4.996e+0	-	7.41%	-
Gen Tq	kN-m	1.6	1.4	1.3	2.21e+2	2.213e+2	1.999e+2	0.10%	-9.57%
Gen Pwr	kW	1.6	1.6	1.6	1.49e+4	1.587e+4	1.505e+4	6.76%	1.23%
Aero Thrust	N	1.6	1.6	1.6	2.61e+6	2.776e+6	1.724e+7	6.36%	560.49%
Aero Torque	Nm	1.6	1.6	-	4.10e+7	4.405e+7	-	7.35%	-
TT Fx	kN	1.6	1.6	6.1	4.88e+3	4.802e+3	5.327e+3	-1.59%	9.16%
TT Fy	kN	6.2	6.3	6.2	2.76e+3	3.539e+3	2.443e+3	28.03%	-11.63%
TB Fx	kN	6.2	6.2	1.6	1.00e+4	1.038e+4	9.234e+3	3.49%	-7.91%
TB Fy	kN	6.2	6.2	6.2	6.10e+3	5.571e+3	5.464e+3	-8.61%	-10.36%
TB Mx	kN-m	6.2	6.3	6.2	3.45e+5	3.801e+5	3.898e+5	10.09%	12.91%
TB My	kN-m	6.2	6.2	6.1	7.27e+5	6.838e+5	8.397e+5	-5.88%	15.59%
T ML1	kN	6.1	6.1	6.1	4.786e+3	5.130e+3	4.524e+3	7.19%	-5.48%
T ML2	kN	6.2	6.1	6.2	5.979e+3	5.110e+3	4.941e+3	-14.55%	-17.37%
T ML3	kN	6.2	6.2	6.1	6.378e+3	6.942e+3	5.730e+3	8.84%	-10.16%
Surge	m	6.2	6.1	6.1	1.942e+1	2.319e+1	2.701e+1	19.39%	39.08%
Sway	m	6.2	6.2	1.4	9.021e+0	1.004e+1	9.356e+0	11.35%	3.71%
Heave	m	6.1	6.1	6.2	9.968e-1	3.279e+0	4.887e+0	229.00%	390.24%
Roll	°	6.2	6.2	6.2	4.148e+0	3.999e+0	5.465e+0	-3.60%	31.74%
Pitch	°	6.2	6.2	6.1	1.006e+1	9.950e+0	1.365e+1	-1.13%	35.60%
Yaw	°	1.3	6.2	1.3	4.387	18.24	5.717	315.76%	30.30%

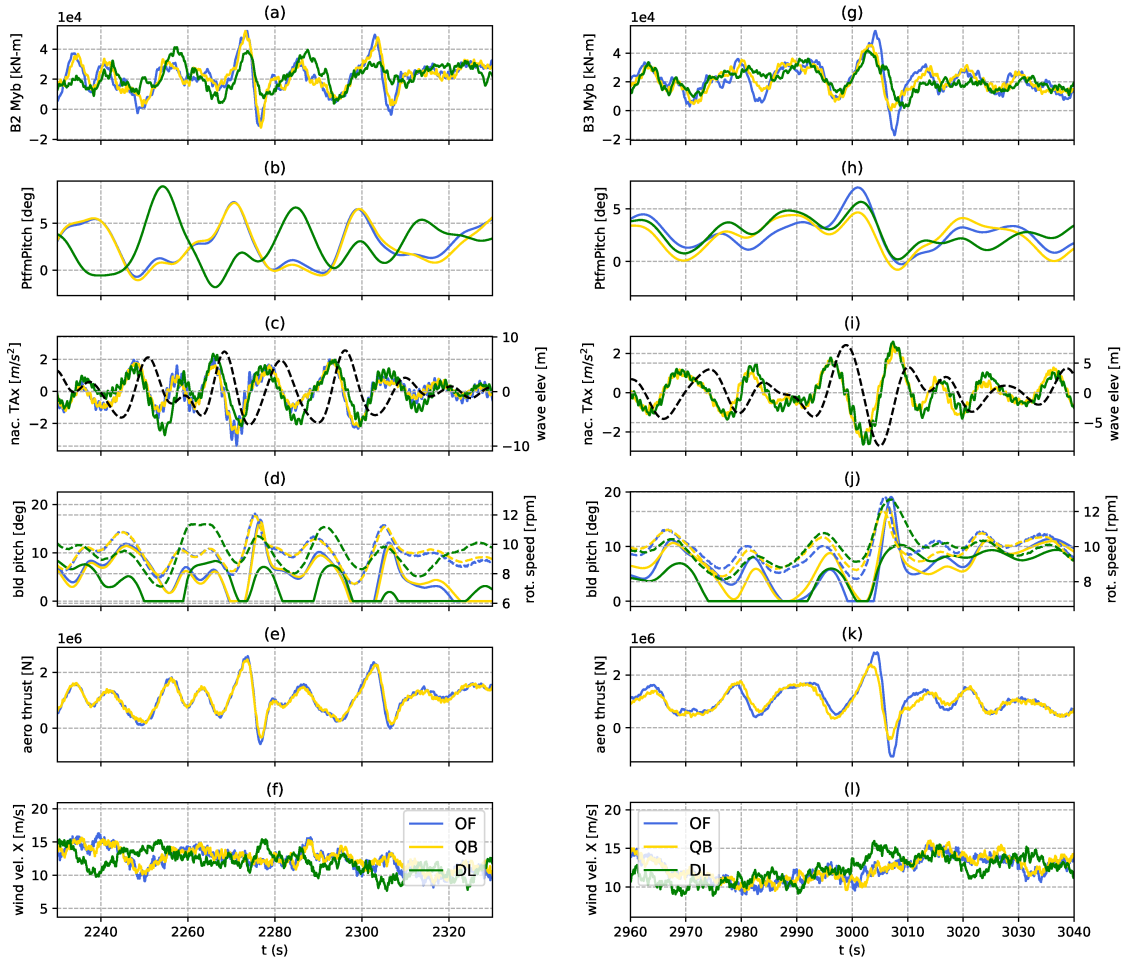

Figure 4.13: (a,g) Peak flapwise root bending moment (My) for QB (left, DLC1.6 seed 1039) and OF (right, DLC1.6 seed 1042). (b,h) Platform Pitch, (c,i) nacelle fore-aft acceleration and wave elevation (right axis, dashed line), (d,j) blade pitch and rotor speed (right axis, dashed lines), (e,k) rotor aero thrust and torque (right axis, dashed line), (f,l) wind speed. Max(My) is also in DLC1.6, seed 1039 for DL, but at different timestep

peak wave event that occurs around 3000 s, however differences with respect to QB and OF can be seen in the control signals and in the blade root flapwise bending moment. For the former, the time-shift in the instantaneous wind speed shown in Fig. 4.13 (f) plays a role, while the latter are not in the same reference system as OF and QB.

Blade root edgewise extreme load time series for QB and OF are shown in Fig. 4.13. For QB and DL (not shown for brevity), maximum edgewise load is located in DLC1.4, and, as expected, is located in correspondence of the Extreme Operating Gust with Direction Change (ECD) event. In correspondence with the transient event, due to the combination of high wind speed and yaw angle, the turbine shuts down. The shut-down procedure

is simulated by imposing a pitch-to-feather maneuverer starting at 506 s with a 10 °/s pitch rate. In DL, although the pitching maneuverer starts at 506 s, the blade reaches 90° pitch angle at 523 s, later than QB and OF. This delay is caused by differences in the way an override pitch procedure can be imposed in DL. For this reason, a comparison to DL is once again hard, and Fig. 4.13 is intended to rigorously compare OF and QB. Regardless of the differences, the shutdown procedure coupled with the transient event triggers similar behavior in the three analyzed codes. Some response at the blade and tower natural frequencies can be seen in the edgewise root bending moment and nacelle fore-aft acceleration in OF. Traces of this can also be seen in DL and QB but to a much lesser extent. High-amplitude oscillations at the edgewise natural frequency can be seen in Fig. 4.13, in DLC 6.3 where the peak loads of OF are recorded. Such instabilities were noted mostly in OF computation, sometimes even leading to crashes and incomplete simulations.

The highest tower base loads for this test case tend to be found in DLCs 6.1, 6.2 and 6.3, where the turbine is parked in extreme winds. With the exception of TB Fx for DL, that is recorded in DLC 1.6, this observation is consistent in all three codes. In particular, fore-aft force (TB Fx) and bending moment (TB My) are located in DLC 6.2 for QB and OF, and in DLC 1.6 and 6.1 for DL. Moreover, fore-aft loads are in good agreement between the codes, with QB often falling between OF and DL (table 4.4). Side-side tower base forces are located in DLC 6.2 for all three codes, indicating that parked conditions in severe yaw misalignment are the most severe for this load-sensor and test case combination. The dynamics that lead to fore-aft peak bending moments can be analyzed in more detail in Fig. 4.15. Peak load is shown on the left in DLC 6.2 for OF and QB, and it occurs in the same time instant in both codes. In this load case, although the shift in mean wind-speed is present for DL, all three codes agree quite well. Peak tower load occurs when platform pitch is at its peak and nacelle fore-aft acceleration is at its minimum, indicating a strong contribution to this load of inertial and gravitational loads. Inertial and gravitation loads on the tower have proven to be an important source of additional loading of FOWT towers, as shown, amongst others, in the studies of Robertson et. al. [101], Jonkman et al. [102], and more recently Papi et al. [103]. It must be noted that such loads are particularly significant for this test case as the tower developed for the OO-Star platform in the LifeS50+ H2020 project [104] was used, which is particularly heavy. In parekd conditions, good agreement in aerodynamic thrust is seen between OF and QB, although a large spike in thrust between 3020 and 3030 s can be seen in OF and not in QB. As can also be seen in Fig. 4.13, rotor thrust and torque tend to broadly follow the time series of pitch motion and nacelle acceleration although a time-lag is present as expected, as aerodynamic loads depend on relative wind velocity.

Time series where side-side peak bending moments are shown in Fig. 4.16 for OF (rigth) and QB (left). Platform roll, since this is a side-side load the side-side oscillation of the platform is plotted, and tower base load correlates nicely, as does nacelle side-side acceleration for QB and DL. For OF, nacelle acceleration is exported in a reference system that yaws with the nacelle, and therefore this output does not correspond to the one shown for QB and OF for this test case. When peak TB Mx is recorded for QB (Fig. 4.16 (a-f)), it can be noted that the dynamics of the system are very similar in all three codes. The srong correlation between roll oscillation and tower base bending moment indicates that

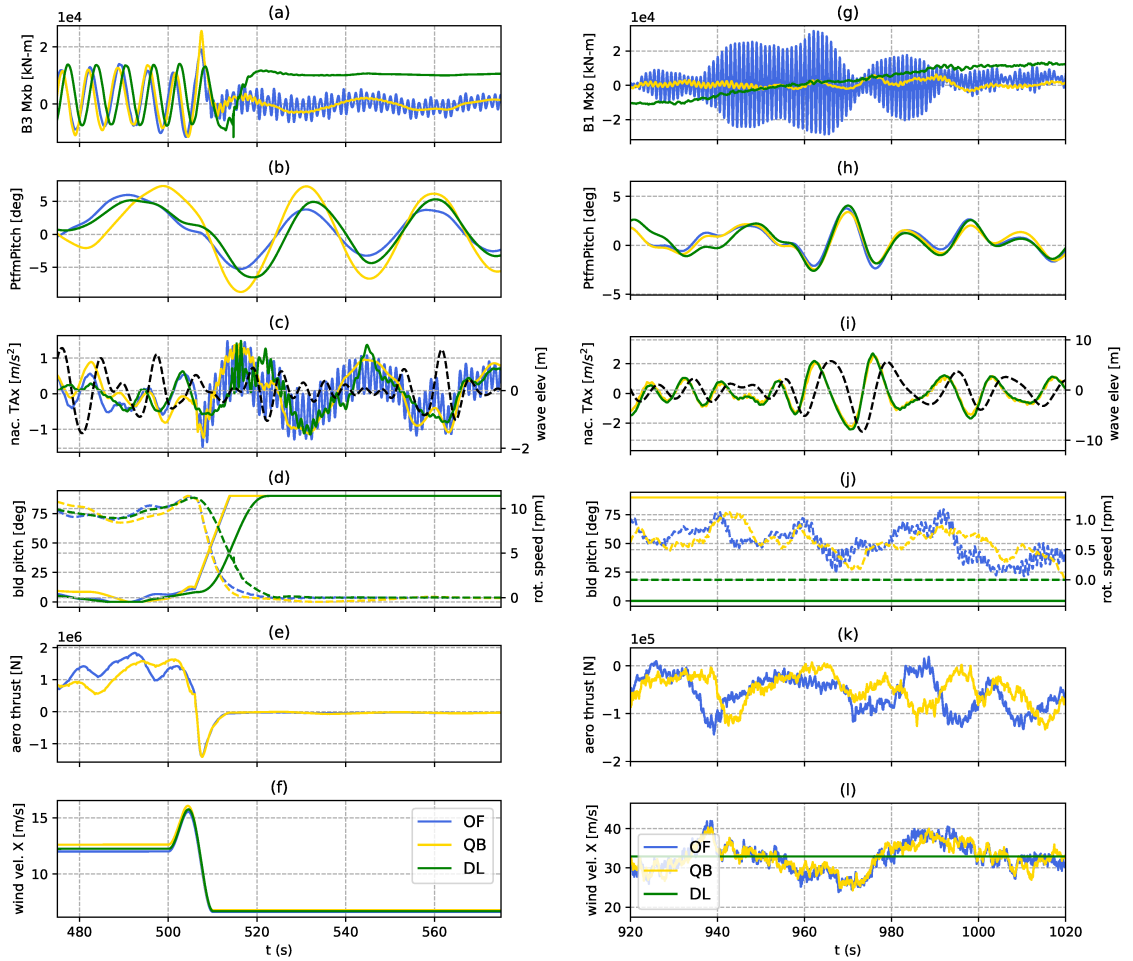

Figure 4.14: (a,g) Peak edgewise root bending moment (Mx) for QB (left, DLC1.4 seed 619 ECD+) and OF (right, DLC6.3 seed 10000 wave misalignment 0°, yaw 20°). (b,h) Platform Pitch, (c,i) nacelle fore-aft acceleration and wave elevation (right axis, dashed line), (d,j) blade pitch and rotor speed (right axis, dashed lines), (k,e) rotor aero thrust and torque (right axis, dashed line), (f,l) wind speed. Max(Mx) in DLC1.4, seed 638 ECD+ for DL.

gravitational and inertial loading are causing the most stress on the structure. On the other hand, when peak TB Mx is recorded for OF (Fig. 4.16 (g-l)), a strong oscillation at the tower first natural side-side frequency can be seen in OF, while DL exhibits almost no roll oscillations and thus very low side-side loads on the tower. The difference shown for DL may be due to different hydrodynamic tuning. As discussed previously, OF has consistently predicted higher natural frequency response in absence of aerodynamic damping, as this test case shows.

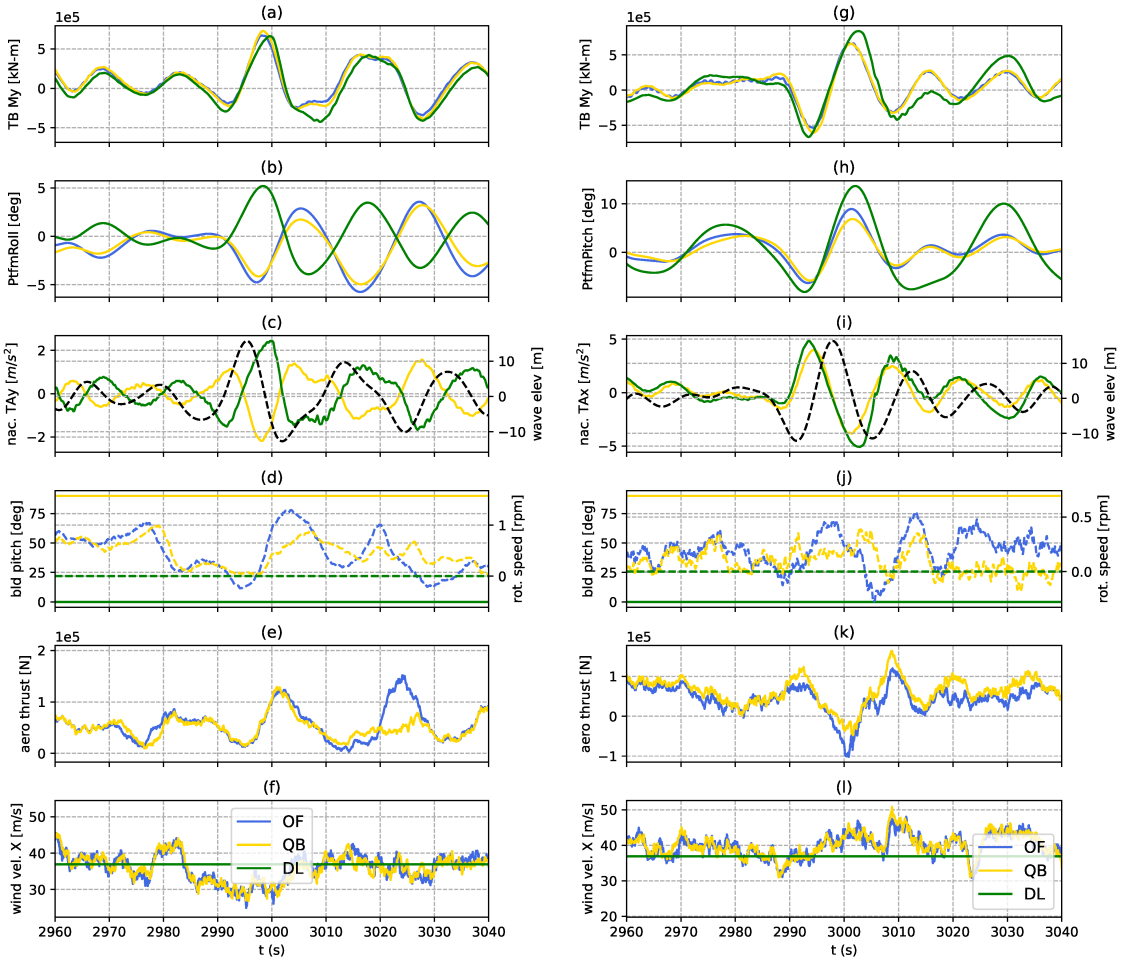

Figure 4.15: (a,g) Peak fore-aft tower base bending moment (My) for QB and OF (left, DLC6.2 seed 10002 yaw 135° -30° misalignment) and DL (right, DLC6.1 seed 10001 misalignment -30° yaw 0°). (b,h) Platform Pitch, (c,i) nacelle fore-aft acceleration and wave elevation (right axis, dashed line), (d,j) blade pitch and rotor speed (right axis, dashed lines), (e,k) rotor aero thrust and torque (right axis, dashed line), (f,l) wind speed.

NREL 5MW

Extreme loads of selected load sensors for the OC4 test case are shown in Table 4.5. Flapwise (BR Myb) and fore-aft (BR Myc) blade root bending moments are in good agreement. Fore-aft tower top force (TT Fx) and tower base bending moment (TB My) are also within 2% of each other. Tower base fore-aft force differs approximately 7%, very good agreement considering all the design situations involved. The large differences in blade root edgewise loads for OF are due to resonance issues in parked conditions, were aerodynamic damping is absent, as shown in the following. The relatively large difference in TB My can be imputed

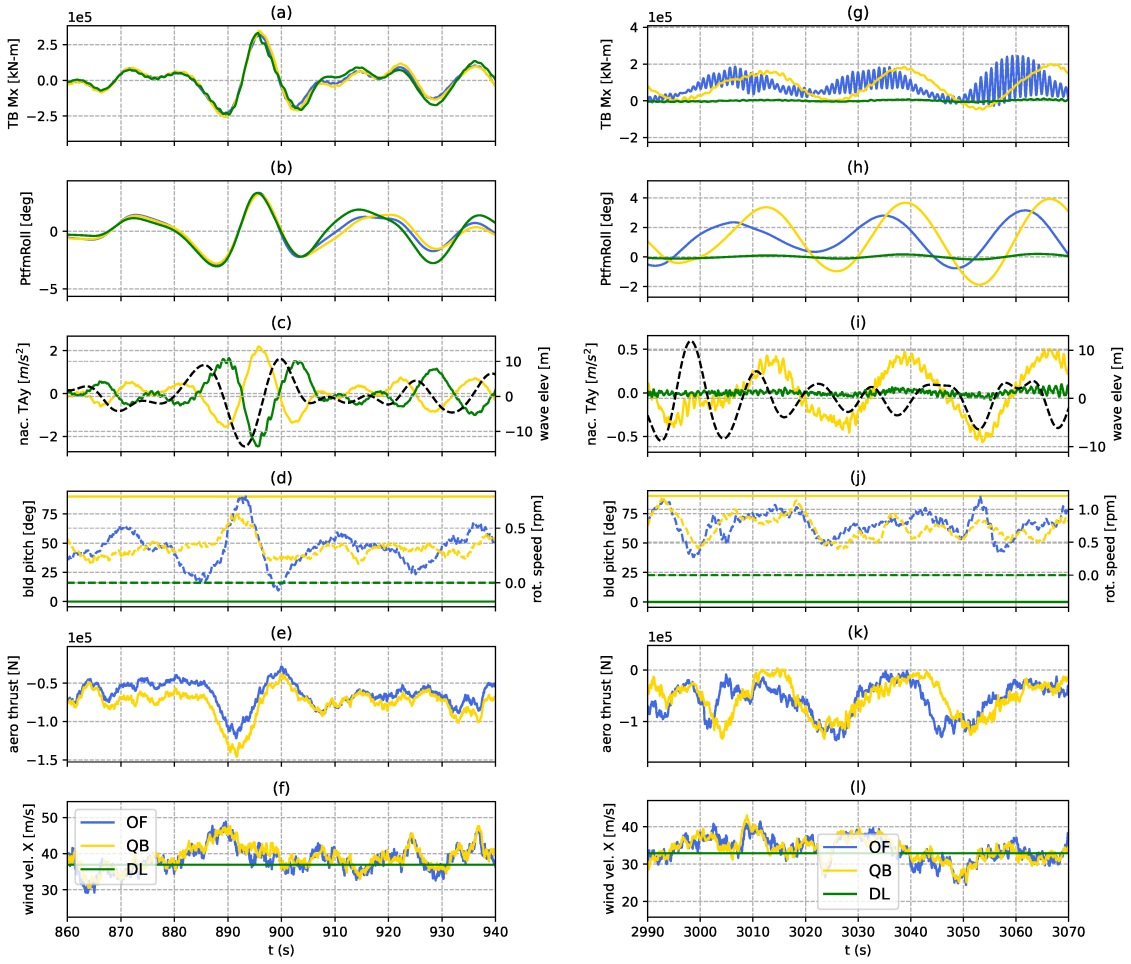

Figure 4.16: (a,g) Peak edgewise side-side tower base bending moment (Mx) for QB (left, DLC6.2 seed 10002 misalignment -30° yaw 135°) and OF (right, DLC6.1 seed 10001 misalignment 0° yaw 20°). (b,h) Platform Pitch, (c,i) nacelle fore-aft acceleration and wave elevation (right axis, dashed line), (d,j) blade pitch and rotor speed (right axis, dashed lines), (k,e) rotor aero thrust and torque (right axis, dashed line), (f,l) wind speed.

to structural dynamics, as shown in the following.

Time series relative to the recorded peaks in blade root flapwise bending moment (BR Myb) in QB and OF are shown in Fig. 4.17 (a-f) and (g-l), respectively. For this test case peak BR Myb is recorded in DLC 1.3, in simulations near rated, with 11 m/s mean wind speed. BR Myb is mainly influenced by aerodynamic loads and thus depends on the relative inflow velocity. Because of wind shear, the local azimuth of each blade has an influence on loads and since QB and OF predict different rotor speeds, blade azimuth will be different in the two codes. Fig. 4.17 (d,j) shows how rotor speed is higher for QB when wind speed dips below rated. This characteristic is noted in both the OC4 and SOFTWIND test cases

Table 4.5: Maximum component loads for the OC4 test case predicted with QB and OF.

Label	Units	DLC QB	DLC OF	QB value	OF value	OF-QB diff. (%)
B1R Mxb	kNm	1.4	6.2	9.095e+3	1.823e+4	100.42%
B2R Mxb	kNm	1.4	1.4	6.563e+3	8.791e+3	33.94%
B3R Mxb	kNm	1.3	6.2	5.997e+3	1.495e+4	149.23%
B1R Myb	kNm	1.3	1.3	1.418e+4	1.428e+4	0.72%
B2R Myb	kNm	1.3	1.3	1.389e+4	1.357e+4	-2.29%
B3R Myb	kNm	1.3	1.3	1.398e+4	1.412e+4	1.02%
BR Mxb	kNm	1.4	6.2	9.095e+3	1.823e+4	100.42%
BR Myb	kNm	1.3	1.3	1.418e+4	1.428e+4	0.72%
B1R Mxc	kNm	1.3	6.2	8.516e+3	9.780e+3	14.85%
B2R Mxc	kNm	1.3	1.4	8.585e+3	1.080e+4	25.77%
B3R Mxc	kNm	1.3	1.3	8.428e+3	8.667e+3	2.84%
B1R Myc	kNm	1.3	1.3	1.418e+4	1.420e+4	0.16%
B2R Myc	kNm	1.3	1.3	1.384e+4	1.355e+4	-2.09%
B3R Myc	kNm	1.3	1.3	1.369e+4	1.353e+4	-1.15%
BR Mxc	kNm	1.3	1.4	8.585e+3	1.080e+4	25.77%
BR Myc	kNm	1.3	1.3	1.418e+4	1.420e+4	0.16%
Thrust	kN	1.4	1.4	1.079e+3	1.049e+3	-2.78%
B1 Tip DX	m	1.6	1.3	7.465e+0	7.072e+0	-5.26%
B1 Tip DY	m	1.4	1.4	3.573e+0	4.814e+0	34.72%
Gen Tq	kNm	1.3	1.3	4.409e+1	4.309e+1	-2.26%
Gen Pwr	kW	1.6	1.6	6.686e+3	6.959e+3	4.09%
Aero Th	N	1.4	1.4	8.889e+5	8.531e+5	-4.02%
Aero Tq	Nm	1.6	1.6	1.195e+7	1.131e+7	-5.33%
TT Fx	kN	1.6	1.6	1.416e+3	1.439e+3	1.60%
TT Fy	kN	6.2	6.2	7.485e+2	6.879e+2	-8.10%
TB Fx	kN	6.2	6.2	1.898e+3	1.892e+3	-0.31%
TB Fy	kN	6.2	6.2	1.076e+3	9.803e+2	-8.93%
TB Mx	kNm	6.2	6.2	7.700e+4	6.464e+4	-16.05%
TB My	kNm	1.6	1.6	1.321e+5	1.307e+5	-1.07%
T ML1	kN	6.2	6.2	2.156e+3	2.360e+3	9.46%
T ML2	kN	6.1	6.1	6.065e+3	5.702e+3	-5.99%
T ML3	kN	6.1	6.1	2.235e+3	2.345e+3	4.93%
Surge	m	6.1	6.1	1.725e+1	1.555e+1	-9.86%
Sway	m	1.4	1.4	6.499e+0	6.699e+0	3.07%
Heave	m	6.2	6.2	1.115e+1	1.140e+1	2.21%
Roll	°	6.2	6.2	4.626e+0	4.506e+0	-2.59%
Pitch	°	6.2	6.2	9.314e+0	9.241e+0	-0.78%
Yaw	°	6.2	6.2	5.046e+0	4.657e+0	-7.72%

(Fig. 4.9 and 4.10) and also in previous code-to-code comparisons in onshore conditions [8]. In practice, this implies that the Tip Speed Ratio (TSR) is higher for QB, leading to higher aerodynamic thrust (Fig. 4.17 (e, k)). The higher thrust seems to be influencing platform pitch, that is on average higher for QB thrust (Fig. 4.17 (b, h)). Despite this, overall, blade root bending moments are very similar in magnitude, as if we consider the maximum value of BR Myb on all three blades OF is only 1% higher than QB (Table 4.5).

Time histories in correspondence with blade root edgewise peak loads are shown in Fig. 4.18. For this sensor, the DLC where peak loading occurs is not the same: DLC 1.4 for QB

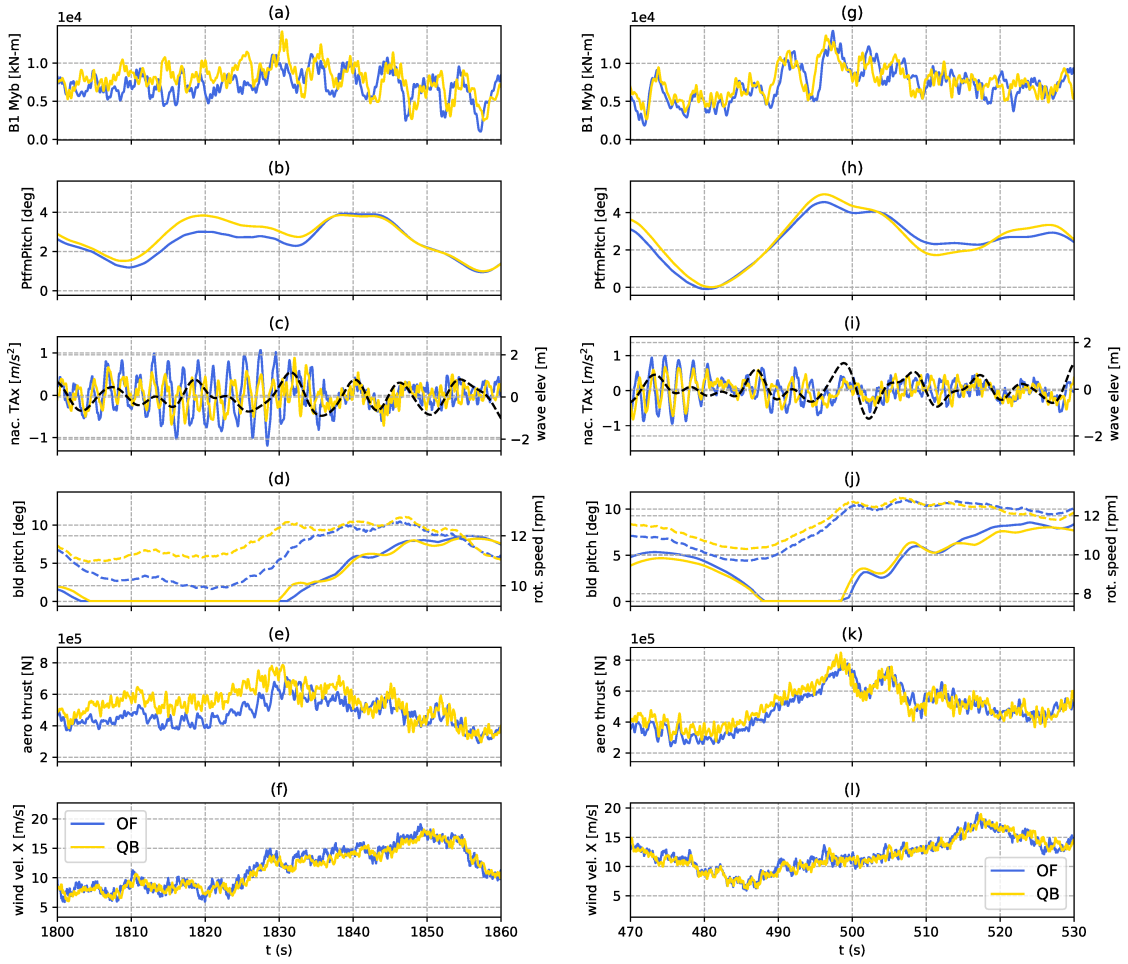

Figure 4.17: (a,g) Peak flapwise blade root bending moment (My) for QB (left, DLC1.3 seed 638) and OF (right, DLC1.3 seed 634). (b,h) Platform Pitch, (c,i) nacelle fore-aft acceleration and wave elevation (right axis, dashed line), (d,j) blade pitch and rotor speed (right axis, dashed lines), (e,k) rotor aero thrust (f,i) wind speed.

and DLC 6.2 for OF. These correspond respectively to operation with extreme direction change and parked in Extreme Sea State (ESS) with grid loss. Focusing on DLC 1.4 first, QB and OF behave very similarly in terms of rotor speed, blade pitch and aerodynamic thrust. The strong variation in aerodynamic thrust in correspondence with the transient wind gust event and subsequent shutdown is predicted quite well by the DBEM routine in OF if compared to the higher fidelity LLFVW model in QB. Once the rotor reaches a full stop, high frequency edgewise oscillations in blade root bending moment can be seen for OF in Fig. 4.18 (a). In QB these oscillations are much better damped. The same can be said for the tower. In fact, looking at tower fore-aft acceleration, it is apparent how OF exhibits large and less damped oscillations at the tower's natural frequency (Fig. 4.18 (c)). These

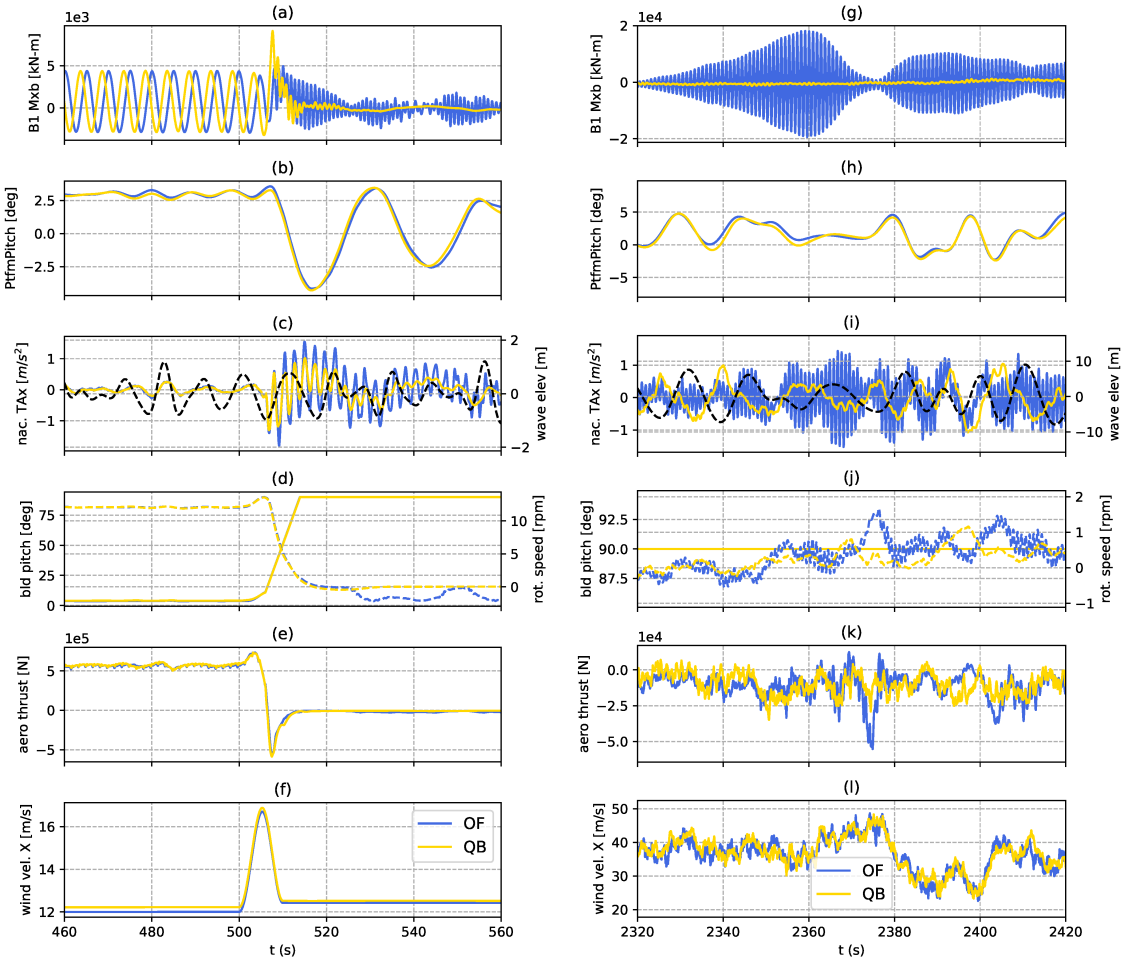

Figure 4.18: (a,g) Peak edgewise blade root bending moment (Mx) for QB (left, DLC1.4 seed 638) and OF (right, DLC6.2 seed 10002 mis 30° yaw 45°). (b,h) Platform pitch, (c,i) nacelle fore-aft acceleration and wave elevation (right axis, dashed line), (d,j) blade pitch and rotor speed (right axis, dashed lines), (e,k) rotor aero thrust (f,l) wind speed.

oscillations only become relevant once the rotor is parked and aerodynamic fore-aft damping is missing. Now analyzing DLC 6.2 (Fig. 4.18 (g-l)), a clear edgewise blade resonance in OF can be seen. This leads to peak loads that are nearly three times those recorded in QB. Instability at the system's natural frequencies was noted multiple times in OF (Figure 31) and also influences fatigue loads (Figure 80) and is most likely linked to the fact that OF uses a lower-fidelity modal based structural model.

Time series in proximity of the extreme recorded TB My are shown in Fig. 4.19. In both codes the extreme value is recorded in Severe Sea State (SSS) conditions (DLC 1.6) at an average wind speed of 23 m/s. In this condition, the higher rotor speed for QB that was visible in Fig. 4.19 (d, j) is not present, and aerodynamic thrust is quite similar in the

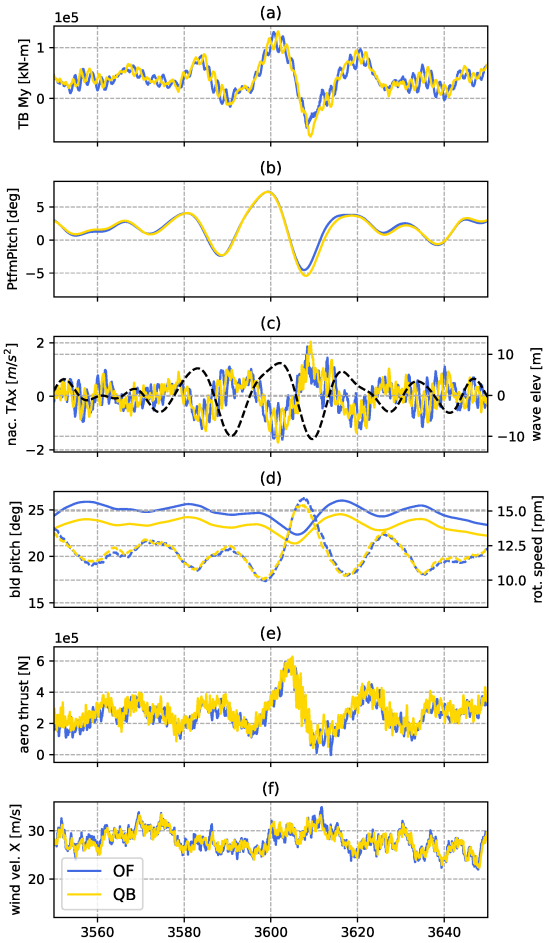

Figure 4.19: (a) Peak fore-aft tower base bending moment (My) for QB and OF (DLC1.6 seed 1096) Platform pitch, (c) nacelle fore-aft acceleration and wave elevation (right axis, dashed line), (d) blade pitch and rotor speed (right axis, dashed lines), (e) rotor aero thrust (f) wind speed.

two codes. Similar to the SOFTWIND test case, the TB My signal correlates quite well with the platform pitch Time series; this is an indication that hydrodynamic loading is an important driver of tower base bending moment on this test case too. In both Figs. 4.19 (a) and (g) oscillations around the tower's natural frequency of approximately 0.4 Hz can also be noted, more marked for OF than QB.

Finally, Time series in proximity of peak TB Mx are shown in Fig. 4.20. For both codes peak loads are recorded in parked conditions, in presence of grid loss (DLC 6.2), and large platform motions appear to be the main contributor to the peak loading. Although similar prediction of dynamics in parked conditions is noted between QB and OF in both Fig. 4.19 and Fig. 4.20, higher ultimate TB My s recorded in OF. Two main frequency components can be seen in the TB Mx signal in Fig. 4.20: one at wave-frequency, and the other, which

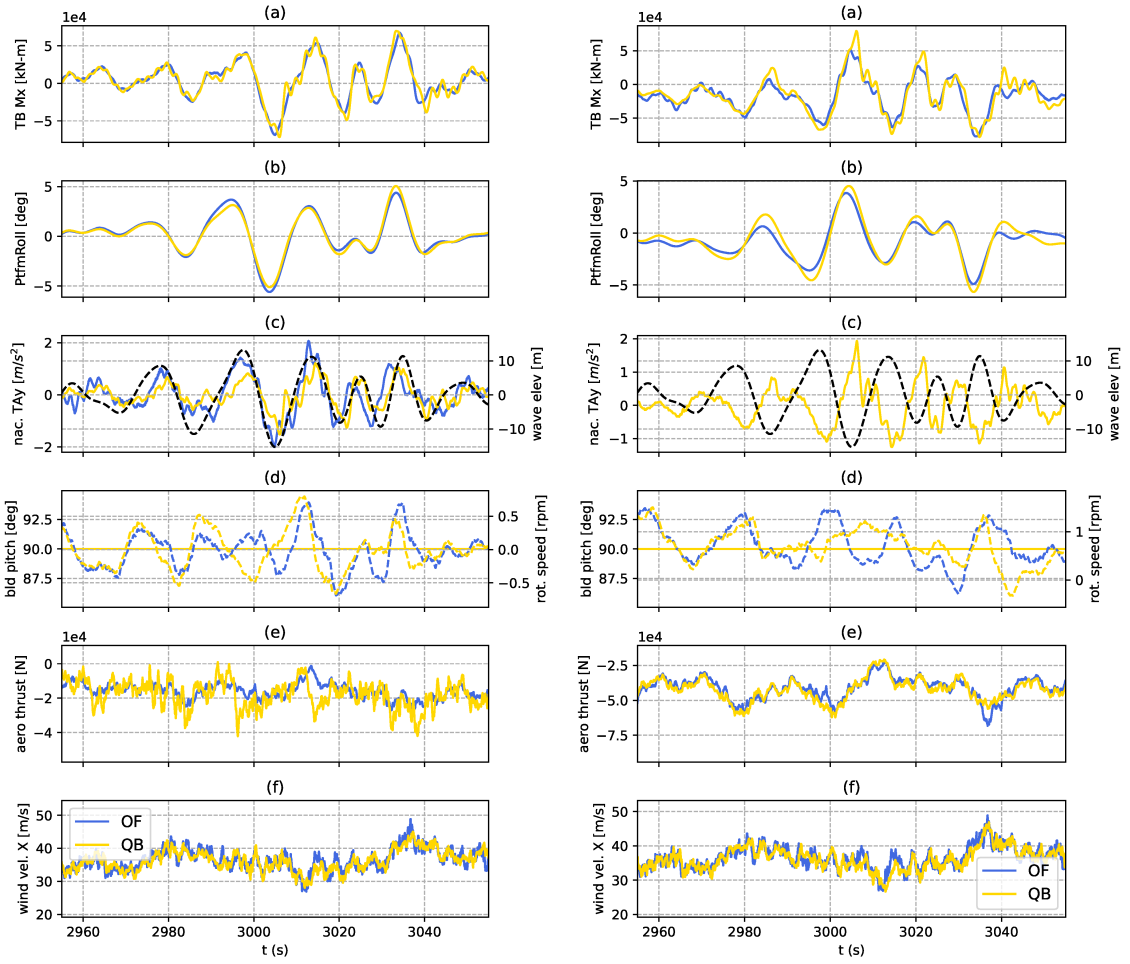

Figure 4.20: Peak side-side tower base bending moment (Mx) for QB (left, DLC6.2 seed 10003 mis 30° yaw 90°) and OF (right, DLC6.2 seed 10002 mis -30° yaw 90°) (b) Platform pitch, (c) nacelle fore-aft acceleration and wave elevation (right axis, dashed line), (d) blade pitch and rotor speed (right axis, dashed lines), (e) rotor aero thrust (f) wind speed.

generates a much smaller response, at the first tower side-side bending frequency. The latter seems to be more prominent in OF, and it's combination with wave-frequency excitation leads to the higher ultimate loads.

4.6.3 Fatigue loads

Structural fatigue is the accumulation of damage in a structure subject to stresses lower than the failure or tensile stresses of the structure. Wind turbine components are designed with a relatively long service life in mind, typically at least twenty years. Therefore, fatigue loads must be considered in the design of these structure and may be, in fact, design driving.

Comparisons of fatigue loads obtained with different fidelity modeling approaches have been performed in the past. Boorsma et al. [9] performed an extensive comparison of fatigue loads predicted by BEM and LLFVW models on an on-shore turbine. They found BEM to overestimate blade root flapwise fatigue loads with respect to LLFVW. Perez-Becker et al. [8] compared DELs predicted by the DBEM model in OF with the LLFVW model in QB during normal power production for the on-shore version of the DTU 10MW RWT. The same modal-based structural model that is used in OF, ElastoDyn, was used in both codes. The authors analyzed both blade root fin-plane bending moments and tower base fore-aft bending moment. Higher fatigue loads for BEM with respect to LLFVW were found.

In the case of FOWTs, Robertson et al. [67], compared several simulation codes to experiments of a scaled model of the NREL 5MW OC4 semi-submersible, commonly called NREL 5MW OC5, during the OC5 Phase II project. The participants to the project used various approaches for structural dynamics, hydrodynamics and moorings but most of them used BEM for aerodynamics. Most codes were found to under-predict fatigue loads. Average underprediction of 17% for tower top loads, and approximately 20% for tower base and mooring lines. The suggestions present is this work to help improve agreement with experiments, such as using a dynamic mooring line model, combining linear potential flow theory with second order load modeling and strip theory for quadratic drag, including wheeler wave stretching, using a dynamic wake and dynamic stall model for aerodynamics have all been included in the compared models.

In the recent work by Corniglion [105], aero-elastic LLFVW and BEM models of the IEA 15MW RWT in floating conditions are compared. Much like on onshore wind turbines, higher flapwise fatigue loads are found in case of the BEM model.

In this subsection, fatigue loads computed on the SOFTWIND 10MW and OC4 5MW test cases with varying fidelity models are compared. For the first time, the comparison is conducted on a significant number of simulations, encompassing various combinations of wind speed, wave height, peak spectral period and wind and wave direction, rather than on a limited number of test cases.

10MW SOFTWIND

Zero mean lifetime DELs for the SOFTWIND test case are shown in Fig. 4.6. Flapwise (BR Myb) and out of plane (BR Myc) lifetime DELs are significantly higher for OF respect to QB: 17% and 14% respectively. DL on the other hand predicts lifetime DELs smaller than QB, being approximately 2.7% lower. It must be noted that some simulations could not be completed in DL due to numerical instability. The effect of the missing simulations was not quantified but it will cause lower Lifetime DELs.

Despite blade root fatigue loads being higher for OF, this trend is not repeated as clearly

in other load sensors. In particular, tower top fore-aft force lifetime DEL (TT Fx) is lower for both OF and DL with respect to QB. However TT Fy is significantly higher for OF. The same conclusion can be drawn for side-side lower base loads such as TB Mx and TB Fy, that are higher for OF than they are in QB. In both cases, lifetime DELs predicted from DL are in much better agreement with QB. Although not shown in Fig. 4.24, the reason for the overestimation of tower side-side lifetime DELs for OF can be found in the higher response that is recorded at the tower side-side natural frequency of approximately 0.97 Hz. In particular, the response is markedly higher for OF than it is in QB and DL, that use more sophisticated modal-base structural models.

Table 4.6: Zero mean lifetime DELs for key load sensors for the SOFTWIND model. Percentage difference of DL values respect to QB predictions in right column.

Sensor	Units	Value QB	Value OF	Value DL	OF-QB diff. (%)	DL-QB diff. (%)
B1R Mxb	kNm	1.83E+04	1.90E+04	-	4.11%	-
B1R Myb	kNm	1.82E+04	2.11E+04	-	17.67%	-
B1R Mzb	kNm	3.26E+02	3.85E+02	-	23.70%	-
B1R Mxc	kNm	1.88E+04	1.98E+04	1.83E+04	5.27%	-2.62%
B1R Myc	kNm	1.70E+04	1.94E+04	1.65E+04	14.02%	-3.09%
B1R Mzc	kNm	3.26E+02	3.85E+02	6.22E+02	18.21%	90.93%
TT Fx	kN	7.48E+02	7.16E+02	6.86E+02	-4.27%	-8.30%
TT Fy	kN	3.56E+02	4.70E+02	3.46E+02	32.05%	-2.68%
TT Fz	kN	1.15E+02	1.19E+02	1.13E+02	3.99%	-1.79%
TT Mx	kNm	2.54E+03	1.91E+03	1.81E+03	-24.51%	-28.75%
TT My	kNm	9.06E+03	8.10E+03	8.04E+03	-10.55%	-11.22%
TT Mz	kNm	6.78E+03	6.88E+03	7.16E+03	1.43%	5.56%
TB Fx	kN	1.30E+03	1.24E+03	1.21E+03	-4.77%	-6.94%
TB Fy	kN	6.77E+02	7.07E+02	6.85E+02	4.46%	1.11%
TB Fz	kN	1.89E+02	1.90E+02	1.95E+02	0.48%	3.59%
TB Mx	kNm	5.12E+04	5.85E+04	5.07E+04	14.30%	-1.05%
TB My	kNm	1.03E+05	9.60E+04	9.40E+04	-6.70%	-8.66%
TB Mz	kNm	6.71E+03	6.88E+03	7.09E+03	2.49%	5.64%
RotThrust	kN	4.00E+02	4.07E+02	3.57E+02	1.71%	-10.84%
T ML1	kN	1.38E+02	1.47E+02	1.44E+02	6.97%	4.69%
T ML2	kN	1.58E+02	1.70E+02	1.66E+02	7.75%	4.89%
T ML3	kN	1.67E+02	1.77E+02	1.70E+02	6.07%	2.01%

Blade root 1 Hz DELs grouped by wind speed in the blade reference system are shown in Fig. 4.21. Placeholder values for DL in the coned reference system, that does not pitch with the blades are shown. Because the reference system does not pitch with the blades for DL, as blade pitch increases with increasing wind speed, we can expect differences to amplify. With respect to flapwise loads (BR My) OF tends to overestimate DELs respect to the other two codes at all wind speeds.

PSDs of edgewise (BR Mx) and flapwise (BR My) blade root loads are shown in Fig. 4.22 for various wind speeds during normal operation (DLC 1.2). For DL in-plane and out-of-plane loads are shown as placeholders. Edgewise bending moment is dominated by response at the blade passing frequency (1P). OF and QB are similar in this regard, but peaks are lower for DL at this frequency. Flapwise loads on the other hand are also influenced by low frequency components. These are the frequencies that turbulent wind is most likely to excite and where the controller is active. At 13 m/s (Fig. 4.22 (e)) a

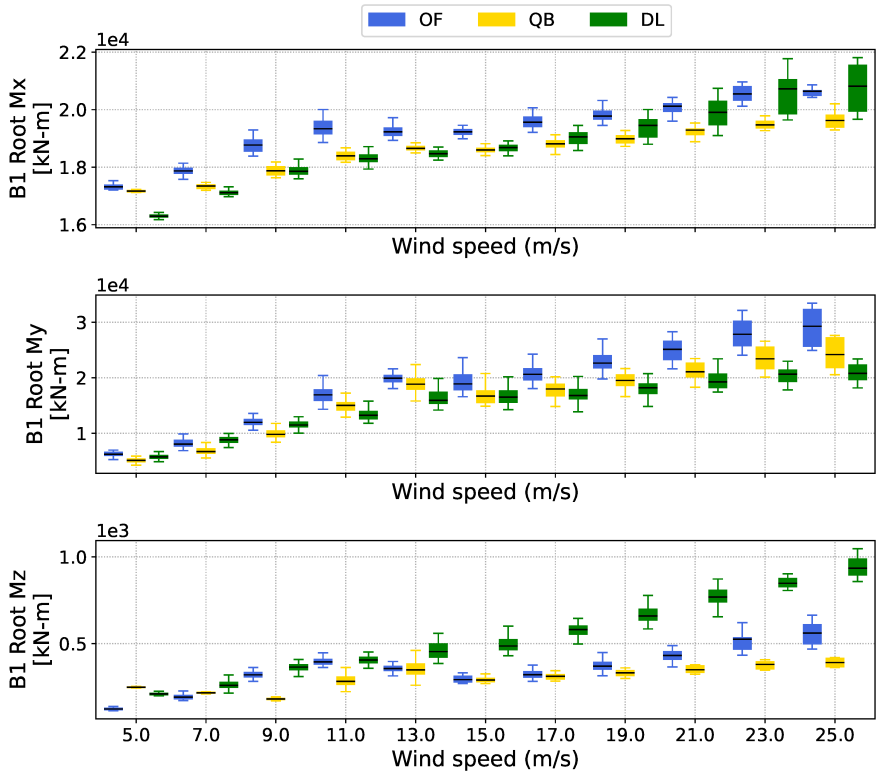

Figure 4.21: SOFTWIND spar floater DELs grouped by wind speed. Blade 1 root actions in blade reference system. The box extends from the lower to upper quartile values (boxes), medians (lines), whiskers (range of the data).

strong peak in correspondence of the floater pitch natural frequency appears in the BR My PSD. At 23 m/s (Fig. 4.22 (f)) mean wind speed response is again dominated by the blade passing frequency. Higher PSDs at the 1P frequency were also noted by some of the authors in a previous study, focused on onshore wind turbines [8], where they were attributed to differences in aerodynamic modeling. Particularly in differences in how non-uniform wind fields are treated.

1Hz DELs for the SOFTWIND testcase grouped by mean wind speed are shown in Fig. 4.23. The three codes generally agree well. Side-side DELs tend do increase linearly throughout the wind speed range, as these loads tend to be affected by the sea conditions, which get harsher as the wind speed increases (higher significant wave heights). On th other hand, fore-aft DELs show the influence of aerodynamic loading as well, as they tend to increase less rapidly after rated wind speed. From a comparative analysis, two main aspects stand out: Tower base fore-aft force and fore-aft bending moment 1-Hz DELs at 13 m/s mean wind speed are higher for QB than they are for DL and OF, and tower base side-side bending moment is higher for OF, and difference with respect to DL and QB tends

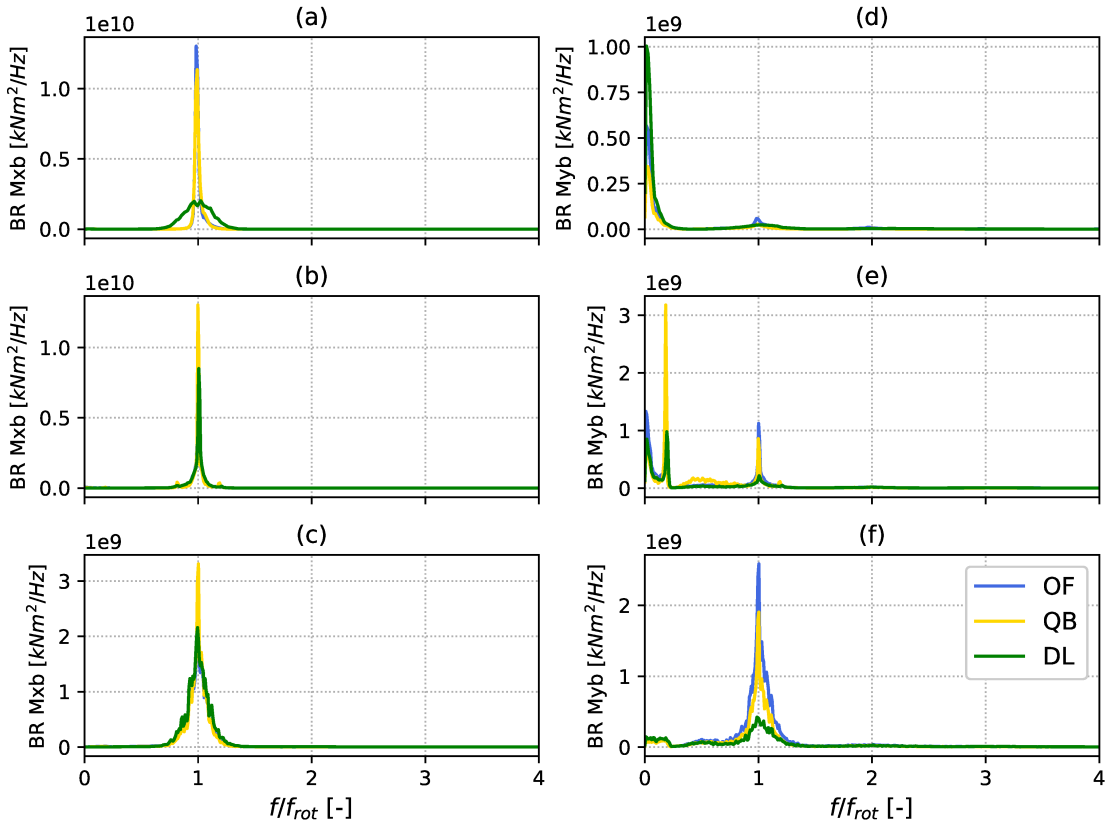

Figure 4.22: Power spectral density plots for edgewise (BR Mx) and flapwise (BR My) blade 1 root bending moments for SOFTWIND test case in DLC1.2: (a,d) 7 m/s wind speed, (b,e) 13 m/s wind speed, (c,f) 23 m/s wind speed. All simulations in a wind speed bin are concatenated and PSD is calculated on entire bin. For DL in-plane and out-of-plane loads are shown (BR Myb, BR Mxb).

to increase as wind speed increases. This latter aspect is caused by the tower side-side resonance effect that is noted in OF and was briefly discussed previously. It is apparent from Fig. 4.23 and from perusal of PSDs, that this effect tends to be more marked at higher wind speeds. On the other hand, the former difference explains why higher lifetime DELs are recorded in QB for fore-aft tower base sensors.

The PSDs of tower base bending moments for simulations with various mean wind speeds are shown in Fig. 4.23. The three codes generally show good agreement. The most notable difference among the three codes is shown in Fig. 4.23 (e), where the PSD of the tower base fore-aft bending moment in 13 m/s simulations is shown. The low frequency peak in correspondence of the platform pitch natural frequency is markedly higher in QB than it is in the other codes. Upon examination of time series data at this mean wind speed, this peak in response is found to be caused by strong interaction between platform

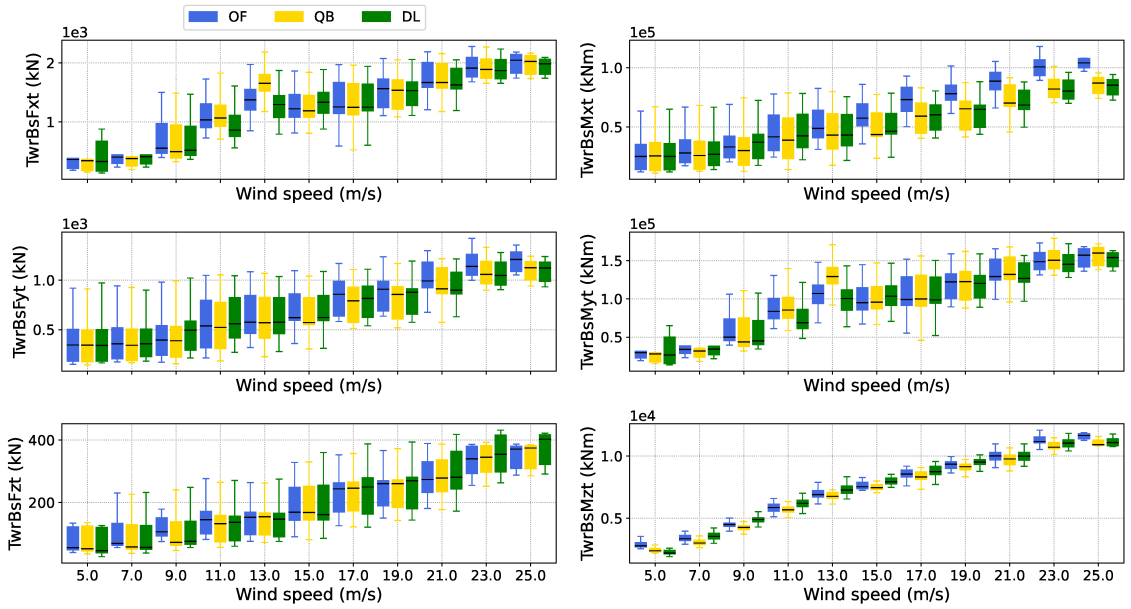

Figure 4.23: SOFTWIND spar floater DELs grouped by wind speed. Tower base data. The box extends from the lower to upper quartile values (boxes), medians (lines), whiskers (range of the data).

pitch and blade pitch at the platform resonance frequency. In fact, although the blade pitch controller's natural frequency was set to 0.02 Hz, well below the 0.03 Hz of the platform pitch resonance frequency, as discussed in section 4.5, the bandwidth of the controller resulted to be too high for certain wind speeds, notably 13 m/s simulations. The self excitation instability is noted in all three codes, but appears to be more severe in QB. While the reason for which this phenomenon is more severe in QB is unclear, it must be noted that as found in [8], especially near rated wind speed, where the controller may transition from below rated to above rated operation, slight differences in aerodynamic modeling may cause large differences in controller response.

5MW OC4

Zero mean Lifetime DELs for the OC4 test case are shown in Table 4.7. Lifetime DELs are generally higher for OF. Moderate increases of around 2-3% respect to QB can be seen for flapwise and in-plane blade root loads. TT Mx is affected by the minimum blade pitch saturation phenomenon that was discussed in section 4.5. Tower base fore-aft lifetime DELs (TB Fx, TB My) are approximately 11.5% higher for OF.

The blade root flapwise and edgewise 1Hz DELs grouped by mean wind speed are shown in Fig. 4.25. The relative difference between OF and QB tends to increase as wind speed increases for edgewise bending moment (Mx) and to decrease for flapwise bending moment (My).

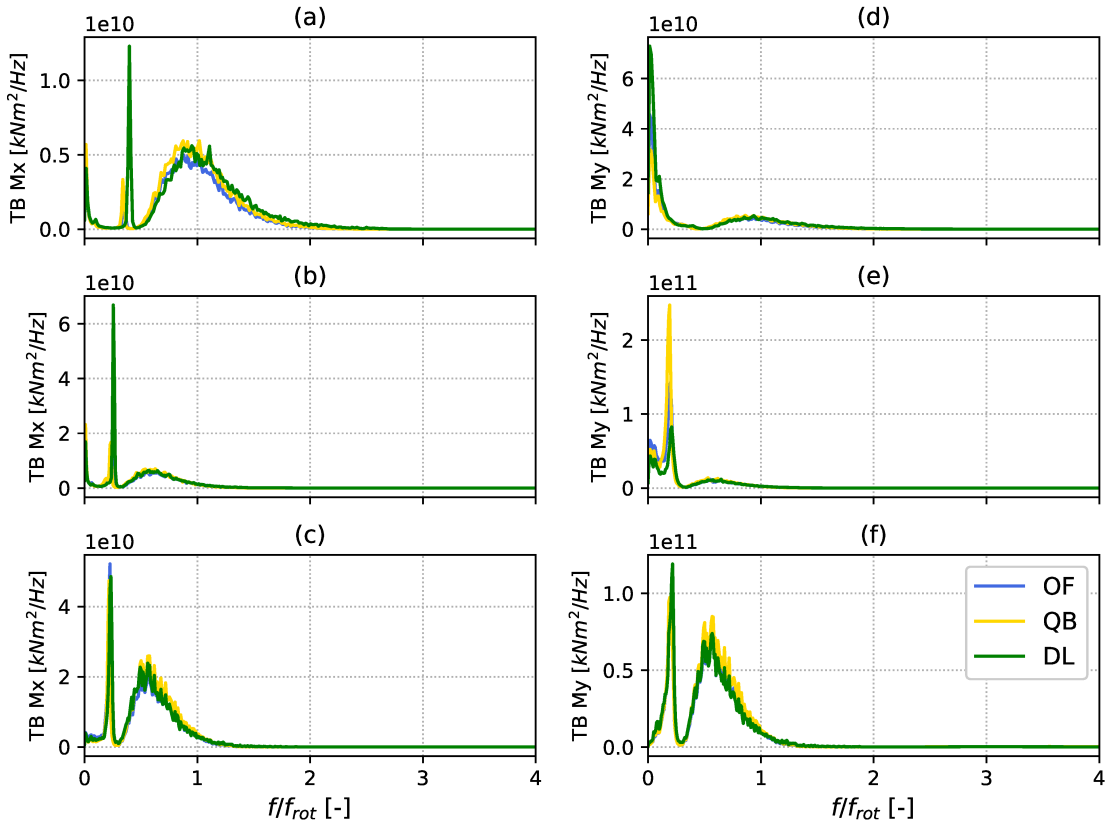

Figure 4.24: Power spectral density plots for side-side (TB Mx) and fore-aft (TB My) tower base bending moments for SOFTWIND test case in DLC1.2: (a,d) 7 m/s wind speed, (b,e) 13 m/s wind speed, (c,f) 23 m/s wind speed. All simulations in a wind speed bin are concatenated and PSD is calculated on entire bin. OF underprediction of TB My in wave frequency range discussed in section 9.2.2.

Further insight can be derived from observing Fig, 4.26, where Power Spectral Densities (PSD) of blade root edgewise (a-c) and flapwise (d-e) bending moments are shown. At 7 m/s mean wind speed (Fig. 4.26 (a,d)), the most energetic frequencies for edgewise bending moments are located around 1P. The frequency in Fig. 4.26 is normalized by the mean revolution frequency for each wind speed and for each code. Therefore, as rotational speed is not constant, a larger spread in Fig. 4.26 (a) indicates larger variations in rotor speed. Flapwise loads on the other hand (Fig. 4.26 (d)) are mostly driven by low-frequency components. These low frequencies are mostly excited by the turbulent wind and by the apparent wind that low frequency platform motions may cause. Response is larger for OF at these frequencies, as well as around 1P, although mostly insignificant at this mean wind speed. At higher wind speeds, BR Mx is dominated by 1P response, which is quite similar between the two codes (Fig. 4.26 (b,c)). Flapwise bending moment now also shows strong

Table 4.7: Zero mean lifetime DELs for key load sensors for the OC4 model. Percentage difference of OF values respect to QB predictions in right column.

Sensor	Units	Value QB	Value OF	OF-QB diff. (%)
BR Mxb	kNm	6304	6418	1.82%
BR Myb	kNm	6678	6794	1.74%
BR Mzb	kNm	114.8	99.93	-12.98%
BR Mxc	kNm	6523	6699	2.70%
BR Myc	kNm	6150	6185	0.58%
BR Mzc	kNm	114.8	99.93	-12.98%
TT Fx	kN	210	235.6	12.20%
TT Fy	kN	118.2	131	10.84%
TT Fz	kN	67.91	71.25	4.93%
TT Mx	kN	677.4	891.1	31.56%
TT My	kN	2819	2837	0.65%
TT Mz	kN	2888	2744	-4.99%
TB Fx	kN	260.4	290.1	11.43%
TB Fy	kN	154.6	168.9	9.24%
TB Fz	kNm	91.15	93.15	2.19%
TB Mx	kNm	10970	12020	9.63%
TB My	kNm	18200	20320	11.68%
TB Mz	kNm	2912	2744	-5.80%
RotThrust	[kN]	127.4	127.7	0.24%
T ML1	kN	44.56	46.16	3.60%
T ML2	kN	152.6	144.9	-5.03%
T ML3	kN	38.75	40.59	4.76%

response at the blade passing frequency ((Fig. 4.26 (e,f)). At 13 m/s mean wind speed the controller is transitioning between below rated operation – where torque control is active – to above-rated operation – where blade pitch control is active. In this region, small differences in aerodynamic loads can trigger this transition and cause significant loading differences, as observed in [8]. The de-rated controller that is used in the current study, is active in the low frequency range, below 1P, where QB and OF behave quite similarly. The most significant differences are observed at blade passing frequency. Such differences are also noted in [8] and could be attributed to the different treatment of the non-homogeneous turbulent wind field between QB and OF. At 23 m/s average wind speed ((Fig. 4.26 (f)), the most energetic signal components are again around 1P. A larger spread in frequencies can be noted for OF due to the increased variability in rotor speed respect to QB.

The near absence of low-frequency excitation in the PSDs can be attributed to the following factors; firstly, at high wind speeds relative speed variations are smaller than at lower wind ones, as defined by IEC standards [86]. Secondly, as blade pitch increases, loading shifts from the outer to the inner parts of the blades, decreasing the effect of load variations of bending moments. As observed by [8], 1P loads dominate the response, and they are mainly caused by the inhomogeneities in the wind field. Differently from [8], however, QB and OF are found to be in good agreement, and consequently the difference in DELs (table 4.7) are found to be small. Interestingly, there is no apparent trace in the PSDs of blade root bending moments, of response at the wave excitation frequency (located

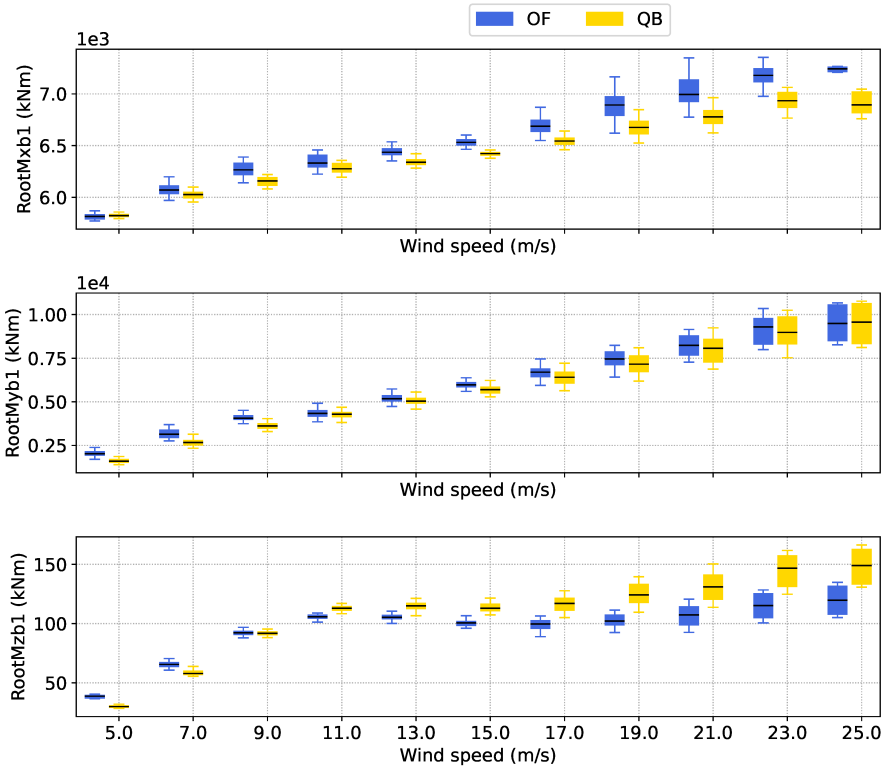

Figure 4.25: OC4 semi-sub floater DELs grouped by wind speed. Blade 1 root actions in blade ref. system. The box extends from the lower to upper quartile values (boxes), medians (lines), whiskers (range of the data).

approximately around half of the blade passing frequency for this test case). Finally, the PSDs inFig. 4.28 (e,f) suggest that wave induced motions do not contribute significantly to BR My loading for this test case. This is in contrast with the SOFTWIND test case, and also with the Hexafloat test case, as discussed later on, where the effect of platform motion on the BR My PSD can be clearly seen. A possible explanation for the reduced amplitude of the PSD of BR My in the wave-frequency range is given by Goupee et al. [64]. In fact, the authors found that the unique characteristics of the OC4 semi-submersible yield a net zero motion of the nacelle at 90m above sea water level in intermediate sea states. This is due to the fact that surge and pitch response are out of phase and tend to compensate each-other. If the wave-induced motion of the rotor is small, the fluctuations in relative velocity on the blade at the wave frequencies will also be small, leading to the observed differences with respect to the SOFTWIND test case

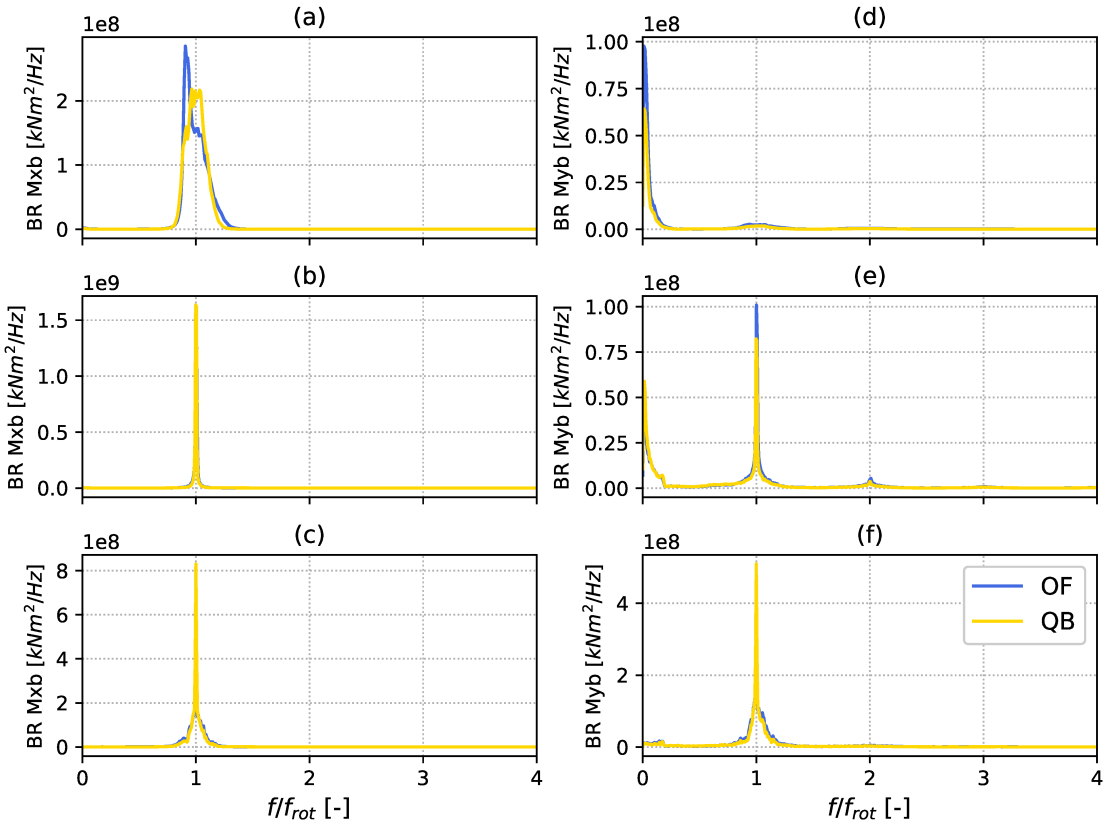

Figure 4.26: Power spectral density plots for edgewise (BR Mx) and flapwise (BR My) blade 1 root bending moments for OC4 test case in DLC1.2: (a,d) 7 m/s wind speed, (b,e) 13 m/s wind speed, (c,f) 23 m/s wind speed. All simulations in a wind speed bin are concatenated and PSD is calculated on entire bin.

4.7 Conclusions and outlook

In conclusion, the NREL 5MW on the OC4 semi-submersible platform and the DTU 10MW on the SOFTWIND spar platform, have both shown particular traits. For instance, blade root bending moments in the OC4 test cases look quite similar to an onshore turbine: peak flapwise loads are found in extreme turbulent inflow (DLC 1.3) and fatigue loads are mainly driven by wind excitation and 1P response. On the other hand, for the SOFTWIND platform, DLC 1.6 with extreme waves was often the DLC where the highest blade loads were recorded. Large variations in platform pitch angle have been noted in severe seas, that coupled with the structure's low center of gravity and high tower, have resulted in large platform-induced rotor motions and velocities, with negative values of aerodynamic thrust being recorded at times.

A statistical analysis of platform motions and control sensors during normal operation in a large variety of normal sea states, revealed good agreement between the codes. The

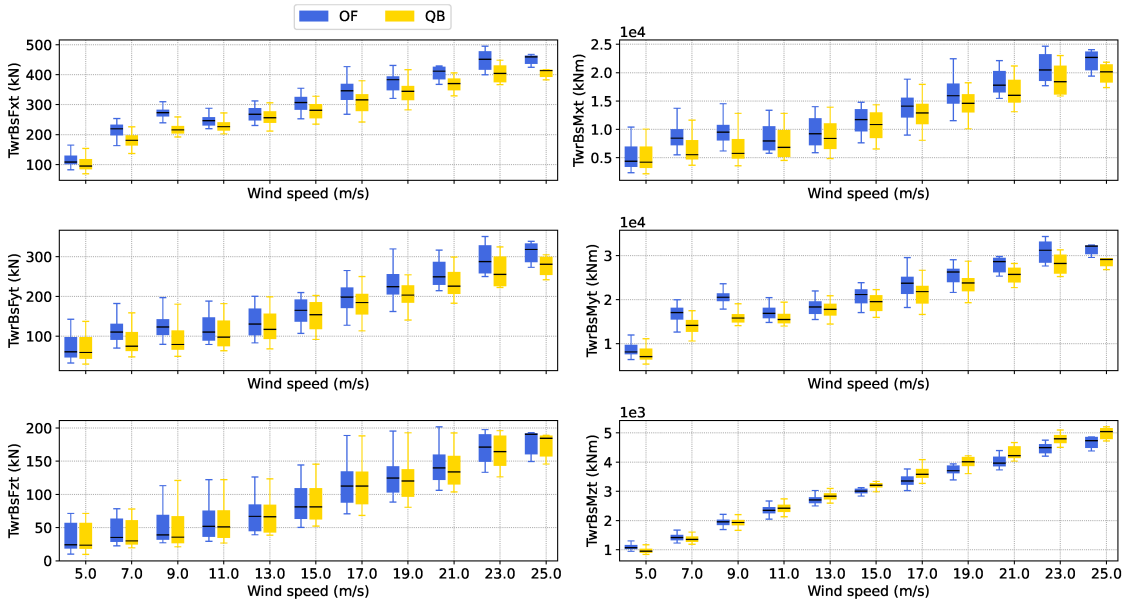

Figure 4.27: OC4 ssemi-sub floater DELs grouped by wind speed. Tower base data. The box extends from the lower to upper quartile values (boxes), medians (lines), whiskers (range of the data).

general operation of the wind turbine is predicted well during normal operation.

Extreme loads in the fore-aft - at tower base - and in the flapwise - at blade root - directions are also similar in the compared models. For the OC4 test case good consistency is note in the predicted extreme flapwise blade root loads. For this metric QB and OF are very similar. The predicted fore-aft tower top and tower base forces and moments are also very similar, being 1-1.6% lower in OF. Similar differences are noted for the SOFTWIND platform, flapwise blade root loads are 2-10% higher than QB for OF and and tower base fore-aft load predictions are within 6% of each-other. For the SOFTWIND tescase, blade root extreme loads are recorded during operation in DLC 1.3 or 1.6, while tower base extreme loads are recorded in parked conditions in DLC 6.1 and 6.3. The dynamics of the floating systems is relevant. In fact, platform motion influences rotor loads as it affects the inflow velocity, and also tower loads, as it introduces additional gravitational and inertial loading on the structure. For this reason, time series at and in proximity of the recorded extreme loads were analyzed. Very good agreement between OF and QB was noted for both test cases. For instance, for the SOFTWIND test case, extreme blade root flapwise loads are recorded in DLC 1.6, at high mean wind speeds, where the severe wave trains with a 50-year recurrence period induce large oscillations on the platform. Despite rotor thrust becoming negative due to the platform-induced large variations in inflow, the blade pitch controller reacts in a very similar manner in OF and QB.

In a previous study, extreme and fatigue loads in normal power production (DLC 1.2) for an on-shore turbine computed using a LLFVW and DBEM model are compared (Perez-

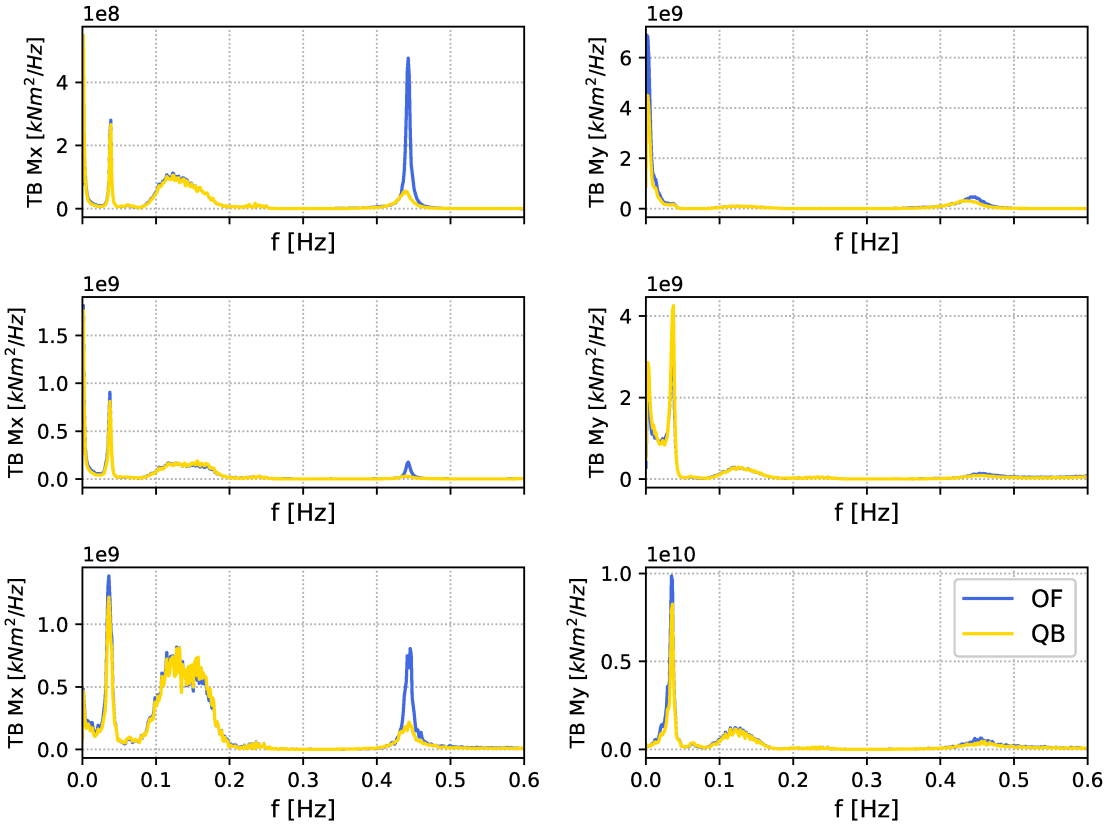

Figure 4.28: Power spectral density plots for side-side (TB Mx) and fore-aft (TB My) tower base bending moments for OC4 test case in DLC1.2: (a,d) 7 m/s wind speed, (b,e) 13 m/s wind speed, (c,f) 23 m/s wind speed. All simulations in a wind speed bin are concatenated and PSD is calculated on entire bin.

Becker et al. [8]). The same design codes, QB and OF are compared, although differently from the present study the same structural model used in OF is also implemented in QB, to compare aerodynamic models only. The two aerodynamic models are found to be similar in their prediction of out-of-plane blade root bending moment and fore-aft tower base bending moment ultimate load values. In this study, results are consistent with the findings of Perez-Becker et al. [8] in regard to ultimate loads: the different wake models and structural models used in OF and QB did not influence system dynamics significantly at the moment ultimate loads are recorded, and fore-aft ultimate loads are similar.

Load sensors whose extreme loads are recorded in DLCs where the turbine is parked are significantly influenced by the different structural models. These differences can be linked to the lack of aerodynamic damping when the turbine is parked. To explain aerodynamic damping let's consider a fore-aft oscillation of a rotor subject to steady uniform inflow with constant rotor speed. The oscillation will cause variations in thrust force: if the rotor

moves forward thrust increases and if it moves backwards it decreases. This aerodynamic force opposes fore-aft rotor - or blade - motion, and thus damps structural oscillations in this direction. In a wind turbine, this source of damping is much higher than structural damping in the structure. In absence of aerodynamic damping, large oscillations at the blade edgewise natural frequency are noted in OF, leading to very high edgewise loads. Similar phenomena were observed for side-side tower oscillations. As noted by Jonkman and Buhl [87], it is often hard to discern if these oscillations are a result of a numerical or physical instability. In fact on a FOWT, many external actions may excite the tower or blades natural frequencies, and could lead to resonance if undamped. In this work however, these oscillations were not noticed in DL and in QB, that both feature higher fidelity multibody structural models, indicating that the instability noted in OF is most likely numerical.

Contrary to extreme loads, differences in flapwise and fore-aft fatigue loads are noticed. Comparing zero-mean lifetime DELs, flapwise bending moments predicted by OF are 2% higher than QB in OC4 and 12% higher in SOFTWIND. The same was noted on fore-aft tower top and tower base loads for OC4, where OF predictions are 10-12% higher. On the other hand, OF and DL predictions of fore-aft tower fatigue loads for SOFTWIND are higher than QB. As explained in detail in the previous sections, this is due to higher floater pitch and blade pitch interaction that is noted near rated wind speed in QB. In a brader context, Corniglion [105] also noticed increases in DELs when using a DBEM aerodynamic model in the coupled simulation of a FOWT as opposed to a LLFVW model. Increases in out-of-plane and flapwise fatigue loads when using lower-fidelity DBEM models as opposed to LLFVW in the simulation of onshore turbines is also noticed by Perez-Becker et al. [8] and Boorsma et al. [9]. In both these works, the overestimation noted in DBEM is attributed to poor induction tracking with respect to LLFVW. In particular, in [9], authors show how in presence of sheared inflow, yaw misalignment and turbulence, all of which contribute to introducing 1P inflow variation on the blades, variations in axial induction in DBEM differ from those of LLFVW models. The spectral analyses performed on the data gathered in this study are in-line with these observations, as most of the differences between OF and QB are at the blade passing frequency or at low frequency, where the turbulence spectra carries significant energy.

A detailed comparison between fatigue loads computed on an offshore wind turbine and on a floating one was not performed in this study. Some examples of such can be found in the scientific literature such as the study performed by AlShuwaykh and Sharman [106] where DELs on the fixed and floating (OC4 semi-submersible platform) configurations of the NREL 5MW OC4 wind turbine are performed. In a previous study by Papi and Bianchini [103], fixed and floating configurations of the NREL 5MW and IEA 15MW (mounted on the U-Maine semi-submersible) are compared. In both cases blade root fatigue loads are found to be very similar to those computed for an onshore configuration of the machine and largely unaffected by floating installation. On the other hand, tower base fatigue loads increase significantly due to the additional gravitational and inertial loading cycles. In this context, the results of this study, comparing LLFVW and DBEM models with respect to Lifetime DELs of a FOWT, are in line with the load reductions that are observed for onshore turbines when using a higher fidelity LLFVW model.

Lastly, blade edgewise loads are similar in QB and OF as they are mostly driven by gravitational loading, as on an onshore wind turbine. Tower side-side fatigue loads on the OC4 test case are slightly higher in OF due to larger response at the first side-side tower bending frequency. As noted previously, in the cases were aerodynamic damping is low, differences in structural modeling affect loads significantly.

In this chapter the most sophisticated aerodynamic model that was considered is the LLFVW model, and no ALM simulations are performed. In fact, running a full set of DLCs like the ones performed within this study would currently require supercomputer level computational resources. Moreover, exactly matching input conditions, thus allowing for a time series comparison such as the one performed in this study, is more challenging when using a high fidelity tool such as ALM instead of engineering models such as LLFVW and BEM. In fact, when running test cases that include inflow turbulence, one must ensure a good match between turbulent inflow specified at the domain inlet in a CFD simulation and at the rotor plane in an engineering model. Crucially however, very good agreement between LLFVW and ALM is noted in Chapter 2. Therefore, rather than comparing low and medium fidelity aerodynamic models such as BEM and LLFVW to ALM, a three-way comparison between LLFVW, ALM and blade-resolved CFD could be a more interesting future prospect. In fact, while ALM models allow for high-fidelity wake modeling, they are subject to all the limitations of BEM and LLFVW in terms of blade modeling, as they still rely on spanwise 2D lift and drag distributions. Indeed some comparisons including high-fidelity models in simplified conditions have been attempted in the past, one such example being the study of Ortolani et al. [107]. In this study, good match in aggregated quantities such as rotor thrust and torque between a OF DBEMT and a blade-resolved CFD model of the NREL 5MW RWT was noted. However, differences of note were seen when considering blade-related values such as root bending moment, especially when yaw error is introduced in combination with the pitch oscillations. In the context of the current comparison, high-fidelity CFD could be applied to selected load cases in DLC 1.6, where especially in the SOFTWIND test case, negative rotor thrust is recorded as a result to extreme wave-induced motions, as shown in Fig. 4.13

In summary, the predictions of all three compared codes are similar in terms of overall system motion and behavior. The structural model is found to be important, as numerical instabilities are noted in OF, which uses a simple linear modal-based structural model, but not in QB and DL that use a multi-body FEA model. These differences emerged especially when aerodynamic damping is low. Difference in aerodynamic models are found to influence fatigue loads, where a reduction in fore-aft and flapwise DELs is noted for QB, but not extreme loads that are well predicted by both OF and QB. This difference is similar to that found in previous studies focusing on multi-fidelity analyses of onshore wind turbine and similar to the recent findings of other authors. The limits of of BEM-based aerodynamic theories that have been highlighted for onshore wind turbines carry over to floating ones, despite the large rotor movements that these turbines are subject to.

Chapter 5

Conclusions

In this dissertation, multi-fidelity simulation codes for the analysis of floating wind turbines are critically compared. Comparisons are mainly focused on the impact of different aerodynamic models, but the influence of multi-fidelity structural modeling and the effects of hydrodynamic engineering submodels such as wave stretching are also assessed. A three step approach is followed. At each step, the complexity of the problems that are simulated increases and a different aspect of the FOWT response is analyzed. In the first step, unsteady aerodynamic tests on the UNAFLOW 1/75 scale rotor, tested in the Politecnico di Milano wind tunnel are performed. Various wake models, namely BEM, DBEM, LLFVW and ALM are compared in their ability to predict oscillation in thrust and torque of a surging or pitching rotor. Various combinations of amplitude, frequency and operating conditions of the rotor in terms of tip speed ratio and wind speed are tested. In the second step, coupled aero-hydro-elastic simulations of the 1/50 scale NREL 5MW OC5 wave basin model tested at MARIN are performed. In this phase, the influence of BEM and LLFVW aerodynamics on the coupled response of the system in irregular wind and waves is evaluated. In the third and final step, code-to-code comparisons on full-scale turbines operating in realistic environmental conditions are performed. The influence of different sea states, operating conditions, wind-wave misalignment, to name a few, are assessed on two different rotors and floating platform archetypes: the DTU 10MW RWT mounted on the SOFTWIND spar platform and the NREL 5MW RWT mounted on the OC4 semi-submersible platform. Differently from the previous steps, the coupled influence of control and elastic rotor blades are considered in this step. Performance statistics, fatigue loads and ultimate loads predictions are compared.

5.1 Key findings

The most important findings of this three-phase work are summarized as follows:

- There is little agreement in the scientific community regarding how unsteady platform motion should be included into BEM-based aerodynamic models. In this dissertation, structural velocity, be it caused by aeroelastic deformation or by floating platform

motion, is treated the same way as a variation in relative wind speed. Therefore, it influences the undisturbed wind speed and it is included directly in the momentum balance. While this approach is questionable from a theoretical standpoint, it has proven to agree reasonably well with higher order theories in this work.

- Harmonic oscillations in pitch and surge of the UNAFLOW rotor in design conditions did not lead to the observation of significant dynamic inflow effects. Quasi-static BEM theory performed well with respect to higher-order models with the addition of the Øye dynamic induction model (DBEM). All the tested aerodyanic theories are in-line with experiments. Even relatively high-amplitude and high-frequency oscillations, leading to significant platform-induced relative velocities, did not lead to significant differences being observed. A possible explanation for this phenomenon can be found in the work of Corniglion et al. [59]. The authors argue that the change in the shape of the tip-vortex helix after a step change in surge speed, partially compensates for the change in induction. The relative magnitude of the two compensating effects is dependent on the specific rotor design and operating condition, therefore this conclusion may not be valid for a different turbine.

- Differences between models that include and don't include dynamic induction are observed if, in addition to a harmonic surge excitation, harmonic variations in rotor speed and blade pitch are introduced. In this case, DBEM predicts oscillations in rotor thrust and torque that are more similar to the higher order models than quasi-steady BEM. This was observed despite variations in axial induction being, in some cases, similar to those achieved in imposed surge tests with no variation of blade pitch or rotor speed. This observation is again in line with previous studies. In fact, as stated in [59], no variation in tip vortex helix can compensate for the induction change in the case of rotor speed or blade pitch variation, possibly explaining the observation of the dynamic inflow effect. On an actual floating turbine, which is influenced by the combined action of wind and waves, variations in rotor speed or blade pitch can be expected in the case of changes in relative inflow, making the variation that is found between aerodynamic models in this case significant.

- Forced surge and pitch oscillation tests at low wind speeds were also performed. This is a particularly challenging condition aerodynamically because the turbine is operating at a high TSR, and rotor load and induction are high as a consequence. Momentum-based aerodynamic theories are invalid for axial induction values above 0.5, and start to deviate from experiments, requiring empirical corrections, for axial induction values of approximately 0.4. In addition, because wind speed is low, platform induced velocity is comparable to the wind speed, leading to the observation of rotor-wake interaction. In these operating conditions, quasi-steady BEM is found to underpredict the unsteady rotor thrust and torque oscillations predicted by higher order aerodynamic models such as LLFVW and ALM. On the other hand, DBEM is found to improve agreement with these higher-order models.

- In the second phase of this work, LLFVW and DBEM are compared to experiments

of the NREL 5MW OC5 semi-submerisble model. Both LLFVW and DBEM are able to predict coupled dynamics comparatively well. In irregular wind and wave tests underprediction of ultimate and fatigue loads with respect to experiments is noted. Sensors that were measured experimentally, such as tower base loads and platform motion, where used as basis for the comparisons. Little to no improvement in this regard is granted by the use of a higher-fidelity LLFVW aerodynamic model. In this phase, the influence of control, and thus variations in blade pitch or rotor speed were not evaluated. As noted during simplified aerodynamic tests, these aspects may increase the differences between the numerical models.

- In realistic inflow conditions, under the influence of different sea states and misaligned wind and waves, the general dynamics of the system are also comparatively well predicted by the tested simulation codes featuring LLFVW and DBEM aerodynamic models, as well as multibody FEA and modal-based structural models.

- If OpenFAST, which features a DBEM aerodynamic model and a modal-based structural dynamics model and QBlade-Ocean, which features LLFVW aerodynamics and a multibody FEA structural model, are compared in terms of the predicted extreme design loads, no clear trend is noted and the predicted extreme loads are very similar, as long as extreme loads occur during normal operation. This consideration is valid for both the evaluated test cases, featuring a semi-submersible and spar-buoy floater designs. This result is in line with previous studies focused on onshore wind turbines [8], and floating installation did not change this aspect significantly. On the other hand, in parked conditions, or generally for degrees of freedom for which aerodynamic damping is low, large discrepancies between OpenFAST and QBlade-Ocean are noted. In particular, OpenFAST over-estimated extreme loads in parked conditions, where large oscillations at the natural frequencies of the affected components were noted. This phenomenon is attributed to the simplified modal-based structural dynamics, and is not present in DeepLines and QBlade-Ocean that feature higher-fidelity structural models.

- For load sensors that are influenced by aerodynamic loads, higher fatigue loads are predicted by OpenFAST. The overestimation is of the order of 2% to 15% approximately. Similar observations were made in previous studies [8], and in studies by other authors [9], where the higher fatigue loads with respect to LLFVW of the BEM based models are attributed to poor induction tracking in the BEM models. Given the fact that relative differences are found to be similar to the ones found on onshore turbines, the additional degrees of freedom granted to the rotor by the floating installation did not amplify or reduce the discrepancies between BEM and LLFVW models significantly.

5.2 Recommendations

In conclusion, relatively small but potentially significant differences between the multi-fidelity models that are evaluated in this work are found. In particular, Dynamic-BEM,

and specifically the implementation of DBEM that was tested within this work, consisting of the BEM theory described in section 1.1.1 and Øye's dynamic induction model as described in section 1.1.3, has shown good agreement with higher order aerodynamic theories. In addition to performing comparatively well in simplified aerodynamic tests with unsteady pitch and surge motion, BEM models with corrections for dynamic induction (DBEM), were able to reproduce the dynamics of a floating wind turbine similarly to LLFVW models. However, LLFVW remains a more solid theory, and does not need as many engineering submodels to extend its range of applicability as momentum theory based models do. Therefore, the use of these models should be pursued in medium-fidelity tools as much as possible. This is true especially in light of the differences in fatigue loads prediction that were found in this work as well as in other recent research of floating and onshore wind turbines. It is important to note that these considerations are valid for the numerical and physical models and conditions that were tested herein, and while representing a good indication of what sort of difference to expect between aerodynamic models for FOWTs, they are not of general validity. However, based on the results shown herein, despite its flaws, DBEM has shown to be a reliable method and to give good results in practice. Therefore it can represent a good basis for low-fidelity time-domain design exploration tools moving forward. The results of this dissertation also offer the opportunity of discussing the potential role of high-fidelity blade resolved simulations and experimental validation in improving FOWT modeling. Both are powerful tools that need to be exploited in combination with lower-fidelity tools that do not include explicit solution of the blades - such as the methods analyzed in this dissertation - to further understand and improve upon the limits of the latter models. Given the computational expense and complexity of these methods efforts should be put on simulations or tests that are more likely to lead to rotor-wake interaction, as none of the aerodynamic theories considered herein are able to fully resolve this phenomenon. Complex test-cases including coupled physics or complex motions should also be considered. In fact, as shown in this work, interaction with severe sea states in realistic met-ocean conditions can lead to large excursions in relative inflow, with instances where negative rotor thrust is observed. Multi-body FEA based structural models have proven to be more stable, especially in conditions where aerodynamic damping is low or absent. The use of these models over lower-fidelity modal based models should be promoted, especially for the modern highly flexible and complex turbine designs we have today. Lastly, all the multi-fidelity models compared in this work fell short of experimental load measurements of the NREL 5MW OC5 semi-submersible test model, despite the use of higher fidelity LLFVW aerodynamics and multibody structural dynamics. The deficiencies are ultimately related to hydrodynamics. This work has underlined the need, previously indicated by others [67], to move past second-order potential flow hydrodynamic modeling in pursue of improved low-frequency load prediction.

Bibliography

[1] Paul Veers et al. "Grand Challenges: wind energy research needs for a global energy transition". en. In: *Wind Energy Science* 7.6 (Dec. 2022), pp. 2491–2496. ISSN: 2366-7451. DOI: 10.5194/wes-7-2491-2022.

[2] Birte Holst Jørgensen et al. *DTU International Energy Report 2021 – Perspectives on Wind Energy*. en. Tech. rep. Artwork Size: 171 pages Medium: pdf. Danmarks Tekniske Universitet, Institut for Vindenergi, Risø Campus, 4000, Roskilde, Danmark, 2021, 171 pages. DOI: 10.11581/DTU.00000200.

[3] Paul Veers et al. "Grand challenges in the science of wind energy". en. In: *Science* 366.6464 (Oct. 2019), eaau2027. ISSN: 0036-8075, 1095-9203. DOI: 10.1126/science.aau2027.

[4] Paul Veers et al. *Grand Challenges in the Design, Manufacture, and Operation of Future Wind Turbine Systems*. en. preprint. Aerodynamics and hydrodynamics, Apr. 2022. DOI: 10.5194/wes-2022-32.

[5] Equinor. *HYWIND SCOTLAND - The world's first commercial floating wind farm*. EN.

[6] *WindFloat Atlantic Project*. en-US.

[7] J. Gordon Leishman. *Principles of Helicopter Aerodynamics*. en. Cambridge University Press, Dec. 2016. ISBN: 978-1-107-01335-3.

[8] Sebastian Perez-Becker et al. "Is the Blade Element Momentum theory overestimating wind turbine loads? – An aeroelastic comparison between OpenFAST's AeroDyn and QBlade's Lifting-Line Free Vortex Wake method". en. In: *Wind Energy Science* 5.2 (June 2020), pp. 721–743. ISSN: 2366-7451. DOI: 10.5194/wes-5-721-2020.

[9] K Boorsma and M Caboni. *Numerical analysis and validation of unsteady aerodynamics for floating offshore wind turbines*. en. Tech. rep. Delft, Netherlands: TNO, 2020, p. 136.

[10] T. Sebastian and M.A. Lackner. "Characterization of the unsteady aerodynamics of offshore floating wind turbines: Unsteady aerodynamics of offshore floating wind turbines". en. In: *Wind Energy* 16.3 (Apr. 2013), pp. 339–352. ISSN: 10954244. DOI: 10.1002/we.545.

[11] Néstor Ramos-García et al. "Investigation of the floating IEA Wind 15 MW RWT using vortex methods Part I: Flow regimes and wake recovery". en. In: *Wind Energy* 25.3 (2022). _eprint: https://onlinelibrary.wiley.com/doi/pdf/10.1002/we.2682, pp. 468–504. ISSN: 1099-1824. DOI: 10.1002/we.2682.

[12] Carlos Ferreira et al. "Dynamic inflow model for a Floating Horizontal Axis Wind Turbine in surge motion". en. In: *Wind Energ. Sci.* 7 (2022), pp. 469–485. DOI: 10.5194/wes-2021-34.

[13] M.L. Buhl Jr. *New Empirical Relationship between Thrust Coefficient and Induction Factor for the Turbulent Windmill State*. en. Tech. rep. NREL/TP-500-36834, 15016819. Aug. 2005, NREL/TP–500–36834, 15016819. DOI: 10.2172/15016819.

[14] Martin O. L. Hansen. *Aerodynamics of wind turbines*. en. 2nd ed. OCLC: ocm86172940. London ; Sterling, VA: Earthscan, 2008. ISBN: 978-1-84407-438-9.

[15] S. Andrew Ning. "A simple solution method for the blade element momentum equations with guaranteed convergence: Guaranteed solution of the BEM equations". en. In: *Wind Energy* (July 2013), n/a–n/a. ISSN: 10954244. DOI: 10.1002/we.1636.

[16] Andrew Ning et al. "Development and Validation of a New Blade Element Momentum Skewed-Wake Model within AeroDyn". en. In: *33rd Wind Energy Symposium*. Kissimmee, Florida: American Institute of Aeronautics and Astronautics, Jan. 2015. ISBN: 978-1-62410-344-5. DOI: 10.2514/6.2015-0215.

[17] J.M. Jonkman et al. *AeroDyn User's Guide and Theory Manual*. Technical Report. NREL.

[18] J.M. Jonkman et al. *AeroDyn v15 User's Guide and Theory Manual*. Technical Report. NREL.

[19] H. Snel and J. G. Schepers. "Joint investigation of dynamic inflow effects and implementation of an engineering method". English. In: (Apr. 1995).

[20] E. Branlard et al. "Dynamic inflow and unsteady aerodynamics models for modal and stability analyses in OpenFAST". en. In: *Journal of Physics: Conference Series* 2265.3 (May 2022). Publisher: IOP Publishing, p. 032044. ISSN: 1742-6596. DOI: 10.1088/1742-6596/2265/3/032044.

[21] Kelsey Shaler, Emmanuel Branlard, and Andrew Platt. *OLAF User's Guide and Theory Manual*. English. Tech. rep. NREL/TP-5000-75959. National Renewable Energy Lab. (NREL), Golden, CO (United States), June 2020. DOI: 10.2172/1659853.

[22] David Marten. "QBlade: a modern tool for the aeroelastic simulation of wind turbines". en. In: (2020).

[23] A. Van Garrel. "Development of a wind turbine aerodynamics simulation module". English. In: (Aug. 2003).

[24] Jens No"rkær So"rensen and Wen Zhong Shen. "Numerical Modeling of Wind Turbine Wakes". In: *Journal of Fluids Engineering* 124.2 (May 2002), pp. 393–399. ISSN: 0098-2202. DOI: 10.1115/1.1471361.

[25] Shengbai Xie. "An actuator-line model with Lagrangian-averaged velocity sampling and piecewise projection for wind turbine simulations". en. In: *Wind Energy* 24.10 (2021). _eprint: https://onlinelibrary.wiley.com/doi/pdf/10.1002/we.2619, pp. 1095–1106. ISSN: 1099-1824. DOI: 10.1002/we.2619.

[26] Eva Jost et al. "Extracting the angle of attack on rotor blades from CFD simulations". en. In: *Wind Energy* 21.10 (2018), pp. 807–822. ISSN: 1099-1824. DOI: 10.1002/we.2196.

[27] Francesco Papi et al. "Development and Validation of an Advanced Actuator Line Model for Wind Turbines". en. In: *E3S Web of Conferences* 312 (2021). Publisher: EDP Sciences, p. 08004. ISSN: 2267-1242. DOI: 10.1051/e3sconf/202131208004.

[28] Pier Francesco Melani et al. "An experimental and numerical analysis of the dynamic variation of the angle of attack in a vertical-axis wind turbine". In: *Journal of Physics: Conference Series* 1618 (Sept. 2020), p. 052064. DOI: 10.1088/1742-6596/1618/5/052064.

[29] Jason M. Jonkman, Amy N Robertson, and Gregory J. Hayman. *HydroDyn User's Guide and Theory Manual*. Tech. rep.

[30] C. H. Lee. *WAMIT Theory Manual*. Tech. rep. 95-2. Massachussetes Institute of Technology, Oct. 1995.

[31] *4.2.7. ElastoDyn Users Guide and Theory Manual — OpenFAST v3.3.0 documentation*.

[32] Matthew Hall. *MoorDyn User's Guide*. Tech. rep.

[33] Alessandro Tasora et al. "Chrono: An Open Source Multi-physics Dynamics Engine". en. In: *High Performance Computing in Science and Engineering*. Ed. by Tomáš Kozubek et al. Lecture Notes in Computer Science. Cham: Springer International Publishing, 2016, pp. 19–49. ISBN: 978-3-319-40361-8. DOI: 10.1007/978-3-319-40361-8_2.

[34] Sebastian Perez-Becker et al. *D2.2. Validation Report of QBlade-Ocean*. en. Tech. rep., p. 93.

[35] J. N. Sørensen, W. Z. Shen, and X. Munduate. "Analysis of wake states by a full-field actuator disc model". en. In: *Wind Energy* 1.2 (1998), pp. 73–88. ISSN: 1099-1824. DOI: 10.1002/(SICI)1099-1824(199812)1:2<73::AID-WE12>3.0.CO;2-L.

[36] Stig Øye. *Tjæreborg Wind Turbine: 4. dynamic inflow measurement*. Report. Publication Title: Tjæreborg Wind Turbine. Lyngby, 1991.

[37] J. G. Schepers. "Engineering models in wind energy aerodynamics: Development, implementation and analysis using dedicated aerodynamic measurements". en. In: (2012).

[38] Roger Bergua and et. al. "OC6 Project Phase III: Validation of the Aerodynamic Loading on a Wind Turbine Rotor Undergoing Large Motion Caused by a Floating Support Structure". In: *submitted to Wind Energy Science Journal [preprint]* (Aug. 2022).

[39] Alessandro Fontanella et al. "UNAFLOW: a holistic wind tunnel experiment about the aerodynamic response of floating wind turbines under imposed surge motion". English. In: *Wind Energy Science* 6.5 (Sept. 2021). Publisher: Copernicus GmbH, pp. 1169–1190. ISSN: 2366-7443. DOI: 10.5194/wes-6-1169-2021.

[40] Christian Bak et al. *Description of the DTU 10MW Reference Wind Turbine*. EN. Tech. rep. DTU Wind Energy Report I-0092. Roskilde, Denmark: DTU Wind Energy, July 2013, p. 138.

[41] Simone Mancini et al. "Characterization of the unsteady aerodynamic response of a floating offshore wind turbine to surge motion". en. In: *Wind Energy Science* 5.4 (Dec. 2020), pp. 1713–1730. ISSN: 2366-7451. DOI: 10.5194/wes-5-1713-2020.

[42] I. Bayati et al. "On the functional design of the DTU10 MW wind turbine scale model of LIFES50+ project". en. In: *Journal of Physics: Conference Series* 753 (Sept. 2016), p. 052018. ISSN: 1742-6588, 1742-6596. DOI: 10.1088/1742-6596/753/5/052018.

[43] Ilmas Bayati et al. "Scale model technology for floating offshore wind turbines". en. In: *IET Renewable Power Generation* 11.9 (2017), pp. 1120–1126. ISSN: 1752-1424. DOI: 10.1049/iet-rpg.2016.0956.

[44] Luca Bernini et al. *UNsteady Aerodynamics for Floating Wind (UNAFLOW)*. EN. Tech. rep. IRPWIND, Feb. 2018, p. 37.

[45] Amy Robertson et al. "OC6 Phase III Definition Document". en. In: (), p. 22.

[46] I. Bayati et al. "Experimental investigation of the unsteady aerodynamics of FOWT through PIV and hot-wire wake measurements". en. In: *Journal of Physics: Conference Series* 1037 (June 2018), p. 052024. ISSN: 1742-6588, 1742-6596. DOI: 10.1088/1742-6596/1037/5/052024.

[47] Stefano et al. Cioni. "On the Charachteristics of the Near and Far Wake of a Wind Turbine Undergoing Large Motions Caused by a Floating Structire: an Insight Based on Experiments and Multi-fidelity Simulations from the OC6 Phase III Project - to be subitted". In: *Wind Energy Science Discussions - TO BE SUBMITTED* (2023).

[48] Pieter Inghels. "Wind tunnel blockage corrections for wind turbine measurements". en. In: ().

[49] Rick R. Damiani and Gregory Hayman. *The Unsteady Aerodynamics Module For FAST8*. en. Tech. rep. NREL/TP–5000-66347, 1576488. Nov. 2019, NREL/TP–5000–66347, 1576488. DOI: 10.2172/1576488.

[50] Emmanuel Branlard et al. "A multipurpose lifting-line flow solver for arbitrary wind energy concepts". English. In: *Wind Energy Science* 7.2 (Mar. 2022). Publisher: Copernicus GmbH, pp. 455–467. ISSN: 2366-7443. DOI: 10.5194/wes-7-455-2022.

[51] *CONVERGE Manual v3.0*. Tech. rep. Convergent Science, May 2020.

[52] Rèmi Corniglion et al. "Comparison of the free vortex wake and actuator line methods to study the loads of a wind turbine in imposed surge motion". en. In: *Journal of Physics: Conference Series* 1618.5 (Sept. 2020). Publisher: IOP Publishing, p. 052045. ISSN: 1742-6596. DOI: 10.1088/1742-6596/1618/5/052045.

[53] A F P Ribeiro, D Casalino, and C S Ferreira. "Surging Wind Turbine Simulations with a Free Wake Panel Method". en. In: *Journal of Physics: Conference Series* 2265.4 (May 2022), p. 042027. ISSN: 1742-6588, 1742-6596. DOI: 10.1088/1742-6596/2265/4/042027.

[54] Matthew Lackner. "Challenges in Offshore Wind Energy Aerodynamics: Floating Wind Turbines and Wind Farms". en. In: (), p. 21.

[55] I. Bayati et al. "Wind tunnel validation of AeroDyn within LIFES50+ project: imposed Surge and Pitch tests". en. In: *Journal of Physics: Conference Series* 753 (Sept. 2016). Publisher: IOP Publishing, p. 092001. ISSN: 1742-6596. DOI: 10.1088/1742-6596/753/9/092001.

[56] P J Moriarty and A C Hansen. *AeroDyn Theory Manual*. en. Tech. rep. NREL/TP-500-36881, 15014831. Jan. 2005, NREL/TP–500–36881, 15014831. DOI: 10.2172/15014831.

[57] J. Jonkman et al. *Definition of a 5-MW Reference Wind Turbine for Offshore System Development*. en. Tech. rep. NREL/TP-500-38060, 947422. Feb. 2009, NREL/TP–500–38060, 947422. DOI: 10.2172/947422.

[58] Evan Gaertner et al. *Definition of the IEA 15-Megawatt Offshore Reference Wind Turbine*. Technical Report NREL/TP-5000-76773. Golden, CO: NREL, July 2020.

[59] Rémi Corniglion, Jeffrey C. Harris, and Christophe Peyrard. "The aerodynamics of a blade pitch, rotor speed, and surge step for a wind turbine regarding dynamic inflow". en. In: *Wind Energy* 25.5 (May 2022), pp. 858–880. ISSN: 1095-4244, 1099-1824. DOI: 10.1002/we.2702.

[60] Cédric Le Cunff et al. "Fully Coupled Floating Wind Turbine Simulator Based on Nonlinear Finite Element Method: Part I — Methodology". en. In: *Volume 8: Ocean Renewable Energy*. Nantes, France: American Society of Mechanical Engineers, June 2013, V008T09A050. ISBN: 978-0-7918-5542-3. DOI: 10.1115/OMAE2013-10780.

[61] F. Blondel et al. "Validation and comparison of aerodynamic modelling approaches for wind turbines". en. In: *Journal of Physics: Conference Series* 753 (Sept. 2016), p. 022029. ISSN: 1742-6588, 1742-6596. DOI: 10.1088/1742-6596/753/2/022029.

[62] Simone Mancini et al. "An engineering modification to the blade element momentum method for floating wind turbines". en. In: *Journal of Physics: Conference Series* 2265.4 (May 2022), p. 042017. ISSN: 1742-6588, 1742-6596. DOI: 10.1088/1742-6596/2265/4/042017.

[63] A Robertson et al. *Definition of the OC5 DeepCwind Semisubmersible Floating System*. en. Tech. rep., p. 44.

[64] Andrew J. Goupee et al. "Experimental Comparison of Three Floating Wind Turbine Concepts". en. In: *Journal of Offshore Mechanics and Arctic Engineering* 136.2 (May 2014), p. 020906. ISSN: 0892-7219, 1528-896X. DOI: 10.1115/1.4025804.

[65] Richard Kimball et al. "Wind/Wave Basin Verification of a Performance-Matched Scale-Model Wind Turbine on a Floating Offshore Wind Turbine Platform". en. In: *Volume 9B: Ocean Renewable Energy*. San Francisco, California, USA: American Society of Mechanical Engineers, June 2014, V09BT09A025. ISBN: 978-0-7918-4554-7. DOI: 10.1115/OMAE2014-24166.

[66] R. Behrens de Luna et al. "Comparison of different fidelity aerodynamic solvers on the IEA 10 MW turbine including novel tip extension geometries". en. In: *Journal of Physics: Conference Series* 2265.3 (May 2022). Publisher: IOP Publishing, p. 032002. ISSN: 1742-6596. DOI: 10.1088/1742-6596/2265/3/032002.

[67] Amy N. Robertson et al. "OC5 Project Phase II: Validation of Global Loads of the DeepCwind Floating Semisubmersible Wind Turbine". en. In: *Energy Procedia* 137 (Oct. 2017), pp. 38–57. ISSN: 18766102. DOI: 10.1016/j.egypro.2017.10.333.

[68] Fabian Wendt, Amy Robertson, and Jason Jonkman. "Verification and Validation of the New Dynamic Mooring Modules Available in FAST v8: Preprint". en. In: (), p. 14.

[69] A Goupee. "A Calibrated Blade-Element/Momentum Theory Aerodynamic Model of the MARIN Stock Wind Turbine: Preprint". en. In: Kona, Hawaii, 2015, p. 11.

[70] Fabian Wendt, Amy Robertson, and Jason Jonkman. "FAST Model Calibration and Validation of the OC5-DeepCwind Floating Offshore Wind System Against Wave Tank Test Data". en. In: *International Journal of Offshore and Polar Engineering*. Vol. 29. San Francisco, California, 2017, pp. 15–23. DOI: 10.17736/ijope.2019.jc729.

[71] A N Robertson et al. "OC6 Phase I: Investigating the underprediction of low-frequency hydrodynamic loads and responses of a floating wind turbine". en. In: *Journal of Physics: Conference Series* 1618 (Sept. 2020), p. 032033. ISSN: 1742-6588, 1742-6596. DOI: 10.1088/1742-6596/1618/3/032033.

[72] Lu Wang et al. "OC6 phase I: Improvements to the OpenFAST predictions of nonlinear, low-frequency responses of a floating offshore wind turbine platform". English. In: *Renewable Energy* 187 (Jan. 2022). Institution: National Renewable Energy Lab. (NREL), Golden, CO (United States) Number: NREL/JA-5000-81554 Publisher: Elsevier. ISSN: 0960-1481. DOI: 10.1016/j.renene.2022.01.053.

[73] Antonia Krieger et al. *D7.2 LIFEs50+ Design Basis*.

[74] Fernando Vigara et al. *COREWIND D1.2 Design Basis*. Sept. 2020. DOI: 10.5281/zenodo.4518828.

[75] Gordon M Stewart. "Design Load Analysis of Two Floating Offshore Wind Turbine Concepts". en. PhD thesis. University of Massachusetts Amherst. DOI: 10.7275/7627466.0.

[76] F. Papi, Y. Perignon, and A. Bianchini. "Derivation of Met-Ocean Conditions for the Simulation of Floating Wind Turbines: a European case study". en. In: *Journal of Physics: Conference Series* 2385.1 (Dec. 2022). Publisher: IOP Publishing, p. 012117. ISSN: 1742-6596. DOI: 10.1088/1742-6596/2385/1/012117.

[77] Andreas F. Haselsteiner et al. "Global Hierarchical Models for Wind and Wave Contours: Physical Interpretations of the Dependence Functions". en. In: *Volume 2A: Structures, Safety, and Reliability*. Virtual, Online: American Society of Mechanical Engineers, Aug. 2020, V02AT02A047. ISBN: 978-0-7918-8432-4. DOI: 10.1115/OMAE2020-18668.

[78] Andreas F. Haselsteiner et al. "ViroCon: A software to compute multivariate extremes using the environmental contour method". en. In: *SoftwareX* 9 (Jan. 2019), pp. 95–101. ISSN: 2352-7110. DOI: 10.1016/j.softx.2019.01.003.

[79] Gordon M. Stewart et al. "The creation of a comprehensive metocean data set for offshore wind turbine simulations: Comprehensive metocean data set". en. In: *Wind Energy* 19.6 (June 2016), pp. 1151–1159. ISSN: 10954244. DOI: 10.1002/we.1881.

[80] Hans Hersbach et al. "The ERA5 global reanalysis". en. In: *Quarterly Journal of the Royal Meteorological Society* 146.730 (July 2020), pp. 1999–2049. ISSN: 0035-9009, 1477-870X. DOI: 10.1002/qj.3803.

[81] Joanne Jeppesen. *Fact sheet: Earth system data assimilation*. en. Text. Mar. 2020.

[82] Internationale Elektrotechnische Kommission, ed. *Design requirements for floating offshore wind turbines*. eng. Edition 1.0. Wind energy generation systems / International Electrotechnical Commission Part 3 2. Geneva, Switzerland: International Electrotechnical Commission, 2019. ISBN: 978-2-8322-5986-3.

[83] Murray Rosenblatt. "REMARKS ON A MULTIVARIATE TRANSFORMATION". en. In: *The Annals of Mathematical Statistics* Vol. 23, No. 3, pp. 470-472 (Sept. 1952), p. 3.

[84] Steven R Winterstein, Alok K Jha, and Satyendra Kumar. "Reliability of Floating Structures: Extreme Response and Load Factor Design". en. In: *Journal of Waterway, Port, Coastal and Ocean Engineering* 125 (1999), p. 7.

[85] V. Valamanesh, A. T. Myers, and S. R. Arwade. "Multivariate analysis of extreme metocean conditions for offshore wind turbines". en. In: *Structural Safety* 55 (July 2015), pp. 60–69. ISSN: 0167-4730. DOI: 10.1016/j.strusafe.2015.03.002.

[86] Internationale Elektrotechnische Kommission, ed. *Design requirements for floating offshore wind turbines*. eng. Edition 1.0. Wind energy generation systems / International Electrotechnical Commission Part 3 1. Geneva, Switzerland: International Electrotechnical Commission, 2019. ISBN: 978-2-8322-7609-9.

[87] J M Jonkman and M L Buhl. "Loads Analysis of a Floating Offshore Wind Turbine Using Fully Coupled Simulation: Preprint". en. In: Los Angeles, California, 2007, p. 35.

[88] Gkv Ramachandran et al. "Design Basis for the Feasibility Evaluation of Four Different Floater Designs". en. In: *Energy Procedia* 137 (Oct. 2017), pp. 186–195. ISSN: 18766102. DOI: 10.1016/j.egypro.2017.10.345.

[89] Christopher Allen et al. *Definition of the UMaine VolturnUS-S Reference Platform Developed for the IEA Wind 15-Megawatt Offshore Reference Wind Turbine*. en. Tech. rep. NREL/TP-5000-76773, 1660012, MainId:9434. July 2020, NREL/TP–5000–76773, 1660012, MainId:9434. DOI: 10.2172/1660012.

[90] A. Robertson et al. *Definition of the Semisubmersible Floating System for Phase II of OC4*. en. Tech. rep. NREL/TP-5000-60601, 1155123. Sept. 2014, NREL/TP–5000–60601, 1155123. DOI: 10.2172/1155123.

[91] J. Jonkman. *Definition of the Floating System for Phase IV of OC3*. en. Tech. rep. NREL/TP-500-47535, 979456. May 2010, NREL/TP–500–47535, 979456. DOI: 10.2172/979456.

[92] Vincent Arnal. "Experimental modelling of a floating wind turbine using a "software-in-the-loop" approach". These de doctorat. Ecole centrale de Nantes, Dec. 2020.

[93] Mareike Leimeister, Athanasios Kolios, and Maurizio Collu. "Development and Verification of an Aero-Hydro-Servo-Elastic Coupled Model of Dynamics for FOWT, Based on the MoWiT Library". en. In: (2020), p. 33.

[94] Francesco Papi et al. *D2.3. Design Load Case Database for Code-to-Code Comparison*. Tech. rep. Oct. 2022.

[95] B J Jonkman. "TurbSim User's Guide v2.00.00". en. In: *Renewable Energy* (2014).

[96] O. Falstein. *Sea Loads on Ships and Offshore Structures*. Technology Series. Cambridge University Press, 1993.

[97] Nikhar J. Abbas et al. "A reference open-source controller for fixed and floating offshore wind turbines". English. In: *Wind Energy Science* 7.1 (Jan. 2022). Publisher: Copernicus GmbH, pp. 53–73. ISSN: 2366-7443. DOI: 10.5194/wes-7-53-2022.

[98] *ROSCO Toolbox. Version 1.0.0*. Tech. rep. GitHub, 2020.

[99] Nikhar J. Abbas, Alan D. Wright, and Lucy Pao. *An Update to the NREL Baseline Wind Turbine Controller: Preprint*. English. Tech. rep. NREL/CP-5000-75433. National Renewable Energy Lab. (NREL), Golden, CO (United States), Feb. 2020.

[100] Marshall Buhl. "MExtremes User's Guide". en. In: (2015), p. 9.

[101] A Robertson and J Jonkman. "Loads Analysis of Several Offshore Floating Wind Turbine Concepts". en. In: (), p. 10.

[102] J. M. Jonkman. *Dynamics Modeling and Loads Analysis of an Offshore Floating Wind Turbine*. en. Tech. rep. NREL/TP-500-41958, 921803. Dec. 2007, NREL/TP–500–41958, 921803. DOI: 10.2172/921803.

[103] F. Papi and A. Bianchini. "Technical challenges in floating offshore wind turbine upscaling: A critical analysis based on the NREL 5 MW and IEA 15 MW Reference Turbines". en. In: *Renewable and Sustainable Energy Reviews* 162 (July 2022), p. 112489. ISSN: 1364-0321. DOI: 10.1016/j.rser.2022.112489.

[104] Wei Yu. "D4.2 Public Definition of the Two LIFES50+ 10MW Floater Concepts". en. In: (), p. 32.

[105] Rémi Corniglion. "aero-elastic modeling of floating wind turbines with vortex methods". en. PhD Thesis. École des Ponts ParisTech, 2022.

[106] Ahmed AlShuwaykh and Krish Thiagarajan Sharman. "Analysis of platform motions effect on the fatigue loads and aerodynamic unsteadiness in floating offshore wind turbines". en. In: *Journal of Physics: Conference Series*. Proceeding of NAWEA Wind Tech 2019 1452.1 (Jan. 2020), p. 012030. ISSN: 1742-6588, 1742-6596. DOI: 10.1088/1742-6596/1452/1/012030.

[107] Andrea Ortolani et al. "Computational Fluid Dynamics Analysis of Floating Offshore Wind Turbines in Severe Pitching Conditions". en. In: *Journal of Engineering for Gas Turbines and Power* 142.12 (Dec. 2020), p. 121003. ISSN: 0742-4795, 1528-8919. DOI: 10.1115/1.4048776.